Thèse n° 8384

Three-dimensional fabrication of sub-micron optical waveguides in PDMS and other polymer materials

Présentée le 9 septembre 2021

Faculté des sciences et techniques de l’ingénieur
Laboratoire d’optique
Programme doctoral en photonique

pour l’obtention du grade de Docteur ès Sciences

par

Giulia PANUSA

Acceptée sur proposition du jury

Prof. Y. Bellouard, président du jury
Prof. D. Psaltis, Dr Y. Pu, directeurs de thèse
Prof. A. d’Alessandro, rapporteur
Prof. M. Farsari, rapporteuse
Prof. S. Lacour, rapporteuse

École
polytechnique
fédérale
de Lausanne

2021

Macte nova virtute, puer, sic itur ad astra.

Publio Virgilio Marone

Acknowledgements

First of all and foremost, I would like to express my gratitude to Prof. Demetri Psaltis, for giving me the precious opportunity to be a member of his research group and for trusting me from the very beginning of my PhD. I would like to thank him for his advises, the ideas and the support; most importantly I would like to thank him for showing me what passion for Science means.

My immense gratitude goes to Ye Pu, incredible scientist and important reference person in our group. I want to thank him for his guidance and supervision throughout my entire PhD. Thank you for your patience and for being always available to teach, discuss and clarify my doubts. This work wouldn't have been possible without your fundamental presence. I also want to thank you for becoming my friend, and for supporting me personally in the difficult moments.

I would like to thank Prof. Christophe Moser for all his ideas and the fruitful discussions we had in the past years.

Importantly, I would like to thank the members of my thesis committee, Prof. Yves Bellouard, Prof. Stephanie Lacour, Prof. Maria Farsari and Prof. Antonio d'Alessandro. I would like to thank them for the time they devoted reading this thesis, and for giving me their insightful contribution.

I would like to express my gratitude to my project partner team from Sonova, Martin Grossöhmichen, Tim Nauwelaers and Konstantin Silberzahn. I would like to thank them for trusting my work and for their professionality.

I would like to thank the present members of the Optics Laboratory, Steven, Pooria, Kyriakos, Ilker, Leo, Sylvain, Abhijit, Ugur, Joowon and Elizabeth. I want to thank them all for being always there to help, exchange ideas and laughs. In particular I want to thank Ahmed, Navid and Amir for being always there and for giving me the chance to be their friend. A special thank you goes to Ulas, for his perseverance and his support, especially during the last months of my PhD. Thank you all.

Not less importantly, I want to thank the former members of LO, Mohammad, Greg, Thomas, Morteza, Jacob and Don; special thanks go to Alex, Miguel and Nico. I want to thank Jieping for his scientific contribution to my work.

An important mention goes to Sabrina, Silke, Anne and Carole, who always make and made things work properly in the lab.

My daily life wouldn't have been the same without the LO girls Fauzia, Marilisa and Alexa; my life wouldn't be the same without my friend (and great scientist) Eirini. Thank you for everything.

A big thank you goes to our twin laboratory LAPD and to all its members. I want to thank them not only on a professional level, but also for their friendship, especially Chiara (e Gianni), Maya, Jorge, Jan, Damien and Enrico.

I want to say thank you to Catherine and Bruno for welcoming me in their family. Lausanne wouldn't be home without you here.

There are so many people I would like to thank, and probably I will forget to write some of their names (sorry for that); what won't be forgotten are all the memories of moments spent in Lausanne with people that made me feel like home. I want to thank my friends Andrea, Alberto, Alberto, Michele, Davide, Marcella and Andrea (e Cecilia). Thank you for being irreplaceable and for the uncountable bottles of wine. I also want to thank Tania, Daniele and Francesco.

I thank friends that sometimes leave.

I want to thank old and new friends. I want to thank my theatre troupe for giving me the chance to dream and live different lifes. I want to thank Andrea, Elia, Marzio and Beatrice. I thank Iliana, Sezin and the Italo-Greek food exchange crew, ready to share many other experiences together. I thank Miguel, Albano, Matteo, Ben, Senan and Ilias, the swing-rock’n’roll dancing people and the beach volley crew. Many thanks to Luana, for being there always, no matter what, no matter where or why.

My immense gratitude goes to Matteo, who supports me always. Thank you for helping me going through this past difficult year and for sharing your life with me. Thank you for bringing love into mine.

Last but not least, I want to thank my family: my brother Federico, Silvia and Elia, a newborn shining little star. My endless gratitude is for my parents, Giuseppe and Lucia, which make my dreams come true and make me the person that I am. Grazie.

Abstract

Optical waveguides are one of the most important photonic components. They are indispensable tools in many of today's technologies because of their capacity of guiding light. In particular, compact, low loss, flexible polymer optical waveguides are crucial in optofluidic and microfluidic devices for a dense integration of optical functionalities. The sought after suitable materials and innovative fabrication techniques to achieve low loss long polymer optical waveguides and interconnects has proven to be challenging.

Single-mode (SM) optical fibers are a fundamental building block for compact fiber optic endoscopes, capable of accessing confined places in the human body with minimal invasion. In a fiber optic endoscope, thousands of single-mode optical fibers acting as single pixels are closely packed together, delivering the local information to a camera chip. Biocompatible polymer-based waveguides increasingly became valid alternatives to silica fibers to deliver and collect light for optical diagnosis, therapy and surgery. In particular, polydimethylsiloxane (PDMS) is well known to be a suitable polymer for biomedical implantation devices, thanks to its excellent physical and chemical properties.

Multi-photon polymerization (MPP) is one of the most important technological achievements for the microfabrication of fine polymeric structures, because of its nonlinear feature resulting in a precisely localized and highly confined material modification. Typically, polymer formulations for photopolymerization applications comprise a polymerizable component, the monomer, and a photosensitive component, the photoinitiator (PI). Developments in these two-component materials are central to the field of MPP.

In this thesis, I demonstrate the fabrication of compact optical waveguides in PDMS through multiphoton laser direct writing (MP-LDW). The core of this research consists of the investigation of suitable combinations of monomer and PI capable of efficient photopolymerization in a cured PDMS matrix. We achieved, for the first time, the photoinitiator-free fabrication of optical waveguides employing phenylacetylene as the photosensitive monomer via multi-photon absorption. Because of the dense π-electrons in phenylacetylene, we achieved a high refractive index contrast ($\Delta n \geq 0.06$) between the waveguide core and the PDMS cladding. This allowed for efficient waveguiding at a core size of 1.3-μm with a measured loss of 0.03 dB/cm in the spectral band of 650-700 nm.

In a photoinduced polymerization process, the reaction probability of polymerization is proportional to a power function of the laser intensity depending on the order of the nonlinearity involved. This nonlinear process results in occasional structural defects due to material damages during the fabrication, which is caused by self-focusing and beam collapse. Motivated by the need of minimizing self-focusing, we investigated alternative chemical schemes and demonstrated the fabrication of submicron optical waveguides in PDMS using divinylbenzene (DVB) as the monomer through two-photon polymerization (2PP). We show that the commercial oxime ester photoinitiator Irgacure OXE02 is suitable for triggering the DVB polymerization, resulting in a stable and controllable fabrication process for the fabrication of defect-free, 5-cm long waveguides. As a proof of concept, we accomplished simple patterns delivery through such waveguide bundles, demonstrating their potentials for imaging applications.

Moreover, I present the methodologies we have developed for the fabrication of polymer rectangular step-index (STIN) optical waveguides using a commercial 3D printing system (Photonic Professional GT, Nanoscribe GmbH), using the proprietary IP-dip resist (Nanoscribe GmbH). We performed a full calibration and implemented a printing strategy for the fabrication of a 720 μm long SM-fiber bundle. We characterized it in terms of refractive index, transmission loss and imaging capabilities.

We further demonstrate how a convolutional neural network (CNN) can reconstruct the original images from a scrambled output from the waveguide bundle due to crosstalk. To achieve this, we have constructed a CNN of the U-net type and trained the network with the input images and their corresponding output from the bundle. Owing to the CNN, the image sampling effect due to waveguide pixel discretization and the noise present in the data can be removed, providing quality enhancement of the images from the fiber bundles we have realized using innovative and substitute materials to conventional glass.

Overall, the presented work provides innovative materials and new insights into the fabrication of polymer optical microstructures, opening new scenarios for future technological development in the field of microfabrication using MP-LDW. We expect such waveguides will receive a wide range of applications in biosensors, microfluidic flow cytometry, wearable photonic devices, electro-elastic optical modulators, flexible optical circuit boards, and optical neural networks.

Keywords

Optical waveguides, polydimethylsiloxane (PDMS), multi-photon absorption, two-photon polymerization, micro-nano fabrication, laser direct writing (LDW).

Résumé

Les guides d'ondes optiques sont l'un des composants photoniques les plus importants. Ils sont un outil indispensable dans les technologies actuelles de part à leur capacité à guider la lumière. Leur taille réduite et leur faible perte, font des guides d'onde polymères flexibles des composés essentiels en opto-fluidique et micro-fluidique permettant une intégration compacte de systèmes optiques. La recherche de matériaux adaptés et de méthodes de fabrication novatrices pour la conception de longs guides optiques polymères à faible perte et d'interconnexions de circuits intégrés est donc capitale et présente de nombreux défis.

Les fibres optiques monomodes (SM) sont un élément fondamental dans la conception d'endoscopes en fibre optique compacte, permettant l'accès à des parties exiguës du corps humain lors d'opérations peu invasives. Dans un endoscope à fibre optique, des milliers de fibres optiques monomodes, opérant chacune comme pixel unique, sont assemblées pour transmettre des informations à une caméra. Les guides d'onde polymères biocompatibles deviennent une alternative grandissante aux traditionnelles fibres silicates pour transmettre et recueillir de la lumière pour des méthodes optiques de diagnostic, de thérapie et de chirurgie. Le polydimethylsiloxane (PDMS) s'est déjà démarqué comme étant un polymère adapté aux implants biomédicaux par ses excellentes propriétés physiques et chimiques.

La polymérisation à plusieurs photons (MPP) est l'une des découvertes technologiques dominantes dans le domaine de la micro-fabrication de structures polymères minces. Grâce à sa nature non-linéaire, elle permet une modification précise et localisée du matériau traité. Dans les applications de photopolymérisation, les polymères sont généralement constitués d'un composé polymérisable, le monomère, et d'un composé photo sensible, le photo-initiateur (PI). La recherche et le développement de ses deux composés est cruciale dans le domaine de la MPP.

Dans cette thèse, nous avons étudié et démontré un procédé de fabrication de guide optique polymère compact en PDMS via « multi photon laser direct writing (MP-LDW) ». Le cœur de cette recherche consiste en la découverte de combinaisons de monomère et de photo-initiateur compatibles à une polymérisation efficace dans une matrice de PDMS solide. Nous avons réussi pour la première fois, une fabrication de guide optique sans l'aide de photo-initiateur par absorption multi-photonique du phenylacetylene, monomère photosensible. Grace à sa densité en électron- π, le phenylacetylene nous a permis d'atteindre une différence d'indice de réfraction conséquente (Δn ≥ 0.06) entre le cœur du guide optique et de son enveloppe en PDMS. Cela permet une transmission efficace avec un cœur de seulement 1.3 µm et une perte mesurée de 0.03 dB/cm dans la bande spectrale allant de 650 à 700 nm.

Dans une polymérisation photoinduite, la probabilité qu'une réaction se produise est proportionnelle à une fonction puissance de l'intensité du laser, dont l'exposant dépendant de l'ordre des non-linéarités présentes. Ce procédé non-linéaire crée occasionnellement des défauts structurels causés par des imperfections de fabrication du matériau, elles-mêmes provoqués par des phénomènes d'auto-focalisation et d'affaissement du rayon. Motivés par le besoin de minimiser l'auto-focalisation, nous avons recherché des modèles chimiques alternatifs et démontré la fabrication de guide d'onde optique de taille inférieure au micromètre dans une enveloppe de PDMS en utilisant un monomère de divinylbenzene (DVB) et une polymérisation à deux photons (2PP). Nous avons aussi démontré que l'oxime ester photoinitiator Irgacure OXE02, disponible commercialement, était compatible pour le déclenchement de la polymérisation du DVB, résultant en une méthode de fabrication contrôlable et sans défauts de guide d'onde long de 5cm. Nous avons réussi la transmission de motifs simples à travers de telles fibres démontrant leur potentiel dans le domaine de l'imagerie optique.

De plus, nous présentons une méthodologie développée pour la fabrication de guides d'ondes optiques polymères à saut d'indice rectangulaire (STIN) par un système d'impression 3D commercial (Photonic Professional GT+, Nanoscribe GmbH) en utilisant la résine propriétaire IP-dip (Nanoscribe GmbH). Pour ce faire, nous avons effectué une calibration complète et établie une méthode de fabrication de faisceau de fibre monomode de 720 µm. Ces faisceaux de fibre ont ensuite été caractérisés selon leur indice de réfraction, la perte de transmission et leur potentiel en imagerie.

Nous avons également démontré les bénéfices de l'utilisation d'un réseau neural convolutionel (CNN) dans la reconstruction d'image à partir de données corrompues par effet « crosstalk » lors de la transmission par un faisceau de guide d'onde. Pour ce faire, nous avons construit un CNN de type U-net. Ce réseau a été ensuite entrainé avec des images et leur résultat après transmission par le faisceau. Grâce au CNN, la pixellisation de l'image lors l'acquisition de celle-ci due au guide d'onde ainsi que le bruit présent dans les données ont pu être réduits voir éliminés. Cela nous a permis d'améliorer la qualité des images après transmission par les faisceaux de fibres que nous avons réalisé en matériaux innovants substituants les fibres classiques en verre.

Pour résumé, le travail de ce manuscrit présente des matériaux novateurs et des idées nouvelles dans le domaine de la fabrication de microstructure optique polymère, ouvrant la voie à de future développement dans le domaine de la micro-fabrication via MP-LDW. Nous estimons que de tels guides d'onde auront un large champ d'application dans les domaines des biocapteurs, de la cyrtométrie en micro-flux, des systèmes photoniques portables, des modulateurs optiques électro-élastiques, des circuits optiques flexibles imprimés et des réseaux neuraux.

Mots-clés

Guides d'onde optique, polydimethylsiloxane (PDMS), absorption à plusieurs photons, polymérisation à deux photons, micro-nano fabrication, laser direct writing (LDW).

Contents

Acknowledgements i

Abstract iii

Keywords iv

Résumé v

Mots-clés vi

Contents vii

List of Figures x

List of Tables xvii

List of Equations xvii

Chapter 1 Introduction 21

1.1 3D microfabrication of polymer optical waveguides 21

1.1.1 Polymer optical waveguides 21

1.1.2 Laser-based three-dimensional (3D) microfabrication 22

1.1.3 Overview of the thesis 22

1.2 Principles of optical waveguides 24

1.2.1 Light propagation in optical waveguides 24

1.2.2 Single-mode optical fibers 26

1.2.3 Fiber types and imaging 27

1.2.4 Imaging in multi-core fiber bundles 29

1.3 Multiphoton absorption 31

1.3.1 Technical foundation: multi-photon absorption 31

1.3.2 Free-radical chain polymerization mechanism 33

1.3.3 One-photon and two-photon radical photoinitiators 36

1.4 Summary 37

Chapter 2 Experimental apparatus 39

2.1 Femtosecond laser three dimensional micro-nanofabrication 39

2.1.1 Optical apparatus 39

2.2 Optical waveguides characterization: digital holography 40

2.2.1 Basic concepts of holography 41

2.2.2 Offset-reference holography 43

2.2.3 Digital holography 44

2.2.4 Optical apparatus 46

2.3 Characterization platform ... 47

2.3.1 Set-up design requirements ... 47

2.3.2 Optical apparatus ... 47

2.4 Summary ... 49

Chapter 3 Photoinitiator-free microfabrication of optical waveguides in PDMS ... 51

3.1 Introduction ... 51

3.2 Materials and methods ... 52

3.2.1 Sample preparation ... 52

3.3 Results and discussion ... 53

3.3.1 Waveguides verification ... 53

3.3.2 Waveguides characterization ... 56

3.3.3 The self-focusing problem and luminescence signal detection ... 60

3.4 Alternative chemical schemes ... 61

3.5 Summary ... 62

Chapter 4 Sub-micron poly-DVB waveguides in PDMS ... 63

4.1 Introduction ... 63

4.2 Materials and methods ... 64

4.2.1 Chemical scheme ... 64

4.2.2 Materials and sample preparation ... 65

4.3 Results ... 66

4.3.1 Simple waveguides ... 66

4.3.2 Compound waveguides ... 69

4.4 Discussion and conclusions ... 71

4.5 Summary ... 73

Chapter 5 Poly-DVB waveguide arrays ... 75

5.1 Polymer optical waveguide arrays for cochlear microendoscopy ... 75

5.2 Beam propagation method ... 77

5.2.1 Cross-talk simulations and verification ... 79

5.3 Poly-DVB waveguide bundles ... 81

5.4 Intracochlear endoscope module ... 85

5.4.1 Intracochlear endoscope implementation ... 86

5.4.2 Stepwise manufacturing based on casting and injection Silicon dioxide wafer molds ... 87

5.4.3 Conclusions and future work ... 91

5.5 Summary ... 91

Chapter 6 Fabrication of waveguide bundles using a commercial 3D printing system ... 93

6.1 Introduction ... 93

6.2 Nanoscribe apparatus ... 94

6.3 Calibration procedure ... 96

6.3.1 Voxels calibration ... 96

6.3.2 Cladding calibration ... 97

6.4 Step-index (STIN) multi-core waveguide bundle 3D printing ... 99

6.4.1 Vertical vs horizontal waveguides 3D printing approach ... 99

6.4.2 Horizontal waveguides 3D printing approach ... 102

6.5 Light coupling into 3D printed STIN multi-core waveguide bundles ... 104

6.6 BPM Simulations ... 105

6.7 Image reconstruction using deep neural networks (DNNs) ... 107

6.7.1 Convolutional U-net DNNs ... 107

6.7.2 Training and testing with synthetic data ... 110

6.7.3 Test results with experimental data ... 112

6.8 Summary ... 112

Chapter 7 Summary and outlook ... 115

Appendix ... 119

Appendix 1 ... 119

Appendix 2 ... 123

Appendix 2.1 ... 123

Appendix 2.2 ... 125

Appendix 2.3 ... 126

Appendix 3 ... 128

Appendix 4 ... 131

Appendix 5 ... 131

References ... 135

Curriculum vitae ... 143

List of Figures

Figure 1.1 An envisioned example of 3D optical waveguides integrated in one flexible PDMS substrate with microfluidic channels. Blue wires illustrate an imaging waveguide bundle. Red wires exemplify optical communication channels. Green wires depict optical systems of flow cytometry or spectroscopy. ..23

Figure 1.2 (a) Light guided in a step- index optical fiber, where a higher refractive index material constitutes the core (n_1) surrounded by a lower refractive index cladding material (n_2). Rays coming at the core-cladding interface at an angle greater than ϕc will be guided until the other end of the fiber. (b) Refractive index distribution of a step-index optical fiber along the radial direction. 25

Figure 1.3 Light rays and phase fronts propagating in the waveguide. The resulting constructive and destructive interference patterns from light rays satisfying the phase matching condition are the modes of the waveguide. 25

Figure 1.4 Computed fundamental mode for an optical fiber with $n1$=1.47, $n2$=1.455, a= 1.5 µm, at an illumination wavelength λ=0.633 µm; the v number fot this fiber is v=1.56, therefore it is a single mode fiber. 27

Figure 1.5 (a) Light guided in a graded-index (GRIN) optical fiber. (b) Parabolic refractive index distribution of the core $n1$ in a GRIN fiber. 28

Figure 1.6 Examples of holey fibers (PCFs) in different configurations; (a). Small air holes surround the solid fiber core (dashed line); the diameter of the air holes can be smaller than the operation wavelength (b). Periodic arrangement of larger air holes surrounding the solid core of the PCF. (c) Periodic arrangement of air holes surrounding the small hollow core; the size difference between the air holes in the cladding and the hollow core results in a lower average cladding refractive index with respect to the core. 28

Figure 1.7 (a) Schematic of a multicore step-index fiber bundle. (b) Bundle refractive index distribution with $n1$ and $n2$ being the cores and cladding refractive index, respectively. 30

Figure 1.8 (a) A digit from the MNIST data base is used as an input. Output intensity from a multicore fiber bundle having a core-to-core spacing of 5 µm (b) and 3 µm (c). The diameter of the fibers is a= 1.5 µm, Δn= 0.015, the illumination wavelength is λ=0.633 µm and the propagation distance is 2.5 mm. 31

Figure 1.9 Diagram of the atomic transition in the one-photon (a) and two-photon (b) absorption processes. In one-photon excitation the atom makes the transition from its ground state to an excited state through the absorption of a single photon; in the two-photon absorption mechanism, the transition is made by absorbing two lower-energy photons. Fluorescence can occur after the absorption of photons and it is the same in both linear and nonlinear processes. 32

Figure 1.10 One-photon vs two-photon normalized intensity distribution along the radial coordinate for a light source having λ=680 nm and a NA=0.7...33

Figure 1.11 Liquid photopolymer hardening as a result of cross-linking of monomer/oligomer molecules via light absorption..34

Figure 1.12 Irgacure 369 bond cleavage under light illumination and consequent generation of two radicals $R\cdot$...34

Figure 1.13 Bimolecular reaction of benzophenone and a tertiary amine; the amine is radicalized and triggers the polymerization reaction. 35

Figure 1.14 One-photon (a) and two-photon (b) polymerization profile assuming a Gaussian beam illumination, 0.7 NA and a polymer refractive index n=1.5. 37

Figure 2.1 Femtosecond direct laser writing (LDW) system schematic implemented for the waveguides fabrication. A pulsed femtosecond Ti: Sapphire laser beam is expanded and collimated by means of a 5× (NA=0.1, Newport) microscope objective (L1) and an achromatic lens (L2). A water-immersion, 0.7 numerical aperture objective (OBJ: Nikon, working distance WD=2.3 mm) is used to focus the laser beam into the samples. A dichroic mirror allows for 50% transmission/reflection at 650 nm, and lets a very small amount of leaked laser light reflected from the top surface of the sample cover slip to reach the CCD camera (Chameleon 3, Point Grey Research) after a focusing lens (L3) in 4f configuration with the focusing objective. 40

Figure 2.2 Working principle of holography. An input field is split into a reference beam and an object beam by means of a beam splitter. The reference optical beam travels unperturbed towards the recording medium and interferes with the object beam which has been scattered from the object. 41

Figure 2.3 Wavefront reconstruction by illuminating the hologram with the reference wave. 42

Figure 2.4 Fourier spectrum of the hologram. 44

Figure 2.5 (a) Hologram recording on a camera and selection of the region of interest ROI (in the red square); (b) Region of interest ROI; (c) Fourier transform of the cropped hologram and selection of the diffraction order (red circle); (d) digital shift to the centre of the computational window of the diffraction order (red circle), where everything else is put equal to zero; amplitude (e) and phase (f) information extracted from the back Fourier transform of the shifted diffraction order. 45

Figure 2.6 Digital holography block diagram. 46

Figure 2.7 Off-axis holographic interferometer built for the measurement of the refractive index difference of the polymer waveguides. A HeNe laser ((λ=632.8 nm, Thorlabs) is split by means of a beam splitter (BS1) into a reference arm (red) and an object arm (blue). The object plane wave travels through the PDMS sample and recombines with the reference arm through a second beam splitter (BS2). The waveguides are imaged on a camera (CAM) using a long working distance objective (OBJ) in 4f configuration with the lens L3. The reconstructed holograms are digitally processed with a computer (PC). 46

Figure 2.8 Light coupling set up schematic: a 2-mm HeNe laser spot (λ=632.8 nm, Thorlabs) is magnified and collimated through a beam expansion block (L1 and L2) and then focused on the proximal facet of the sample by means of a high numerical aperture objective (OBJ1). Light is collected at the sample distal end by means of a long working distance objective (OBJ2) and imaged on a camera (CAM1) by means of a lens (L3). The back-reflected light is redirected using a beam splitter (BS1) on a second camera (CAM2) after being focused by the lens L4. A broadband thermal light source (Introlux 6000-1) is collimated using a long focal length lens (L5) and an iris (Iris2). A beam splitter (BS2) splits the illumination beam into two arms: the first arm is redirected towards the input objective (OBJ1) by a thin pellicle beam splitter (BS3) to be coupled into the waveguides contained in the sample. The second arm is focused by means of a lens (L6) into the back focal plane of the output objective (OBJ2) by means of another pellicle beam splitter (BS4). 48

Figure 3.1 Principle of waveguides fabrication in PDMS. (a) Preparation of a pristine platinum-cured PDMS substrate. (b) Permeation of the monomer molecules into the PDMS matrix by immersing the PDMS substrate into the monomer liquid formulation for 24 hours. (c) Exposure of the monomer-permeated PDMS substrate to a focused ultrashort laser irradiation for waveguide writing. (d) Removal of the unreacted monomer through an optional ethanol washing and a heating at 100-130 °C for two hours. (e) Absorption spectrum of 0.01 mM phenylacetylene in acetonitrile. Violet arrows indicate energies of two-photon (2PA) and three-photon absorption (3PA). Inset illustrates the chemical structure of the phenylacetylene molecule. 52

Figure 3.2 (a) Experimental set up for poly-phenylacetylene waveguide writing in PDMS through MP-LDW. (b) After monomer infiltration, the pre-crosslinked PDMS slab is sandwiched between a glass slide and a 170 µm thick microscope coverslip to avoid monomer evaporation. (c) Phenylacetylene multi-photon polymerization reaction scheme under laser irradiation. 53

Figure 3.3 (a) Phase contrast microscope (Olympus IX-71) image of written PDMS optical waveguides. (b) Bright field microscope image of an optical waveguide (100× magnification objective), written at 1.3 mm below the sample top surface, 1.9 ×10^{12} W/cm^2 laser peak intensity and 0.7 mm/s writing speed. ..54

Figure 3.4 (a) Top view image and (c) waveguide width and height for optical waveguides written at 0.7 mm/s, 1.1 mm below the sample coverslip interface, for different laser peak intensities; cross-sectional image (b) and width and height (d) for waveguides written at 1.9 ×10^{12} W/cm^2 peak intensity, 1.1 mm below the sample coverslip interface, for different writing speeds. 55

Figure 3.5 (a) Waveguide cross section for optical waveguides written at laser peak intensity of 1.9 ×10^{12} W/cm^2 and a writing speed of 0.7 mm/s, for 900 µm (top panel), 1.1 mm (middle panel) and 1.3 mm (low panel) focusing depth. (b) Plot of waveguide width and height as a function of writing depth, showing linear decrease of both lateral and vertical waveguides dimensions with increasing writing depth. 56

Figure 3.6 (a) Raman spectra of phenylacetylene (PA) and Sylgard 184 PDMS taken in a Renishaw confocal Raman microscope. (b) Bright field microscopy image taken using a 5× magnification objective in the Raman Renishaw microscope. A 488 nm laser was focused in an area of the sample with no polymerized waveguide (point A), 100 µm into the PDMS material. In order to confirm the presence of the PA, the laser was then focused on a waveguide and the Raman signal was acquired at three different focusing depth in the proximity of the waveguide focusing plane, at 20 µm, 0 µm and 20 µm, respectively (point B). The strong peak related to the carbon-carbon triple bond stretching at 2111 cm^{-1} reported in literature [131, 132] doesn't appear, proofing the $C \equiv C$ bond opening and consequent PA polymerization. 57

Figure 3.7 Measurement of the phase profile and refractive index contrast of the waveguide. (a) Principle of the measurement. A laser beam of plane wave is sent to pass the PDMS sample where the waveguide induces an additional phase change in the wave front, which is measured in the interferometric imaging system. (b) An example interferometric image of the waveguide. Fringes parallel to the waveguide are due to the aberration resulted from the PDMS material. (c) Extracted average phase profile of the waveguide, which is broadened due to the aberration introduced by the PDMS material. The corresponding refractive index contrast, after taking into account the broadening, is Δn=0.06. 58

Figure 3.8 Phase contrast cross-sectional view of a PDMS sample containing waveguides before (a) and after (b) the fiber ends polishing using Teflon and spin-coated Silicon oil. 59

Figure 3.9 Characterization of the waveguide transmission. (a) Diagram of the optical set-up used for optical transmission loss characterization. (b) Broadband light output from three individual waveguides written at 800 µm under the top surface, using 1.9×1012 W/cm2 peak intensity and 0.7 mm/s writing speed. (c) Broadband waveguiding output from one waveguide. (d) Laser (HeNe) waveguiding output from the same waveguide; (e) – (h) Filtered narrowband waveguiding output from the same waveguide: (e) 592/43 nm, (f) 675/50 nm, (g) 609/53 nm, and (h) 800/40 nm; (i) Waveguide transmissivity measured by the intensity ratio between the outputs from waveguides cut at different lengths. Light blue, orange, red, brown and black bars show the measured transmissivity at 1 cm in 600 – 800 nm, 570 – 613 nm, 582 – 635 nm, 650 – 700 nm, and 780 – 820 nm, respectively. 59

Figure 3.10 Fluorescence intensity signal of different writing intensities as a function of time during a writing process at 0.7 mm/sec and 800 µm below the PDMS-cover slide interface. Each data point was taken every 1 ms; the initial swinging behaviour is related to the opening of the laser source which causes light fluctuations in the detector. (b) Phase microscopy top view (top) and cross-sectional (bottom) image of defected waveguides. The uncontrollable self-focusing takes place above the critical power for self-focusing that is ~5.4×10^3 W, causing randomly distributed defects (blue arrows). 61

Figure 4.1 (a) Molecular structure of the divinylbenzene (DVB) monomer and Irgacure OXE02 and the polymerization of the monomer upon laser irradiation. (b) Absorption spectrum of 0.2 mM DVB and 0.5 mM Irgacure OXE02 in acetonitrile. Blue arrows indicate the absorption wavelength peak of the photoinitiator (PI) (337 nm) and the excitation wavelength of our system tuned to 680 nm. 64

Figure 4.2 Weight gain upon swelling of pristine cured polydimethylsiloxane (PDMS) slabs, for 1, 2.5, and 5 wt% of Irgacure OXE02 in the DVB monomer. 65

Figure 4.3 (a) Experimental MP-LDW vertical set up for polymer waveguide writing integrated with high precision piezo-stages and (b) close up look to the writing process by means of a water immersion objective (Nikon, NA=0.7). 66

Figure 4.4 (a) Phase-contrast microscopy top view image of the recorded poly-DVB optical waveguides written at constant peak intensity I ~ 2.25 × 10^{12} W/cm^2 and varying fabrication speed, ranging from 1.3 to 2.5 mm/s. (b) Waveguide width and height evolution as a function of increasing writing speed where the error bar derives from the measurement of three waveguides; the inset shows the cross-sectional view of a single-track waveguide where the scale bar measures 5 µm. (c) and (b) display the same as above as a function of increasing fabrication peak intensity from 1.93 to 2.74 × 10^{12} W/cm^2 and constant speed v = 1.8 mm/s. Error bars indicate the standard deviation derived from the measurement of five different waveguides geometry. Scale bars dimension in (a) and (c) is 50 µm. 67

Figure 4.5 (a) Evolution of the refractive index as a function of increasing peak intensity (and constant writing speed v = 1.8 mm/s) is displayed. The laser peak intensity ranged between ~2.10 × 10^{12} W/cm^2 and ~2.74 × 10^{12} W/cm^2. (b) Refractive index contrast for waveguides recorded at ~2.25 × 10^{12} W/cm^2 constant laser intensity and different writing speed, increasing from 1.3 to 2.5 mm/s. The insets display the measurement of the phase profile for different laser peak intensities and velocities, where each phase profile is the mean profile measured from three waveguides written with the same fabrication parameters. (c) Transmission loss in dB/cm as a function of wavelength, where colored filters have been inserted in the optical path to measure the output from three different simple waveguides written 500 µm apart from each other. (d) Output intensity profile of three simple waveguides at an inter-waveguide distance of ~18 µm; light in the 535/43 nm spectral band has been coupled in the central waveguide. Waveguide outputs are displayed in the image inset. Error bars indicate the standard deviation from three waveguides fabricated with the same experimental parameters. 68

Figure 4.6 Schematic of the writing of compound waveguides. The PDMS sample is displaced by a small distance δ by means of a piezoelectric stage in the y direction. A long travel range mechanical stage moves the sample over centimeters in the x-direction. 69

Figure 4.7 Normalized output mode profile from a single laser pass (a) and from a double pass laser waveguide in the different spectral regions, both written at the same experimental parameters. The compound waveguides show improved mode light confinement if compared to the single waveguides which exhibit light escaping from the core region. Insets in (a) and (b) show the output mode for white light illumination and the plot cross-cuts (dotted red line). 70

Figure 4.8 (a) Waveguide dimensions as a function of the Irgacure OXE02 concentration into the DVB monomer. The size of the waveguides increases with increasing PI concentration. The isolated, single waveguides were fabricated at an intensity of ~1.78 × 10^{12} W/cm^2 and a velocity of 3.2 mm/s. Scale bars measure 5 µm; error bars indicate the standard deviation from five different waveguides; cross-sectional view taken in a phase contrast microscope (Olympus IX-71) of a double-cored (b) and a triple-cored (c) poly-DVB waveguides; top view image of double (d) and triple-track (e) poly-DVB waveguides. 70

Figure 4.9 (a) Output intensity profile of a double-cored (blue) and triple-cored (red) waveguides (wgs), at 535/43 nm spectral band. Waveguide outputs are displayed in the image inset. (b) Transmission loss in dB/cm as a function of wavelength for simple (green), double- (blue) and triple- (red) track waveguides. Dot lines indicate the linear fit with –4.0 slope, for both double- and triple-track waveguides, typical of pure Rayleigh scattering. 71

Figure 4.10 Plot of the measured phase change in the waveguides as a function of the writing intensity. The error bar indicates the standard deviation among three different waveguides. Dashed line shows a quadratic regression. 72

Figure 5.1 Schematic of a cochlear implant (CI) electrode array module inserted inside the human cochlea (picture taken from https://www.sonova.com/en); the red box indicates the location of the implanted CI. The CI containing the electrode array (right hand side of the figure) is made of PDMS. 75

Figure 5.2 Proposed implementation of the endoscopy-assisted cochlear implant. (a) The soft microendoscope (blue structure) to be attached to a regular implant electrode array (grey structure). (b) Cross-sectional view of the auxiliary microendoscope in the scala tympani. 76

Figure 5.3 Triplet waveguide refractive index distribution with Δn=0.005, minor axis a=0.9 µm, major axis b=3.5 µm and δ=1.2 µm. 78

Figure 5.4 Physical (a) and simulated (b) 1.4 µm FWHM Gaussian beam profile at λ=633 nm. Green and yellow dashed lines indicate the transversal and longitudinal profiles traced in (c) and (d), respectively. 79

Figure 5.5 BPM simulations of cross talk taking place when a 1.4 µm FWHM Gaussian beam at 633 nm is coupled into the central waveguide of 6 x 6 triplet waveguide arrays. The first column displays the refractive index distribution at four different waveguide pitch D, namely 5, 10, 15 and 20 µm. The middle and third column show the yz propagation profiles and the output intensity in linear scale, respectively. The propagation length is 2 cm. 80

Figure 5.6 (a) Output intensity from a 3 x 3 poly-DVB triplet waveguide array when a 633 nm HeNe is coupled to the central waveguide. The waveguide pitch is 20 µm. Transversal (blue) and longitudinal (red) normalized output profiles. 81

Figure 5.7 Pilot 2-cm long, 6 x 6 triple-track poly-DVB waveguide bundles in PDMS written at 3.2 mm/s and 1.29 $\times 10^{12}$ W/cm^2 (a), 1.45 $\times 10^{12}$ W/cm^2 (b), 1.61 $\times 10^{12}$ W/cm2 (c) and 1.78 $\times 10^{12}$ W/cm^2 (d) laser peak intensities. The small bundles are written following a bottom-up fabrication approach: as a single layer is complete, the piezo stage moves away from the substrate of about Δz=20 µm (e), allowing for the consecutive waveguide layer to be completed in a meander-like fashion. The waveguide pitch is Δy=20 µm, while the inner core-to-core distance (δ), exemplified in the close up look red box in (f), is 1.2 µm. 82

Figure 5.8 White light illumination coupling set up for pattern delivering tests. A careful alignment of a Newport, NA=0.4, 20× magnification has been done in order to enlarge the illumination spot size, which is visible in reflection (CAM2) in the top left yellow panel. Bottom-right yellow panel shows the 100 µm wide white light illumination spot in transmission on the distal camera (CAM1). The red box shows a picture of the sample being aligned with the two objectives. 82

Figure 5.9 (a) A 25 µm diameter, incoherent light illumination beam is demagnified and projected on the proximal sample facet and randomly moved in *x, y*. (b), (c) and (d) show the waveguide bundle output recorded by CAM1 as the pattern is randomly moved at different coupling positions. (e) 80 µm sized square pattern from a USAF 1951 resolution chart is projected on the proximal sample facet; the pattern progressively obscures the waveguide matrix rows, while the output has been recorded on the distal camera CAM1; six (f), four (g) and three rows (h) light up. 83

Figure 5.10 (a) Fully illuminated, 6 x 6, 2 cm-long waveguide bundle. (b), (c) and (d) show the recorded waveguide bundle output as the square pattern from the USAF 1951 resolution chart is randomly moved in *x* and *y*. 84

Figure 5.11 (a) and (b) show the cross-sectional phase contrast microscopy images of a triple-track, 12 x 12 poly-DVB waveguide bundle where the waveguides sit at distance $\Delta y = \Delta z =$20 µm from each other. The waveguide bundle array can be written only 20 µm below the air-PDMS interface. (c) Picture of the 4 cm long, flexible PDMS slab containing the waveguide bundle. 84

Figure 5.12 Input from the MNIST database (a) and refractive index distribution of a 12 x 12 poly-DVB waveguide bundle (b). x,z (c) and y,z (d) propagation profiles along 2 cm propagation length at 600 nm wavelength. Output intensity profile after 2 cm (e) and 4 cm (f) propagation length. 85

Figure 5.13 Cochlear implant module with polymer waveguide bundle endoscope. 86

Figure 5.14 Endoscope prototype cross-section. 86

Figure 5.15 Endoscope prototype fabrication steps. 87

Figure 5.16 Silicon and Silicon dioxide wafer molds to be used for the endoscope prototype fabrication. 87

Figure 5.17 Detailed process flow for the fabrication of the waveguide bundle endoscope, using the Silicon and Silicon dioxide wafers as molds. 90

Figure 5.18 Example of ray tracing simulation results of the imaging ball lens for the endoscope. Through the choice of different refractive index of the ball lens, a large range of field of view (FOV) is enabled; p represents the distance from the object plane. 91

Figure 6.1 (a) Nanoscribe GmbH (Photonic Professional GT+) 3D printing system (ref: www.nanoscribe.com). (b) 3D printing process workflow: a CAD design is created using the DeScribe and imported into the NanoWrite software. Before the commencement of the process, the software slices it into horizontal and vertical layers (slicing and hatching). The laser scans the trajectory traced by the CAD design until the final object is polymerized into the photoresin. When the 3D printing is finalized, the sample is developed by immersing it into poly(glycidyl methacrylate (PGMEA) and isopropanol for about 17 and 5 minutes, respectively. 94

Figure 6.2 (a) Dill printing configuration: the objective is directly immersed into the photoresist which acts as a refractive index matching medium as well as the photoactive material to be polymerized. (b) Oil immersion printing configuration: the laser beam travels through a refractive index matching medium (typically oil) and a thin substrate (170 µm borosilicate glass) to polymerize the photoresist which is dropped on top of the substrate. 95

Figure 6.3 (a) Example of a SEM image showing the three printed lines composed of 5x5, 5x1 and 3x1 voxels at a power level of 35% and 10000 µm/s writing speed. The red arrows indicate the width dimension we have measured for the calibration of the printed 5 x 5 and 3 x 1 voxels line sets, while the yellow box shows the structural instability of a 5 x 1 voxels structure because of the high aspect ratio. (b) Voxel scaling law as a function of power percentage for 5 x 5 (red), and 3 x 1 (blue) voxels line sets. 96

Figure 6.4 (a) 3D printing of photonic waveguides using Photonic Professional GT+ with a 63× magnification objective and the IP-dip resist in dill: high refractive index cores (high exposure) are embedded into lower refractive index cladding (low exposure). (b) Schematic of a 40 x 13 x2 00 µm (D x H x L) block for the calibration of the cladding. Power percentage was swept between 35% and 45%; scanning speed ranged between 6000 and 10000 µm/s. 97

Figure 6.5 Hologram (a), wrapped (b) and PUMA unwrapped 2D phase map (c) of a 3D printed block at 40% laser power and 7000 µm/s scanning speed. A) and B) represent the transversal and longitudinal averaged cross cut profiles as a function of laser power percentage (and constant speed v=7000 µm/s). 98

Figure 6.6 Longitudinal (a) and transversal (b) averaged cross cut profiles as a function of laser power percentage (and constant speed v=7000 µm/s).The effect of the lens aberrations results in a lower polymerization efficiency at the edges of the field of view, limiting the printable length dimension when lower laser power percentages are used; this effect is more evident across the longitudinal dimension compared to the transversal dimension which measures only 40 µm. (c) 2D mapping of the refractive index difference between the printed objects and the index matching oil as a function of the laser power percentage and the scanning speed, extrapolated from the cladding calibration; we have measured a minimum and a maximum Δn of 0.02 and 0.04, respectively. 99

Figure 6.7 Vertical (a) and horizontal (b) bottom-up printing approach of STIN multicore fiber bundles using Nanoscribe GmbH Photonic Professional GT+. In (a) the waveguide cores lay perpendicularly to the x-y plane, while in (b) they are printed in a parallel fashion, perpendicularly to the optical axis. 100

Figure 6.8 (a) Unwrapped 2D phase map PUMA reconstruction of a 20 µm high STIN multicore fiber bundle printed using a Photonic Professional GT+ system. The cladding and core power percentage are set at 40% and 64%, respectively; the speed is 7000 µm/s for both cores and cladding. (b) Phase profile along the cross-cut (highlighted in red in (a)); the phase difference between cores and cladding measures 3 rad on average. 100

Figure 6.9 (a) SEM image of a 7 x 7, 20 µm high waveguide bundle fabricated at $P_{cladding}$=40%, P_{core}=64%, and v=7000 µm/s; as it can be seen in the red framed inset, different exposure zones experience a different shrinkage, resulting in an additional protrusion in correspondence of the cores. The waveguides measure ~3 µm in size. (b) Refractive index difference scaling law of waveguides fabricated at 58% (11.6 mW), 61% (12.2 mW), 64% (12.8 mW), and varying speed from 6000 to 10000 µm/s; the experimental fabrication parameters for the cladding are constant ($P_{cladding}$=40%, v=7000 µm/s). The mean and standard deviation values have been measured over five waveguides. 101

Figure 6.10 (a) DeScribe 3D rendering of vertical multicore fiber bundles designed at variable heights H=150, 100, 50 and 20 µm. Phase contrast microscopy images of waveguide bundles with H_1= 20 µm (b), H_2= 50 µm (c), H_3= 100 µm (d) and H_4= 150 µm (e). At $P_{cladding}$=40%, v=7000 µm/s and P_{core}=64%, v=7000 µm/s, microexplosions irreversibly damage the waveguide bundles higher than 20 µm. 102

Figure 6.11 (a) Block-by-block and (b) layer-by-layer 3D printing approaches for the printing of horizontal STIN rectangular optical waveguides using Nanoscribe GmbH Photonic Professional GT+. Phase contrast (c) and bright field (d) microscopy of a waveguide bundle composed of 5 blocks following the block-by-block approach; phase contrast (e) and bright field (f) microscopy of a waveguide bundle composed of 5 blocks and 5 layers following the layer-by-layer approach. In both cases the printing parameters are the same ($P_{cladding}$=40%, v=7000 µm/s and P_{core}=64%, v=7000 µm/s), the waveguide pitch is 10 µm and one single block measures 120 µm. Hatching, slicing and stitching measure 0.1, 0.3 and 0.15 µm, respectively. 103

Figure 6.12 (a) SEM images of a 3 x 3 waveguide bundle with a hatching distance of 0.2 µm; (b) sample detachment from the glass substrate and (c) aggressive sample development in PGMEA causing material etching at the junctions. 104

Figure 6.13 Transmission loss in dB/mm of the rectangular STIN optical waveguides fabricated Nanoscribe Photonic Professional GT+. Inset shows the output intensity profile of one waveguide recorded at 609/50 nm wavelength filter. The loss at short wavelengths is highly affected from scattering, most probably due to material roughness. 104

Figure 6.14 (a) Refractive index distribution of a 2 µm x 2.5 µm (W x H) STIN optical waveguide. (b) Mode intensity distribution of the waveguide at λ=600 nm. (c) Refractive index distribution of a 3 x 3 STIN waveguide grid for cross-talk simulations. 105

Figure 6.15 xz (first column) and yz (second column) propagation profiles at λ=500 nm, λ=600 nm and λ=700 nm and 10 mm propagation distance, considering the propagation of the mode at each simulated wavelength and the refractive index distribution shown in Figure 6.14 (c)......106

Figure 6.16 Custom made sample target, fabricated by means of standard sputtering and photolithographic techniques. This target contains digits from 0 to 9, with different sizes and feature thicknesses. ...106

Figure 6.17 Input (a) and output (b) camera images of the 12 x 12 STIN waveguide bundle with incoherent light illumination and no image pattern projected. In (c) and (e) two different digits are projected from a custom made pattern, recorded in reflection on the input camera (CAM2 in Figure 5.8); (d) and (f) show the transmitted, pixelated version of the digits delivered from the waveguide bundle and recorded in transmission by means of the output camera (CAM1 in Figure 5.8)......107

Figure 6.18 U-net type DNN architecture used to reconstruct the output images from the fiber bundle. 109

Figure 6.19 Schematic of synthetic dataset creation for the training of the network. 1170 digits have been propagated through a 12 x 12 STIN waveguide bundle with core dimensions W=2 µm, H=2.5 µm and refractive index difference Δn=0.007. We set the illumination wavelength λ=600 nm, the sample length to be L=720 µm and the waveguide pitch D=10 µm. 110

Figure 6.20 (a) BPM output intensity of a digit, propagated in the bundle for 720 µm propagation distance; digit output intensity with a superimposed propagated plane wave (b) and a Gaussian-like noise distribution (c); scale bar measures 20 µm. 110

Figure 6.21 Mean squared error (a) and mean absolute error (b) of the training and validation datasets as a function of the epoch number. 111

Figure 6.22 Five examples of synthetic inputs we used to test the DNN (first column), their corresponding reconstruction (second column) and the ground truths used for the training; scale bars measure 20 µm. 111

Figure 6.23 Output intensity from the fiber bundle, fabricated using Nanoscribe Photonic Professional GT+, recorded by means of CAM1 (left column) and DNN reconstructed images (right column); scale bars measure 20 µm. 112

List of Tables

Table 1 List of the Sylgard 184 [133] and the recognized PA Raman peaks [131, 132]........................57

Table 2 Summary of transmission loss for the different waveguide types in different wavelength ranges in dB/cm. 71

Table 3 Physical parameters for the computation of the one-photon polymerization profile. 126

Table 4 Physical parameters for the computation of the two-photon polymerization profile. 127

Table 5 Monomer/PI combinations we have tested throughout the project. 130

List of Equations

Equation 1 Total internal reflection condition. 24

Equation 2 Numerical aperture of an optical fiber. 24

Equation 3 Phase matching condition. It shows that the propagation angles θr that satisfy it are discrete and they depend on the fiber radius a and relative refractive index difference Δ between core and cladding. 25

Equation 4 Helmholtz equation for each of the electric field component. 26

Equation 5 Electric field in cylindrical coordinates. 26

Equation 6 Radial distribution of the electromagnetic field components inside the core and inside the cladding. l is the order of the Bessel function. 26

Equation 7 Dispersion equation for the modes in a symmetric step-index optical fibers. 26

Equation 8 Transverse wavenumbers u and w, and relationship with the v parameter. 26

Equation 9 v parameter of an optical fiber. It is related to the fiber properties, such as radius and numerical aperture. It depends also on the source wavelength λ. 27

Equation 10 Number of modes supported inside a step-index multimode optical fiber taking into consideration the degenerate modes in the azimuthal direction and the two polarizations. 27

Equation 11 Coupling length formula. It predicts at which fiber length the 100% of the input signal is transferred to an adjacent fiber..30

Equation 12 Coupling length for cylindrical optical fibers [65]. 30

Equation 13 Material polarization as a function of the electric field strength and the nonlinear susceptibilities. 31

Equation 14 Material susceptibility. 31

Equation 15 Linear Lambert-Beer's law for a plane wave illumination. 31

Equation 16 One-photon absorption coefficient. 32

Equation 17 Two-photon absorption Lambert-Beer's law. 32

Equation 18 Two-photon absorption coefficient. 32

Equation 19 Solution for the nonlinear Lambert-Beer's law..32

Equation 20 Intensity distribution of a circular aperture. 33

Equation 21 Normalized optical radial coordinate. 33

Equation 22 Photoinitiation step of Norrish type I photoinitiators. 34

Equation 23 Photoinitiation step of Norrish type II photoinitiators. 34

Equation 24 Propagation step. 35

Equation 25 Termination step. 35

Equation 26 One-photon absorption coefficient. 36

Equation 27 Rate of polymerization in free-radical chain polymerization. 36

Equation 28 Rate equation for the generation of radicals in two-photon polymerization processes [36]. 36

Equation 29 Reference field mathematical expression. 41

Equation 30 Object field mathematical expression. 41

Equation 31 Interference intensity pattern. 42

Equation 32 In-plane wavefront reconstruction mathematical expression. 42

Equation 33 Reference complex field propagating at an angle θ with the optical axis. 43

Equation 34 Hologram intensity with an incoming reference beam at an angle $\theta = (\theta x, \theta y)$. 43

Equation 35 Fourier transform of the hologram intensity when the reference beam is tilted at an angle $\theta = (\theta x, \theta y)$. 43

Equation 36 Minimum reference angle in off-axis holography. 44

Equation 37 Refractive index difference between core and cladding of the polymer waveguides as a function of the accumulated phase. 45

Equation 38 Waveguide transmission loss formula in $[dBcm]$. 59

Equation 39 Nonlinear refractive index. 60

Equation 40 Nonlinear contribution to the material refractive index. 60

Equation 41 Helmholtz equation. 77

Equation 42 x-component of the optical field under the slow varying envelope approximation. 77

Equation 43 Beam propagation equation for a homogeneous medium. 77

Equation 44 Fourier Transform of the beam beam propagation equation. 78

Equation 45 Fourier Transform of an optical field which has propagated at a distance z. 78

Equation 46 Rectified linear activation function. 109

Equation 47 Mean squared error loss function. 109

Chapter 1 Introduction

1.1 3D microfabrication of polymer optical waveguides

1.1.1 Polymer optical waveguides

Optical waveguides are one of the most important photonic components. They are indispensable tools in many of today's technologies because of their capacity of guiding light [1, 2]. Optical waveguides traditionally consist of a glassy material embedded into a cladding, which is better known as optical fibers, and this revolutionary idea was first conceived by Charles K. Kaos, who won the Nobel Prize in 2009, stating:

'A fibre of glassy material constructed in a cladded structure represents a possible practical optical waveguide with important potential as a new form of communication medium. Compared with existing coaxial-cable and radio systems, this form of waveguide has a larger information capacity and possible advantages in basic material cost.'

The most well known application field of optical fibers is telecommunications [3, 4]; however, they also find a wide range of applicability in many other technological fields, such as fiber laser sources [5, 6], temperature and pressure sensors [7], and medical imaging [8]. More specifically, optical waveguides are a key element in the development of multifunctional platforms with tailored geometries, and the development of new materials together with novel fabrication technologies for their realization have attracted great attention in recent years. In particular, polymer-based waveguides are crucial soft photonic building blocks [9-11] for the development of complex multifunctional platforms, such as chip-to-chip interconnects in electronic systems [12, 13], optical printed circuit boards [14-16], and optofluidic platforms [17]. Because polymer materials well suit body and body fluids exposure [18], polymer-based waveguides find wide range of relevance in applications which require biocompatibility with the environment, such as, for example, in biomedical sensing [19, 20], wearable photonics [21] and physiological monitoring [22] , optogenetics [23-25] and microfluidic flow cytometry [26]. Therefore, dense integration of optical and fluidic functionalities are increasingly essential, calling for compact, low-loss, three-dimensional (3D) optical waveguides in such devices.

Several techniques aiming at inducing a refractive index change in polymers have been developed. Because of the versatility of polymers, it is possible to combine standard microfabrication technologies with the advantage of embedding the desired pattern directly into a preformed material, where undoped PMMA is the most commonly used polymer for optical waveguide writing applications [27-29]. Electro-optic polymers show a change of the refractive index under photo-bleaching from femtosecond laser irradiation [30], and photosensitive resists have been investigated for the realization of stand-alone photonic wire bonding [31]. Single-mode optical waveguides have been fabricated through *laser direct writing* (LDW) [32, 33], soft lithography and thermal curing methods using poly-siloxane and other commercially available polymer materials [34, 35]. However, the implementation of miniaturized photonic components with increased integration density calls for new, versatile fabrication technologies, which enable the formation of arbitrary submicron 3D shapes within a bulk material, such as *two-photon laser direct writing* (TP- LDW).

1.1.2 Laser-based three-dimensional (3D) microfabrication

Direct-write technologies refer to technological processes capable of modifying or precisely deposit functional materials on a substrate, over digitally designed trajectories or locations. The increasing demand for miniaturized, portable microcomponents for the assembling of electronic devices, sensors and mechanical sophisticated microparts led to the continuously growing sought after simpler, faster and low-cost alternatives to traditional photolithographic processes. Direct-write technologies allow for a straightforward three-dimensional (3D) implementation rather than 2D, removing more complicated process flow steps, such as the realization of masks, the multiple deposition of materials and the etching. In general, all direct-write techniques transfer or modify a tailored material by four basic mechanisms: dispensing, flow, particle beam and laser [36]. In this thesis we worked with a laser-based direct-write microfabrication technique, namely the *laser direct write* (LDW), which in general comprises the removal (i.e. laser micromachining), the addition (i.e. laser printing) and the modification (i.e. multiphoton photopolymerization) of different types of materials.

Femtosecond laser LDW is a technique for the fabrication of complex structures inside glass and polymer based materials that exploits both additive and subtractive manufacturing strategies [37]. When a high laser intensity is reached inside a medium, nonlinear optical processes occur, one of which is the simultaneous absorption of multiple photons whose combined energy induces a molecular transition that leads to structural modifications in that material. Besides submicron resolution, the nonlinearity of multi-photon absorption also enables the formation of an arbitrary 3D shape within a bulk material. The first 3D microstructure fabricated by means of *multiphoton lithography* (MPL) was proposed by Maruo et al. in 1997 [38]. He showed, for the first time, an experimental system which comprises a 790 nm, 200 fs pulse width Ti:Sapphire laser, for the fabrication of several kinds of microstructures using different resins made of photoinitiators, acrylate monomers and oligomers. However, the field of two-photon fabrication started in 1965, with the work of Pao and Rentzepis, where they described the photopolymerization of styrene using a red ruby laser [39]. 24 years later, in 1989, a book chapter by Cabrera et al. discussed the fundamentals of a multiphotonic process to induce local photopolymerization, triggered by two crossing laser beams [40]; in 1992, Strickler and Webb showed experimental evidence of polymerization induced by the simultaneous absorption of two photons coming from the same laser [41], while the first photoinitiators specifically designed for MPL were proposed by Perry and published in his work in 1999 [42]. Since then, the number of papers published about this topic has grown exponentially, showing increasing complexity and sophistication of the printed microparts, thanks to the remarkable improvements in the field of optics and chemical synthesis of polymerizable compounds. A large number of works have focused on the structural modification through multiphoton laser direct writing (MP-LDW), particularly in polymeric materials. This has led to the development of a wide number of processes for the fabrication of submicron fine systems, such as miniaturized mechanical and bioengineered parts [43-49], small photonic [50, 51] and micro-optical elements, i.e. lenses, prisms, gratings, axicons and multi-lens objectives for endoscopic imaging [52-54]. Several works about the LDW microfabrication of polymer optical waveguides via two-photon polymerization have been reported in the last decades [28, 29, 31, 55-57]. However, very little research about the structural modification of functionalized PDMS has been reported [58, 59]. In this work we exploited the optimized photon flux from a femtosecond pulsed laser for the fabrication of polymer optical waveguides embedded into a pristine pre-cured PDMS bulk.

1.1.3 Overview of the thesis

Polydimethylsiloxane (PDMS) is an elastomer of great technological importance, having excellent elasticity, wide spectral range of transparency [60, 61], and outstanding chemical [62] and thermal stability. Because of its easy handling and low cost, PDMS is widely used in the fabrication of microfluidic [63] and optofluidic devices in particular [64]. PDMS can be also used for the realization of optical waveguides by combining hot embossing and standard soft lithography processes [20-22]. However, these methods are generally constrained to the fabrication of two-dimensional structures.

In this thesis, I study the fabrication of polymer optical waveguides in PDMS, exploiting the nonlinear feature of multiphoton absorption in the presence of suitable chemical compounds. I will describe a host-guest system approach which includes a PDMS matrix as the host, and a liquid monomer/photoinitiator solution capable of permeating into the PDMS intermolecular space as a guest. Figure 1.1 illustrates an envisioned example PDMS hybrid photonic/fluidic device where 3D optical waveguides in several different configurations and microfluidic channels are tightly integrated. The core of this work consists of the fabrication of polymer waveguides in PDMS and other polymer materials through multiphoton polymerization.

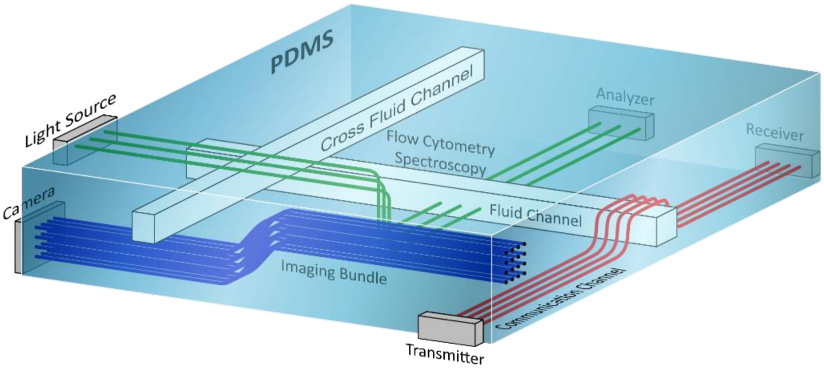

Figure 1.1 An envisioned example of 3D optical waveguides integrated in one flexible PDMS substrate with microfluidic channels. Blue wires illustrate an imaging waveguide bundle. Red wires exemplify optical communication channels. Green wires depict optical systems of flow cytometry or spectroscopy.

After this introductory section, **Chapter 1** will give the theoretical insight about optical waveguides and their working principle. The most important types of fibers will be discussed, with a special mention to single-mode optical fibers and multicore fiber bundles. I will discuss the basic theoretical background about the physical and chemical processes which stand behind the multiphoton polymerization technology, highlighting the intrinsic difference between one- and two-photon absorption mechanisms.

The experimental apparatus for the fabrication of polymer waveguides in PDMS is described in **Chapter 2**. We have built a LDW optical set up, integrated with a tunable femtosecond-pulsed laser, conferring experimental flexibility in terms of wavelength, peak intensity and motion speed, which are the fundamental parameters to be investigated in multiphoton fabrication technology. We have characterized the polymerized structures in terms of refractive index difference between core and cladding, and light transmission properties. To this end, I will give the theoretical background about digital holography and describe in detail the optical set up we have built for the phase reconstruction. The optical loss has been measured in a transmission loss characterization platform, which will be described in Chapter 2.

Throughout this research, we have extensively investigated a wide range of monomers and photoinitiators, which combination could efficiently yield polymerization inside PDMS. In **Chapter 3**, we demonstrate, for the first time, the photo-induced radical chain polymerization initiated by the monomer molecule itself without a photoinitiator. Our fabrication technique employs phenylacetylene as the photosensitive monomer for the fabrication of compact optical waveguides in polydimethylsiloxane through multiphoton laser direct writing. However, the intrinsic nonlinear effects, such as self-focusing, leads to beam collapse and, therefore, to irreversible material damage. Motivated by the need to minimize self-focusing, we further explored other monomer/PI combinations that could suit our purpose.

Chapter 4 will show the results we obtained by selecting the divinylbenzene (DVB) monomer in combination with a commercial photoinitiator from the Irgacure family, the OXE02. The use of a photoinitiator results in a stable and controllable fabrication process, and defect-free, 5-cm long waveguides. The trade-off in achieving this, is the use of lower peak intensities and higher writing speed. This synergy led to a lower refractive index contrast in the fabricated waveguide, resulting in higher transmission loss and less confined light compared with the PI-free process. Therefore, we propose the fabrication of enlarged cored structures to better confine the mode, and show their optical characterization.

In **Chapter 5** we simulate the light propagation inside poly-DVB waveguides using the beam propagation method (BPM), and describe poly-DVB multicore waveguide bundles, discussing their imaging capabilities. As a proof of concept, we show the delivering of easy patterns through small pilot 6 x 6 waveguide bundles. The primary goal of this work was to provide a solution to the demanding problem of cochlear implants (CIs) guiding endoscopes: an auxiliary optical micro-endoscope based on a waveguide bundle for giving visual feedback to the surgeon while inserting the cochlear implant in the human ear. We wanted to provide a PDMS optical waveguide bundle which would be flexible, biocompatible and that could deliver light from the outside to the inside of the cochlea, and vice versa, providing an image of the inner ear. I will describe the PDMS waveguide bundle prototype design and the process flow we have developed together with our working partner Sonova for its fabrication. Technological limitations and ideas for future work will be discussed, to represent fruitful scenarios for new and future development.

Chapter 6 presents the methodologies we have developed for the fabrication of polymer rectangular step-index (STIN) optical waveguides using the Photonic Professional GT+, a commercial 3D printing system developed by Nanoscribe GmbH. We selected the IP-dip photoresist in dill configuration to guarantee the highest optical quality and morphological smoothness. In this work we present a full calibration of the printing system parameters for a successful STIN waveguides fabrication. Transmission loss measurements have been performed, as well as optical phase reconstruction for refractive index measurements. We identified a successful 3D printing approach for the realization of 720 µm long STIN waveguide bundles and performed BPM simulations, experimental light coupling tests and deep neural network (DNN) image reconstruction.

This thesis will conclude with a summary of the presented research and an outlook with new ideas for the future work (**Chapter 7**).

1.2 Principles of optical waveguides

1.2.1 Light propagation in optical waveguides

Optical waveguides and optical fibers are light guiding structures made of dielectric materials, and they consist of a core with refractive index n_1, and a surrounding cladding with refractive index n_2, where $n_1 > n_2$ (see Figure 1.2). For a simple representation, we can describe the propagation of light with geometrical rays and apply the Snell's law at the refractive index discontinuity between the waveguide core and cladding. When the rays propagating in the waveguide reach the core-cladding interface at an angle greater than the critical angle ϕ_c, where $\phi_c = sin^{-1}\left(\frac{n_2}{n_1}\right)$, the condition for total internal reflection (TIR) is satisfied (Equation 1), and light is propagated with low losses.

$$n_1 \sin(\phi_c) \geq n_2$$

Equation 1 Total internal reflection condition.

However, only the light coming at a certain angle θ_{ic} can enter the waveguide. Therefore, the critical angle ϕ_c is linked to the light rays that can be accepted at the entrance of the waveguide and is depicted as the minimum angle at which corresponds a maximum θ_{ic} for the incoming light rays to be waveguided. This is the *numerical aperture* of the waveguide (NA) and can be expressed as:

$$NA = n_0 sin\theta_{ic} = n_1 sin\theta_{rc} = n_1 sin\left(\frac{\pi}{2} - \phi_c\right) = n_1\sqrt{1 - \frac{n_2^2}{n_1^2}} = \sqrt{n_1^2 - n_2^2}$$

Equation 2 Numerical aperture of an optical fiber.

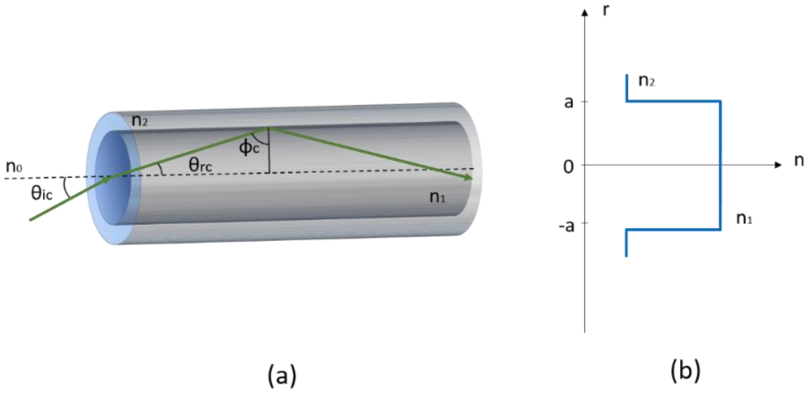

Figure 1.2 (a) Light guided in a step- index optical fiber, where a higher refractive index material constitutes the core (*n₁*) surrounded by a lower refractive index cladding material (*n₂*). Rays coming at the core-cladding interface at an angle greater than ϕ_c will be guided until the other end of the fiber. (b) Refractive index distribution of a step-index optical fiber along the radial direction.

As depicted in Figure 1.2, the optical fiber showing a constant distribution of the refractive index along the radial dimension is called step-index (STIN) optical fiber. All the possible ways (*modes*) for the light to be propagated are the results of constructive and destructive interference among the TIR-reflected rays within the waveguide (Figure 1.3). However, not all of these light rays will be guided until the fiber end: light rays need to satisfy a phase matching condition (Equation 3) in order to be propagated. This comes from the fact that the optical path of two consecutive reflections belonging to the same phase front needs to be an integral multiple of 2π. This implies a discretization of the angles at which rays can travel in the waveguide structure.

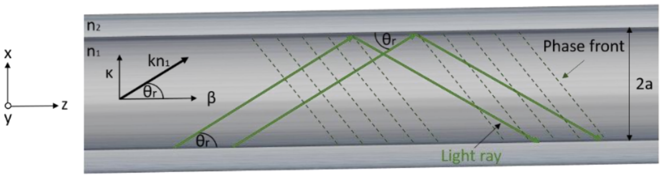

Figure 1.3 Light rays and phase fronts propagating in the waveguide. The resulting constructive and destructive interference patterns from light rays satisfying the phase matching condition are the modes of the waveguide.

$$tan\left(kn_1 asin\theta_r - \frac{m\pi}{2}\right) = \sqrt{\frac{2\Delta}{sin^2\theta_r} - 1}$$

Equation 3 Phase matching condition. It shows that the propagation angles θ_r that satisfy it are discrete and they depend on the fiber radius a and relative refractive index difference Δ between core and cladding.

Equation 3 represents the phase matching condition, where $k = \frac{2\pi}{\lambda}$ is the wavenumber in vacuum, λ is the source wavelength and *n₁* is the core refractive index. Therefore, the discrete propagation angles depend on the waveguide properties, particularly on its dimension a and on the relative refractive index difference between core and cladding $\Delta = \frac{n_1^2 - n_2^2}{2n_1^2}$. The optical field distributions satisfying Equation 3 are the modes of the waveguide, with being m an integer. The fundamental mode is found to be the one for which we obtain the minimum angle θ_r ($m = 0$). For $m \geq 1$ the so called *higher-order modes* are allowed for the propagation in the waveguide structure. Each propagation mode is an egeinfunction of the system and is associated to their eigenvalues: the *propagation constant* $\beta = kn_1 cos\theta_r$ along z, and the lateral propagation constant $\kappa = kn_1 sin\theta_r$.

1.2.2 Single-mode optical fibers

In order to calculate the field distribution in an optical fiber we need to perform an electromagnetic analysis: we need to solve the Maxwell's equations in cylindrical coordinates (Appendix 1) by applying proper boundary conditions for the electromagnetic field. For the sake of simplicity, we will consider only the electric part of the electromagnetic field, but the same equations remain valid for the magnetic field, as well. Let us describe the optical fiber depicted in Figure 1.2 (a) by introducing ρ, θ and z, namely the polar, azimuthal and axial coordinate. In a step-index optical fiber, the refractive index distribution can be described as $n(r) = n_1$ for $r \leq a$ (core) and $n(r) = n_2$ for $r > a$ (cladding). Moreover, we introduce the weakly guiding approximation, according to which $\frac{n_1}{n_2} \cong 1$, and that simplifies the analysis. Assuming monochromatic light and dielectric materials, each component of the electric field follows the Helmholtz equation, which in the Fourier domain and in cylindrical coordinates can be written as:

$$\frac{\partial^2 \tilde{E}_{\rho,\theta,z}}{\partial \rho^2} + \frac{1}{\rho}\frac{\partial \tilde{E}_{\rho,\theta,z}}{\partial \rho} + \frac{1}{\rho^2}\frac{\partial^2 \tilde{E}_{\rho,\theta,z}}{\partial \theta^2} + \frac{\partial^2 \tilde{E}_{\rho,\theta,z}}{\partial z^2} + n^2 k_0^2 \tilde{E}_{\rho,\theta,z} = 0$$

Equation 4 Helmholtz equation for each of the electric field component.

where the electric field is given by:

$$\boldsymbol{E}(\rho, z, \theta, t) = (E_\rho \boldsymbol{\rho} + E_\theta \boldsymbol{\theta} + E_z \boldsymbol{z}) e^{j(\omega t - \beta z)}$$

Equation 5 Electric field in cylindrical coordinates.

and $\tilde{\boldsymbol{E}}$ is its Fourier transform.

By applying the method of separation of variables (more details in Appendix 1), solutions for the radial distribution of the electromagnetic field derived from Equation 4 are found to be the Bessel functions of the first kind, and the modified Bessel functions of the second kind, in the core and in the cladding region, respectively:

$$E_{\rho,\theta,z}(\rho) = \begin{cases} A J_l(k_T \rho), & \rho \leq a \\ B K_l(\gamma \rho), & \rho > a \end{cases}$$

Equation 6 Radial distribution of the electromagnetic field components inside the core and inside the cladding. l is the order of the Bessel function.

where $k_T = \sqrt{k^2 n_1^2 - \beta^2}$ and $\gamma = \sqrt{\beta^2 - k^2 n_0^2}$ are introduced, A and B are two constants, and l is the order of the Bessel function. The continuity of the field and its derivatives needs to be guaranteed, and following the Bessel functions properties [65, 66], the formulation of the dispersion equation is obtained:

$$u \frac{\mathrm{J}_{\mathrm{l}\pm 1}(u)}{\mathrm{J}_{\mathrm{l}}(u)} = \pm w \frac{\mathrm{K}_{\mathrm{l}\pm 1}(\mathrm{w})}{\mathrm{K}_{\mathrm{l}}(\mathrm{w})}$$

Equation 7 Dispersion equation for the modes in a symmetric step-index optical fibers.

In this formula, expressions of the transverse wavenumbers are used:

$$u = k_T a = a\sqrt{k^2 n_1^2 - \beta^2}$$

$$w = \gamma a = a\sqrt{\beta^2 - k^2 n_0^2}$$

$$u^2 + w^2 = k^2 (n_1^2 - n_0^2) a^2 = v^2$$

Equation 8 Transverse wavenumbers u and w, and relationship with the v parameter.

being u, w the *transverse wavenumbers* and v is the *fiber parameter*, that can be rewritten as:

$$v = a\frac{2\pi}{\lambda}NA$$

Equation 9 v parameter of an optical fiber. It is related to the fiber properties, such as radius and numerical aperture. It depends also on the source wavelength λ.

Knowing the illumination wavelength and the fiber parameters, we are able to find solutions for the characteristic equation (Equation 7), for example by plotting and identifying the intersections between the two graphs resulting from Equation 7 and Equation 8. It can be shown that if v <2.405, the fiber is in single mode condition (SMC), which means that only one mode (fundamental mode) is allowed to propagate inside the fiber. Figure 1.4 shows the fundamental mode computed for an optical fiber with n_1 =1.47, n_1 =1.455, a =1.5 µm, at an illumination wavelength λ =0.633 µm.

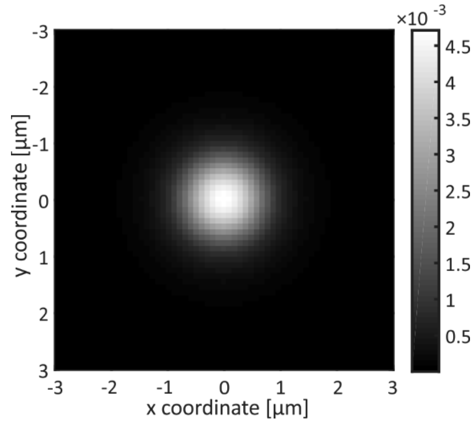

Figure 1.4 Computed fundamental mode for an optical fiber with n_1=1.47, n_2=1.455, a= 1.5 µm, at an illumination wavelength λ=0.633 µm; the v number fot this fiber is v=1.56, therefore it is a single mode fiber.

1.2.3 Fiber types and imaging

In the previous paragraphs I gave the technical basis about the working principle of optical waveguides, with a special mention to single mode optical fibers. Nevertheless, it is important to cite the other existing optical fiber types, which became available because of the technological advances in the drawing techniques. We know that for given physical fiber parameters, if the v number is greater than 2.405, multiple modes are supported inside the waveguide structure. More specifically, it is shown [65] that the number of modes N in a step-index multimode fiber (MMF), with V being the V-number can be expressed as:

$$N = \frac{4}{\pi^2}V^2$$

Equation 10 Number of modes supported inside a step-index multimode optical fiber taking into consideration the degenerate modes in the azimuthal direction and the two polarizations.

Each mode inside a multimode fiber has a specific propagation constant β, resulting in different velocities along the propagation direction inside the MMF. In simple words, a pulsed input light would suffer time broadening because of the difference in the time arrival of the different modes. Moreover, small changes in the MMF configuration, as bending or structural defects, can degrade the information delivery, due to modal coupling inside the fiber. Because of these intrinsic phenomena, MMFs are not normally utilized for imaging, since what we would see at the fiber end is a scrambled version of the input, called *speckle pattern*. However, the use of MMFs for imaging applications has turned to be lately a very active and promising research field, because of the advances introduced by wavefront shaping techniques such as optimization algorithms [67, 68], digital phase conjugation (DPC) [69, 70], transmission matrix [71, 72], and deep neural network approaches (DNNs) [73-76].

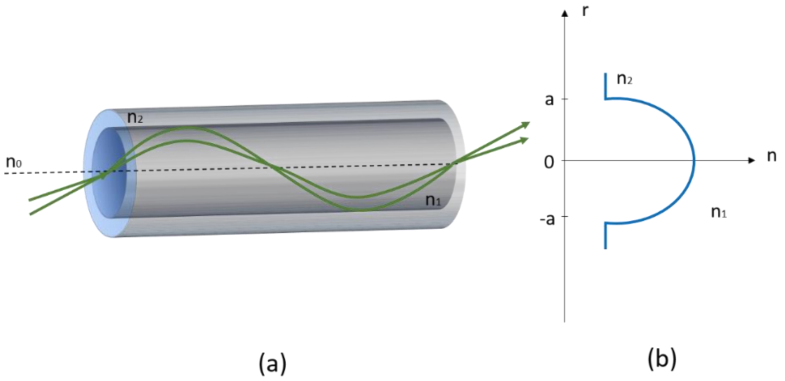

Figure 1.5 (a) Light guided in a graded-index (GRIN) optical fiber. (b) Parabolic refractive index distribution of the core n_1 in a GRIN fiber.

As I mentioned above, each mode in a MMF propagates at a different velocity, and the effects can be seen already after a few hundreds of microns along the optical axis. Graded-index fibers (GRINs) are optical fibers where the core refractive index follows a parabolic distribution to compensate the modal dispersion (Figure 1.5); in other words, the refractive index distribution of the core is engineered in a way that all the supported modes of the fiber will arrive at the same moment at the end of the GRIN fiber, leading to zero modal dispersion [65, 66]; this holds assuming a perfectly fabricated GRIN fiber without any structural imperfection. Considering equal fiber physical parameters and wavelength, a GRIN fiber with a quadratic refractive index distribution, as depicted in Figure 1.5 (b), would approximately support half of the modes number N supported by the corresponding MMF [65, 66].

The small size of fiber probes represents a key advantage in biomedical microendoscopy applications, because of the need of reaching confined and remote places inside the human body. Big endoscopes, distal lenses and additional optical components generally increase the total size of microendoscopes and imaging fiber probes, leading to severe tissue damage. Researchers have put a lot of efforts for the implementation of novel technologies capable of scaling down the size of medical endoscopes, with a particular attention on the removal of distal optical components, such as lenses. Consequently, the replacement of GRIN lenses with GRIN fibers at the distal side of fiber bundles represents a valid alternative for the implementation of microendoscopes, because of their small size and process compatibility [77-80].

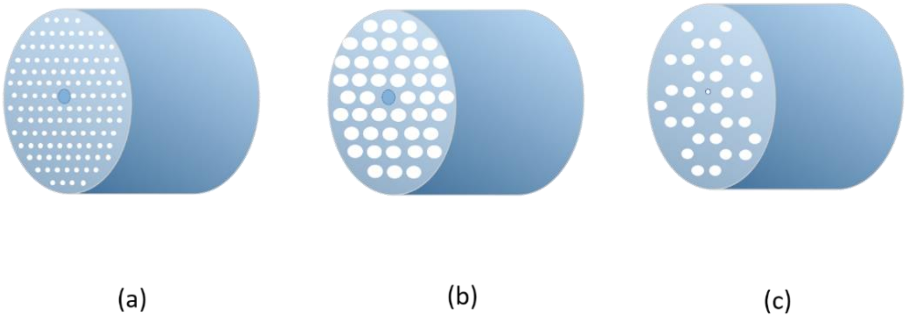

Figure 1.6 Examples of holey fibers (PCFs) in different configurations; (a) Small air holes surround the solid fiber core (dashed line); the diameter of the air holes can be smaller than the operation wavelength. (b) Periodic arrangement of larger air holes surrounding the solid core of the PCF. (c) Periodic arrangement of air holes surrounding the small hollow core; the size difference between the air holes in the cladding and the hollow core results in a lower average cladding refractive index with respect to the core.

Another important type of fibers which deserve to be mentioned are the photonic crystal fibers (PCFs). This type of fibers are made of pure silica and feature a periodic arrangement of air holes surrounding the fiber core, which in general can be solid (Figure 1.6 (a)-(b)) or hollow (Figure 1.6 (c)). The first type of PCFs are called *solid-core PFC* (SC-PCFs) and the latter ones are the *hollow-core PCFs* (HC-PCFs). In all this types of PCFs, the average cladding refractive index is always smaller than the core refractive index, causing light to be guided via two main mechanisms: the effective-index guidance mechanism in the case of SC-PCFs, and the photonic-bandgap guidance (PBG) in HC-PCFs [66]. The holey cladding can be seen as a 2D periodic structure (photonic crystal), which implies the existence of a frequency-wave vector dispersion diagram with photonic bandgaps: if the optical frequency lies within the photonic bandgap, light cannot travel in the cladding, and consequently being trapped in the fiber core. Because of their low-loss feature, hollow-core PCFs don't suffer of drawbacks caused by nonlinear effects and, therefore, became important tools in those applications where high optical power pulses delivering is needed [81-83]; however, it has been also demonstrated that lensed PCF can serve as side view tools in compact OCT imaging probes [84, 85], offering an alternative to conventional multi-core fiber bundles.

1.2.4 Imaging in multi-core fiber bundles

In the previous subchapter, I briefly described some of the existing fiber types, with a particular mention to their imaging capabilities; however, further description and deeper mathematical analysis of these types of fibers is beyond the scope of this thesis, as the main work consisted in the fabrication of single mode optical waveguides in polymer materials.

Single mode fibers are the fundamental building block of multicore fiber bundles (MCFs). As depicted in Figure 1.7, a multicore fiber bundle consists of many small step-index cores placed together in a common cladding. Another type of bundles, the so-called *leached fiber bundles*, consists of individual cores, where each of them is surrounded by a separate cladding, held together by a mesh. Multicore fibers are mostly used for one-photon confocal microscopy [86-88] and multi-photon imaging [89-92]. They are also widely used in telecommunications [93-95], optical coherence tomography (OCT) [96, 97] and optical sensing [98, 99].

Each small core supports generally one mode (or few modes depending on the wavelength [100]) and acts as a single pixel, capable of detecting the information in a specific point of the object under observation, and deliver it to the fiber end. Unlike MMFs, MCFs can directly transfer an image on a detector, most likely by means of additional optics, and it doesn't require further data processing. Therefore, there is a direct spatial correspondence between the object at the distal side of the fiber bundle and the image which is transferred to its proximal facet. In the case of MCF bundles, the resolution is given by the core-to-core spacing, which on average is about 5 µm in commercially available endoscopes [101, 102].

However, the high packing density of the cores doesn't come without a price, which in this case is payed in terms of cross-talk between the cores. For a given refractive index difference between cores and cladding, if the cores sit too close to each other, the information travelling in one core will be transferred to another adjacent core, leading to blurred images and low signal to noise ratio. A lot of effort has been done in order to study and propose solutions to highly cross-talking MCFs [103-106]. It has been shown that the strength of the cross-talk decreases with the degree of the core size variation in the bundle [103, 104], which makes it an additional element to play with, besides the physical fiber parameters and the source wavelength and polarization.

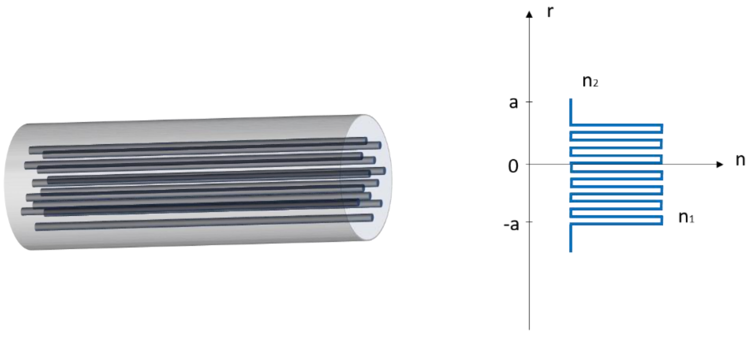

(a) (b)

Figure 1.7 (a) Schematic of a multicore step-index fiber bundle. (b) Bundle refractive index distribution with n_1 and n_2 being the cores and cladding refractive index, respectively.

Depending on the fiber structure and physical parameters, one could theoretically predict what the critical core-to-core spacing D should be in order not to have information transfer between the cores [65]. In the case of cylindrical optical fibers, the distance in the optical propagation direction at which 100% of the signal is transferred from one core to the other is called *coupling length* L_c, and is given by:

$$L_c = \frac{\pi}{2\kappa}$$

Equation 11 Coupling length formula. It predicts at which fiber length the 100% of the input signal is transferred to an adjacent fiber.

with κ being the coupling coefficient for a cylindrical structure:

$$\kappa = \frac{\sqrt{\Delta}}{a} \frac{u^2}{K_1^2(w)v^3} \sqrt{\frac{\pi a}{wD}} \exp[-\frac{w}{a}D]$$

Equation 12 Coupling length for cylindrical optical fibers [65].

where D is the core-to-core spacing (pitch), considering as a starting and ending points of this segment the two wave-guide core centers. Therefore, the imaging performance of a multicore fiber bundle depends mainly on the refractive index difference between cores and cladding, the size of the cores, the pitch between the cores and the illumination wavelength.

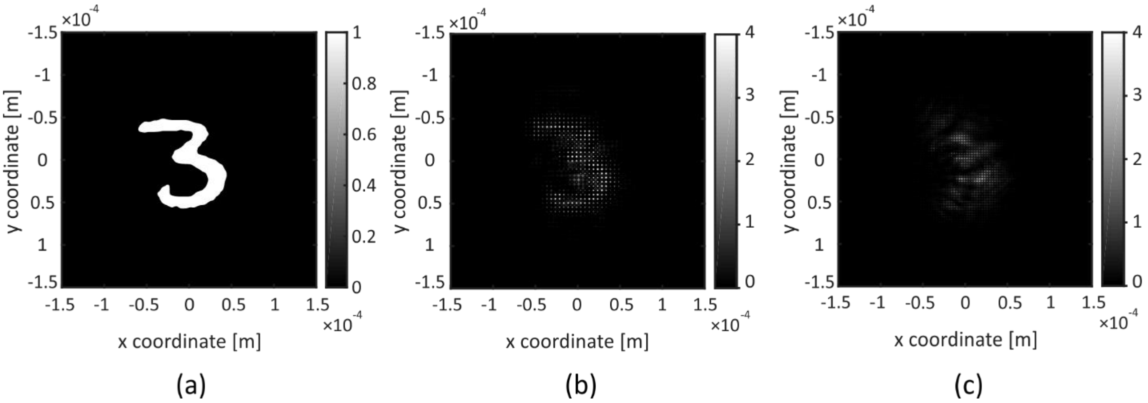

Figure 1.8 (a) A digit from the MNIST data base is used as an input. Output intensity from a multicore fiber bundle having a core-to-core spacing of 5 µm (b) and 3 µm (c). The diameter of the fibers is a= 1.5 µm, Δn= 0.015, the illumination wavelength is λ=0.633 µm and the propagation distance is 2.5 mm.

It appears immediately clear that the resolution of the transmitted image is limited by the intrinsic pixelation of the imaging system and the degree of cross-talk between the cores (Figure 1.8).

1.3 Multiphoton absorption

1.3.1 Technical foundation: multi-photon absorption

Multi-photon absorption is a nonlinear optical phenomenon which is implemented in multi-photon polymerization techniques. It involves the simultaneous absorption of multiple photons in the transition of an atom from its ground state to an excited state (Figure 1.9). The dipole moment per unit volume, or polarization $\widetilde{\boldsymbol{P}}(t)$ of a material is dependent on the strength of the electric field $\widetilde{\boldsymbol{E}}(t)$, the dielectric constant ε_0, and the susceptibility of the first and higher orders $\chi^{(n)}$. The general expression of the polarization takes the form:

$$\widetilde{\boldsymbol{P}}(t) = \widetilde{\boldsymbol{P}}_{\boldsymbol{1}}(t) + \widetilde{\boldsymbol{P}}_{\boldsymbol{2}}(t) + \widetilde{\boldsymbol{P}}_{\boldsymbol{3}}(t) = \varepsilon_0\chi^{(1)}\widetilde{\boldsymbol{E}}(t) + \varepsilon_0\chi^{(2)}\widetilde{\boldsymbol{E}}(t)^2 + \varepsilon_0\chi^{(3)}\widetilde{\boldsymbol{E}}(t)^3 + \cdots + \varepsilon_0\chi^{(n)}\widetilde{\boldsymbol{E}}(t)^n$$

Equation 13 Material polarization as a function of the electric field strength and the nonlinear susceptibilities.

where the material susceptibility which is dependent on otpical frequency ω and can be written as:

$$\chi(r,\omega) = Re[\chi(r,\omega)] + jIm[\chi(r,\omega)]$$

Equation 14 Material susceptibility.

If we consider a plane wave illumination, in the linear approximation the way light is absorbed when travelling through a material is described by the Lambert-Beer's law:

$$dI = -\alpha I dz$$

Equation 15 Linear Lambert-Beer's law for a plane wave illumination.

with I being the light intensity throughout the absorbing medium, and α the one-photon absorption coefficient, proportional to the imaginary part of the material susceptibility [107]:

$$\alpha = \frac{\omega}{nc} Im[\chi(r,\omega)]$$

Equation 16 One-photon absorption coefficient.

where n being the material refractive index and c the speed of light. If we consider the absorption of two photons, the Lambert-Beer's law takes the form:

$$dI = -(\alpha + \beta I)Idz$$

Equation 17 Two-photon absorption Lambert-Beer's law.

β is the two-photon absorption coefficient and can be written as [107]:

$$\beta = \frac{8\pi^2\omega}{c^2n^2} Im[\chi^{(3)}]$$

Equation 18 Two-photon absorption coefficient.

Equation 18 links the two-photon absorption coefficient to the third order nonlinear susceptibility, and this is therefore a nonlinear effect of third order. If we assume negligible linear absorption ($\alpha = 0$), Equation 17 has a solution in the form:

$$I = \frac{I_0}{1 + \beta I_0 z}$$

Equation 19 Solution for the nonlinear Lambert-Beer's law.

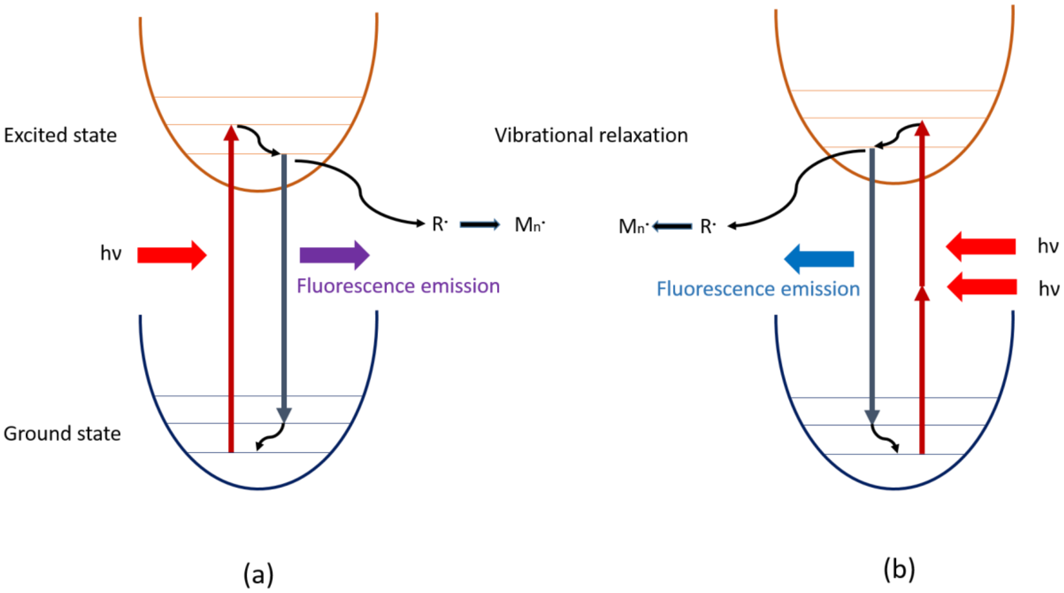

Figure 1.9 Diagram of the atomic transition in the one-photon (a) and two-photon (b) absorption processes. In one-photon excitation the atom makes the transition from its ground state to an excited state through the absorption of a single photon; in the two-photon absorption mechanism, the transition is made by absorbing two lower-energy photons. Fluorescence can occur after the absorption of photons and it is the same in both linear and nonlinear processes.

Typically, in most two-photon polymerization systems, the absorption of multiple photons is achieved by focusing femtosecond pulsed lasers by means of high numerical aperture objectives; this is because of the need of increasing the probability of having multiple photons at the same time and in the same focus region. The one-photon absorption is proportional to the intensity of the laser beam, while in the two-photon case it is proportional to the laser beam intensity squared. The characteristic spatial intensity profile of an aberration-free circular aperture with numerical aperture NA is described by the Airy disk:

$$I = 2\left(\frac{J_1(v)}{v}\right)^2$$

Equation 20 Intensity distribution of a circular aperture.

with $J_1(v)$ being the first order Bessel function and v the normalized radial optical coordinate:

$$v = krNA$$

Equation 21 Normalized optical radial coordinate.

where $k = \frac{2\pi}{\lambda}$ is the wavenumber, NA the numerical aperture of the lens and r the radial coordinate. Figure 1.10 shows the one-photon (blue) and the two-photon (red) spatial distribution for a laser source having λ=680 nm and NA=0.7, and since they represent the geometry of the absorption volume, they can be directly compared. Photopolymerization is a threshold mechanism, which means there is a certain energy which is required in order to trigger the photopolymerization reaction. When the threshold is achieved, the optical resolution of a two-photon polymerization mechanism is proportional to the one of linear absorption by a factor of $\frac{1}{\sqrt{2}}$; this, together with the very high confinement of the excitation at the focus spot, makes it a powerful technique for the fabrication of nm-sized features through femtosecond laser direct writing (LDW).

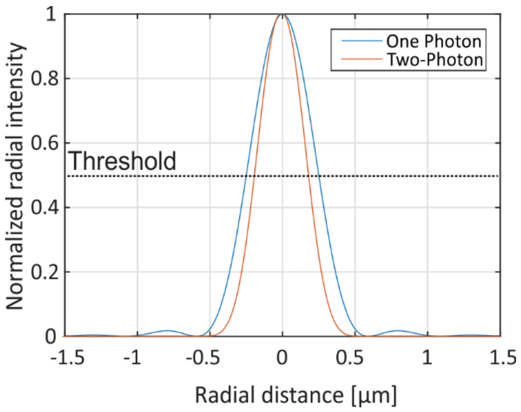

Figure 1.10 One-photon vs two-photon normalized intensity distribution along the radial coordinate for a light source having λ =680 nm and a NA=0.7.

1.3.2 Free-radical chain polymerization mechanism

As mentioned in the previous subchapter, nonlinear multi-photon absorption is the ground physical phenomenon which rules the multi-photon polymerization mechanism. I will now introduce the general concept of free-radical chain photopolymerization and give some technical terminology that will help understanding the methodologies we followed for the fabrication of polymer optical waveguides.

Photopolymerization is a chemical reaction that converts light into chemical energy; one *photopolymer* is a polymer that changes its properties if exposed to light. *Polymer* from Greek: πολυ-μέρος, literally means *that has many parts*; one photopolymer consists of subunits called *monomers* and/or *oligomers*, which are mixed together with a photoactive molecule called *photoinitiator* (PI). When photons, generally in the UV or visible range of the electromagnetic spectrum, are shined on a photoactive resin, they can change its structural properties, for example by hardening, as a result of the cross-linking between the single unit monomer molecules (Figure 1.11). In *free-radical chain photopolymerization* this is achieved via photo-produced reactive species, the radicals. The free-radical chain photopolymerization consists of three main steps: the *initiation*, the *propagation* and the *termination* [108].

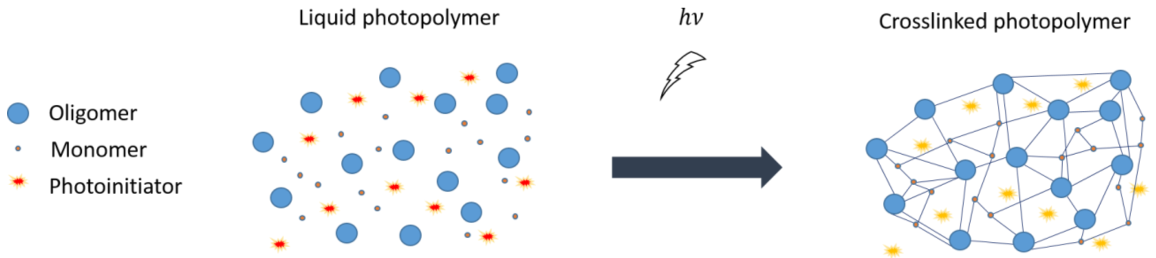

Figure 1.11 Liquid photopolymer hardening as a result of cross-linking of monomer/oligomer molecules via light absorption.

The initiation step is considered to involve two reactions: the first is the dissociation of the photoinitiator species I to yield two initiating radicals $R^{\cdot}$; the second reaction involves the production of the first initiated monomer $M_1{}^{\cdot}$. Both reactions are governated by two rate constants, the *dissociation rate constant* k_d of the initiating molecule I and the initiation rate constant of reactive centers k_i:

$$\begin{cases} I \xrightarrow{h\nu,k_d} 2R^{\cdot} \\ R^{\cdot} + M \overset{k_i}{\rightarrow} M_1{}^{\cdot} \end{cases}$$

Equation 22 Photoinitiation step of Norrish type I photoinitiators.

This type of photoinitiation is depicted as *Norrish type I*, and the photoinitiator molecule undergoes bond cleavage, generating free radicals upon absorption of light. Irgacure 369 is a very common one-photon radical Norrish type I photoinitiator and the bond cleavage mechanism is shown in Figure 1.12.

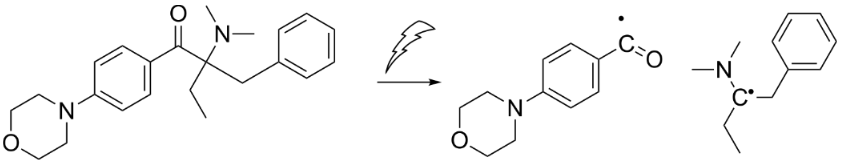

Figure 1.12 Irgacure 369 bond cleavage under light illumination and consequent generation of two radicals $R^{\cdot}$.

Photoinitiators of *Norrish Type II* involve a bimolecular reaction with a co-initiator C, resulting in slower curing rate and easier to be quenched by monomers with low triplet energy (such as styrene) or by oxygen.

$$\begin{cases} I + C \xrightarrow{h\nu,k_d} 2R^{\cdot} \\ R^{\cdot} + M \overset{k_i}{\rightarrow} M_1{}^{\cdot} \end{cases}$$

Equation 23 Photoinitiation step of Norrish type II photoinitiators.

Benzophenone and its derivatives are typical Norrish Type II photoinitiators; they work together with synergists (e.g. tertiary amines) which donate a hydrogen atom to the excited PI. Very reactive alkyl-amino radicals are produced after hydrogen abstraction, which subsequently initiate polymerization (Figure 1.13).

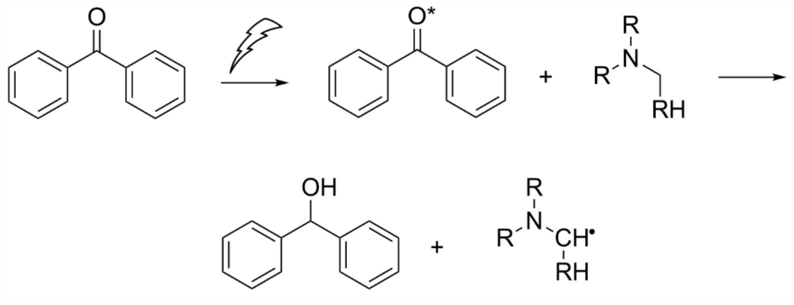

Figure 1.13 Bimolecular reaction of benzophenone and a tertiary amine; the amine is radicalized and triggers the polymerization reaction.

In both cases, the second reaction of the initiation step starts the chain growth along the polymer chain caused by the propagation of reactive monomers. The propagation step follows the initiation and is characterized by the successive addition of monomer molecules. Monomers continue to add, creating larger and larger macroreactive molecules $M_{n+1}{}^{\cdot}$; the *propagation rate constant* k_p, regulates this process, making the polymer growth rapid and efficient [108]:

$$\begin{cases} M_1{}^{\cdot} + M \overset{k_p}{\rightarrow} M_2{}^{\cdot} \\ M_2{}^{\cdot} + M \overset{k_p}{\rightarrow} M_3{}^{\cdot} \\ \vdots \\ M_n{}^{\cdot} + M \overset{k_p}{\rightarrow} M_{n+1}{}^{\cdot} \end{cases}$$

Equation 24 Propagation step.

The polymer growth termination involves two chain radicals and according to the termination mechanism, *combination* or *disproportionation*, it leads to the formation of one or two dead polymers, respectively. This is the termination step:

$$\begin{cases} M_n{}^{\cdot} + M_m{}^{\cdot} \overset{k_{tc}}{\longrightarrow} M_{n+m} \\ M_n{}^{\cdot} + M_m{}^{\cdot} \overset{k_{td}}{\longrightarrow} M_n + M_m \end{cases}$$

Equation 25 Termination step.

It is important to specify that depending on the nature of the reactive species, which can be free radicals, anion or cation reactive centers, the monomers show a certain degree of selectivity towards the photoinitiators, which depends on their capability of triggering the monomer polymerization. As it will be described more accurately in the next sections, the main goal of this work consisted in the direct femtosecond laser writing of high refractive index waveguides in pre-crosslinked PDMS. I will describe a host-guest approach which includes a PDMS matrix as the host and a liquid monomer/PI solution capable of permeating into the PDMS intramolecular space as a guest. Therefore, besides being polymerizable with good reactivity, further requirements on the monomer formulation came into play:

- the refractive index of the monomer must be higher than that of the PDMS host matrix;
- the monomer molecule must be small and nonpolar to allow for a high solubility in PDMS and an easy extraction after laser exposure;
- the absorption spectrum of the monomer must not overlap with the PDMS host.

Based on these fundamental constrains, an important part of this work focused on the investigation of suitable monomer/PIs compounds for the fabrication of optical waveguides in PDMS. The first requirement generally necessitate π-electron rich phenyl group in the monomer formulation. The third requirement is usually satisfied in most nonpolar small-molecule monomer formulations: styrene, phenylacetylene and divinylbenzene were identified as the best candidates for our purpose.

1.3.3 One-photon and two-photon radical photoinitiators

The photoinitiator efficiency is an essential prerequisite for the preparation of performing photopolymers. At the early stage of two-photon polymerization (TPP), one-photon photoinitiators, such as Irgacure 369 [38, 109, 110] and Irgacure 184 [36], have been used to demonstrate TPP. The two-photon absorption (TPA) efficiency is measured in GM [Göppert-Mayer], to honor Maria Göppert-Mayer that in 1931 predicted multi-photon excitation processes in her doctoral dissertation on the theory of two-photon quantum transitions in atoms [111]. 1 $GM = 10^{-50} cm^4 s\ photon^{-1}$ is the unit of the so called *two photon absorption cross-section* δ_{2A} of a photosensitive molecule, and can be considered the corresponding extinction coefficient ε in one-photon absorption processes described by the Lambert-Beer's law (Equation 15). α is the one-photon absorption coefficient and is dependent on the extinction coefficient ε and the photoinitiator concentration $[I]$:

$$\alpha = \varepsilon[I]$$

Equation 26 One-photon absorption coefficient.

ε is expressed in $\left[\frac{L}{mol\ cm}\right]$ and $[I]$ in $\left[\frac{mol}{L}\right]$. Predicting how much monomer is polymerized in a photopolymerization process is not an easy task because of several unknowns in the system, but we can estimate the photopolymerization profile by retrieving the rate equations under specific assumptions and the important steady-state approximation, according to which the rate of change of radicals concentration is zero during the course of the process (Appendix 2). Both in one-photon and two-photon polymerization mechanisms, the rate of polymerization R_p governates the kinetic of the process and corresponds to the rate of monomer disappearance [108]:

$$R_p = -\frac{d[M(t)]}{dt} = k_p[M(t)]\sqrt{\frac{R_{i_{1PP/2PP}}}{2k_t}}$$

Equation 27 Rate of polymerization in free-radical chain polymerization.

being $[M(t)]$ the monomer concentration at a certain instant t, and $R_{i_{1PP/2PP}}$ the *rate of initiation*, wether for one-photon or two-photon polymerization mechanism. Therefore, the determination of R_i is crucial for understanding the intrinsic differences which reside between linear and nonlinear processes. The main difference between one-photon and two-photon polymerization mechanisms is that, while in 1PP the concentration of photoactive molecules $[I(t)]$ at any instant t is linearly proportional to the photoinitating beam intensity, in two-photon polymerization $[I(t)]$ depends on the square of the flux of the initiating beam [36]:

$$R_{i_{2PP}} = -\frac{d\,[I(t)]}{dt} = \frac{1}{2}\delta_{2A}[I(t)]F^2$$

Equation 28 Rate equation for the generation of radicals in two-photon polymerization processes [36].

with F being the photon flux of the photoinitiating beam ($\left[\frac{photons}{s\,m^2}\right]$). Therefore, appears immediately clear that a large δ_{2A} is an essential prerequisite to guarantee an efficient and succesful two-photon polymerization and, therefore, precise microstructures during the fabrication process; however, δ_{2A} is a physical property of a molecule, thus strongly dependent on its molecular structure. The molecular properties which can affect the magnitude of δ_{2A} can be, for example, the strength of electron donor and/or acceptors [112-114], the π-conjugation length [115-117] and the molecular coplanarity [118, 119]. Rhodamine B is a modest two-photon absorber and exhibits a TPA cross-section δ_{2A} of 220 GM at 840 nm wavelength illumination [120]. Strong two-photon absorbing molecules exhibit a 10-50 fold two-photon absorption cross-section [36]. In recent years, because of the remarkable developments of two-photon microfabrication techniques, a lot of work has been done in order to increase the δ_{2A} of photoactive molecules [36]. The experimental investigation and chemical structure modification of new molecular formulas with increased δ_{2A} is outside the scope of this thesis, and therefore it won't be deepen in the following chapters; nevertheless, we based our experimental research on previous studies and literature on this topic to find good PI candidates for our purpose (Chapter 3 and Chapter 4).

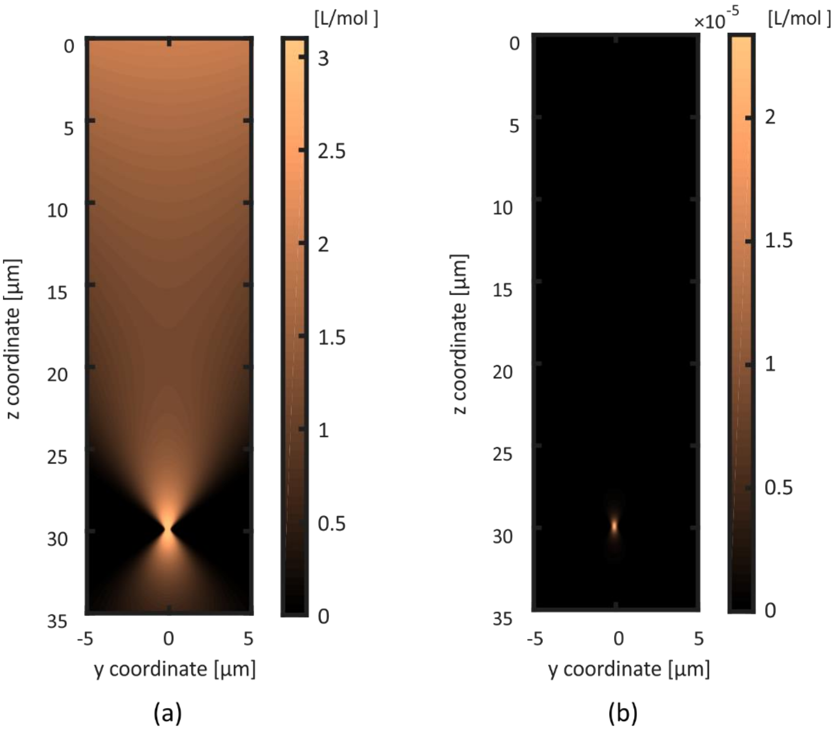

Figure 1.14 One-photon (a) and two-photon (b) polymerization profile assuming a Gaussian beam illumination, 0.7 NA and a polymer refractive index n=1.5.

Assuming negligible photons absorption and a Gaussian beam intensity distribution one can see that in one-photon polymerization mechanism (Figure 1.14 (a)) the polymerization falls within the illumination cone described by the optics, while in two-photon polymerization (Figure 1.14 (b)) the polymer formation is confined only to the laser focus. This represents a very important advantage and allows for a precise and circumscribed fabrication of µm-sized features. Details about the physical parameters and computational environment for the qualitative comparison between one-photon and two-photon polymerization processes using Irgacure OXE01 as a photoinitiator are described in Appendix 2.

1.4 Summary

In this chapter I explained the basic concepts of light propagation in optical fibers. The modes formation in optical fibers was discussed with a special mention for single-mode optical fibers. The imaging capabilities and applications of the different types of fibers have been described, in particular of multicore fiber bundles. Moreover, I gave the basics about the physics and chemistry beyond single- and multi-photon absorption and described the free-radical chain photopolymerization process. The description of the nonlinear dependence of the photopolymerization on the light intensity is the fundamental aspect for a full understanding of the intrinsic differences between one and two-photon polymerization processes. In the next chapter I will present the experimental methodologies we followed for the fabrication of µm-sized polymer waveguides in PDMS, describing the LDW fabrication set-up, and the techniques we used for the characterization of the waveguides.

Chapter 2 Experimental apparatus

This chapter presents the experimental methodologies we implemented for the fabrication and characterization of polymer waveguides in PDMS. A two-photon polymerization fabrication system has been built, together with a holographic interferometer and a transmission loss/light coupling platform for the investigation of the optical properties of the polymer waveguides.

Most of the material presented in this chapter can be found in publications ([121, 122]):

- Panusa, G., Pu, Y., Wang, J., Moser, C., & Psaltis, D. (2019). *Photoinitiator-free multi-photon fabrication of compact optical waveguides in polydimethylsiloxane. Optical Materials Express, 9(1), 128-138. doi: 10.1364/OME.9.000128.*
- Panusa, G., Pu, Y., Wang, J., Moser, C., & Psaltis, D. (2020). *Fabrication of Sub-Micron Polymer Waveguides through Two-Photon Polymerization in Polydimethylsiloxane. Polymers 2020, 12(11), 2485; doi:10.3390/polym12112485.*

2.1 Femtosecond laser three dimensional micro-nanofabrication

2.1.1 Optical apparatus

Multi-photon polymerization can be achieved by focusing high intensity pulses from a femtosecond laser by means of high numerical aperture objectives into a photopolymer. For this purpose we used a femtosecond Ti:Sapphire tunable laser (Coherent Chameleon Ultra II, 80 MHz repetition rate, 140 fs pulse width), which is capable of tuning its wavelength from a minimum wavelength of 680 nm to a maximum wavelength of 1050 nm. The tunability of the laser source is of great importance because of the possibility of setting the irradiation wavelength according to the absorption spectra of the photoactive molecules we have tested throughout all the research. A scheme of the femtosecond laser direct writing (LDW) system is depicted in Figure 2.1.

The beam diameter measures approximately 1.2 mm and reaches a maximum average power of 4 W. The laser beam is expanded and collimated by means of a 5× (NA=0.1, Newport) microscope objective (L1) and an achromatic lens (L2) with focal length f= 100 mm. The collimation system magnifies the laser beam to approximately 5 mm, to fill the back aperture of the focusing objective (OBJ). We have used a water-immersion, 0.7 numerical aperture objective (Nikon, working distance WD=2.3 mm) to focus the laser beam into the samples. As it will be described in the next chapters, we have tested two different PDMS materials, the Sylgard 184 (n=1.4225 at 632.8 nm) and the biomedical grade NuSil MED6215 (reported n=1.406). Water has a refractive index of 1.33 at 590 nm. Higher NA objectives can be used in combination with higher refractive index matching media closer to PDMS, such as oil or glycerol, but there is a price which experimentally needs to be payed, that is the short available working distance ($\sim$570 µm at 170 µm cover slip) during the waveguide writing. The alignment and the precise sample positioning along the writing direction are crucial aspects, as the polymer waveguides written by means of this set up reach 5 cm.

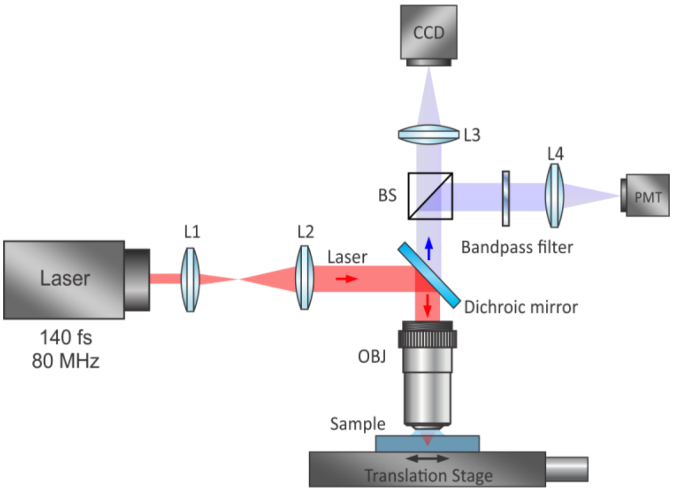

Figure 2.1 Femtosecond direct laser writing (LDW) system schematic implemented for the waveguides fabrication. A pulsed femtosecond Ti: Sapphire laser beam is expanded and collimated by means of a 5× (NA=0.1, Newport) microscope objective (L1) and an achromatic lens (L2). A water-immersion, 0.7 numerical aperture objective (OBJ: Nikon, working distance WD=2.3 mm) is used to focus the laser beam into the samples. A dichroic mirror allows for 50% transmission/reflection at 650 nm, and lets a very small amount of leaked laser light reflected from the top surface of the sample cover slip to reach the CCD camera (Chameleon 3, Point Grey Research) after a focusing lens (L3) in 4f configuration with the focusing objective.

The optical average power is varied by means of a Glan-Thompson polarizer; this allowed for a systematic calibration procedure before the commencement of each printing. As we will see in the following sections, the laser power together with the writing speed imprinted by the motion stages are fundamental parameters during a photopolymerization process, and a calibration procedure is always needed. The careful adjustment of these two parameters avoids material damages and leads to a successful printing; therefore, the presence of this optical element is of crucial importance. As it will be described in the following chapters, most of the photoinitiators we have tested had their maximum absorption peak in the UV region of the electromagnetic spectrum, around 320-340 nm; this is the reason why we mostly worked by tuning the laser wavelength to 680 nm, so that the photoinitiator molecule excitation is reached via the absorption of two photons at ∼340 nm. The way the samples have been prepared will be fully described in the next chapters, but at this point is important to mention the presence of a thin (∼170 μm) glass coverslip on top of the PDMS sample. A dichroic mirror inserted in the optical path allows for 50% transmission/reflection at 650 nm, and lets a very small amount of leaked laser light reflected from the top surface of the sample cover slip to reach the Silicon photomultiplier (Si PMT Hamamatsu 320-900 nm), in order to monitor the fluorescence signal during the photopolymerization, after passing a band pass filter (335-610 nm) and a focusing lens (L4). A beam splitter (BS: 700:1100 nm, 90:10, Thorlabs) redirects the laser beam reflected at the top cover slip surface towards the CCD camera (Chameleon 3, Point Grey Research), after being focused by a lens (L3) in 4f configuration with the focusing objective. A good focus spot on the camera indicates that the laser is focusing on the top surface of the coverslip, and the consequent depth control is achieved by moving the objective using a translation stage with a micrometer drive, while the samples are placed on a 50 mm-long travel range stage (Newport motorized stage UTS50CC).

2.2 Optical waveguides characterization: digital holography

The word *holography* comes from Greek *Ολογραφία* (όλος=holos; γραφή=graphy) and it means *total recording*. This concept was first introduced by Dennis Gabor in 1948 who called this imaging process *wavefront reconstruction* [123]. Gabor was proposing a lensless imaging technique, according to which it is possible to fully reconstruct an optical field, both in amplitude and phase, by letting interfering an optical field, scattered by or diffracted from an object, with a coherent reference field [123]. Recording media are sensitive only to light intensity, and Gabor's revolutionary idea demonstrated that it is possible to retrieve also the phase information of a complex field from interference patterns recordings. More specifically, the fundamental problem addressed by its idea was the phase reconstruction through intensity measurements, and this becomes possible thanks to interferometric techniques, which are capable of translating phase modulations into amplitude variations. The interference between the two beams produces an interference pattern, in which the phase information is encoded. However, it is only thanks to the technological developments in the second half of the 20th century, particularly the invention of lasers (T. H. Maiman, 1960), that his invention got more attention, and he finally won the Nobel prize in physics in 1971. Lasers were providing the right degree of coherence for holographic reconstructions, and from then on holography has undergone a real revolution. The above mentioned interference pattern takes the name of *hologram*, and it represents an extremely useful tool for a complete field reconstruction on intensity only recording media.

2.2.1 Basic concepts of holography

Holography is an imaging technique based on the coherent interference between two optical fields, and provides amplitude and phase information from intensity measurements at a specific spatial plane. In general, a known reference field (reference beam in Figure 2.2) is summed with an unknown field (object beam in Figure 2.2), in which is encoded the information we are interested in. If we do not have a purely monochromatic source, then our ability to observe interference is generally impaired, since the correlation length of a light source is inversely proportional to its bandwidth; therefore, coherent light sources such as lasers are needed.

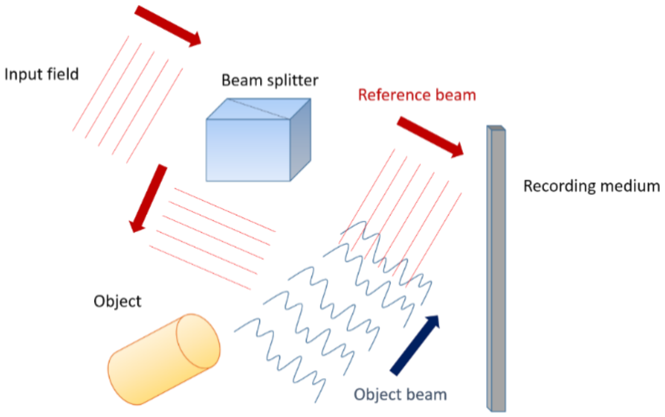

Figure 2.2 Working principle of holography. An input field is split into a reference beam and an object beam by means of a beam splitter. The reference optical beam travels unperturbed towards the recording medium and interferes with the object beam which has been scattered from the object.

The reference field can be mathematically described as:

$$R(x,y) = |R(x,y)|e^{j\varphi_R(x,y)}$$

Equation 29 Reference field mathematical expression.

and the object field as:

$$O(x,y) = |O(x,y)|e^{j\varphi_O(x,y)}$$

Equation 30 Object field mathematical expression.

where (x,y) are the spatial coordinates and $\varphi_R(x,y)$ and $\varphi_O(x,y)$ are the spatial phase distribution of the reference and object beam, respectively. The intensity of the sum is given by:

$$\begin{aligned} I(x,y) &= |R(x,y)+O(x,y)|^2 = [R(x,y)+O(x,y)][R(x,y)+O(x,y)]^* \\ &= |R(x,y)|^2 + |O(x,y)|^2 + R(x,y)O(x,y)^* + R(x,y)^*O(x,y) \\ &= |R(x,y)|^2 + |O(x,y)|^2 + 2|R(x,y)||O(x,y)|\cos\big(\varphi_R(x,y)-\varphi_O(x,y)\big) \\ &= I_R(x,y) + I_O(x,y) + 2\sqrt{I_R(x,y)I_O(x,y)}\cos\big(\varphi_R(x,y)-\varphi_O(x,y)\big) \end{aligned}$$

Equation 31 Interference intensity pattern.

The first two terms in Equation 31 are related only to the intensity of the two interfering beams I_R and I_O; however, the intensity of the recorded hologram depends also on both the amplitude and phase of the unknown field. Once the hologram intensity is recorded, we can illuminate the hologram with the same reference illumination beam in order to reconstruct optically the complex field of the object (Figure 2.3). This leads to:

$$R(x,y)I(x,y) = R(x,y)I_R(x,y) + R(x,y)I_O(x,y) + R(x,y)^2O(x,y)^* + I_R(x,y)O(x,y)$$

Equation 32 In-plane wavefront reconstruction mathematical expression.

The first two terms on the right side of Equation 32 describe the read-out light that goes through the transparency (the hologram), slightly modulated by the sum of the intensities of the reference and object beams $I_R(x,y)$ and $I_O(x,y)$. The fourth term is the term of interest, since it contains the original wave multiplied by the reference intensity, which is constant assuming a uniform reference field such as a plane wave [2]. In other words, if the object wave in Figure 2.2 was a light field scattered from a 3D object, the reconstruction described by Equation 32 would reproduce the same optical field of the object, giving rise to a 3D sensation (the reconstructed image of the object). The third term in Equation 32 is the conjugated version of the original object wave, modulated by the squared reference field; in fact, a hologram can be thought as a grating where the third and fourth term on the right side of Equation 32 represent the +1 and -1 diffraction orders, and the first two terms represent the light travelling straight through the transparency (DC term) [123].

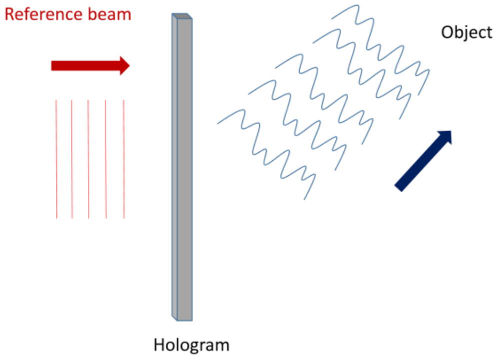

Figure 2.3 Wavefront reconstruction by illuminating the hologram with the reference wave.

The holograms created using a reference beam which travels in-line with the object under investigation are called the *Gabor's holograms*; however, these kind of holograms suffer background noise due to the unmodulated light propagating through the transparency (along the optical axis), and twin images formation from the +1 diffraction order [123]. In this thesis, I made use of the so called *offset-reference holography* (also known as *Leith-Upatniekis holography* or *off-axis holography*), where the reference beam during the hologram recording interferes at an angle with the object beam. This leads to a clear separation of the hologram diffraction orders, which makes their analysis more efficient. The holograms we have recorded have been processed digitally using the software Matlab and the encoded polymer waveguides phase has been reconstructed.

2.2.2 Offset-reference holography

As discussed in the previous paragraph, offset-reference holography (or off-axis holography) differs from the inline holography for the fact that the reference and the object beams interfere at an angle to create the hologram. This variant of the holographic technique presents an important advantage, as it provides a separated DC term and well spaced diffracted orders. If we consider the reference wave to be a plane wave coming at an angle $\theta = (\theta_x, \theta_y)$, k_0 the free space wavevector amplitude and λ the beam wavelength, the dependency on the spatial coordinates (x, y) is lost, and its complex field can be written as:

$$R(x,y) = Re^{j(k_0 \sin\theta_x x + k_0 \sin\theta_y y)}$$

Equation 33 Reference complex field propagating at an angle θ with the optical axis.

By substituting Equation 33 into Equation 31 we obtain:

$$I(x,y) = \underbrace{|R|^2 + |O(x,y)|^2}_{\substack{DC\ term\ along \\ the\ optical\ axis}} + \underbrace{Re^{j(k_0 \sin\theta_x x + k_0 \sin\theta_y y)} O(x,y)^*}_{Propagates\ at\ angle\ \theta} + \underbrace{R^* e^{-j(k_0 \sin\theta_x x + k_0 \sin\theta_y y)} O(x,y)}_{Propagates\ at\ angle -\theta}$$

Equation 34 Hologram intensity with an incoming reference beam at an angle $\theta = (\theta_x, \theta_y)$.

The first two terms are referred as DC and they don't contain any information about the phase of the object; they correspond to that portion of light which travels straight through the recording plane, which means at zero angle respect to the optical axis. The third and the fourth entities are two complex conjugate terms and they contain information both of the amplitude and phase of the object field. If the hologram is illuminated with an illumination normal to the recording plane, these two field component would diffract in opposite directions, at angle θ and $-\theta$, respectively, because of the phase carried by the reference field. It appears immediately clear that a good orders separation facilitates the object reconstruction, and this is achieved by optimizing the incident reference angle.

Any signal can be represented as a superposition of harmonic functions of different frequencies and complex amplitudes [66, 123]; this is the basic idea of the Fourier analysis, which is widely used in signal processing to retrieve the information encoded in digital signals. Also an optical signal as a beam light can be thought this way, thinking at the wave vector coordinates k_x, k_y, k_z as its spatial frequencies; an image is nothing but a 2D signal, therefore we can apply a Fourier transformation to decompose it and analyse it. Here, if we apply the Fourier transform to Equation 34, we obtain:

$$\begin{aligned}
&F\{I(x,y)\}(k_x,\ k_y) \\
&\qquad = F\{|R|^2\}(k_x,\ k_y) + F\{|O(x,y)|^2\}(k_x,\ k_y) + F\left\{Re^{j(k_0 \sin\theta_x x + k_0 \sin\theta_y y)} O(x,y)^*\right\}(k_x,\ k_y) \\
&\qquad + F\left\{R^* e^{-j(k_0 \sin\theta_x x + k_0 \sin\theta_y y)} O(x,y)\right\}(k_x,\ k_y) \\
&\qquad = \delta(k_x,\ k_y) + F\{|O(x,y)|\}(k_x,\ k_y) \star F\{|O(x,y)|\}(k_x,\ k_y) \\
&\qquad + RF\left\{O(x,y)^*(k_x - k_0 \sin\theta_x,\ k_y - k_0 \sin\theta_y)\right\} + R^* F\left\{O(x,y)(k_x + k_0 \sin\theta_x,\ k_y + k_0 \sin\theta_y)\right\}
\end{aligned}$$

Equation 35 Fourier transform of the hologram intensity when the reference beam is tilted at an angle $\theta = (\theta_x, \theta_y)$.

Equation 35 is the frequency spatial distribution of the hologram intensity expressed by Equation 34; the first term is a Dirac function related to the constant reference beam, the second term is derived by taking into consideration the autocorrelation property of the Fourier transform, while the third and fourth terms are the two diffracted orders related to the object in the frequency domain.

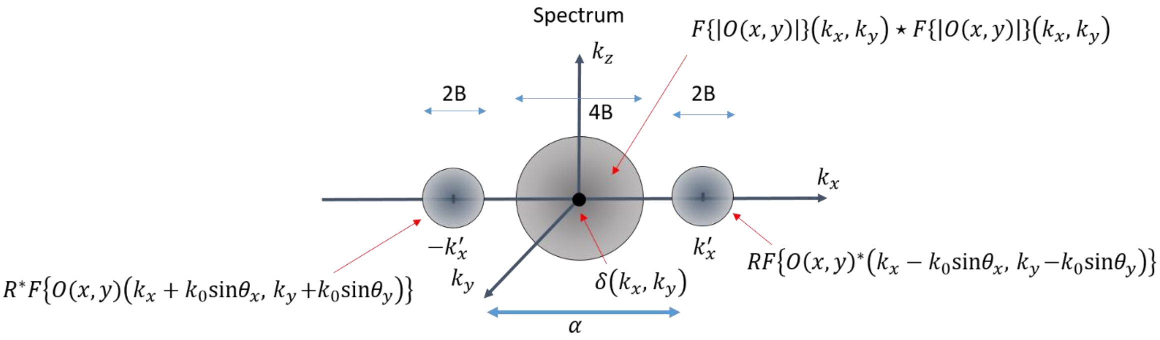
Spectrum
k_z
$F\{|O(x,y)|\}(k_x,k_y) \star F\{|O(x,y)|\}(k_x,k_y)$
2B
4B
2B
k_x
$-k'_x$
k'_x
$RF\{O(x,y)^*(k_x - k_0\sin\theta_x,\ k_y - k_0\sin\theta_y)\}$
$R^*F\{O(x,y)(k_x + k_0\sin\theta_x,\ k_y + k_0\sin\theta_y)\}$
k_y
$\delta(k_x,k_y)$
α

Figure 2.4 Fourier spectrum of the hologram.

Considering $k'_x = k_0 sen\theta_x$, $k'_y = k_0 sen\theta_y$, and k'_y=0 for the sake of simplicity, Figure 2.4 represents the Fourier spectral components of the recorded hologram. B is half of the bandwidth of the object signal, therefore, it appears immediately clear that in order to have nicely separated diffracted orders it needs to be [123]:

$$\alpha \geq 3B$$

or equivalently:

$$k_{x,min} \geq 3B$$

Analysing it further, we obtain the expression of the theoretical minimum reference angle:

$$k_0 sen\theta_x \geq 3B$$

$$\frac{2\pi}{\lambda} sen\theta_x \geq 3B$$

$$sen\theta_x \geq \frac{3\lambda}{2\pi} B$$

$$\theta_{x,min} = arcsen(\frac{3\lambda}{2\pi} B)$$

Equation 36 Minimum reference angle in off-axis holography.

2.2.3 Digital holography

A hologram is nothing but an interferometric recording of a complex field; as discussed in the previous paragraphs, a first step consists of the hologram recording, followed by a second step which is the original image reconstruction. When the holograms are acquired by a camera and they are processed digitally, this technique takes the name of *digital holography*. Therefore, in order to fully recover the complex field from holography interferometric measurements, we have to digitize the hologram and demodulate the carrier. This way it is possible to retrieve amplitude and phase of the unknown optical field, where the information is encoded. The polymer optical waveguides reported in this thesis presented an unknown refractive index difference Δn that needed to be measured. The waveguides phase information in the holograms has been measured and the refractive index change between core and cladding has been calculated following the equation:

$$\Delta n = \frac{\lambda}{2\pi d} \Delta\varphi$$

Equation 37 Refractive index difference between core and cladding of the polymer waveguides as a function of the accumulated phase.

where λ is the illumination wavelength, d is the waveguide dimension and $\Delta\varphi$ is the phase difference encompassed in the acquired holograms.

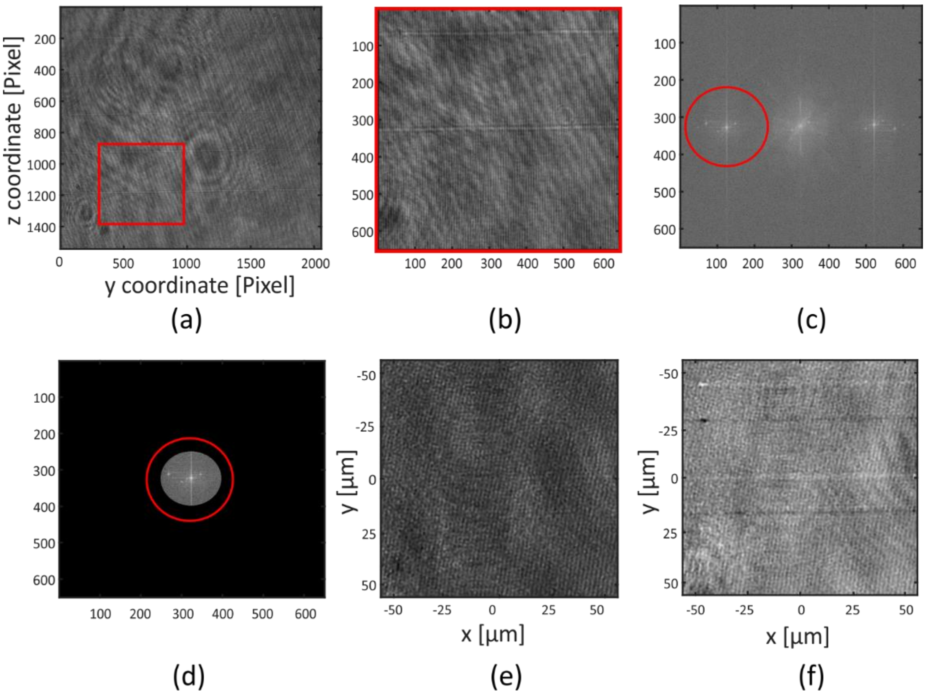

Figure 2.5 (a) Hologram recording on a camera and selection of the region of interest ROI (in the red square); (b) Region of interest ROI; (c) Fourier transform of the cropped hologram and selection of the diffraction order (red circle); (d) digital shift to the centre of the computational window of the diffraction order (red circle), where everything else is put equal to zero; amplitude (e) and phase (f) information extracted from the back Fourier transform of the shifted diffraction order.

The extraction of the phase and amplitude from a digital hologram is performed following the block diagram showed in Figure 2.6, which comprises the following steps:

- the optical recording of the hologram on a digital camera (Figure 2.5 (a)), and crop of the region of interest (ROI in Figure 2.5 (b));
- digital Fourier transformation of the hologram (Figure 2.5 (c));
- selection of the desired diffraction order (+1 or -1) which contains the object phase information (red circle in Figure 2.5 (c));
- filtering of the desired diffraction order (+1) by means of a digital mask in order to remove contribution from the DC term and the other diffracted component (Figure 2.5 (d));
- digital shift of the selected order to the centre of the k vectors computational space; this digital operation corresponds to an experimental hologram illumination with the conjugate reference wave (wavefront reconstruction step, Figure 2.5 (d));
- back Fourier transformation to obtain the complex field of the object, namely amplitude Figure 2.5 (e) and phase (Figure 2.5 (f));

- apply a digital refocusing step, if needed.

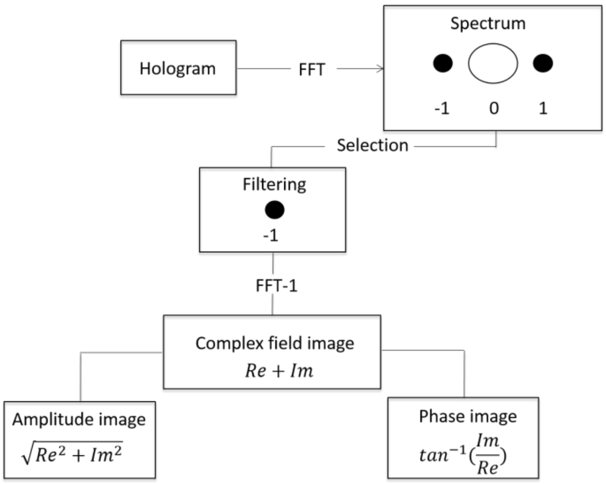
Hologram
FFT
Spectrum
-1
0
1
Selection
Filtering
-1
FFT-1
Complex field image
$Re + Im$
Amplitude image
$\sqrt{Re^2 + Im^2}$
Phase image
$tan^{-1}(\frac{Im}{Re})$

Figure 2.6 Digital holography block diagram.

The hologram processing has been carried out by subtracting the background information, which is contained both in the reference and object wavefront; this is made by digitally subtract a blank hologram (in a different area of the sample), from the original hologram. By doing so, any phase accumulation which is not proper of the object can be removed, and the sample thickness phase delay can be neglected; however, this leads to a 'duplication' of the object of interest (the waveguides in Figure 2.5 (f)), which is not anyway critical for the purposes of the measurement.

2.2.4 Optical apparatus

In the previous paragraphs I gave the theoretical basics about the off-axis digital holographic interferometric technique we have used for measuring the refractive index contrast of the polymer structures. Here, I propose the experimental set up we have built for the phase recording, showed in Figure 2.7. In holographic recording techniques a coherent light source beam is split into two arms, an object beam (Object) and a reference beam (Reference) by means of a beam splitter (BS1). In this experimental set up we have used a 632.8 nm wavelength HeNe laser and separated it by means of a beam splitter (BS1: 400:700 nm 50:50, Thorlabs). The object beam is a plane wave which travels unexpanded through the sample and recombines with the reference beam by means of a second beam splitter (BS2: 400:700 nm 50:50, Thorlabs).

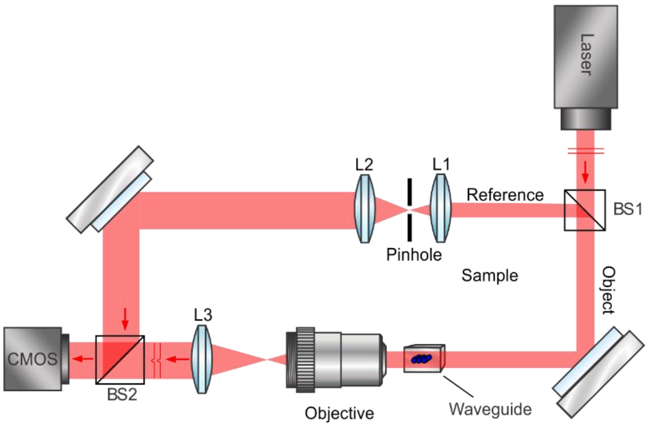
Laser
L2
L1
Reference
BS1
Pinhole
Sample
Object
L3
CMOS
BS2
Objective
Waveguide

Figure 2.7 Off-axis holographic interferometer built for the measurement of the refractive index difference of the polymer waveguides. A HeNe laser ((λ=632.8 nm, Thorlabs) is split by means of a beam splitter (BS1) into a reference and an object arm. The object

plane wave travels through the PDMS sample and recombines with the reference arm through a second beam splitter (BS2). The waveguides are imaged on a camera (CMOS) using a long working distance objective (Objective) in 4f configuration with the lens L3. The reconstructed holograms are digitally processed with a computer.

The reference arm is expanded and collimated through a Newport, 5× magnification objective, NA=0.1 (L1) and a lens with focal length f=250 mm (L2); a pinhole with diameter d=20 µm is inserted at the Fourier plane of L1 to clean spatially the beam. A long working distance objective (Objective: 20× Mitutoyo, NA=0.42) images the polymer structures on a CMOS camera (Edmund Optics, 2056 x 1542 pixels, 3.45 µm pixel size) in 4f configuration with L3 (f= 200 mm). The polymer optical waveguides are placed perpendicularly to the optical incident field, introducing a phase change that can be revealed and processed with *Matlab*.

2.3 Characterization platform

2.3.1 Set-up design requirements

Together with the refractive index difference between core and cladding, one of the most important properties of a waveguide is its capability of transmitting light. To quantify the transmission loss of the waveguides we have built an in-out light coupling platform (Figure 2.8), where the fine positioning and stability of the samples represented a very important aspect to consider in order to have a repeatable and reliable measurement, especially in this case where the fabricated waveguides were very small (<1 µm). To do so, we mostly used incoherent thermal light source in order to ensure the waveguide alignment with the light illumination spot, using positioning stages with an accuracy better than 1 µm. We have measured the output power of the light source with a power meter, stating a statistical coefficient of variation of 1.5% over two hours. As it will be shown in the next section, the light spot at the waveguide entrance was a demagnified image of the thermal light passing a 1-mm iris (Iris3 in Figure 2.8), which is about 17 µm in diameter with uniform intensity profile; this, together with the small size of the waveguides ensures that the coupling condition was repeatable.

2.3.2 Optical apparatus

For the waveguide transmission loss measurements, we built the optical set up shown in Figure 2.8. The proposed configuration shows the implementation of a double-path which consists of two parts: a coherent light source (red) and an incoherent white light illumination path (green). A 2-mm HeNe laser spot (λ=632.8 nm, Thorlabs) is magnified and collimated through the beam expansion system consisting of the lenses L1 (f=75 mm) and L2 (f=200 mm). A 50 µm pinhole is inserted at the Fourier focal plane of L1 in order to spatially clean and stabilize the laser beam. The beam is then focused on the proximal facet of the sample by means of a high numerical aperture objective (OBJ1: 50× Zeiss, NA=0.7). As we already discussed in the theoretical part about the working principle of fibers, in order to maximize the coupling efficiency of light into a waveguide we need to match its NA; in order to do so we placed an iris (Iris1) just in front of the input objective that could be opened or closed, depending on the NA of the fabricated waveguides. Light is collected at the sample distal end by means of a long working distance objective (OBJ2: 20× Mitutoyo, NA=0.42) and imaged on a camera (CAM1: Andor Ixon 885 EMCCD, 1004x1002 pixels) by means of a lens (L3: f=160 mm). Moreover, the back-reflected light from the proximal facet of the sample is redirected using a beam splitter (BS1: 400-700 nm, 45:55, Thorlabs) on a second CCD camera (CAM2: Chameleon 3, Point Grey Research) after being focused by the lens L4 (f=160 mm). This allowed for a precise localization and alignment of the waveguides with the source illumination; a notch filter placed in front of CAM1 blocked most of the 633 nm wavelength laser light, preventing damages to the camera.

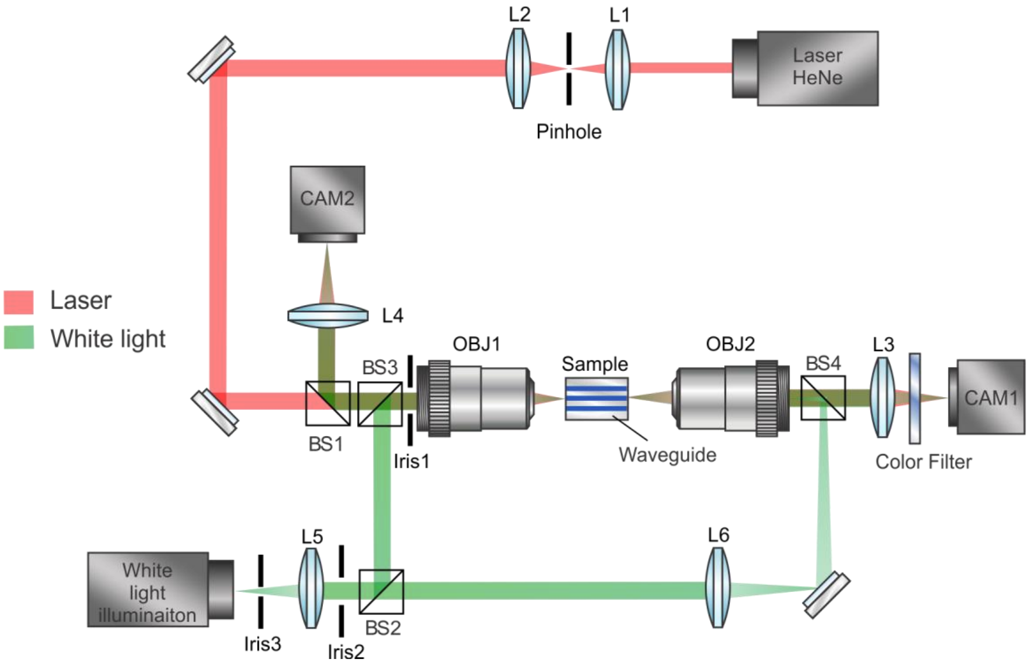

Figure 2.8 Light coupling set up schematic: a 2-mm HeNe laser spot (λ=632.8 nm, Thorlabs) is magnified and collimated through a beam expansion block (L1 and L2) and then focused on the proximal facet of the sample by means of a high numerical aperture objective (OBJ1). Light is collected at the sample distal end by means of a long working distance objective (OBJ2) and imaged on a camera (CAM1) by means of a lens (L3). The back-reflected light is redirected using a beam splitter (BS1) on a second camera (CAM2) after being focused by the lens L4. A broadband thermal light source (Introlux 6000-1) is collimated using a long focal length lens (L5) and an iris (Iris2). A beam splitter (BS2) splits the illumination beam into two arms: the first arm is redirected towards the input objective (OBJ1) by a thin pellicle beam splitter (BS3) to be coupled into the waveguides contained in the sample. The second arm is focused by means of a lens (L6) into the back focal plane of the output objective (OBJ2) by means of another pellicle beam splitter (BS4).

As mentioned already in the previous paragraph, we mostly worked with incoherent light illumination, because of the advantages offered in terms of coupling efficiency. Light transmission measurements are very sensitive to the waveguide facet morphological conditions; PDMS is a soft and flexible material, therefore the air-PDMS interface scratches resulting from the knife cut played a critical role in light coupling experiments. In Chapter 3 it will be further explained how the PDMS waveguide interface was experimentally cleaved, but at this point it is important to mention that an end-face flatness is strictly required in light coupling measurements. Broadband light sources don't show interference and therefore, small material inhomogeneity and defects don't form speckle patterns that would be imaged on the distal camera. We have used a broadband thermal light source (white light illumination Introlux 6000-1) and collimated it over the set up distance using a long focal length lens (L5, f=330 mm) and an iris (Iris2), carefully placed at the right distance from the emitting fiber bundle facet of the light source. A third iris (Iris3) was placed right in front of it on order to change the spot dimension of the incoherent light source. An image of this spot is projected on the proximal sample facet by means of OBJ1, covering the desired sample area. A beam splitter (BS2: 488 nm 50:50, Thorlabs) separates the illumination beam into two arms: the first arm is redirected towards the input objective (OBJ1) by a thin pellicle beam splitter (BS3: 1:2 µm, 8:92, Thorlabs) to be coupled into the waveguides contained in the sample. The second arm is focused by means of a lens (L6, f=200 mm) into the back focal plane of the output objective (OBJ2) by means of another pellicle beam splitter (BS4: 400-700 nm, 45:55, Thorlabs). The laser beam and the white light source are aligned in the same path to ensure that they both illuminate the same area of the sample and in a way their focal plane coincide. Moreover, the second arm of the white light source served as illumination in transmission from the distal facet of the sample, making the coupling procedure more efficient; however, this arm has been always blocked in all the transmission loss measurements with incoherent light illumination.

2.4 Summary

In this chapter I have described the experimental methodologies we have developed for the fabrication and characterization of the polymer optical waveguides. We have built a femtosecond laser direct writing (LDW) set up, together with a digital holographic interferometer for the phase change reconstruction and a light transmission platform. Matlab codes for waveguide writing, phase retrieval and light intensity measurements have been implemented. Compared to commercially available two-photon polymerization platforms (such as Nanoscribe GmbH), the above described LDW platform offered the fundamental feature of wavelength tunability, which made it possible to test a various number of photoinitiators and monomers, in different concentrations and chemical configurations. Another important advantage consists in the high travel range of the motion stages, which allowed for long waveguides fabrication, without stitching; for fine µm-adjustments, piezo stages have been integrated in the sample motion system. Moreover, the digital holographic technique and experimental apparatus for the waveguide phase extraction have been discussed, together with the light coupling platform for the transmission loss measurements.

In the following chapter I will present the results we have obtained in a photoinitiator-free chemical scheme and describe the methodologies we have followed for the fabrication of poly-phenylacetylene waveguides in PDMS.

Chapter 3 Photoinitiator-free microfabrication of optical waveguides in PDMS

In this work, we demonstrate, for the first time, the fabrication of compact (1.3 µm wide) PDMS optical waveguides through multi-photon laser direct writing (MP-LDW) in polydimethylsiloxane (PDMS) using phenylacetylene as the photosensitive monomer without a photoinitiator.

Most of the material presented in this chapter can be found in the publication ([121]):

- Panusa, G., Pu, Y., Wang, J., Moser, C., & Psaltis, D. (2019). *Photoinitiator-free multi-photon fabrication of compact optical waveguides in polydimethylsiloxane. Optical Materials Express, 9(1), 128-138. doi: 10.1364/OME.9.000128.*

3.1 Introduction

PDMS optical waveguides fabrication in a host-guest system has been previously reported [58, 59]. When a preformed PDMS substrate is immersed into a high-refractive index liquid monomer formulation, the monomer molecules will permeate into the intermolecular space of the PDMS matrix. Selective photopolymerization of the permeated monomer by a laser focus can induce a local change of the refractive index in the substrate material. Waveguides with a diameter of 50 µm, a refractive index change of Δn=0.01, and an optical loss between 0.3 and 0.6 dB/cm at a wavelength of 850 nm have been reported [59].

As I have discussed in Chapter 1, in photopolymerization, the energy of light upon absorption must be transformed into suitable chemical energy in the form of reactive intermediates, a process called photoinitiation. This conversion is usually achieved with a photoinitiator, since light absorption in most monomers is only efficient in deep ultraviolet (DUV) region. A photoinitiator is a compound that produces reactive species upon absorption of light in the designated spectral region. The reactive species then start a chain-growth polymerization by transferring the chemical energy to the monomer molecules. In certain circumstances, however, the addition of photoinitiators increases the chemical complexity of a polymer system. In particular, in biomedical applications where biocompatibility is a prerequisite, a great special design effort is required to ensure that the photoinitiator is nontoxic. Regardless of the biocompatibility of the final polymer product, reducing the chemical complexity by eliminating the photoinitiator would be beneficial in all biomedical applications, particularly implanted devices. Although photoinitiators were ubiquitously used in multi-photon photopolymerization [[124-126]], ultrafast lasers provide an opportunity to achieve this goal with multi-photon absorption without the use of photoinitiators. Given sufficient laser intensity, the DUV absorption peak of most monomers becomes accessible through two- or three-photon absorption at an appropriate laser wavelength and intensity.

Here, we demonstrate, for the first time, the fabrication of compact (1.3 µm wide) PDMS optical waveguides through MP-LDW in PDMS without using a photoinitiator. As it will be further discussed in the following section, the basic idea of this work includes PDMS as a pre-crosslinked network, in which a liquid monomer/PI solution is capable of infiltrating the polymer structure (in Figure 3.1 (a)-(d)). It appears immediately clear that, besides the photopolymerization efficiency and constrains listed in Paragraph 1.3.2, the photoactive solution must present the key characteristic of being in a liquid/low viscosity form, feature that consistently restricted the choice of commercially available polymerizing candidates; for this purpose, we have tested phenylacetylene.

3.2 Materials and methods

All chemicals were used as purchased without further purification. Phenylacetylene (98% purity, CAS Number 536-74-3) was purchased from Sigma Aldrich (Buchs, Switzerland); optically transparent PDMS (Sylgard 184, n =1.4225 at 632.8 nm) was purchased from Dow Corning.

3.2.1 Sample preparation

Phenylacetylene (inset in Figure 3.1 (e)) is an alkyne hydrocarbon containing a phenyl group and it appears as a yellowish liquid. It presents a refractive index of 1.549, which is due to the presence of the phenyl ring in the molecule, and this made it an excellent candidate for testing. The host-guest system I describe in this paragraph includes a PDMS matrix as the host and a liquid monomer permeated into the PDMS intermolecular space as the guest.

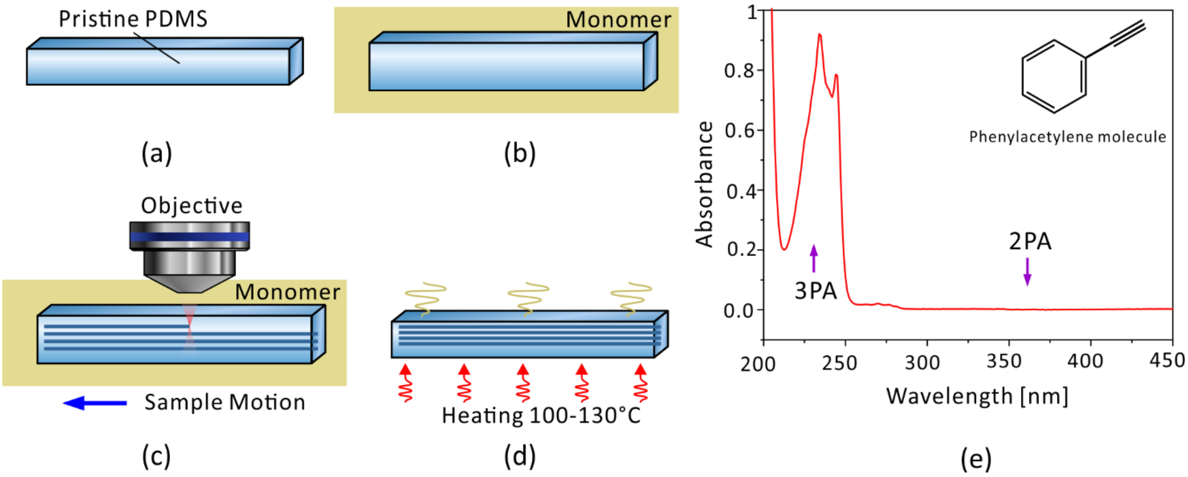

Figure 3.1 Principle of waveguides fabrication in PDMS. (a) Preparation of a pristine platinum-cured PDMS substrate. (b) Permeation of the monomer molecules into the PDMS matrix by immersing the PDMS substrate into the monomer liquid formulation for 24 hours. (c) Exposure of the monomer-permeated PDMS substrate to a focused ultrashort laser irradiation for waveguide writing. (d) Removal of the unreacted monomer through an optional ethanol washing and a heating at 100-130 °C for two hours. (e) Absorption spectrum of 0.01 mM phenylacetylene in acetonitrile. Violet arrows indicate energies of two-photon (2PA) and three-photon absorption (3PA). Inset illustrates the chemical structure of the phenylacetylene molecule.

The fabrication procedure of the waveguides consists of four steps (Figure 3.1 (a)-(d)):

1. the preparation of a pristine Pt-cured PDMS slab (Figure 3.1 (a)). We used the commercially availbale Sylgard 184 throughout all the experiments described in this chapter. It consists of a Part A and a Part B to be combined in a ratio of 10:1 followed by a mixing and defoaming process. To ensure the homogeneity of the PDMS substrate, which is the key to high-quality waveguides, the mixing and defoaming were performed in a Thinky automatic mixer for about 3 min, followed by a final deaeration procedure in a vacuum desiccator. We cured the PDMS samples at room temperature over 48 h to ensure surface flatness and parallelism with the working plane. For the optical clarity of the PDMS substrate, the above preparation was performed in an ISO7 cleanroom; condensation cured PDMS should also work in a similar fashion, although we did not test it specifically;

2. the permeation of the monomer into the PDMS matrix by immersing the PDMS slab in the phenylacetylene liquid formulation (used as purchased from Sigma Aldrich) for 24 hours [58, 127] to ensure the concentration

of phenylacetylene in the PDMS slab reaches the saturation point, after which the PDMS slab gains more than 40% in weight Figure 3.1 (b);

3. the exposure of the monomer-permeated PDMS slab to a focused ultrashort laser irradiation to induce polymerization of phenylacetylene and form waveguide structures (Figure 3.1 (c));
4. the removal of the unreacted monomer through an ethanol washing followed by a heating step at 100-130 °C for two hours (Figure 3.1 (d)).

Phenylacetylene is a small molecule and therefore capable of entering and escaping the PDMS matrix easily. Figure 3.1 (e) shows the UV absorption spectrum measured with a UV-visible spectrophotometer (Cary-100, Agilent Technologies), which reveals an absorption peak in the spectral range of 215-250 nm; therefore, for triggering photopolymerization, the wavelength must be tuned down to the minimum wavelength, 680 nm, offered by our femtosecond pulsed Chameleon laser. Phenylacetylene is responsible of the absorption of light and at the same time of its photopolymerization via a three-photon process, which is in consistency with the heuristics from previous studies in multi-photon photoinitiators [126]. In order to avoid fast monomer evaporation, the phenylacetylene-permeated PDMS slab sample was sandwiched between a glass microscope slide and a coverslip, as exemplified in the close-up look in Figure 3.2 (b) and exposed to the laser focus (Figure 3.2 (a)); the phenylacetylene reaction scheme of the multi-photon polymerization is illustrated Figure 3.2 (c).

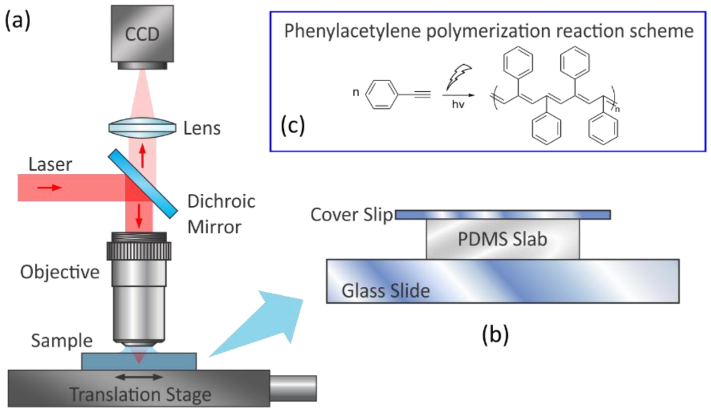

Figure 3.2 (a) Experimental set up for poly-phenylacetylene waveguide writing in PDMS through MP-LDW. (b) After monomer infiltration, the pre-crosslinked PDMS slab is sandwiched between a glass slide and a 170 μm thick microscope coverslip to avoid monomer evaporation. (c) Phenylacetylene multi-photon polymerization reaction scheme under laser irradiation.

Considering an average laser power at the level of 60 mW, 680 nm wavelength source and 0.7 NA lens, we estimate that the focal intensity, ignoring the spherical aberration due to the refractive index mismatch between water and PDMS, and the possible self-focusing effect, reaches approximately 2×10^{12} W/cm^2 with fine adjustments by tuning the laser power. We wrote waveguides at writing speeds ranging between 0.5 and 1.5 mm/s, at a laser peak intensity between 1.6×10^{12} and 2.4×10^{12} W/cm^2, and at a focusing depth between 800 μm and 1.3 mm below the sample top surface.

3.3 Results and discussion

3.3.1 Waveguides verification

A phase contrast microscope (Olympus IX-71) was used to observe the sample after irradiation, and the phase contrast images clearly reveal the formation of the waveguides. An example phase contrast image of the waveguides is shown in

Figure 3.3 (a), which were fabricated at 1.3 mm depth inside the PDMS material, with 1.9 ×10^{12} W/cm^2 peak laser intensity and at 0.7 mm/s writing speed. A bright field microscopy image of the waveguide (Figure 3.3 (b)), obtained using a 1.4 NA oil-immersion objective, reveals a smooth core refractive index structure. The width of the waveguide was measured to be 1.3 µm.

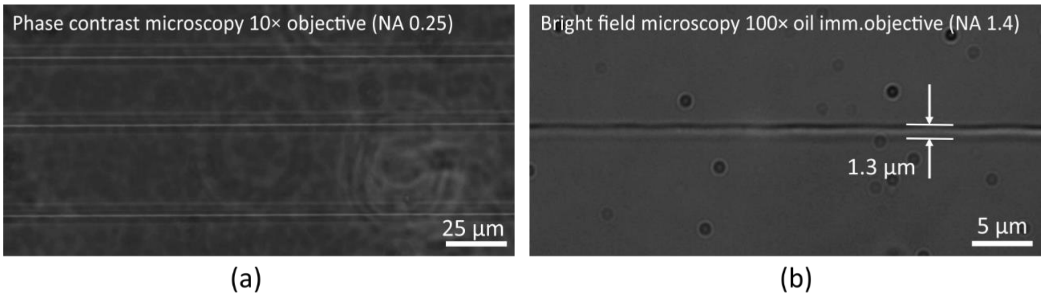
Phase contrast microscopy 10× objective (NA 0.25)
25 µm
(a)
Bright field microscopy 100× oil imm.objective (NA 1.4)
1.3 µm
5 µm
(b)

Figure 3.3 (a) Phase contrast microscope (Olympus IX-71) image of written PDMS optical waveguides. (b) Bright field microscope image of an optical waveguide (100× magnification objective), written at 1.3 mm below the sample top surface, 1.9 ×10^{12} W/cm^2 laser peak intensity and 0.7 mm/s writing speed.

The experimental parameters that determine the width of the focal volume, and therefore the resulting feature size, are the pulse energy, the writing speed, and the numerical aperture of the lens used for focusing the beam on the sample. We performed a series of writing experiments to characterize the material in terms of polymerization threshold power and writing speed. Figure 3.4 (a) exemplifies the strategy followed to determine the writing power threshold, defined as the minimum laser power for which continuous, sharp, and intact polymerized structures are clearly identifiable in our phase contrast microscope. These experiments suggest that the laser peak intensity needed to fabricate a waveguide inside the PDMS slab at the investigated depth is 1.7×10^{12} W/cm^2. This set of experiments was performed at a writing speed of 0.7 mm/s, which is in the optimal range found experimentally to fabricate undamaged polymerized structures. The cross section of each waveguide has been evaluated by performing a cross-sectional cut and inspecting its core with phase contrast microscopy, as shown in Figure 3.4 (b).

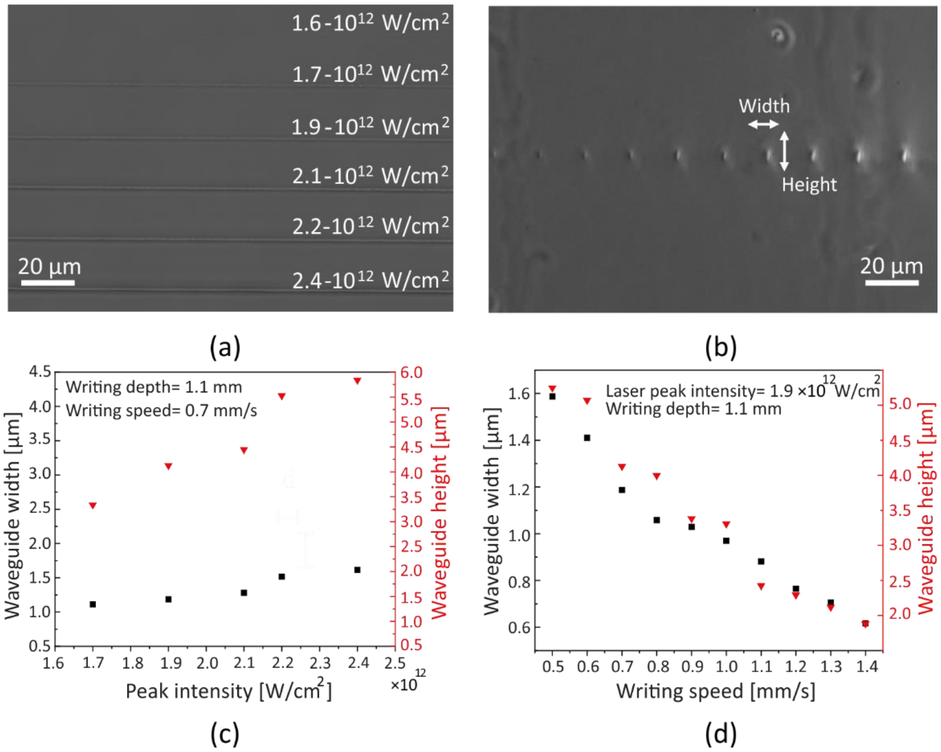

Figure 3.4 (a) Top view image and (c) waveguide width and height for optical waveguides written at 0.7 mm/s, 1.1 mm below the sample coverslip interface, for different laser peak intensities; cross-sectional image (b) and width and height (d) for waveguides written at 1.9 ×10^{12} W/cm^2 peak intensity, 1.1 mm below the sample coverslip interface, for different writing speeds.

Waveguide width and height increase with increasing peak intensity and decreasing writing speed, as revealed in Figure 3.4 (c) and (d). The aspect ratio, considered as the ratio between waveguide height and waveguide width, ranges from approximately 3.8 at the photopolymerization threshold of 1.7×10^{12} W/cm^2 to 4.1 at 2.1×10^{12} W/cm^2. Indeed, the waveguide depth increases at a faster rate compared to its width, resulting in a more elliptical shape at high peak intensities. At constant laser peak intensity and writing depth inside the material, waveguide width and depth decrease linearly with the writing speed, as depicted in Figure 3.4 (d).

We also evaluated the impact of the writing depth at fixed writing speed and laser peak intensity on the waveguide cross section (examples are reported in Figure 3.5 (a)). Plot in Figure 3.5 (b) shows the linear decrease of both lateral and vertical waveguides dimensions with increasing writing depth, as expected considering that a deeper focusing distance corresponds to an increased aberration in the PDMS matrix.

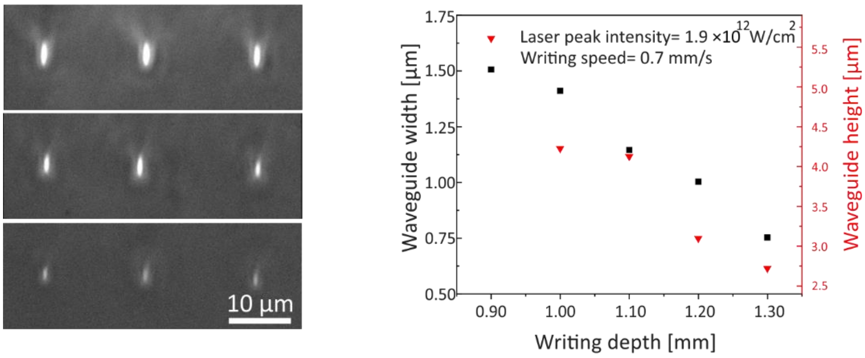

(a) (b)

Figure 3.5 (a) Waveguide cross section for optical waveguides written at laser peak intensity of 1.9 ×10^{12} W/cm^2 and a writing speed of 0.7 mm/s, for 900 µm (top panel), 1.1 mm (middle panel) and 1.3 mm (low panel) focusing depth. (b) Plot of waveguide width and height as a function of writing depth, showing linear decrease of both lateral and vertical waveguides dimensions with increasing writing depth.

3.3.2 Waveguides characterization

Raman spectroscopy

We performed Raman spectroscopy measurements in order to understand the chemical behaviour of phenylacetylene towards photopolymerization. Raman spectroscopy provides the sample molecular information using scattered light. When a material is hit by rays of light, the molecules in the material vibrate in different ways, which are referred as vibrational modes. Each type of chemical bond responds external excitation with different vibrational modes and with different light frequencies k, with $k = \frac{1}{\lambda}$ and λ being the wavelength shift in cm, relative to the illumination wavelength. Vibrational modes can be considered as finger prints of the chemical bonds present in a material; therefore, Raman spectroscopy is a suitable choice to statically evaluate microstructures fabricated by TPP [128-130]. Moreover, it requires a minimal sample preparation, and it provides excellent resolution. For all these reasons it is often used to determine the so-called *degree of conversion* (DC) of a photopolymer, which is defined as the percentage of initial starting material, such as monomers or oligomers covalently bond together, to form the polymer product after being exposed to light. In acrylic monomers (or oligomers), the chain addition which takes place during the propagation step of the polymerization, is characterized by the carbon-carbon double bond ($C = C$) opening, which decreases in favour of the $C - C$ single bond [36].

The ordinary Raman spectrum of neat phenylacetylene (PA) is known from literature [131, 132]; among the ring breathing (at 1001 cm^{-1}) and the $C - C$ stretching vibrational mode (at 1601 cm^{-1}), the phenylacetylene Raman spectrum shows a very strong peak at 2111 cm^{-1}. This is associated to the $C \equiv C$ bond stretching [131, 132]. Raman spectra were acquired by focusing a 488 nm wavelength laser in a Raman spectrometer (Renishaw), at ~14.3 mW using a 5× magnification objective (NA=0.12). The Raman signal was taken at an exposure time $t = 10$ s in two different locations of the sample (Figure 3.6 (b)), specifically, a region where there were no polymerized structures (A), and a region containing the waveguides (B), at three different depth locations with respect to the waveguide plane, +20 µm, 0 µm, and -20µm, respectively. The polymerizable bond in the phenylacetylene molecule is the carbon-carbon triple bond, $C \equiv C$, and its vibrational mode can be detected at 2111 cm^{-1} [131, 132]. Among the vibrational modes detected, which are listed in Table 1, there was clearly no peak of $C \equiv C$ bond stretching, which strongly supports the polymerization process of phenylacetylene we have hypothesized.

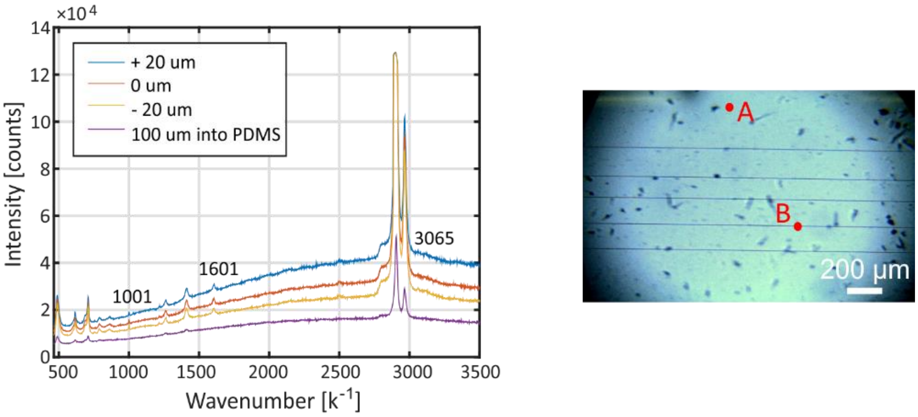

(a) (b)

Figure 3.6 (a) Raman spectra of phenylacetylene (PA) and Sylgard 184 PDMS taken in a Renishaw confocal Raman microscope. (b) Bright field microscopy image taken using a 5× magnification objective in the Raman Renishaw microscope. A 488 nm laser was focused in an area of the sample with no polymerized waveguide (point A), 100 µm into the PDMS material. In order to confirm the presence of the PA, the laser was then focused on a waveguide and the Raman signal was acquired at three different focusing depth in the proximity of the waveguide focusing plane, at 20 µm, 0 µm and 20 µm, respectively (point B). The strong peak related to the carbon-carbon triple bond stretching at 2111 cm^{-1} reported in literature [131, 132] doesn't appear, proofing the $C \equiv C$ bond opening and consequent PA polymerization.

Wavenumber $[k^{-1}]$	**Vibrational assignment**
491	Si-O-Si stretch (PDMS)
614	Si-CH_3 sym. rocking (PDMS)
688	Si-C sym. stretch (PDMS)
710	CH_3 sym. rocking (PDMS)
	Si-C asym. stretch (PDMS)
1264	CH_3 sym. bending (PDMS)
1411	CH_3 asym. bending (PDMS)
2906	CH_3 sym. stretch (PDMS)
2906	CH_3 asym. stretch (PDMS)
1001	Ring breathing (PA)
1601	C-C stretching (PA)
3065	C-H stretching (PA)

Table 1 List of the Sylgard 184 [133] and the recognized PA Raman peaks [131, 132].

Digital holography

We characterized the waveguides in terms of refractive index contrast and transmission loss. Measurements of the refractive index contrast were performed in a custom made off-axis interferometric imaging system (described in Chapter 2 of this thesis). A plane-wave reference beam interferes with the waveguide image through a beam splitter, revealing the phase change induced on the illumination beam as it crosses the waveguide (Figure 3.7 (a)).

An example interferogram is shown in Figure 3.7 (b); the average phase change along the waveguide, as shown in Figure 3.7 (c), is approximately $\Delta\Phi$=1 rad. Due to the aberration caused by the PDMS layer that the object wave has to propagate through, the image of the waveguide broadens from 1.3 µm to ~3 µm. We thus estimate the actual phase change to be $\Delta\Phi$=2.3 rad. Based on the measured height of the waveguide h≈4 µm and the estimated average phase change, we estimate that the refractive index contrast is Δn=0.06. This implies a polymer content of roughly 35% by mass given the refractive index of 1.59 and 1.41 for poly-phenylacetylene and PDMS, respectively.

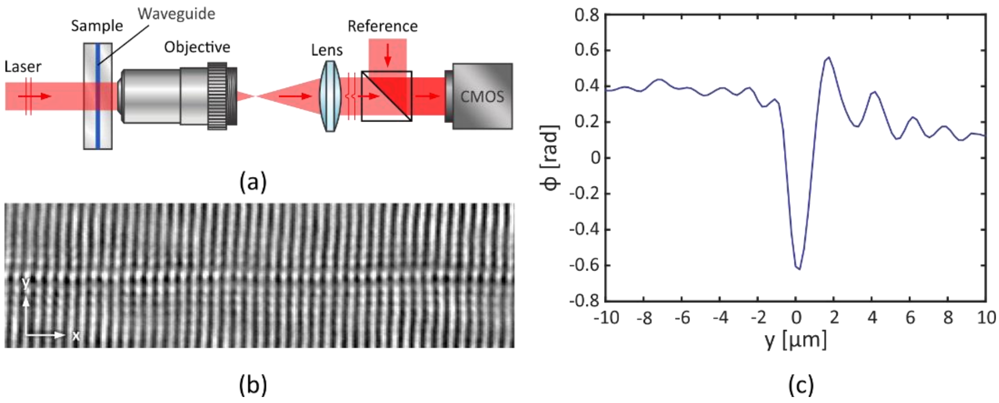

Figure 3.7 Measurement of the phase profile and refractive index contrast of the waveguide. (a) Principle of the measurement. A laser beam of plane wave is sent to pass the PDMS sample where the waveguide induces an additional phase change in the wave front, which is measured in the interferometric imaging system. (b) An example interferometric image of the waveguide. Fringes parallel to the waveguide are due to the aberration resulted from the PDMS material. (c) Extracted average phase profile of the waveguide, which is broadened due to the aberration introduced by the PDMS material. The corresponding refractive index contrast, after taking into account the broadening, is Δn=0.06.

PDMS waveguide end facet polishing

Light transmission measurements are highly sensitive to the waveguide facet morphological conditions. The coupling end face must exhibit extremely good optical quality and must be defectless in order to obtain a high coupling efficiency during the experiments; this can be achieved by polishing or cleaving the waveguides ends. PDMS is a soft and flexible material, therefore the air-PDMS interface scratches resulting from the knife cut play a critical role in light coupling experiments. Excellent optical quality of the waveguide end-surface were obtained by matching the refractive index of PDMS with an additional layer of PDMS that smooths out the uneven cut surface. The process flow for the polymer waveguides polishing includes six steps:

1. dissolving Teflon beads (cas: 37626-13-4) in FC40 solvent (cas: 51142-49-5) in 1 wt%;
2. spincoating of a very thin layer of Teflon solution on a glass slide (60 s at 1500 rpm)
3. evaporation of the solvent present in the solution for 2 min at 80 °C;
4. spincoating of ~50 µm optically clear and degassed PDMS (60 s at 1000 rpm) on top of the Teflon thin layer;
5. the waveguides slab is layed vertically, perpendicularly to the spincoated PDMS layer to allow the knife cuts filling until the PDMS is cured.
6. detachment of the PDMS slab from the glass slide; Teflon facilitates this procedure.

Figure 3.8 shows the phase contrast microscopy cross-sectional view from one PDMS slab interface before (a) and one after (b) the polishing with Teflon and PDMS. As it shown clearly from the figure, the cut scratches impressed by the knife is eliminated because of the refractive index matching. This procedure allows for a repeatable and efficient light coupling during the experiments.

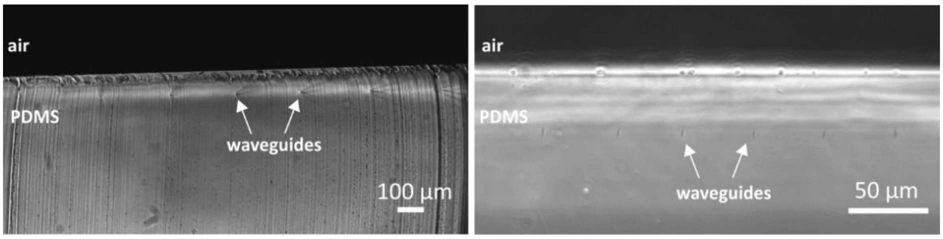

(a) (b)

Figure 3.8 Phase contrast cross-sectional view of a PDMS sample containing waveguides before (a) and after (b) the fiber ends polishing using Teflon and spin-coated Silicon oil.

Transmission loss

To measure the transmission loss, we coupled thermal white light from a halogen lamp passing a 1-mm iris into the waveguide using a 50× 0.7 NA objective and imaged the output using a digital CCD camera (full description of the experimental set up in Chapter 2). The iris was imaged on to the incident facet of the waveguide as a 17-µm spot with nearly homogeneous intensity. The motion stage was able to position the waveguide at the center of the incoherent light spot with better than 1 µm accuracy, ensuring the consistency of the coupling condition across multiple mount and dismount of the sample. Taking advantage of this experimental setting, we measured the ratio of the output power from the same waveguides cut into two different lengths. This power ratio reveals the transmission loss due to the material absorption and the scattering loss caused by the waveguide walls smoothness in the polymer waveguide as:

$$\alpha = -10\log_{10}(\frac{P_1}{P_2})\frac{1}{L_1 - L_2}$$

Equation 38 Waveguide transmission loss formula in $[\frac{dB}{cm}]$.

where α is the transmission loss in dB/cm, and P_1 and P_2 are the measured output power of the waveguide at lengths L_1 and L_2, respectively.

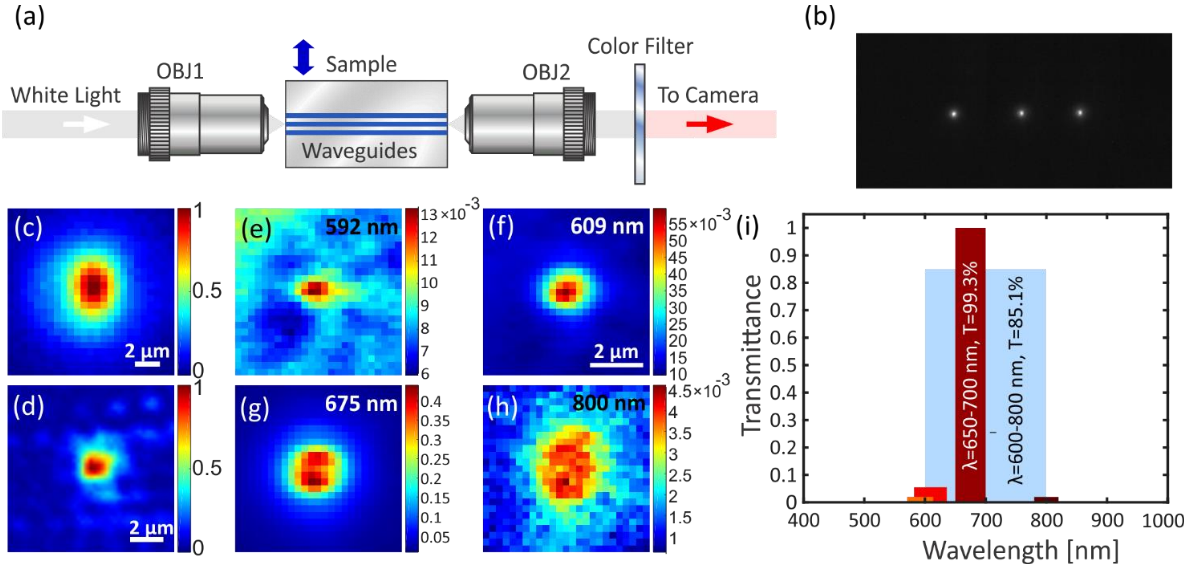

Figure 3.9 Characterization of the waveguide transmission. (a) Diagram of the optical set-up used for optical transmission loss characterization. (b) Broadband light output from three individual waveguides written at 800 µm under the top surface, using 1.9×1012 W/cm2 peak intensity and 0.7 mm/s writing speed. (c) Broadband waveguiding output from one waveguide. (d) Laser (HeNe) wave-

guiding output from the same waveguide; (e) – (h) Filtered narrowband waveguiding output from the same waveguide: (e) 592/43 nm, (f) 675/50 nm, (g) 609/53 nm, and (h) 800/40 nm; (i) Waveguide transmissivity measured by the intensity ratio between the outputs from waveguides cut at different lengths. Light blue, orange, red, brown and black bars show the measured transmissivity at 1 cm in 600 – 800 nm, 570 – 613 nm, 582 – 635 nm, 650 – 700 nm, and 780 – 820 nm, respectively.

We measured the transmission loss using the incoherent thermal source at L_1=16 mm and L_2= 12 mm (Figure 3.9 (a)-(b)). Before each measurement, we performed careful adjustments to ensure a consistent output power. Figure 3.9 (c) shows the output from one waveguide when incoherent thermal white light is launched. Additionally, we also launched laser light of 633 nm wavelength into the waveguide, the output of which is shown in Figure 3.9 (d). The mode field diameter of approximately 2 µm at this wavelength is consistent with the refractive index contrast of 0.06. With the incoherent light, we measured a transmission loss of 6 dB/cm over the entire white light spectrum; however, measurements with color filters suggested that the absorption loss is highly chromatic, as shown in Figure 3.9 (e) – (h). The transmissivity measured using a long pass filter cut at 532 nm is 85% at 1 cm length, corresponding to a loss of 0.7 dB/cm. Three waveguides were measured with a standard deviation of 0.07% in the transmissivity, confirming the consistency of the measurements and the waveguide property. Furthermore, the transmissivity measured at 592 nm and 800 nm using band pass filters of 40 nm bandwidth is nearly zero (orange and black bars in Figure 3.9 (i), respectively), suggesting that the 85% transmission is mainly located in the 600 – 800 nm wavelength range, as shown in Figure 3.9 (i) (light blue bar). In particular, within a narrower band of 650-700 nm, the measured transmissivity becomes 99.3% at 1 cm length, corresponding to a transmission loss of 0.03 dB/cm, as shown in Figure 3.9 (i) (dark red bar).

3.3.3 The self-focusing problem and luminescence signal detection

Due to the high peak intensity at the focus, nonlinear self-focusing is expected to play a role in the high aspect ratio of the waveguide and the occasional spots of material damage. As two-photon absorption, also self-focusing is a nonlinear phenomenon of the third order and depicts a nonlinear contribution to the refractive index of the material, which becomes intensity dependent:

$$n = n_0 + n_2 I$$

Equation 39 Nonlinear refractive index.

with n_0 being the usual material refractive index, I the optical field intensity and n_2 (expressed in $\frac{cm^2}{W}$):

$$n_2 = \frac{12\pi^2}{n_0^2 c}\chi^{(3)}$$

Equation 40 Nonlinear contribution to the material refractive index.

where c is the speed of light and $\chi^{(3)}$ is the third order material susceptibility. If the optical power exceeds the critical power for self-focusing, the material itself acts as a positive lens, modifying the light beam propagation and causing its focusing within the material [134]. This phenomenon leads to uncontrollable beam collapse and worst case to irreversible material damage during photopolymerization [135].

Previous reports have shown that the nonlinear refractive index of electronic origin in poly-phenylacetylene is on the order of 2.8×10^{14}cm^2/W [136], which leads to a critical power for self-focusing on the order of 1.5×10^4 W. Furthermore, the concentration of the photo-induced polymer, and thus the refractive index of the region concerned, is a power function of the laser intensity. This gives an additional intensity-dependent refractive index contribution of a chemical origin with a response time possibly at the level of ms. The quantification of the chemical contribution was beyond the scope of this work, although we expect it to be much greater than the electronic contribution. The writing peak power used in our system, on the other hand, was around 5.4×10^3 W, which is below the critical power for self-focusing by electronic contribution but very probably above the critical power for self-focusing by chemical contribution. Therefore, material damages always take place when the writing speed is low due to uncontrollable beam collapse. At optimal writing speed, the polymerization tends to grow along the depth direction, causing an elongated shape in the fabricated waveguides, but beam collapse does not happen due to the slow response time of the reaction.

Luminescence signal detection has been used as a tool to monitor the photopolymerization process during the waveguide writing. A constant signal emission from the radicalized photoinitiator indicates a successful polymerization process, while the material damage due to self-focusing can be detected as a strong signal peak on the Silicon PMT (Figure 3.10).

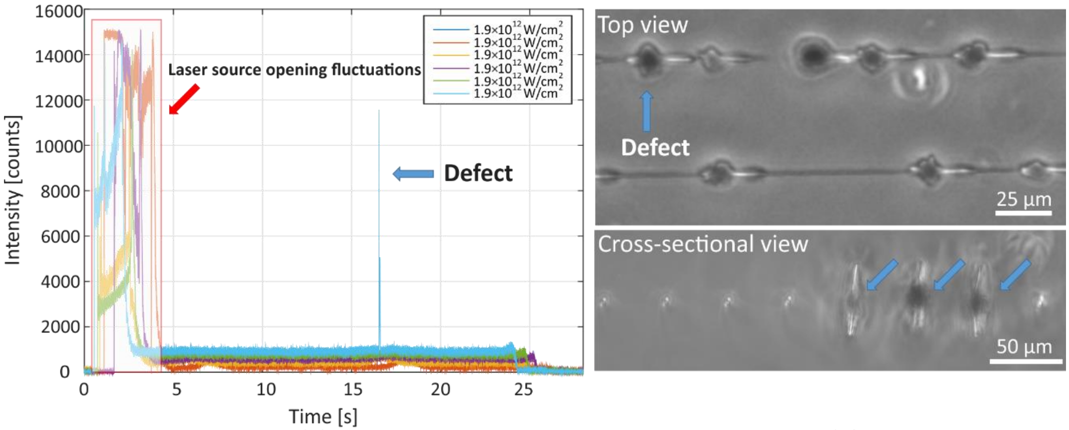

(a) (b)

Figure 3.10 Fluorescence intensity signal of different writing intensities as a function of time during a writing process at 0.7 mm/sec and 800 µm below the PDMS-cover slide interface. Each data point was taken every 1 ms; the initial swinging behaviour is related to the opening of the laser source which causes light fluctuations in the detector. (b) Phase microscopy top view (top) and cross-sectional (bottom) image of defected waveguides. The uncontrollable self-focusing takes place above the critical power for self-focusing that is ~5.4×10^3 W, causing randomly distributed defects (blue arrows).

The carbon-carbon triple bond requires a dissociation energy of 8.39 eV, while it takes a little less than 3.47 eV to break one of the three carbon-carbon bonds within the phenylacetylene molecule. In this multi-photon process, the energy of photons at 680 nm is ~1.82 eV and the intensity required to initiate the polymerization depends on the material properties, such as its two-photon absorption cross-section, which we did not measure empirically. The material damage due to the beam collapse under the unstable self-focusing is largely associated with slow writing speeds, high peak intensities, and material inhomogeneity and defects. A faster and low-intensity fabrication process aleviates the material damage issue, but results in lower refractive index contrast structures.

3.4 Alternative chemical schemes

As already mentioned, the use of photoinitiators is required for efficient writing processes; by virtue of this reason, phenylacetylene has been widely tested also in the presence of several common photoinitiators, such as Irgacure 819, Irgacure OXE01 and 7-diethylamino-3-thenoylcoumarin (DETC), leading to non-guiding structures or unsuccessful polymerization.

We have investigated the photopolymerization of many other light sensitive compounds, with and without photoinitiator (Appendix 3); physical requirements for the monomers included a high refractive index, a nonpolar nature, and appropriate absorption characteristics. The acrylate group, which is one of the most reactive polymerizable groups, did not achieve sufficient monomer loading in PDMS because of its slight polar nature and poor solubility in PDMS. Aware of the aforementioned requirements, we have moved to styrene and divinylbenzene after having considered a number of nonpolar small-molecule monomer formulations.

Concerning the choice of the photoinitiators to test, we have considered the following criteria:

- high degree of solubility in the monomer
- high degree of solubility in PDMS
- high degree of infiltration into PDMS
- capability of triggering monomers photopolymerization,
- high δ_{2A} values if reported
- molecular structure similarity of commercially available (or synthetized) PIs with high δ_{2A}
- ease at use
- low cost and easy supplying

Despite being a widely used building block in polymer science, styrene did not show meaningful polymerization without a photoinitiator in our tests. On the contrary, a formulation containing styrene and DETC as a photoinitiator showed successful two-photon polymerization in PDMS (Appendix 3). However, waveguides fabricated based on styrene were frail and did not sustain the solvent process to remove unreacted monomer and PI, possibly due to an insufficient molecular weight in the polymer product and the lack of crosslinking.

3.5 Summary

In this chapter I have presented the methods and the results about the fabrication of poly-phenylacetylene waveguides in PDMS. I have demonstrated that compact optical waveguides can be fabricated in PDMS through multi-photon laser direct writing and photopolymerization. Photoinitiator-free polymerization was achieved for the first time, tuning the writing laser wavelength to 680 nm such that the absorption band of the phenylacetylene monomer is reached via multi-photon absorption. The fabricated waveguides we characterized are approximately 1.3 µm wide with Δn=0.06 and a transmission loss of 0.03 dB/cm in the spectral range of 650 – 700 nm. These waveguides could receive a wide range of applications in biosensors, microfluidic flow cytometry, wearable photonic devices, electro-elastic optical modulators, flexible optical circuit boards, and optical neural networks.

Nevertheless, self-focusing always takes place and leads to beam collapse and material damage; this is an intrinsic effect that needs to be taken into consideration in the waveguide writing process. I have explained the criteria and guidelines we have followed in order to further explore alternative chemical schemes capable of minimizing self-focusing and successful waveguide writing in PDMS. In the next chapter I will present the results we have obtained using Irgacure OXE02 as a photoinitiator, and describe the methodologies we have implemented for the fabrication of poly-divinylbenzene waveguides in PDMS.

Chapter 4 Sub-micron poly-DVB waveguides in PDMS

In this chapter, I demonstrate the fabrication of submicron optical waveguides in polydimethylsiloxane (PDMS) using divinylbenzene (DVB) as the photopolymerizable monomer through two-photon polymerization (2PP). We show that the commercial oxime ester photoinitiator Irgacure OXE02 is suitable for triggering the DVB photopolymerization, resulting in a stable and controllable fabrication process for the fabrication of defect-free, 5-cm long waveguides. We further explore a multi-track fabrication strategy to enlarge the waveguide core size up to ∼3 µm for better light confinement and reduced cross-talk. In these waveguides, we measure a refractive index contrast on the order of 0.005 and a transmission loss of 0.1 dB/cm at 710 nm wavelength.

Most of the material presented in this chapter can be found in the publication [122]:

- Panusa, G., Pu, Y., Wang, J., Moser, C., & Psaltis, D. (2020). *Fabrication of Sub-Micron Polymer Waveguides through Two-Photon Polymerization in Polydimethylsiloxane. Polymers 2020, 12(11), 2485; doi:10.3390/polym12112485.*

4.1 Introduction

In Chapter 3 I have shown the fabrication of sub-2 µm waveguides in polydimethylsiloxane (PDMS) through multi-photon LDW without a photoinitiator (PI). The PI-free fabrication process using phenylacetylene as the monomer achieved an excellent refractive index contrast of 0.06 and a very low optical loss of 0.03 dB/cm in the 650–700 nm band. While the high refractive index contrast is clearly a result of a high degree of polymerization, the existence of long conjugated π-bonds in the polymer result in very poor transmission in wavelengths shorter than 600 nm. Furthermore, this process was subject to defects in the fabrication of waveguides longer than one cm due to material damage, which is likely a result of the uncontrollable beam collapse caused by the self-focusing of light upon photopolymerization.

In a photoinduced polymerization process, the reaction probability of polymerization is proportional to a power function of the laser intensity depending on the order of the nonlinearity involved. This creates an intensity-dependent refractive index profile during the laser irradiation, which causes self-focusing and beam self-trapping. Different from nonlinear refractive indices of electronic and molecular origin, this chemically originated nonlinear refractive index reacts rather slow, possibly at the millisecond time scale as limited by the monomer diffusion time and is rather large in magnitude. This self-focusing process is a direct function of the refractive index change between the pre- and post-polymerization state, which is dependent on the degree of polymerization and the monomer concentration. The self-focusing that leads to beam collapse and material damage is an intrinsic effect that needs to be taken into consideration in the waveguide writing process. Motivated by the need to minimize self-focusing, we explored other monomer/PI combinations that can lead to different characteristics in PDMS. In particular, styrene and its derivatives are intriguing as a monomer because of the lack of long-chain conjugated π-bonds in the resulting polymer, potentially resulting in a broader transmission band. Furthermore, owing to the continuing efforts in the development of functional PIs [124, 137, 138], the fabrication could benefit from new PIs specifically optimized for two-photon absorption [124].

In this chapter, I demonstrate the fabrication of long, submicron-sized, largely defect-free optical waveguides in PDMS using divinylbenzene (DVB) monomer and a commercial PI, Irgacure OXE02. In addition to the multi-cm waveguide length without defects, the transmission is broadband, limited only by scattering. The trade-off in achieving this, is a lower refractive index contrast in the fabricated waveguide, which results in higher transmission loss and less confined light compared with the PI-free process. Through this approach, we were able to fabricate single-track (simple) waveguides of ~0.5 µm width, which have a nearly flat loss of 13 dB/cm over the spectral range of 535–679 nm and are subject to crosstalk when placed close to one another in parallel. To improve the light confinement, we also used a multi-track (compound) waveguide strategy to increase the waveguide width. Characterizations in the compound waveguides show an optical loss of 0.1 dB/cm in the 710/10 nm spectral band, following the convention of central wavelength/bandwidth, and a refractive index contrast of ~0.005.

4.2 Materials and methods

4.2.1 Chemical scheme

We tested a wide range of PIs and identified the commercial Irgacure OXE02 (BASF, Germany) to be suitable for initiating the photopolymerization of DVB through two-photon absorption in our experiments. As already mentioned, waveguides fabricated based on styrene were frail and did not sustain the solvent process to remove unreacted monomer and PI, possibly due to a small molecular weight in the polymer product and the lack of crosslinking. Therefore, we chose DVB as the monomer to promote crosslinking and address the stability issue. The chemical scheme of the multi-photon polymerization is illustrated in Figure 4.1 (a). The UV-visible absorption spectra of DVB and OXE02 was measured using a UV-visible spectrometer (Cary-100, Agilent Technologies) as shown in Figure 4.1 (b). The absorption bands of both reactants fall in the 200–400 nm spectral range, which fall in the spectral transparency band of the host PDMS [139]. Upon multi-photon absorption, Irgacure OXE02 initiates the polymerization of DVB, forming a cross-linked polymer. Compared with self-initiated photopolymerization in phenylacetylene, the presence of the PI in this reaction likely results in a lower polymer molecular weight due to frequent termination by combination.

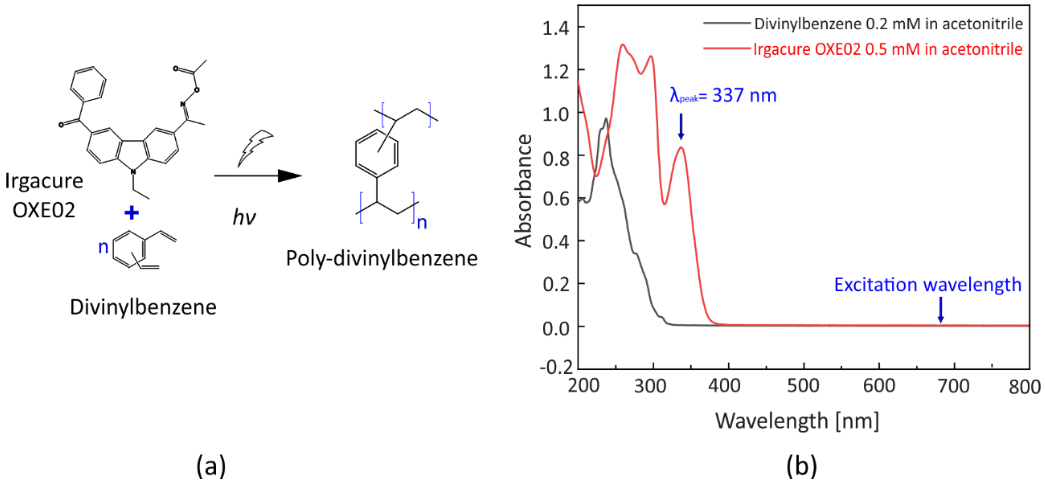

Figure 4.1 (a) Molecular structure of the divinylbenzene (DVB) monomer and Irgacure OXE02 and the polymerization of the monomer upon laser irradiation. (b) Absorption spectrum of 0.2 mM DVB and 0.5 mM Irgacure OXE02 in acetonitrile. Blue arrows indicate the absorption wavelength peak of the photoinitiator (PI) (337 nm) and the excitation wavelength of our system tuned to 680 nm.

4.2.2 Materials and sample preparation

All chemicals were used as purchased without further purification. DVB (80% purity, CAS Number 1321-74-0) was purchased from Sigma Aldrich (Buchs, Switzerland); Irgacure OXE02 (CAS Number 455-590-6) was requisitioned from BASF. The goal of this project consisted in the manufacture of a biomedical cochlear implant imaging device (more details in Chapter 5). In order to meet the requirement of biocompatible optical waveguides, in this project we mostly worked with a widely used for human implantation devices PDMS [140], the NuSil MED6215. Optically transparent biomedical-grade PDMS was purchased from NuSil Technology (Carpinteria, CA, USA). As Sylgard 184, NuSil MED6215 consists of a Part A (refractive index n = 1.406, viscosity η = 5.600 cP) and a Part B to be combined in a ratio of 10:1 followed by a mixing and defoaming process.

We prepared 1-mm thick pristine PDMS slabs of 1 × 5 cm^2 surface area and immersed them in the monomer-PI solution for 144 h to load the monomer and PI molecules into the PDMS intermolecular space. This step was significantly longer than our previous work with phenylacetylene, because the PI molecule is much larger than the monomer and takes a much longer time to permeate the PDMS slab and reach the saturation level. Over the course of this infiltration, we measured the evolution of the weight gain of the PDMS slabs for different concentrations of the PI in the DVB monomer, which is shown in Figure 4.2. Although the weight gain does not change much after the first two hours, quality waveguides could only be fabricated after 144 h of immersion, which clearly reveals the effect of the larger PI molecule. In all three PI concentrations, the weight gain reaches its peak in the first one or two hours, which is an indication of the fast mobility of the small monomer DVB molecules. The weight gain slightly drops in the subsequent few hours possibly due to the leaching of certain small molecules originally presented in the PDMS since DVB is a good solvent. In the succeeding hours, the weight gain slowly increases again, suggesting the slow infiltration of the much larger PI molecules into the PDMS. During the infiltration, a certain number of the PI molecules may be blocked on the surface of the PDMS slab, causing a hindrance for further material infiltration and resulting in lower weight gain in the sample with higher PI concentration.

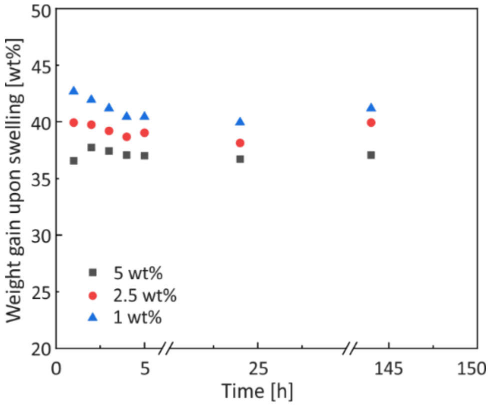

Figure 4.2 Weight gain upon swelling of pristine cured polydimethylsiloxane (PDMS) slabs, for 1, 2.5, and 5 wt% of Irgacure OXE02 in the DVB monomer.

The general procedure of the waveguide fabrication and characterization follows that described in Chapter 3. Based on a fabrication platform for LDW [121], which contains a mechanical motion stage with 5 cm travel range, we further integrated a high-precision piezo stage (Newport Spectra Physics GmbH NPX400SG-D) for accurate positioning and a tip-tilt-rotation stage to ensure the track parallelism with the slab surface over a distance of 5 cm. Moreover, the illuminating objective has been placed in a custom-made stainless steel mount holding a high-precision piezo stage (Newport Spectra Physics GmbH NPO250SG-D) to ensure a finer adjustment of the focus (Figure 4.3). In order to trigger the two-photon polymerization reaction, the laser was tuned to 680 nm to reach the absorption band of Irgacure OXE02 via two-photon absorption. The average beam power used in the fabrication ranges between 60 and 85 mW, and thus the peak intensity can be adjusted between ~1.93 and ~2.74 ×10^{12} W/cm^2 based on an aberration-free, self-focusing-free focal spot. We refer to this intensity as the nominal writing intensity in later sections. During the laser writing, the PDMS slab proceeded at a predetermined constant velocity, while the lateral position of the focus was controlled by the piezoelectric stages. Upon the completion of the waveguide writing, we finished the sample with a 24-h ethanol bath to remove unreacted monomer and the PI.

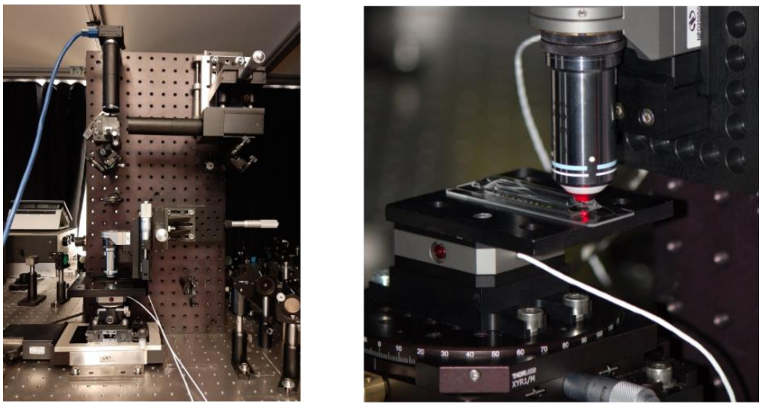

(a) (b)

Figure 4.3 (a) Experimental MP-LDW vertical set up for polymer waveguide writing integrated with high precision piezo-stages and (b) close up look to the writing process by means of a water immersion objective (Nikon, NA=0.7).

4.3 Results

4.3.1 Simple waveguides

Finding the right combination of the various fabrication parameters is a crucial challenge in LDW photopolymerization, requiring a compromise between the irradiating laser intensity and writing speed in order to avoid material damage. We wrote waveguides over 5 cm long samples, isolated from each other by an inter-waveguide distance of about 500 µm to eliminate any crosstalk. For each set of parameters, we fabricated five waveguides, from which three were interrogated for statistics. We investigated the finished samples of isolated single waveguides (simple waveguides) using a phase-contrast microscope (Olympus IX-71) to verify the formation of the poly-DVB waveguides embedded in the PDMS framework (Figure 4.4 (a) and (c)). The cross-section of single-pass laser tracks (see the inset in Figure 4.4 (b) for a typical example) was measured to be ~0.6–1 µm wide and ~1.5–3 µm high depending on the writing parameters, as shown in Figure 4.4 (b) and (d). The dimensions (the width and the height) of the focal volume during the fabrication procedure depend not only on the laser pulse energy and the numerical aperture of the writing objective but also on the writing speed. Figure 4.4 (a) and (b) reveal the evolution of the waveguide geometry (width and height) as a function of increasing writing speed at a constant writing laser intensity ($I \sim 2.25 \times 10^{12}$ W/cm^2). Figure 4.4 (c) and (d) show the waveguide geometry as a function of increasing laser intensity at a constant writing speed v = 1.8 mm/s. Overall, both the axial and lateral dimensions of the waveguide structure depend linearly on laser peak intensity and writing speed, showing an aspect ratio of about 1:3; nevertheless, experimental sample variations such as monomer/PI solution infiltration efficiency, and optical settings during the writing, strongly affect the waveguide fabrication where experimental conditions remain unchanged. This reflects in small geometrical fluctuations in the waveguide size throughout different samples fabricated with the same experimental parameters such as laser focal intensity and writing speed. This can be observed in the plot in Figure 4.4 (d).

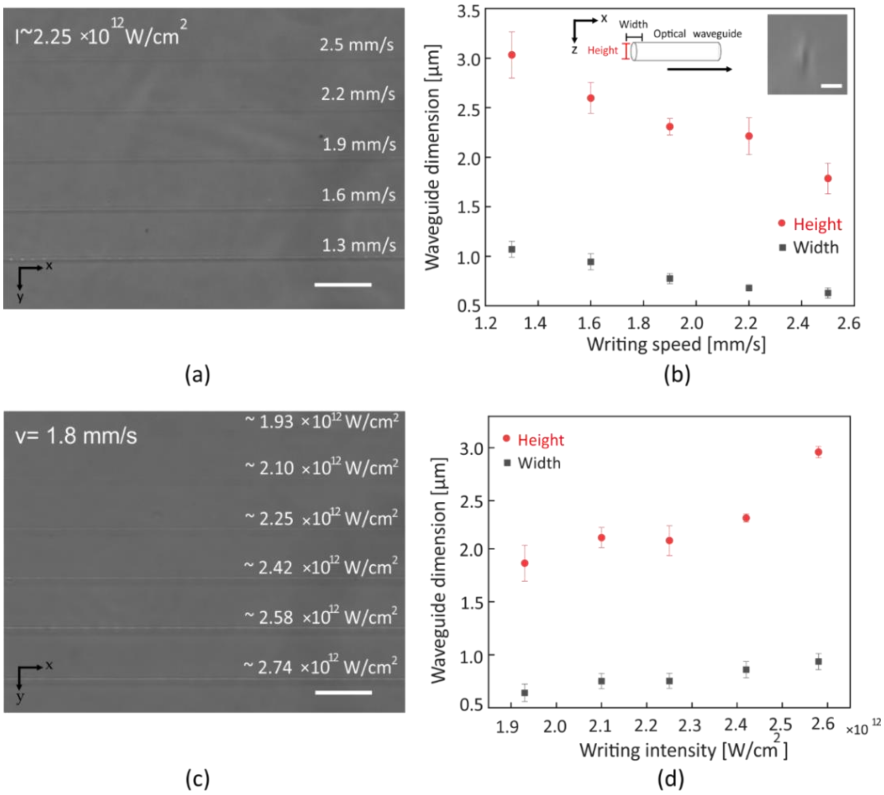

Figure 4.4 (a) Phase-contrast microscopy top view image of the recorded poly-DVB optical waveguides written at constant peak intensity I ~ 2.25 × 10^{12} W/cm^2 and varying fabrication speed, ranging from 1.3 to 2.5 mm/s. (b) Waveguide width and height evolution as a function of increasing writing speed where the error bar derives from the measurement of three waveguides; the inset shows the cross-sectional view of a single-track waveguide where the scale bar measures 5 µm. (c) and (b) display the same as above as a function of increasing fabrication peak intensity from 1.93 to 2.74 × 10^{12} W/cm^2 and constant speed v = 1.8 mm/s. Error bars indicate the standard deviation derived from the measurement of five different waveguides geometry. Scale bars dimension in (a) and (c) is 50 µm.

We measured the refractive index contrast as a function of focal intensity at a constant writing speed and as a function of writing speed at a constant focal intensity, as shown in Figure 4.5 (a) and (b), respectively. These experiments suggest that the polymerization threshold for DVB is about ~1.93 × 10^{12} W/cm^2 for simple waveguides based on visual determination with phase-contrast microscopy. As I will show later on, this is higher than the actual polymerization threshold, and it is possible to write waveguides at a slightly lower intensity, since phase-contrast microscopy cannot detect the presence of low-concentration polymer in such a small volume with sufficient sensitivity. The refractive index change induced in the polymer material increases linearly from 0.005 to 0.012 with laser intensity in the 2.10–2.8 × 10^{12} W/cm^2 range Figure 4.5 (a). We observed a weaker effect of the writing velocity on the measured refractive index change between the polymer waveguides and the PDMS framework, as shown in Figure 4.5 (b), which is in good accordance with other works on photopolymerization [130]. At a constant laser intensity of ~2.25 × 10^{12} W/cm^2 and 1.3 mm/s writing speed, we measured a refractive index change of ~0.0075, while at higher speeds the refractive index contrast stabilizes around 0.005. The insets in both Figure 4.5 (a)-(b) show the mean phase profiles recorded along the waveguides in our interferometric system.

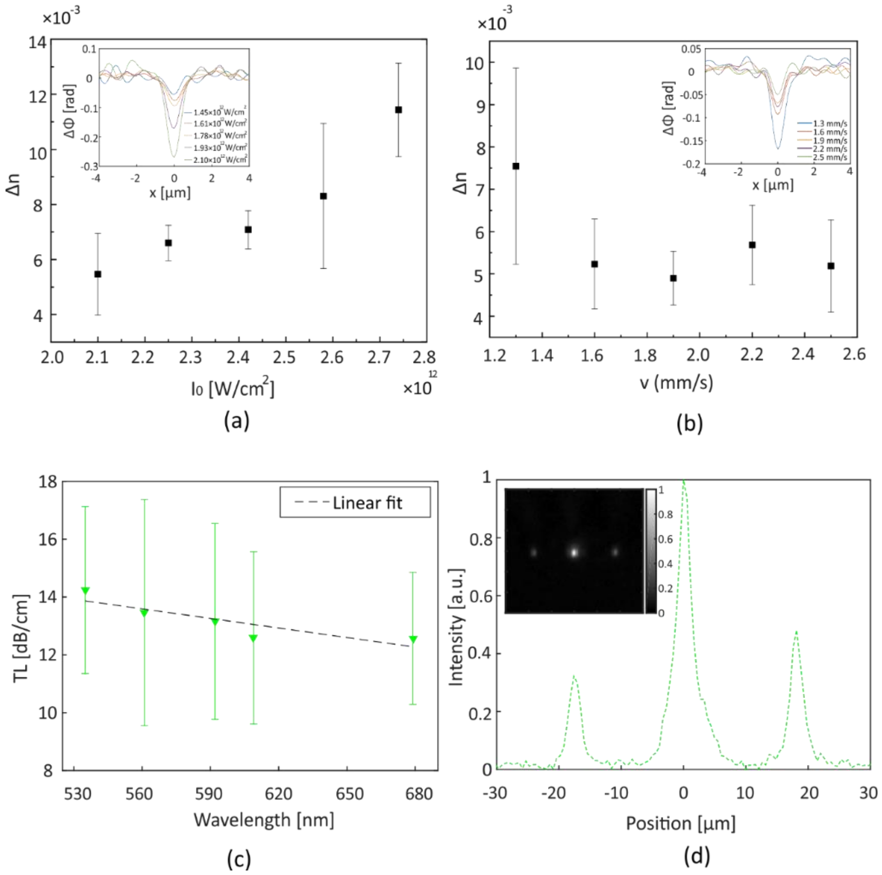

Figure 4.5 (a) Evolution of the refractive index as a function of increasing peak intensity (and constant writing speed v = 1.8 mm/s) is displayed. The laser peak intensity ranged between ~2.10 × 10^{12} W/cm^2 and ~2.74 × 10^{12} W/cm^2. (b) Refractive index contrast for waveguides recorded at ~2.25 × 10^{12} W/cm^2 constant laser intensity and different writing speed, increasing from 1.3 to 2.5 mm/s. The insets display the measurement of the phase profile for different laser peak intensities and velocities, where each phase profile is the mean profile measured from three waveguides written with the same fabrication parameters. (c) Transmission loss in dB/cm as a function of wavelength, where colored filters have been inserted in the optical path to measure the output from three different simple waveguides written 500 µm apart from each other. (d) Output intensity profile of three simple waveguides at an inter-waveguide distance of ~18 µm; light in the 535/43 nm spectral band has been coupled in the central waveguide. Waveguide outputs are displayed in the image inset. Error bars indicate the standard deviation from three waveguides fabricated with the same experimental parameters.

Due to the elliptic cross-section, the V-number and thus the modal properties of the simple waveguides are birefringent. Based on a Δn of 0.005, the semi-major axis length of the elliptical core of about 1.5 µm and the manufacturer-specified PDMS cladding refractive index of 1.406, we thus estimated that the upper limit of the V-number for the simple waveguides is 2.1, at the shorter end of the tested spectral band (535 nm), based on the V-number definition for elliptical waveguides reported in [141]. The V-number may be slightly higher (<0.5% as estimated from Sylgard-184 data) when material dispersion is considered. At the longer end (679 nm), the V-number is 1.6; therefore, the simple waveguides are single-mode.

To show the crosstalk, we wrote simple waveguides with the same fabrication parameters (2.25 × 10^{12} W/cm^2 and 2 mm/s), and tested them at an inter-waveguide spacing of 20 µm, which reduced to ∼18 µm (inset in Figure 4.5 (d)) after the solvent process to remove the unreacted monomer and PI. At this inter-waveguide spacing and 1 cm sample length, the simple waveguides present crosstalk, as shown in Figure 4.5 (d) where the intensity profile along the waveguides is shown. The image inset shows the simple waveguides output in the 535/43 nm spectral band; at ∼18 µm inter-waveguide spacing, the output light is clearly visible also from the two adjacent cores whereas only the central waveguide has been coupled.

4.3.2 Compound waveguides

In order to achieve long, defect-free waveguides we optimized the fabrication parameters for simple waveguides to be 1.78 × 10^{12} W/cm^2 nominal intensity and 3.2 mm/s writing velocity. This intensity is lower than the visually-determined threshold of 1.93 × 10^{12} W/cm^2 but significantly reduces the probability of defects. At this lower fabrication intensity, Δn is further reduced and the crosstalk is more significant. Thus, the simple waveguides present a unique challenge of excessive crosstalk when being implemented in a high-density integration. Although increasing Δn is the most effective way to minimize the crosstalk, it is constrained by the current photochemistry of choice, and more fundamentally, by the intrinsic self-focusing and beam collapse leading to material damage and fabrication defects.

Given the fundamental constraints and a goal of inter-waveguide spacing of 10 µm at the length of 5 cm, the only feasible approach is to increase the waveguide width for better mode confinement. Since this was difficult to achieve with larger focal spot size because of the required light intensity for multi-photon absorption, we instead fabricated compound waveguides where multiple tracks go side-by-side in parallel with a very small interval spacing δ (Figure 4.6). The spacing is so small that the potential barrier between the individual tracks is tunneled through easily and the multiple tracks effectively behave like a single, wider waveguide (a compound waveguide). This approach also calls for a lower fabrication intensity and a higher writing speed in order to avoid material damage caused by the refractive index modification carried by the adjacent core.

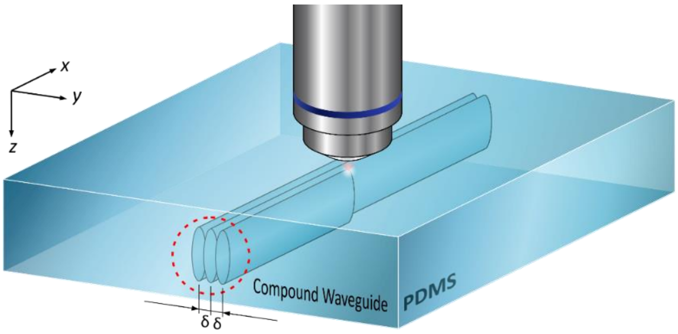

Figure 4.6 Schematic of the writing of compound waveguides. The PDMS sample is displaced by a small distance δ by means of a piezoelectric stage in the y direction. A long travel range mechanical stage moves the sample over centimeters in the x-direction.

The compound waveguides were fabricated with a nominal focal intensity of 1.78 × 10^{12} W/cm^2 and a writing velocity of 3.2 mm/s, which were optimized from the fabrication of simple waveguides. We have investigated the mode confinement for single-, double- and triple-track waveguides, and got the insight about what the optimal tunneling core-to-core distance within the composite waveguides should be in order to deliver the highest light energy. Triple-track waveguide bundles showed better light confinement if compared to double-track waveguide bundles at any sample length (Figure 4.7).

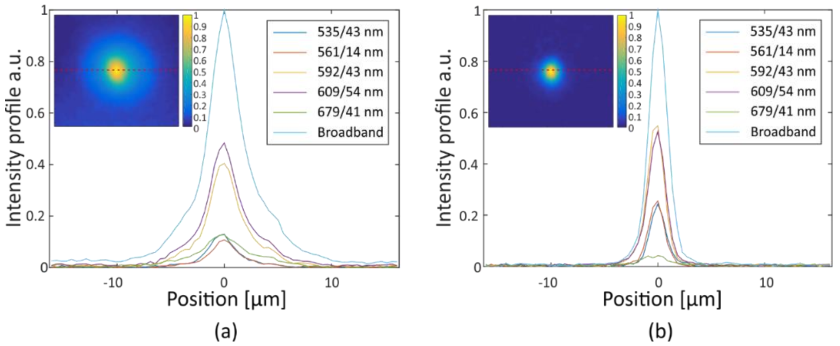

Figure 4.7 Normalized output mode profile from a single laser pass (a) and from a double pass laser waveguide in the different spectral regions, both written at the same experimental parameters. The compound waveguides show improved mode light confinement if compared to the single waveguides which exhibit light escaping from the core region. Insets in (a) and (b) show the output mode for white light illumination and the plot cross-cuts (dotted red line).

We first fabricated short double- or triple-track compound waveguides at an intra-waveguide interval δ = 1.2 µm for a pilot study at three different PI concentrations and measured the dimensions of the individual constituent simple waveguide. At the same fabrication parameters, both waveguide width and height increase when a higher concentration of photoinitiator is used (Figure 4.8 (a)). At 1 wt% PI concentration, the lateral and axial dimension of the waveguides were measured to be ~0.63 µm and ~2 µm on average, respectively, and reached ~0.69 µm and ~2.7 µm, respectively, at a PI concentration of 5 wt%. The cross-sectional and side view of the compound waveguides acquired from a phase contrast microscope is shown in Figure 4.8 (b)-(e).

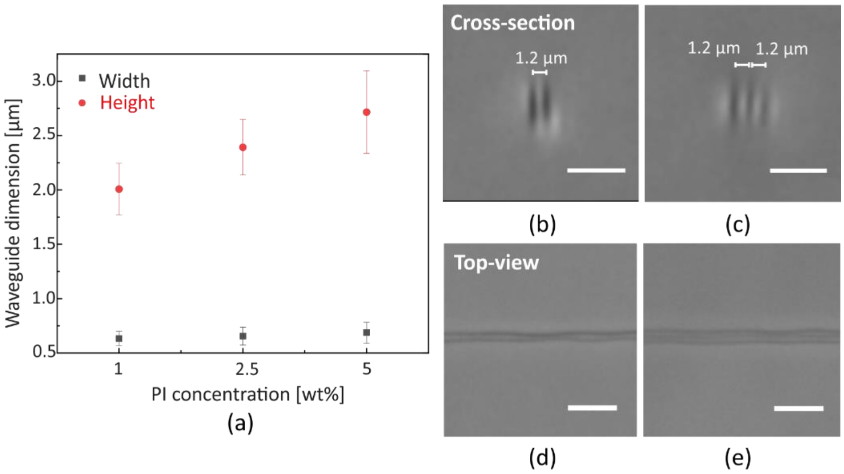

Figure 4.8 (a) Waveguide dimensions as a function of the Irgacure OXE02 concentration into the DVB monomer. The size of the waveguides increases with increasing PI concentration. The isolated, single waveguides were fabricated at an intensity of ~1.78 × 10^{12} W/cm^2 and a velocity of 3.2 mm/s. Scale bars measure 5 µm; error bars indicate the standard deviation from five different waveguides; cross-sectional view taken in a phase contrast microscope (Olympus IX-71) of a double-cored (b) and a triple-cored (c) poly-DVB waveguides; top view image of double (d) and triple-track (e) poly-DVB waveguides.

We then fabricated 5-cm long, double- and triple-track compound waveguides at 5 wt% PI concentration and 1.2 µm intra-waveguide interval for more comprehensive characterization. The refractive index contrast Δn of the compound waveguides was measured using the interferometric imaging system [121]. Both the double- and triple-track waveguides show a refractive index contrast on the order of Δn = 0.005, calculated from the phase we extracted from the interferometric image of the waveguides. The V-number ranges from 2.22 down to 1.68 over the spectral band from 535 nm to 710 nm when we consider the waveguide cross-section as a square of side 2.7 µm. Figure 4.9 (a) shows the waveguide output intensity profiles of a double-track (blue) and a triple-track (red) waveguide in the 535/43 nm spectral band, whose two-dimensional intensity distribution is shown in the inset. Figure 4.9 (b) shows the transmission loss at the spectral points of measurement in a log-log fashion, where a straight line of a −4.0 slope would indicate a loss of pure Rayleigh scattering nature. In Figure 4.9 (b), the double-track and triple-track data fit well to lines of slope −3.8 and −7.1, respectively. Overall, in the double-track waveguides the TL drops from 6.51 dB/cm at 535/43 nm to 2.18 dB/cm at 710/10 nm, while in the triple-track waveguides it changes from 12.40 dB/cm to 0.15 dB/cm at the same two spectral points. The transmission loss for the different types of waveguides and in the different wavelength ranges is summarized in Table 2.

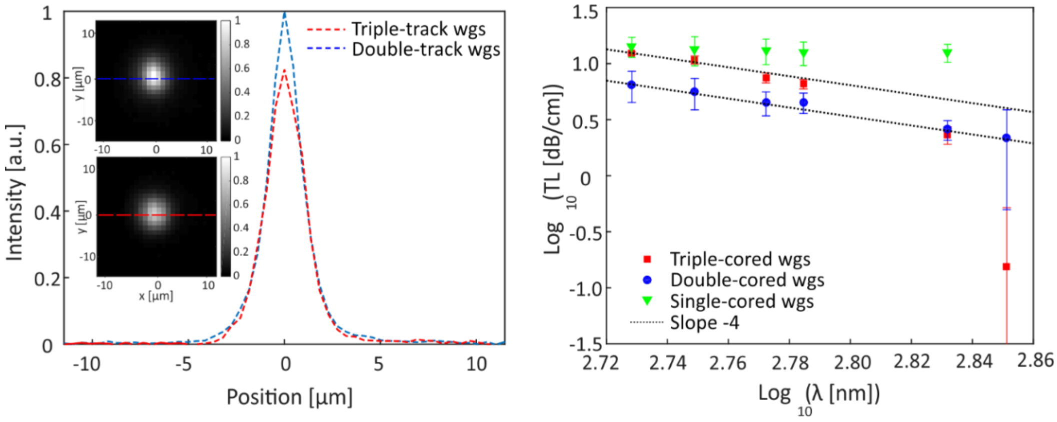

(a) (b)

Figure 4.9 (a) Output intensity profile of a double-cored (blue) and triple-cored (red) waveguides (wgs), at 535/43 nm spectral band. Waveguide outputs are displayed in the image inset. (b) Transmission loss in dB/cm as a function of wavelength for simple (green), double- (blue) and triple- (red) track waveguides. Dot lines indicate the linear fit with –4.0 slope, for both double- and triple-track waveguides, typical of pure Rayleigh scattering.

Wavelength range (nm)	Single	Double	Triple
535/43	14.2 ± 2.9	6.5 ± 2.0	12.4 ± 0.3
561/14	13.5 ± 3.9	5.6 ± 1.7	10.8 ± 0.9
592/43	13.2 ± 3.4	4.5 ± 1.0	7.5 ± 0.7
609/54	12.6 ± 3.0	4.5 ± 0.9	6.6 ± 0.6
679/41	12.6 ± 2.3	2.6 ± 0.5	2.3 ± 0.4
710/10	-	2.2 ± 1.7	0.1 ± 0.4

Table 2 Summary of transmission loss for the different waveguide types in different wavelength ranges in dB/cm.

4.4 Discussion and conclusions

To obtain further insight into the optical process in the photopolymerization in our experiments, we consider the polymerization kinetics, noting that the irradiation time is generally brief (on the order of sub-one ms) in our system and a steady state of the reaction is not reached. We also note from our measurements that the polymer concentration is low and highly localized in the writing region, implying that the monomer concentration remains nearly constant. The final concentration of the polymerized DVB, $c_{pDVB}(\boldsymbol{r})$ where $\boldsymbol{r}$ is the spatial coordinate, is directly proportional to the time-integration of the concentration of the PI radicals $c_{PI*}(\boldsymbol{r},t)$ during the laser irradiation, i.e., $c_{pDVB}(\boldsymbol{r}) = \int \eta_p c_{PI*}(\boldsymbol{r},t)dt$, where η_p is the polymerization coefficient depending on the initiation efficiency, propagation constant, termination constant, and monomer concentration of the specific PI-monomer combination. The instantaneous concentration of the PI radicals generated through two-photon absorption during the laser irradiation is expressed as $\frac{\partial}{\partial t} c_{PI*}(\boldsymbol{r},t) = \sigma_2 I^2(\boldsymbol{r}-vt) c_{PI}(\boldsymbol{r},t)$; where σ_2 is the two-photon absorption cross-section of the photoinitiator molecule in Goeppert–Mayer units; $I(\boldsymbol{r})$ is the irradiation intensity expressed in terms of number of photons; v is the velocity of writing; and $c_{PI}(\boldsymbol{r},t)$ is the concentration of the remaining photoinitiator. Furthermore, due to the small region of writing, PI* is subject to a diffusion process as $\frac{\partial}{\partial t}n_{PI*}(\boldsymbol{r},t) = D_{PI*}\nabla^2 n_{PI*}(\boldsymbol{r},t)$, where D_{PI*} is the diffusion constant. The system is implicitly highly nonlinear, since the intensity $I(\boldsymbol{r}-vt)$ at point $\boldsymbol{r}$ will be modulated by the refractive index profile $\Delta n_{pDVB}(\boldsymbol{r})$ it creates, which can be modeled with the unidirectional pulse propagation equation [142]. Heuristically, the diffusion equation in the coupled equation system causes c_{PI*} to expand spatially from the source term once the PI molecules are radicalized. In the one-dimensional writing of a waveguide, this expansion is two-dimensional in the height and width. Therefore, the refractive index profile of the fabricated waveguide is jointly determined by σ_2 and D_{PI*}. Regardless of the exact distribution of Δn_{pDVB} and the extent of the polymerization region, the total phase change as measured in the interferometric imaging system, where the width of the polymerized structure is below the diffraction limit, is $\Delta\Phi = k\Delta n_{pDVB}h \propto I_0^2$, where $k = \frac{2\pi}{\lambda}$, λ is the laser wavelength used in the measurement of $\Delta\Phi$. Figure 4.10 shows the plot of the measured $\Delta\Phi$ as a function of I_0, which fits well to a second-order curve while also revealing a threshold behavior.

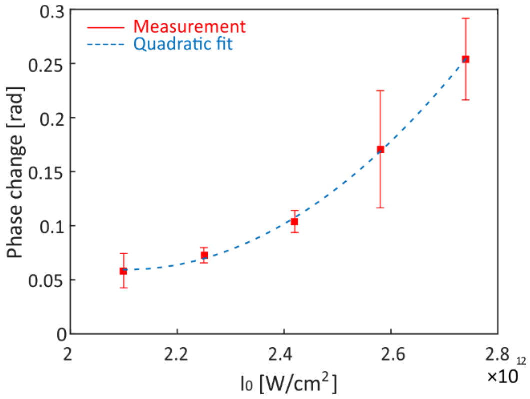

Figure 4.10 Plot of the measured phase change in the waveguides as a function of the writing intensity. The error bar indicates the standard deviation among three different waveguides. Dashed line shows a quadratic regression.

The properties of the polymerization process are largely determined by the parameters η_p, σ_2, and D_{PI*} in the coupled partial differential equation system. The polymerization coefficient η_p is a parameter dependent on the specific combination of PI and monomer and determines how probable the polymerization is initiated, propagated, and terminated given a specific c_{PI*} and c_{DVB}. The parameter σ_2 reflects how efficient two-photon absorption happens to generate PI radicals. Finally, the diffusion constant D_{PI*} controls how far the PI radicals move around, which eventually determines the dimensions of the waveguides. The effect of D_{PI*} is clear when we compare poly-DVB waveguides with poly-phenylacetylene waveguides [121]. In the poly-phenylacetylene system, the small-molecule monomer (molecular weight 102 g/mol) also serves as a PI, which has a relatively larger D_{PI*} resulting in a waveguide width of 1.3 µm. In contrast, the OXE 02 used in this work as a PI is a much larger molecule (molecular weight 412 g/mol), so its D_{PI*} is much smaller yielding waveguides roughly 0.5 µm wide. In a mixed PDMS/DVB system, the nonlinear refractive index is mainly of electronic origin, which usually falls within the order of 10^{-15} cm^2/W. This would project to a refractive index change on the order of 0.001 at the writing focus. In contrast, the refractive index change after polymerization often saturates at the level of 0.1 (refractive index difference between the resulting polymer and the monomer) and increases over time during the laser irradiation. Thus, beam collapse and material damage can happen at any intensity above the polymerization threshold. This is well manifested in the fabrication of phenylacetylene waveguides. Indeed, the good quality of fabrication demonstrated in the present work benefits largely from the lower refractive index contrast. In theory, the self-focusing can be balanced with a well-controlled motion speed during fabrication, which is currently in practice. However, due to the nonlinearity the intensity can grow exponentially at small disturbances, and material homogeneity plays a key role in minimizing the fabrication defects.

Unlike poly-phenylacetylene, which features extensive conjugated carbon-carbon double bonds, poly-DVB is joined with mostly single bonds in the backbone. We thus expect that poly-DVB is mostly non-absorptive like polystyrene. In the waveguides constructed with poly-DVB, the transmission properties would be Rayleigh scattering-dominated in the visible band due to the molecular weight fluctuation in the resulting poly-DVB. This is precisely confirmed by the slope of −4 in the double-track waveguides in Figure 4.9 (b). The transmission loss of triple-track waveguides follows slope −4 in the shorter wavelength region but drops quicker than −4 in the longer wavelength region, which could indicate a constructive interference or resonance condition created by the more complex and larger structure. On the other hand, the high, achromatic transmission loss in the single-track waveguides suggests that their dimension may be below a threshold for low-loss transmission [143], with a significant mode area outside the waveguide core. It also further confirms the non-absorptive nature of poly-DVB in the relevant spectral band. Despite their lossy characteristics, we expect the single-track waveguides to be highly relevant and applicable in constructing photonic sensors.

In our experiments, the fabrication was performed in the open air with dissolved oxygen present in the system, which is a well-known polymerization retarder for styrene-type systems [144], although not an inhibitor. Oxygen is also a major quencher of many photoinitiators. This is manifested by the requirement of a relatively high concentration of PI during the fabrication and the much lower refractive index contrast compared with poly-phenylacetylene waveguides. Thus, potentially significant improvements in the refractive index contrast may be attained through the use of nitrogen- or argon-purged DVB in an air-tight chamber during the fabrication, although the defects due to beam collapse will also be on the rise. This calls for a scheme of closed-loop laser intensity control based on the status of polymerization in the fabrication system.

4.5 Summary

In this chapter I demonstrated the fabrication of submicron poly-DVB waveguides in PDMS through two-photon direct laser writing. Our characterizations indicate a refractive index contrast of 0.005 and a relatively high transmission loss of 13 dB/cm on average, which is nearly achromatic within the spectral band of 535–679 nm. This confirms that poly-DVB is non-absorptive in the measured spectral band while also suggests that the dimensions of the waveguide are below a threshold for low-loss transmission. We further showed that the transmission properties can be significantly improved through the fabrication of compound waveguides, each of which consists of two- or three parallel laser-written tracks in close proximity (1.2 µm). Among the compound waveguides, the double-tracks show a Rayleigh scattering-limited transmission loss spectrum, ranging from 6.5 dB/cm at 535/43 nm to 2.2 dB/cm at 710/10 nm. The transmission loss spectrum of the triple-tracks deviates from a Rayleigh-scattering regime on the longer wavelength side, ranging from 12.4 dB/cm at 535/43 nm to 0.1 dB/cm at 710/10 nm. The deviation from the Rayleigh regime is possibly a result of constructive interference due to the larger and more complex refractive index structures in the triple-track waveguides.

In the next chapter results about and the *beam propagation method* and the fabrication of poly-DVB waveguides arrays for cochlear microendoscopy applications will be presented.

Chapter 5 Poly-DVB waveguide arrays

In this chapter, I show the fabrication of triple-track poly-DVB waveguides arrays and discuss about their imaging capabilities. I will present the main application we have targeted for the use of the polymer optical waveguides in PDMS, which are described in this thesis. Together with our project partner Sonova, we have developed an intracochlear microendoscope to be integrated with a cochlear implants (CIs), to give visual feedback to the surgeon while inserting the CI.

In order to obtain theoretical performance analyses from empirical parameters, we simulated the propagation of light in waveguide structures using the *Beam Propagation Method* (BPM). This numerical method proved to be a very useful tool for the prediction of the bundle characteristics, such as the core-to-core spacing and the total waveguide bundle length.

5.1 Polymer optical waveguide arrays for cochlear microendoscopy

The human ear is one of the most complex structures in the human body and consists of three parts: the outer ear, the middle ear and the inner ear; the cochlea is a spiral-shaped cavity and is the auditory part of the inner ear. Sensorineural hearing loss (SNHL) is the most common type of hearing loss which affects more than 10% of the population worldwide [145]. If there is a damage to the neural and mechanosensory structures inside the cochlea, or to the nerve pathways from the inner ear to the brain, SNHL can occur. A major cause of SNHL is damage to the hair cells inside the cochlea. Today, more and more people take care of their deafness diseases by means of cochlear implants (CIs, Figure 5.1). Therefore, visualization within the cochlea would help diagnose the status of the important intracochlear hearing structures.

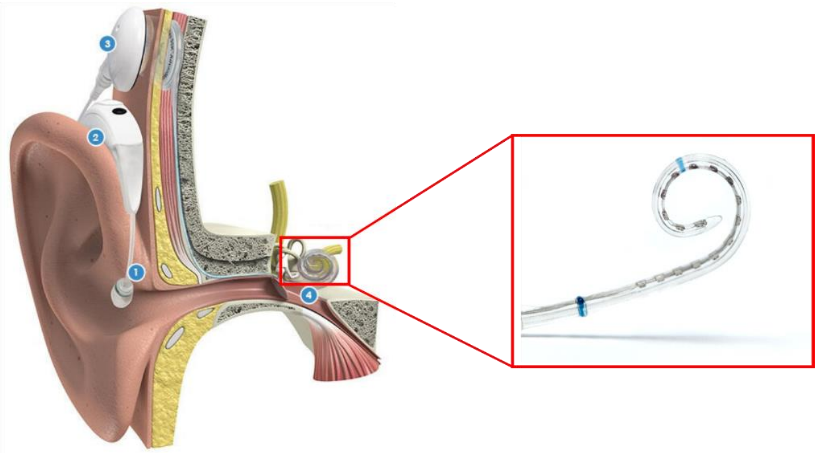

Figure 5.1 Schematic of a cochlear implant (CI) electrode array module inserted inside the human cochlea (picture taken from https://www.sonova.com/en); the red box indicates the location of the implanted CI. The CI containing the electrode array (right hand side of the figure) is made of PDMS.

CIs are medical devices able to generate auditory sensation through electrical stimulation by using an electrode array to be inserted inside one of the three spiral cochlea canal spaces. They consists of an external portion that sits behind the ear and a second internal portion that is surgically placed under the skin. An implant has the following parts:

- a microphone, which picks up the sound from the environment (1 in Figure 5.1);
- a speech processor, which selects and arranges sounds picked up by the microphone (2 in Figure 5.1);
- a transmitter and receiver/stimulator unit, which receive signals from the speech processor and convert them into electric impulses (3 in Figure 5.1);
- an electrode array, which is a group of electrodes that collects the impulses from the stimulator and sends them to different regions of the auditory nerve (4 in Figure 5.1).

However, during the implant surgery, significant damages to the inner ear, or even the total loss of the residual hearing capability of the patience can occur. The cochlear implant can be wrongly inserted, and in the worst case one of the three fragile cochlea membranes (the basilar membrane) can be damaged. The most straightforward solution is to perform the CI surgery under the visual feedback from an optical intracochlear microendoscope. To this end, during the past years, we have developed together with our project partner Sonova, the integration of an optical guidance system in cochlear implants, namely an "auxiliary" optical waveguide bundle to be embedded into the cochlear implant device, or to be placed side by side to it (Figure 5.2). The aim of this work was to implement a new procedure for the fabrication of waveguides in PDMS using multi-photon polymerization (MMP) and a very important part of the research focused on the investigation of new materials capable of yielding photopolymerization inside PDMS. We wanted to fabricate a PDMS optical waveguide bundle which would be flexible, biocompatible and that would deliver light from the outside to the inside of the cochlea and vice versa, providing an image of the inner ear. Besides biocompatibility, this challenging task includes also other key aspects which need to be taken into valuable consideration, such as the desirable high refractive index difference between the cores and the PDMS cladding. As I already mentioned in the first chapter of this thesis, the refractive index difference between cores and cladding constitutes the fundamental constrain for a good quality image reconstruction. The light information which is carried from each waveguide (pixel) needs to be delivered with minimized losses from its proximal to its distal end; moreover, the waveguide pitch must avoid cross-talk between the cores and, therefore, the reconstruction of blurred images. Most importantly, the waveguide bundle must be defect-free in all its length; the targeted length for this application using PDMS was 4 cm.

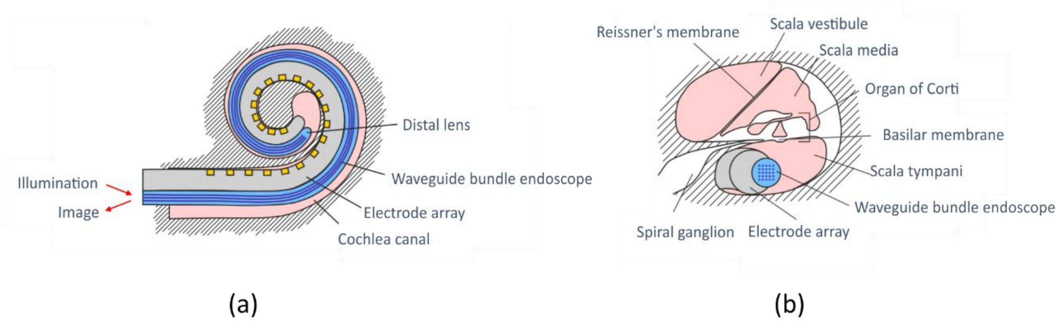

Figure 5.2 Proposed implementation of the endoscopy-assisted cochlear implant. (a) The soft microendoscope (blue structure) to be attached to a regular implant electrode array (grey structure). (b) Cross-sectional view of the auxiliary microendoscope in the scala tympani.

Intracochlear imaging is particularly challenging because of the small dimensions (<1mm) of the cochlear chambers, and their complex, spiraling structure. Taken this into account and considering the presence of the electrode array, the endoscope should be highly flexible with a diameter not exceeding 0.3 mm. At the beginning of the project, the waveguides we were planning to fabricate were around 2 µm in cross section, so that around 1900 of them could be embedded inside a 200 µm wide PDMS bundle. The refractive index contrast should be sufficient for guiding visible light at 1.25 mm curvature radius of the cochlea (Δn≥0.025), and scattering as well as absorption due to the material should be minimized (≤0.3 dB/cm). At this refractive index contrast and waveguide size, inter-waveguide coupling is negligible when the inter-waveguide distance is greater than 4 µm. All these parameters determine the properties and performance of the final waveguide bundle, and therefore are critical for achieving a microendoscope that works efficiently. Particular attention must be given to the waveguiding losses that result from absorption, the maximum bending curvature at which loss can be tolerated with a certain refractive index, and the crosstalk between the waveguides due to coupling. The fabrication of the waveguides represented the most critical challenge in this project.

5.2 Beam propagation method

In order to get theoretical response from the refractive index difference measurement ($\Delta n_{core-cladding}$=0.005) and from empirical observations, we simulated the behavior of light propagating in the waveguide structures, using the *Beam Propagation Method* (BPM). The BPM numerically simulates the propagation of wavefronts under the slow varying envelope approximation [65], predicting the value of the complex field at any point in the light propagated volume. It is a very important tool for the estimation of the bundle performance, such as the core-to-core pitch, and the multicore fiber bundle length.

Any light wavefront can be expressed as a linear superposition of plane waves, and the Fourier Transform of an optical field which has propagated until a distance z relies on the so called *initial value solving problem.* Light obey to the Maxwell's equations (Appendix 1), which can be manipulated to find the Helmholtz equation, which I report here for the sake of completeness:

$$\nabla^2 \boldsymbol{E} = \mu\varepsilon \frac{\partial^2 \boldsymbol{E}}{\partial t^2}$$

Equation 41 Helmholtz equation.

Equation 41 is valid for homogeneous media. If we consider the x-component of the optical field travelling along the z direction, we can express it using the slow varying envelope approximation:

$$E_x(x,y,z,t) = A(x,y,z)e^{j\omega t}e^{-jkz}$$

Equation 42 x-component of the optical field under the slow varying envelope approximation.

where $A(x,y,z)$ is the slow varying envelope and takes into consideration only slow variations in the x,y and z directions of the field. If we plug Equation 42 into Equation 41 and we neglect the second derivative in z of the A envelope we can write:

$$\frac{\partial A}{\partial z} \cong -\frac{j}{2k}\left(\frac{\partial^2 A}{\partial x^2} + \frac{\partial^2 A}{\partial y^2}\right)$$

Equation 43 Beam propagation equation for a homogeneous medium.

with k being the wave vector. Equation 43 is the wave propagation equation for optical fields propagating in homogenous media, such as air and free space. Knowing the Fourier Transform of a function allows us to compute also the Fourier Transform of its second derivative just by multiplying it by $-k_x^2$ or $-k_y^2$. If we perform the Fourier Transform on both sides of Equation 43, we obtain:

$$\frac{\partial \tilde{A}(k_x,k_y,z)}{\partial z} = -\frac{j}{2k}(-k_x^2 - k_y^2)\tilde{A}(k_x,k_y,z) = j[\frac{k_x^2 + k_y^2}{2k}]\tilde{A}(k_x,k_y,z)$$

Equation 44 Fourier Transform of the beam beam propagation equation.

which leads to:

$$\tilde{A}(k_x, k_y, z) = e^{j[\frac{k_x^2+k_y^2}{2k}]}\tilde{A}(k_x, k_y, z = 0)$$

Equation 45 Fourier Transform of an optical field which has propagated at a distance z.

Equation 45 has a very powerful meaning, since it describes a more simplified way to express any optical field after having propagated a distance z. In fact it describes the Fourier Transform of any optical field at a distance z as proportional to the Fourier Transform of the field in z=0, multiplied by a quadratic phase factor. The Fourier Transform turns to be an extremely powerful tool because it avoids mathematical calculations using the second derivatives of the optical field, and this can be easily implemented using Matlab or Python. The beam propagation method we used takes into consideration the symmetrized *Split-step Fourier* method (SSF) [65]; in our simulations, the diffraction step described by Equation 45 is divided into two identical propagation steps. Once the propagation step is computed, we can back Fourier transform the result and find the complex optical field at the propagation distance z.

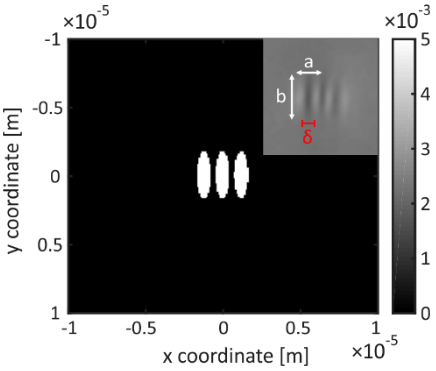

Figure 5.3 Triplet waveguide refractive index distribution with Δn=0.005, minor axis a=0.9 µm, major axis b=3.5 µm and δ=1.2 µm.

The computation of the refractive index distribution is a critical parameter since it is directly related to the phase term of the complex field at each propagation step during the BPM simulation. Figure 5.3 shows the refractive index distribution of a triplet DVB waveguide, composed of three individual elliptical cores having the minor axis a=0.9 µm, the major axis b=3.5 µm and an inter-core spacing δ=1.2 µm; the refractive index difference is Δn=0.005. Considering our physical input emitted from a 633 nm wavelength HeNe laser (Figure 5.4 (a)), we have computed a 1.4 µm FWHM Gaussian beam to match it as close as possible, as shown in Figure 5.4 (b). Transversal (green dashed line) and longitudinal (yellow dashed line) cross-cut profiles have been used to evaluate the similarity with the simulated x and y Gaussian beam profiles, as depicted in Figure 5.4 (c) and (d).

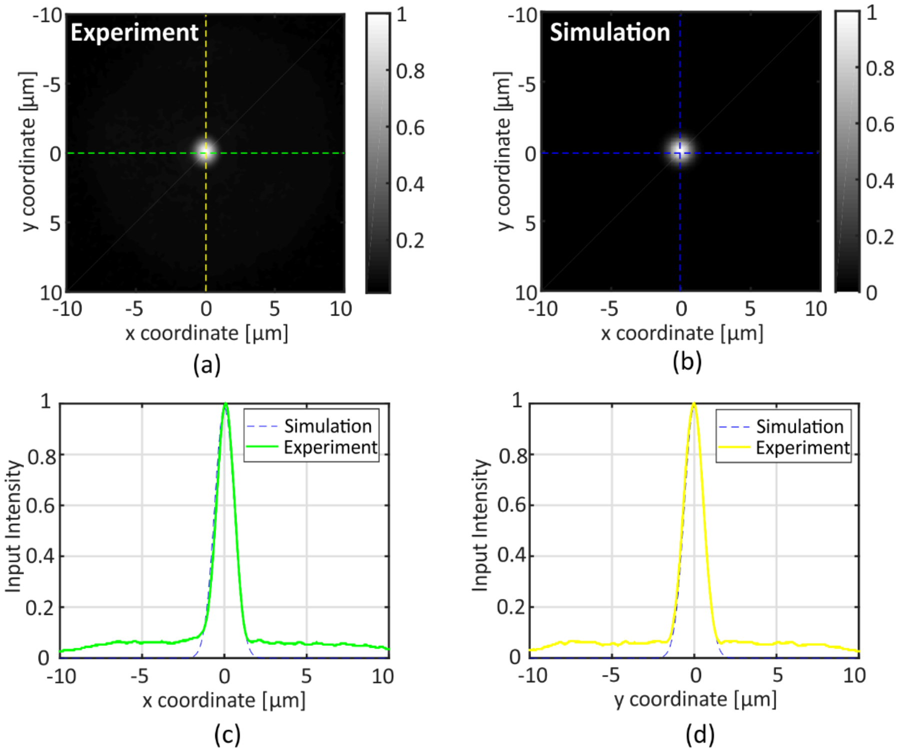

Figure 5.4 Physical (a) and simulated (b) 1.4 µm FWHM Gaussian beam profile at λ=633 nm. Green and yellow dashed lines indicate the transversal and longitudinal profiles traced in (c) and (d), respectively.

5.2.1 Cross-talk simulations and verification

To predict the cross-talk between triple-cored waveguides, we have simulated the propagation of the computed Gaussian beam shown in Figure 5.4 (b) over 2 cm propagation length; we have coupled it into the central waveguide belonging to a 3 x 3 waveguide matrix, at four different waveguide pitch D, namely 5 µm, 10 µm, 15 µm and 20 µm. The first column of Figure 5.5 shows the refractive index distribution of the 3 x 3 triple-cored waveguide arrays at the different pitches D; the second and third columns display the yz propagation profiles and the output fields, both in linear scale. The results from BPM well reflect the theoretical prediction, according to which the cross-talk decreases at increased waveguide spacing D. Considering our experimental observations as well, we have set the pitch D to be 20 µm.

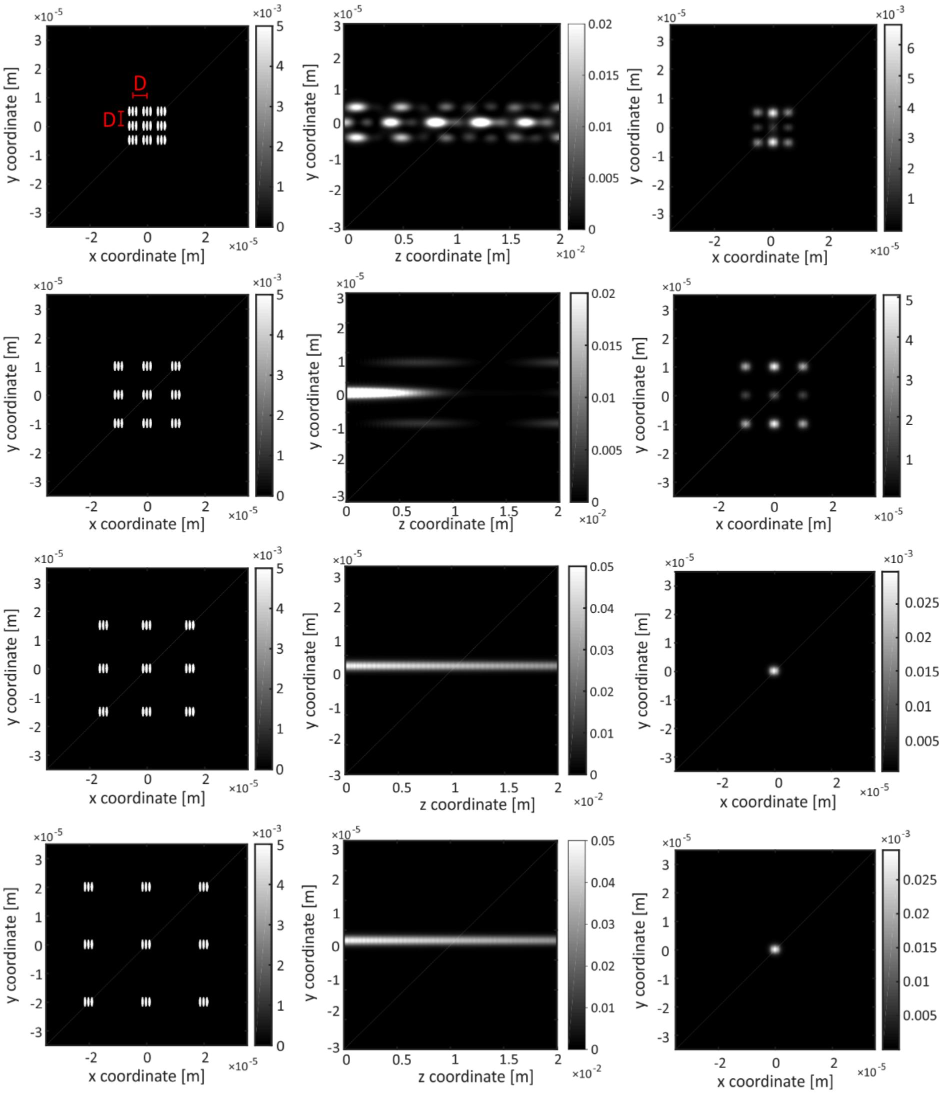

Figure 5.5 BPM simulations of cross talk taking place when a 1.4 µm FWHM Gaussian beam at 633 nm is coupled into the central waveguide of 6 x 6 triplet waveguide arrays. The first column displays the refractive index distribution at four different waveguide pitch D, namely 5, 10, 15 and 20 µm. The middle and third column show the yz propagation profiles and the output intensity in linear scale, respectively. The propagation length is 2 cm.

Figure 5.6 (a) shows the experimental coupling of a 633 nm HeNe laser having 1.4 FWHM; as we can see from the transversal and longitudinal profiles traced along the blue and red dashed lines in (a), mild cross-talk still takes place at D=20 µm (Figure 5.6 (b)).

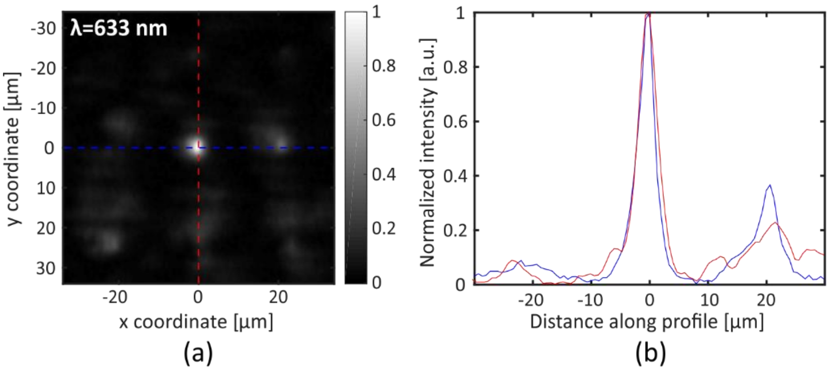

Figure 5.6 (a) Output intensity from a 3 x 3 poly-DVB triplet waveguide array when a 633 nm HeNe is coupled to the central waveguide. The waveguide pitch is 20 µm. Transversal (blue) and longitudinal (red) normalized output profiles.

5.3 Poly-DVB waveguide bundles

The DVB+Irgacure OXE02 chemical scheme drastically improved the yield of waveguide fabrication and enabled the production of full and long waveguide bundles. Because of the presence of the photoinitiator (Irgacure OXE02), we have observed the writing process to be more stable and successful, if compared with the photoinitiator-free approach that we first demonstrated using phenylacetylene. The photoinitiator-free procedure allowed for no longer than tens of mm-long fiber bundles and caused damages in the material, which is the reason why we explored new chemical schemes. To pilot the waveguide bundle fabrication using DVB and Irgacure OXE02, we extensively explored the possible combinations of irradiating laser intensity and writing speed in order to avoid material damage at a sample length of 4 cm. We have fabricated waveguide bundles for both types of waveguides I have introduced in Chapter 4, double- and triple track. In order to do so in an automatic fashion, we implemented a Matlab code for the writing of bundles, for any number of waveguides and length, inter-waveguide distance, core-to-core spacing and focusing depth inside the PDMS material. Triple-track waveguide bundles showed better light confinement if compared to double-track waveguide bundles at any sample length. For this reason, we mostly fabricated triple-cored waveguide bundles and explored their imaging capabilities.

We fabricated small pilot, 2 cm-long, 6×6 triple-track waveguide matrices and tested their light delivering properties for incoherent light illumination. We have used laser peak intensities at 1.29 $\times 10^{12}$ W/cm^2, 1.45 $\times 10^{12}$ W/cm^2, 1.61 $\times 10^{12}$ W/cm^2 and 1.78 $\times 10^{12}$ W/cm^2 at 3.2 mm/s writing speed. Top-view phase contrast images of integral and homogeneous bundles are shown from Figure 5.7 (a) to (d). The waveguide bundles are realized following a bottom-up fabrication approach, which firstly relies on the fabrication of the bottom waveguide layer. At 0.005 refractive index difference, the BPM simulations suggested an optimal inter-waveguide distance $\Delta y = \Delta z =$20 µm. As the mechanical, long travel range stage (UTS50CC, Newport) concludes its movement perpendicularly to the laser optical axis, the piezo stage (NPX400SG-D, Newport) moves laterally of about δ=1.2 µm (Figure 5.7 (f)) and Δy (Figure 5.7 (e)) to structure each individual waveguide core and layer set, respectively. When a single layer is finalized, the NPO250SG-D piezo stage moves the objective focus of about Δz=20 µm away from the PDMS substrate, allowing for the consecutive waveguide layer to be written in a meander-like fashion.

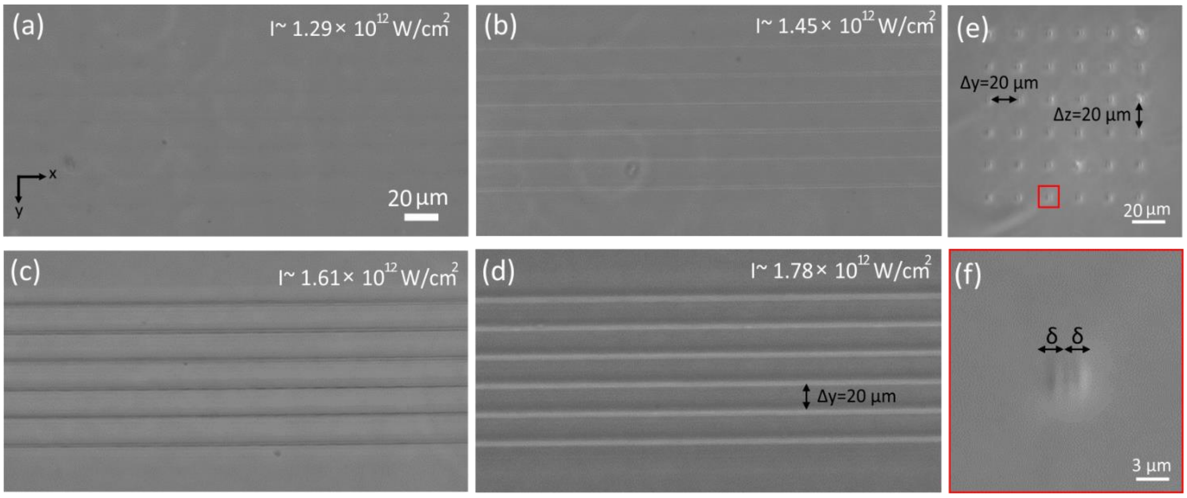
(a)
I~ 1.29× 10^12 W/cm^2
x
y
20 µm
(b)
I~ 1.45× 10^12 W/cm^2
(e)
Δy=20 µm
Δz=20 µm
20 µm
(c)
I~ 1.61× 10^12 W/cm^2
(d)
I~ 1.78× 10^12 W/cm^2
Δy=20 µm
(f)
δ δ
3 µm

Figure 5.7 Pilot 2-cm long, 6 x 6 triple-track poly-DVB waveguide bundles in PDMS written at 3.2 mm/s and 1.29 ×10^{12} W/cm^2 (a), 1.45 ×10^{12} W/cm^2 (b), 1.61 ×10^{12} W/cm2 (c) and 1.78 ×10^{12} W/cm^2 (d) laser peak intensities. The small bundles are written following a bottom-up fabrication approach: as a single layer is complete, the piezo stage moves away from the substrate of about Δz=20 µm (e), allowing for the consecutive waveguide layer to be completed in a meander-like fashion. The waveguide pitch is Δy=20 µm, while the inner core-to-core distance (δ), exemplified in the close up look red box in (f), is 1.2 µm.

To test the imaging properties of the bundles we modified the transmission loss characterization set up presented in Chapter 2, which I report in Figure 5.8 for the sake of simplicity. We substituted the high NA=0.7 input objective (OBJ1) with lower magnification ones, i.e. 10× and 20×, in order to enlarge the illumination spot size on the proximal facet of the bundles. Before placing the sample, a careful alignment of the light spot, both in transmission and reflection without the sample has been made (yellow box insets in Figure 5.8); a picture of the experimental imaging set up is depicted in the red box in Figure 5.8. The use of low magnification objectives allows for a more uniform and homogeneous light illumination, which can cover the entire proximal waveguide bundle facet.

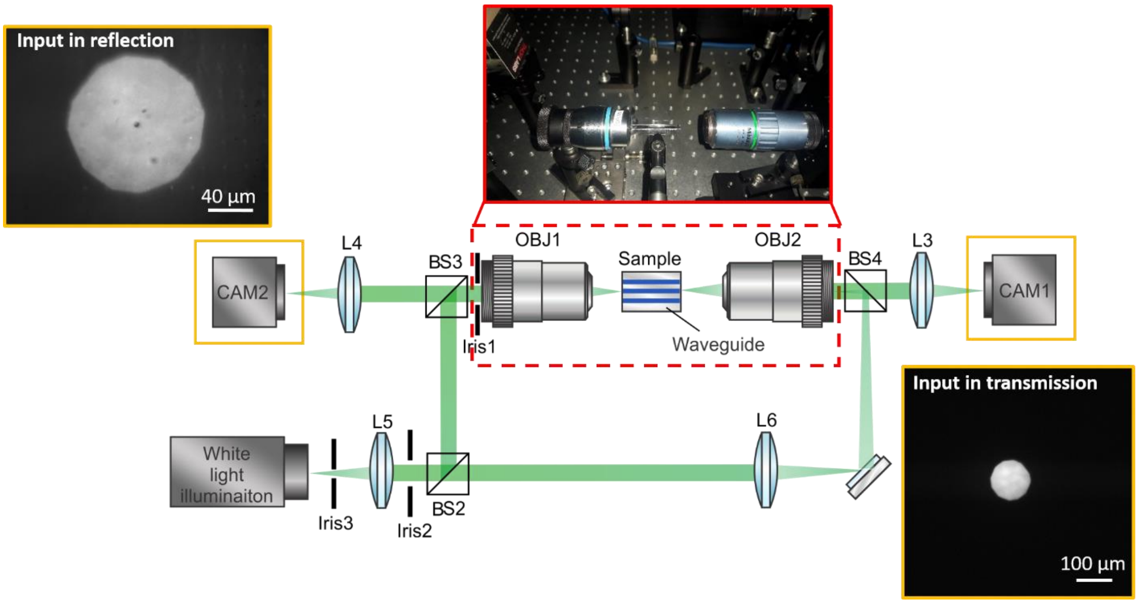
Input in reflection
40 µm
CAM2
L4
BS3
Iris1
OBJ1
Sample
Waveguide
OBJ2
BS4
L3
CAM1
Input in transmission
100 µm
White light illuminaiton
Iris3
L5
Iris2
BS2
L6

Figure 5.8 White light illumination coupling set up for pattern delivering tests. A careful alignment of a Newport, NA=0.4, 20× magnification has been done in order to enlarge the illumination spot size, which is visible in reflection (CAM2) in the top left yellow panel. Bottom-right yellow panel shows the 100 µm wide white light illumination spot in transmission on the distal camera (CAM1). The red box shows a picture of the sample being aligned with the two objectives.

L5 and OBJ1 form an imaging system with the PDMS proximal facet, having the object plane in correspondence of Iris3; therefore, it can image the iris aperture on the proximal facet of the sample, as depicted in the left hand-side yellow box in Figure 5.8. The size of the iris can be reduced or enlarged, while the sample can move in *x-, y-, and z-direction*. The beam splitter BS2 lets half of the white light illumination passing through, and allows for fine focusing of the waveguide cores in transmission from their distal side, and imaging them on the proximal camera (CAM2). Once the proximal side is in focus, the imaging objective (OBJ2), which can move in *x-, y-,* and *z*-direction adjusts the waveguide output focus on the distal camera (CAM1). The waveguide bundle can move in all directions and the iris spot can scan the proximal surface area. Figure 5.9 (a) shows the imaged iris (Iris3) having a diameter of a 25 µm projected on the polished PDMS proximal facet; the demagnification of the imaging system using a 20× as input objective is ~30×. The light is coupled into the waveguides and an image of the iris aperture can be delivered to the fiber ends. The incoherent illumination beam can scan the sample and demonstrate, as a proof of concept, the capability of poly-DVB waveguide arrays in PDMS to deliver light and simple patterns, from the proximal to their distal end, at different coupling positions (Figure 5.9 (b) to (d)).

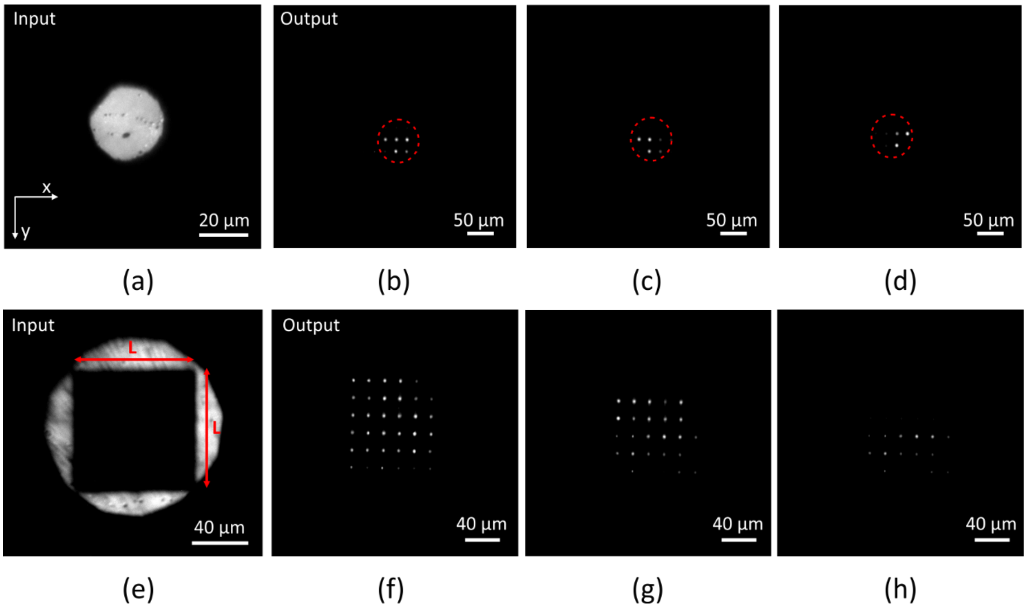

Figure 5.9 (a) A 25 µm diameter, incoherent light illumination beam is demagnified and projected on the proximal sample facet and randomly moved in *x, y*. (b), (c) and (d) show the waveguide bundle output recorded by CAM1 as the pattern is randomly moved at different coupling positions. (e) 80 µm sized square pattern from a USAF 1951 resolution chart is projected on the proximal sample facet; the pattern progressively obscures the waveguide matrix rows, while the output has been recorded on the distal camera CAM1; six (f), four (g) and three rows (h) light up.

The low resolution square pattern (L=2.5 mm shown in Figure 5.9 (e)) from a USAF 1951 target is used to obscure the rows of the small waveguide matrix, showing intensity modulation at the output (Figure 5.9 (f)-(h)). As the imaged square is moved up and down, the waveguides no longer deliver the information behaving like dark pixels in correspondence of the projected square pattern (red dashed line box in Figure 5.10).

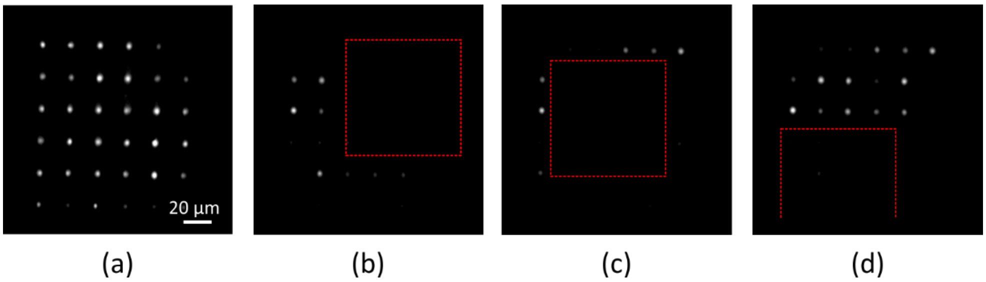

Figure 5.10 (a) Fully illuminated, 6 x 6, 2 cm-long waveguide bundle. (b), (c) and (d) show the recorded waveguide bundle output as the square pattern from the USAF 1951 resolution chart is randomly moved in *x* and *y*.

The goal of this project was to embed the waveguides into a 200 x 200 µm PDMS bundle for imaging applications. Considering the refractive index difference between cores and cladding, the waveguide spacing which has to be guaranteed in order to avoid severe cross-talk, and the latter dimensional constrain, the small waveguides could be written in a 12 × 12 waveguide matrix configuration, as shown in the phase-contrast cross-sectional image in Figure 5.11 (a) and (b).

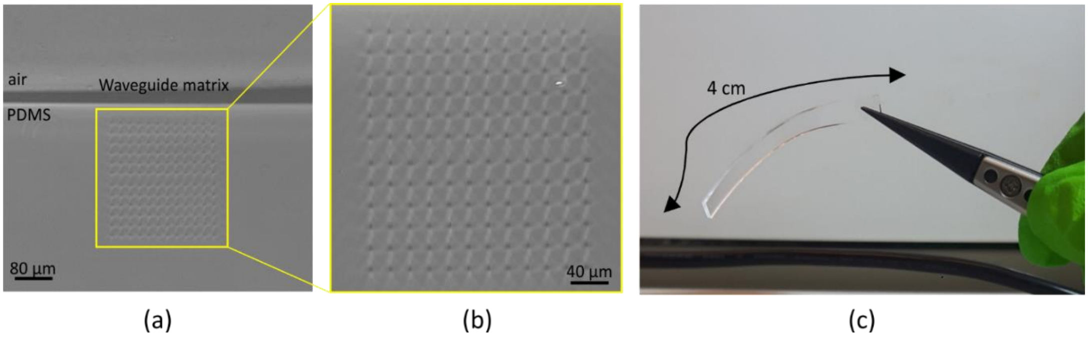

Figure 5.11 (a) and (b) show the cross-sectional phase contrast microscopy images of a triple-track, 12 x 12 poly-DVB waveguide bundle where the waveguides sit at distance $\Delta y = \Delta z =$20 µm from each other. The waveguide bundle array can be written only 20 µm below the air-PDMS interface. (c) Picture of the 4 cm long, flexible PDMS slab containing the waveguide bundle.

At the current stage of this work, it is possible to produce 4 cm-long waveguide matrices in flexible PDMS in a 12 × 12 configuration (Figure 5.11 (c)). We have simulated the propagation of a digit from the MNIST database (Figure 5.12 (a)) into a 12 x 12 waveguide bundle, having a refractive index distribution as the one exemplified in Figure 5.12 (b). Figure 5.12 (c) and (d) show the xz and yz propagation profiles along 2 cm propagation length, respectively, while (e) and (f) display the output intensity profiles after 2 and 4 cm propagation distance. The illumination wavelength was set to be the central and strongest spectral component emitted from our incoherent light illumination, which is 600 nm.

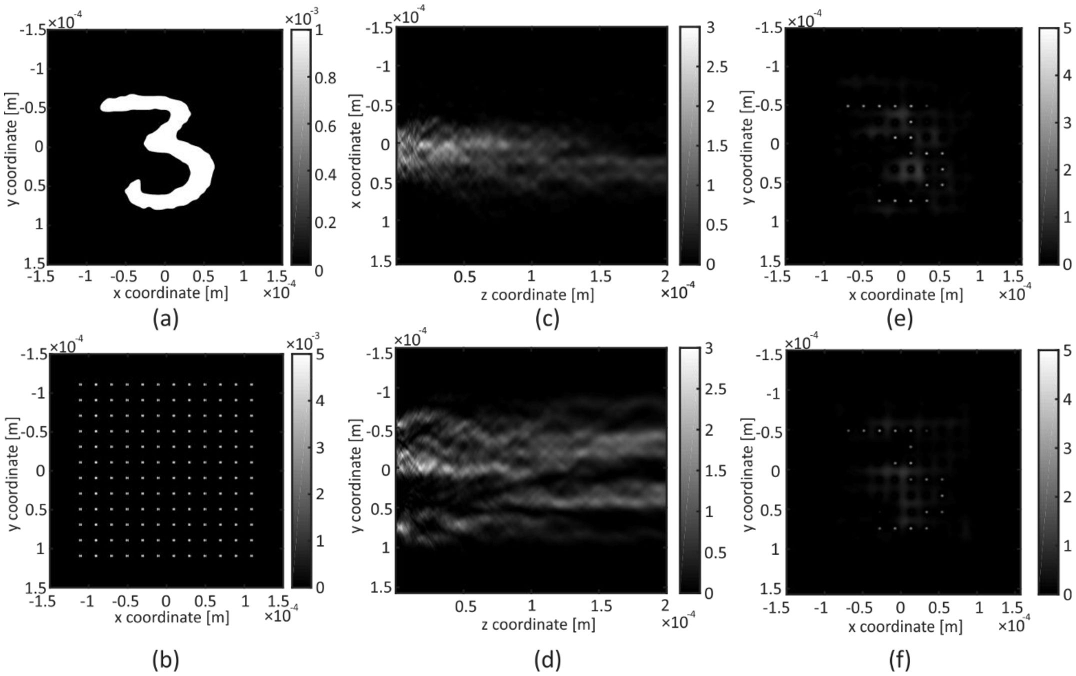

Figure 5.12 Input from the MNIST database (a) and refractive index distribution of a 12 x 12 poly-DVB waveguide bundle (b). x,z (c) and y,z (d) propagation profiles along 2 cm propagation length at 600 nm wavelength. Output intensity profile after 2 cm (e) and 4 cm (f) propagation length.

Considering the refractive index difference we were able to achieve and the waveguide spacing, we believe these type of waveguide bundles could reconstruct image patterns by means of *deep neural network* (DNN) techniques. This, together with a deeper investigation of other chemical compounds represent the most interesting aspect to be explored to further investigate the potentials of polymer waveguide bundles in PDMS for imaging applications.

5.4 Intracochlear endoscope module

CIs are made of PDMS, which ensures biocompatibility with the human ear and mechanical flexibility; from here the need for the implementation of a microendoscope which would be compatible with the already existing CI, and at the same time with the surrounding environment. The used materials should be nontoxic and should not be harmful to human beings in the short- or long-term. The waveguide-bundle endoscope is required to work bidirectionally; it should provide illumination at the tip of the electrode array and image the illuminated area at the distal side, thanks to a ball lens accommodated at its distal tip. A schematic of the intracochlear endoscope module with the CI is depicted in Figure 5.13. It comprises the conventional PDMS bundle containing the electrode array with contacts and wires, the PDMS waveguide bundle to provide an image of the inner ear, a ball lens to collect and focus the light onto the small waveguide distal ends, and a sensor connected to a computer to collect the image from the polymer fibers.

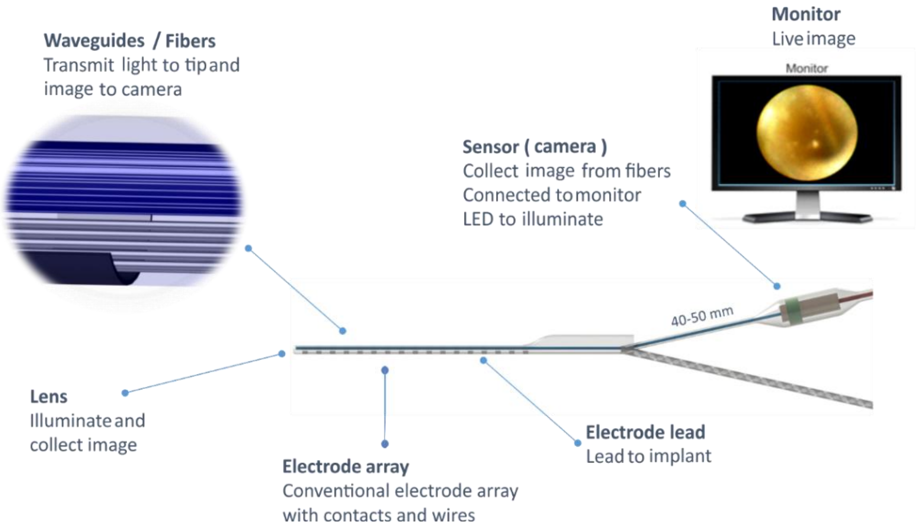
Waveguides / Fibers
Transmit light to tip and image to camera
Monitor
Live image
Monitor
Sensor (camera)
Collect image from fibers
Connected to monitor
LED to illuminate
40-50 mm
Lens
Illuminate and collect image
Electrode array
Conventional electrode array with contacts and wires
Electrode lead
Lead to implant

Figure 5.13 Cochlear implant module with polymer waveguide bundle endoscope.

5.4.1 Intracochlear endoscope implementation

Several EPFL-Sonova AG joined meetings took place during the past years leading to fruitful discussions. The overall endoscope system (cross-sectional CAD design in Figure 5.14) consists of:

1. Lens
2. Lens-waveguide spacer
3. Waveguide bundles
4. Light-guide
5. Imaging cylinder with PDMS lens
6. Light-guide cylinder and camera PDMS pocket
7. Camera

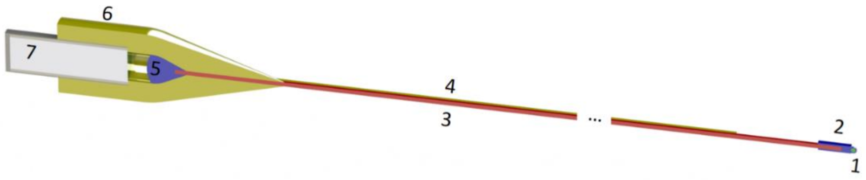

Figure 5.14 Endoscope prototype cross-section.

We outlined together a common guideline for the endoscope system development, which mainly consists of six steps and which are depicted in Figure 5.15. Briefly, a PDMS matrix is cured in a 200 µm x 200 µm x 5 cm long rectangular shape and exposed to the laser focus according to a specific structuring pattern for the waveguides writing. After the waveguides matrix is written (steps 1/2), the PDMS waveguide bundle is coated by means of metal sputtering and molded for the creation of the light delivering sides (3). The ball lens camera molding can be done (4), according to the required specifications, which have to take into account some parameters as for example the distance between the distal end of the endoscope and the curvature of the lens on the optical axis. The next step is characterized by the integration of the camera (5), which we identified to be a Fiscam CMOS from FISBA SA. The final step (6) shows the molding and the assembly of the PDMS cylinder for the integration of the camera.

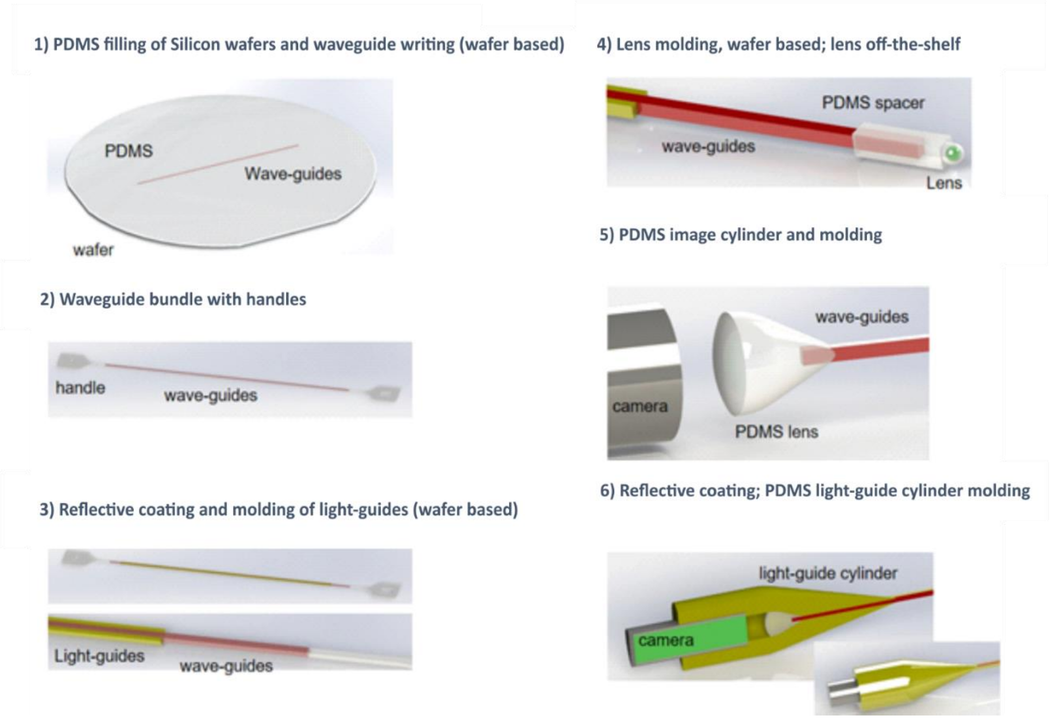
1) PDMS filling of Silicon wafers and waveguide writing (wafer based)

2) Waveguide bundle with handles

3) Reflective coating and molding of light-guides (wafer based)

4) Lens molding, wafer based; lens off-the-shelf

5) PDMS image cylinder and molding

6) Reflective coating; PDMS light-guide cylinder molding

Figure 5.15 Endoscope prototype fabrication steps.

5.4.2 Stepwise manufacturing based on casting and injection Silicon dioxide wafer molds

As we discussed in the previous paragraph, we opted for a stepwise manufacturing of the endoscope prototype using silicon dioxide wafer-based casting molds and injection molds. Four different molds were needed throughout the steps of the endoscope prototype fabrication, and they are shown in Figure 5.16 (Appendix 4 presents the complete schematic of the lithographic process flow for the fabrication of the wafers).

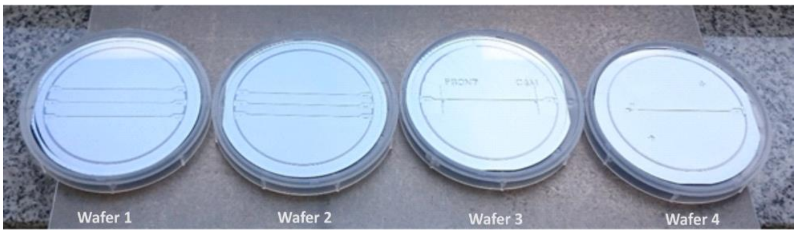

Figure 5.16 Silicon and Silicon dioxide wafer molds to be used for the endoscope prototype fabrication.

Using these wafers the entire process of casting and assembly has been tested at Sonova by producing endoscope dummies without waveguides. All PDMS structures casted in the wafers had the desired dimensions and the work flow of the stepwise production worked as intended. For the sake of clearness and completeness, I report hereafter a more detailed version of the process flow which comprises the use of the Silicon and Silicon dioxide wafers we have fabricated (Figure 5.17):

a) Liquid PDMS is gently deposited with a syringe to fill the 200 µm x 200 µm x 5 cm long grooves into Wafer 1; PDMS needs to be degassed to ensure no air bubbles would interfere with the waveguide writing;
b) After PDMS is cured, the wafer can be accommodated into a custom made stainless steel container. The container we designed is sealed in order to guarantee the monomer would not evaporate during the waveguide fabrication procedure;
c) After the waveguide matrix is structured, the bundle can be now removed from Wafer 1 and metal can be sputtered to create a reflective layer to guide light efficiently; a sputtering recipe consisting in a low oxygen plasma treatment, 5 nm Ti and 25 nm Au sputtering leads to a homogeneous metal layer with minimized cracks and good mechanical adhesion. We did not further investigate the optical and mechanical performances, hence this still represents a loose end to be further explored;
d) The bundle can be now deposited into Wafer 2 and PDMS can be casted to create the light guides surrounding the waveguide bundle;
e) The bundle with the light guides can be removed from Wafer 2 and placed into Wafer 3 for a precise blade cut;
f) A 200 µm diameter ball lens is manipulated by means of a holder or a vacuum gun and placed with high accuracy at the tip of the fiber bundle; PDMS can be further casted to match the refractive index of the waveguides with the one of the ball lens;
g) The PDMS cylinder can be molded;
h) Finally, the FISBA camera can be now inserted and aligned with the fiber bundle to detect the information from its proximal end.

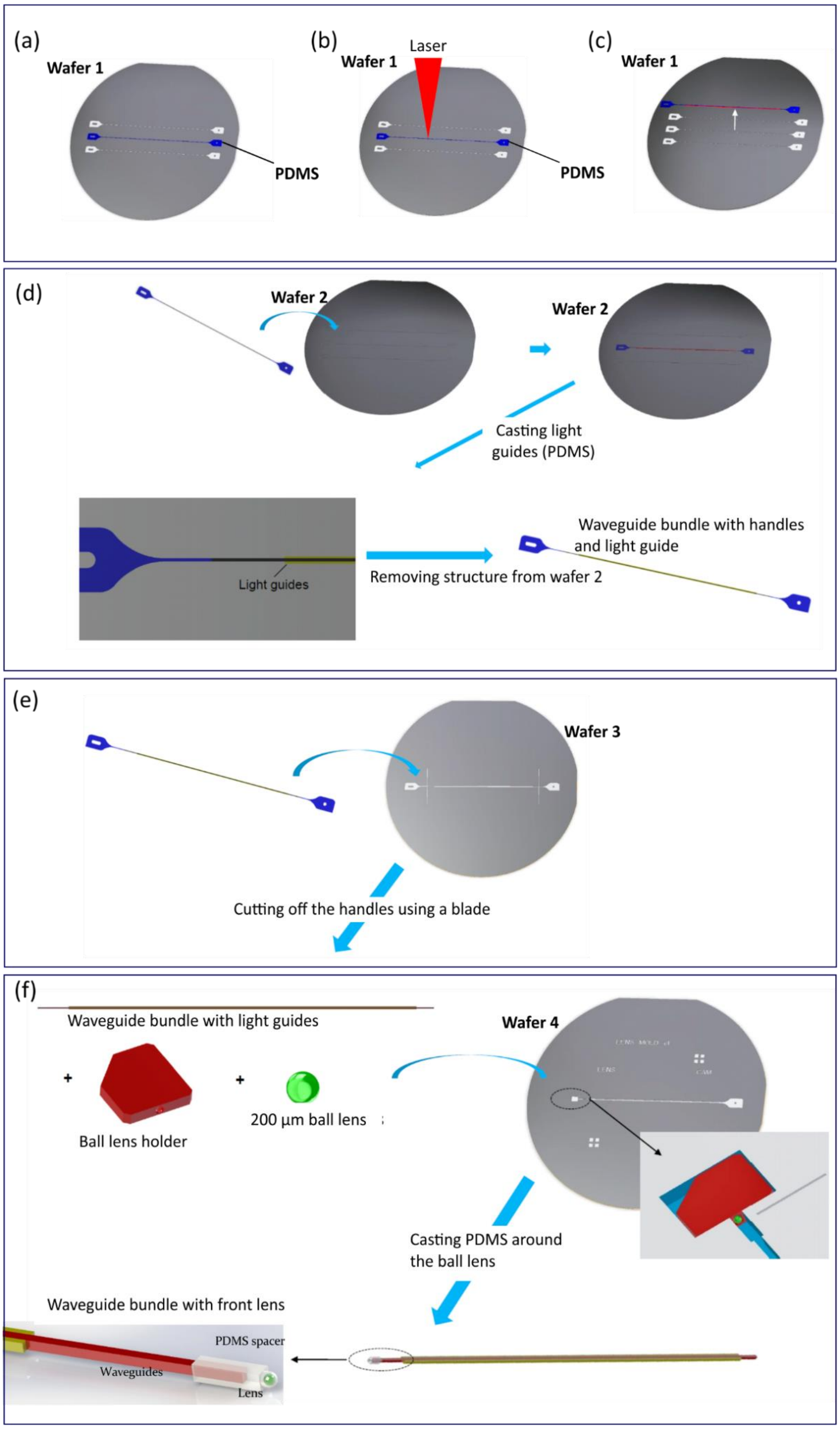
(a)
Wafer 1
PDMS
(b)
Wafer 1
Laser
PDMS
(c)
Wafer 1
(d)
Wafer 2
Wafer 2
Casting light guides (PDMS)
Light guides
Removing structure from wafer 2
Waveguide bundle with handles and light guide
(e)
Wafer 3
Cutting off the handles using a blade
(f)
Waveguide bundle with light guides
+
Ball lens holder
+
200 µm ball lens
Wafer 4
Casting PDMS around the ball lens
Waveguide bundle with front lens
PDMS spacer
Waveguides
Lens

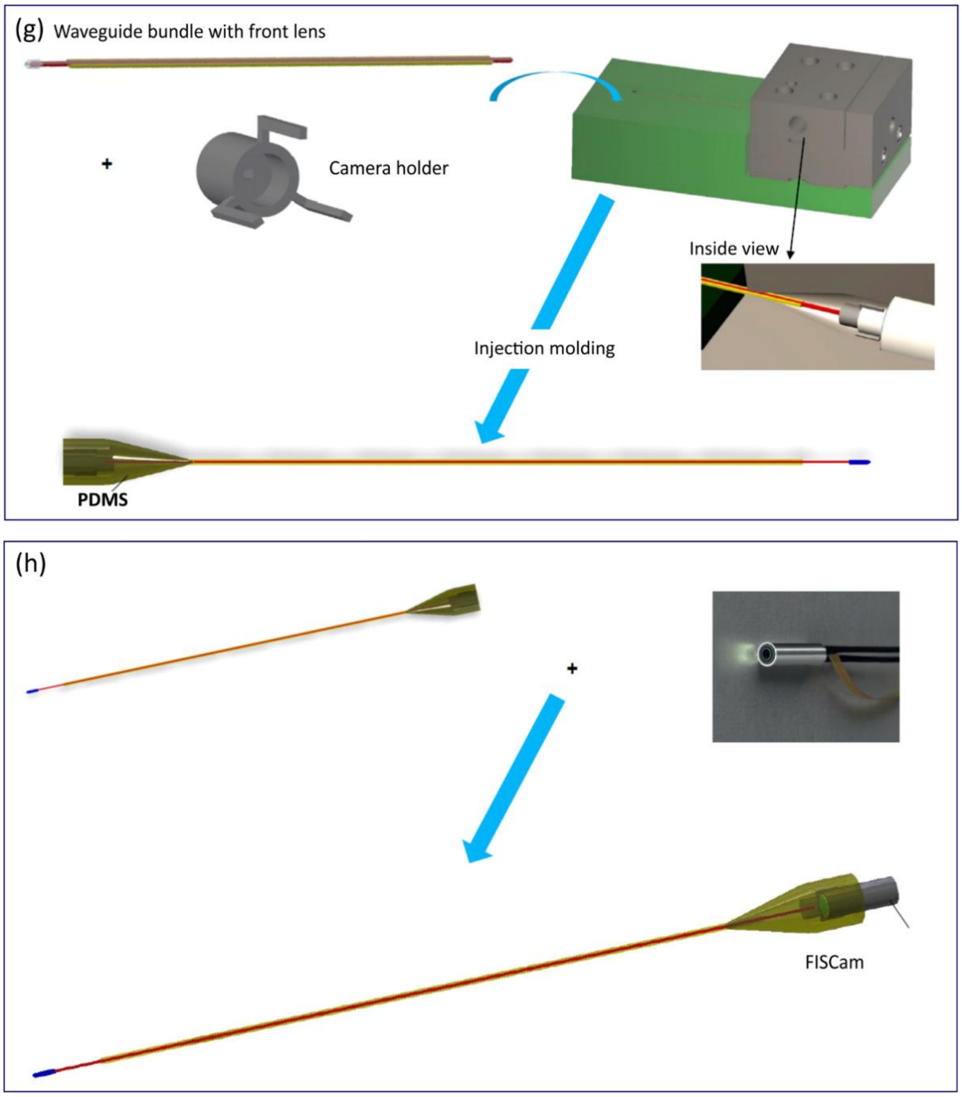

Figure 5.17 Detailed process flow for the fabrication of the waveguide bundle endoscope, using the Silicon and Silicon dioxide wafers as molds.

Ideally, the simplest and most cost-effective solution to attach a lens to the distal end of the endoscope is by molding it directly in PDMS. However, given the low refractive index of the particular type of PDMS we use in this project (n = 1.41) compared with that of the surrounding intracochlear fluid (n ~ 1.33) during operations, such molded lenses results in an insufficient focusing power and thus a very narrow field of view. Therefore, we proposed to use high-refractive index ball lens. Polymers of high refractive index often involve chloro, bromo, or sulfonyl functional groups, which could raise biocompatibility concerns. Therefore, ball lenses of inorganic materials such as lanthanum flint glass (n = 1.5-2.0) and cubic zirconia (n = 2.0) became possible choices, because these materials demonstrate a high degree of biocompatibility. Figure 5.18 shows the scheme of the waveguide bundle with the integrated ball lens at its distal end. This schematic shows an example result based on a ball lens of n = 1.55 and an object distance of 5 mm, where the field of view is 16°. By choosing a ball lens of different refractive index, the field of view can be configured from 36° to 125°. During the course of the project, we identified cubic zirconia ball lenses (n = 2.17) with a diameter of 200 µm from Sandoz to be a good choice for our purpose.

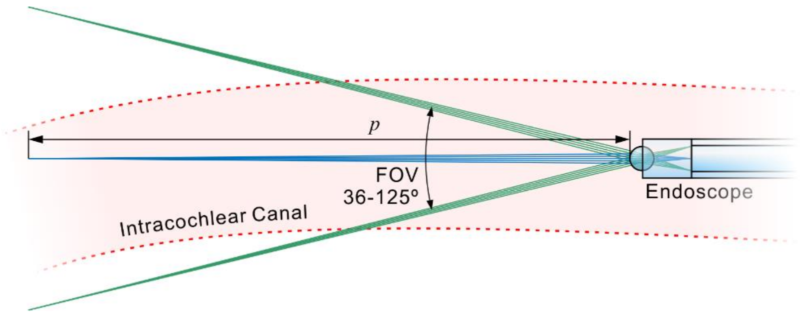

Figure 5.18 Example of ray tracing simulation results of the imaging ball lens for the endoscope. Through the choice of different refractive index of the ball lens, a large range of field of view (FOV) is enabled; p represents the distance from the object plane.

5.4.3 Conclusions and future work

The fabrication procedure of the PDMS waveguide bundle reached a very good stage thanks to the synergic work of both collaborating partners, EPFL and Sonova. In order to meet all the requirements for the successful functioning of the waveguide bundle prototype, the refractive index contrast between the waveguide cores and the PDMS cladding for guiding visible light at 1.25 mm curvature radius should be $\Delta n \geq 0.025$, exhibiting a transmission loss not greater than ≤0.3 dB/cm. As I reported in Chapter 3 of this thesis, the phenylacetylene monomer satisfied these requirements very well, showing Δn=0.06 and a transmission loss of 0.03 dB/cm in the spectral range of 650 – 700 nm. Unfortunately, the photoinitiator-free approach we have proposed didn't allow for the fabrication of 4-cm long waveguides without defects, which was the targeted length for cochlear endoscopy. On the other hand, the poly-DVB waveguides we have fabricated didn't match the requirement of high refractive index contrast and low loss.

A better control on the phenylacetylene polymerization process by means of a feedback control closed loop to regulate the peak intensity of the laser during the waveguide writing would allow for a successful fabrication of long poly-phenylacetylene waveguides, making possible the realization of a functioning cochlear microendoscope device.

5.5 Summary

In this chapter I have introduced the beam propagation method (BPM) as a very useful tool to evaluate the propagation of a complex optical field in a homogeneous medium. We have implemented the computational environment for the simulation of DVB triple-cored waveguides, and simulated the cross-talk over 2 cm propagation length. Moreover, to better understand the imaging capabilites of these types of bundles, we have simulated the propagation of simple patterns through 2- and 4-cm long straight waveguide bundles at 600 nm wavelength.

We have demonstrated the fabrication and imaging capabilities of small pilot 6 x 6, 2-cm long poly-DVB waveguide bundles by delivering simple patterns with incoherent light illumination. Considering a refractive index difference Δn= 0.005, and the goal of a 200 x 200 µm x 4 cm microendoscope device proposed in this chapter, the triple-track waveguides can be written in a 12 x 12 configuration, at an optimal inter-waveguide distance $\Delta y = \Delta z =$20 µm. Thinking of the refractive index difference we were able to achieve and the waveguide spacing, we believe it can be possible to reconstruct image patterns by means of DNN techniques.

In the next chapter, I am going to describe the fabrication of step-index (STIN) polymer waveguides using an alternative and commerical LDW platform, the Nanoscribe GmbH Photonic Professional GT+.

Chapter 6 Fabrication of waveguide bundles using a commercial 3D printing system

In this chapter, I am going to present the methodologies we have developed for the fabrication of polymer rectangular step-index (STIN) optical waveguides using Nanoscribe, a commercial three dimensional (3D) printing system developed by Nanoscribe GmbH, and IP-dip, a commercial photoresist from Nanoscribe GmbH. In this project, we have performed a full calibration of the experimental parameters in order to quantify the refractive index difference between low and high exposure regions for the creation of light guiding structures using IP-dip as a resist. Moreover, we have implemented a printing procedure for the fabrication of µm-sized multicore waveguide bundles, tested their imaging capabilities and implemented a *deep neural network* (DNN) algorithm for the reconstruction of images of digits.

This work serves as a comparison with the previously reported poly-phenylacetylene and poly-divinylbenzene waveguides in PDMS, and offers food for thoughts for the future work regarding the 3D microfabrication of high refractive index difference waveguides in polymer materials by means of LDW.

6.1 Introduction

The sought after the constantly increasing complexity of integrated photonics and the need for flexible hybridization of functionalities among the various technological additive manufacturing platforms has become a very important aspect in the research field of 3D printing. Also, companies that are experts in this field have recently undergone a fast development, coming up with solutions that turned to be helpful for the fabrication of innovative miniaturized 3D components. Nanoscribe GmbH (Photonic Professional GT+) is a commercial 3D direct-laser writing system based on two-photon polymerization of fine engineered photoresists, offering nm-sized resolution, high motion precision and a good variety of standardized processes for the fabrication of several kinds of micro components. Therefore, additive manufacturing by multi-photon direct laser writing using the Nanoscribe technology has become an essential submicron-scale technique for the fabrication of miniaturized three-dimensional optical elements such as micro-objectives [54], lenses [146-148] and metalenses [149], low loss fiber-to-chip couplers [150], and other free-from coupling elements for photonic integration [151]. Because of its high accuracy and precision [152], as well as its user friendly interface, it became also possible to print directly on top of optical fibers [153-157], overcoming the delicate procedure of light coupling efficiency maximization. However, as it will further described in the next section, the Nanoscribe system presents a limited travel range of the motion stages integrated into the optical apparatus, and therefore it suits particularly well the fabrication of spatially confined microstructures. Nevertheless, several works have explored its potential for the realization of spatially extended components, such as polymer connections in photonic wire bonding applications [31, 158], optical waveguides [148, 159] and hollow-core light-cage systems [160, 161].

As described in the previous chapters of this thesis, we have investigated new photoactive compounds for the fabrication of high refractive index difference optical waveguides embedded in PDMS. Moderate to high refractive index difference between core and cladding, as well as good light transmission capabilities have been shown, opening a new scenario on the possibilities offered from PDMS chemical loading approaches, and out-of-the shelf materials usage. However, to the best of our knowledge, the study and a full parameters calibration of the commercially available Nanoscribe tool for waveguides fabrication has not been reported yet, and this topic is extremely important for any printing design, including optical waveguides.

As already mentioned above, the Nanoscribe printing apparatus presents optimal printing precision and efficient photopolymerization is always guaranteed; still, there are some limitations in terms of sample dimension, laser source tunability and software constrains that are not easily addressable. More specifically, at the highest printing resolution configuration, using the 63x magnification objective and IP-dip as the photoresist, no more than 300 µm-sized structures can be printed in the lateral (x-y) and axial (z) dimension by redirecting the beam by means of piezo stages and galvo mirrors. Furthermore, the acrylate-based photoresists provided by Nanoscribe show their maximum two-photon absorption efficiency at 780 nm and the laser beam wavelength cannot be changed, limiting the flexibility of the whole apparatus. The investigation of the potentials of this commercial tool still represents an interesting topic to explore, considering the intense studies that are now focused on the maximization of the refractive index difference in the 3D-printed microstructures.

In this chapter I will show a full calibration of the printing parameters, such as motion speed and laser power, as well as stitching, hatching and slicing distances, identifying the optimal parameter range for the fabrication of rectangular step-index (STIN) optical waveguides and STIN multi-core fiber bundles using a commercial 3D direct-laser writing system from Nanoscribe GmbH (Photonic Professional GT+).

6.2 Nanoscribe apparatus

The Nanoscribe Photonic Professional GT+ system (Figure 6.1 (a)) consists of two main parts: the optical set up and the user interface desk. A femtosecond erbium-doped fiber pulsed laser (80 MHz, 100 fs pulse width) with the center wavelength at 780 nm is directed through optical components in an optics cabinet placed on the optical breadboard. The laser is fully integrated into the 3D printing system containing galvo mirrors and piezo stages for sample motions; additionally, the 3D printer comprises an inverted microscope (Carl Zeiss Axio Observer), for monitoring the beam focus during the photopolymerization of the resin, thanks to fluorescence. A transmission/reflection LEDs system illuminates the sample substrate and allows for good imaging quality during the printing procedure. The motion of the stages can be controlled whether from a touchscreen present on the work desk, or by the dedicated *NanoWrite/DeScribe* software programming.

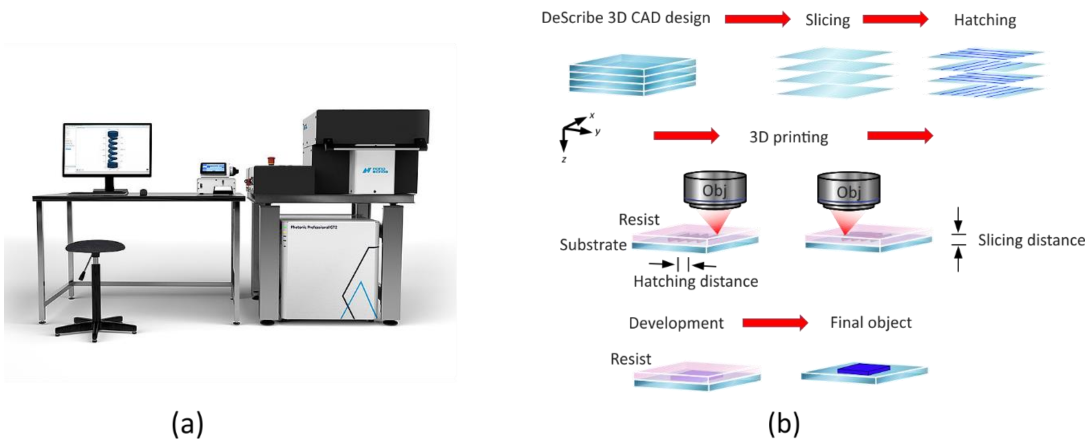

Figure 6.1 (a) Nanoscribe GmbH (Photonic Professional GT+) 3D printing system (ref: www.nanoscribe.com). (b) 3D printing process workflow: a CAD design is created using the DeScribe and imported into the NanoWrite software. Before the commencement of the process, the software slices it into horizontal and vertical layers (slicing and hatching). The laser scans the trajectory traced by the CAD design until the final object is polymerized into the photoresin. When the 3D printing is finalized, the sample is developed by immersing it into poly(glycidyl methacrylate (PGMEA) and isopropanol for about 17 and 5 minutes, respectively.

The lithographic printing system workflow (Figure 6.1 (b)) encompasses the creation of a proprietary *General Writing Language* (GWL) format file to print structures, which can be handled, modified and imported from *Standard Tessellation Language* files (STL) generated from most CAD applications. Once this step is complete, the files can be loaded and compiled using NanoWrite. GWL-files describe the trajectory that the laser focus will have to follow during the printing, and configures the experimental parameters to be set during the writing process, such as laser power and motion speed of the stages (in galvo or piezo configuration). This type of files can be generated and/or modified in any text editor, and Nanoscribe owns its proper one: DeScribe.

DeScribe is a coding environment where syntax errors can be highlighted, offering a user friendly 3D rendering window where the final structures can be displayed, estimating the time that is needed to finalize the printing. The *hatching distance* consists of the maximum x-y voxel displacement imprinted by the galvo mirror tilt, resulting in the separation at which different regions of the material are polymerized. After a slice is printed, the piezo stage moves to the upper one, increasing the distance between objective and substrate, and the printing trajectory can be further executed. Thus, the distance between the slices is called *slicing distance*; prior to each printing, the model is decomposed into slices, in which many parallel hatching lines are distributed. Moreover, DeScribe provides hatching/slicing algorithms which greatly help to obtain the best printing modality to be set as an input to the Photonic Professional GT+ printing tool. When the object exceeds the dimension of the printing field, the whole structure can be split into individual blocks which are printed sequentially: they are the *stitching* blocks and appear as overlapped or touching sub-units.

Nanoscribe GmbH offers several printing modalities, depending mostly on the optical resolution one wants to achieve; in fact, one can choose among 10× (NA=0.3), 20× (NA=0.5), 25× (NA=0.8), and 63× (NA=1.4) magnification objectives, to be used in combination with the correct resist and in the most proper printing configuration, dill or dip (Figure 6.2).

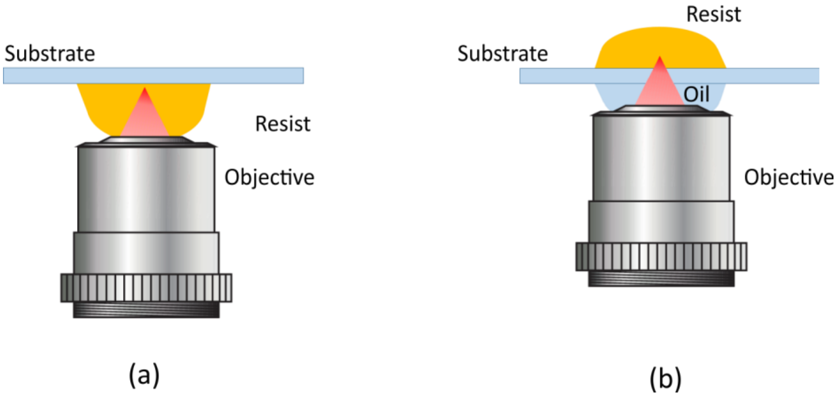

Figure 6.2 (a) Dill printing configuration: the objective is directly immersed into the photoresist which acts as a refractive index matching medium as well as the photoactive material to be polymerized. (b) Oil immersion printing configuration: the laser beam travels through a refractive index matching medium (typically oil) and a thin substrate (170 µm borosilicate glass) to polymerize the photoresist which is dropped on top of the substrate.

Here, we use the system in dill configuration (Figure 6.2 (a)) and focus the femtosecond laser beam into the IP-dip photoresist by means of the 63× magnification objective; the objective is directly immersed into the viscous resist, which is drop-coated on top of a glass substrate and flipped upside down. This printing configuration offers the best quality in terms of resolution and smoothness of the printed components, and this is the main reason why we have decided to fully calibrate the printing parameters for this type of configuration The maximum scanning range in x-y is 200 µm using a pair of galvo mirrors and 300 µm in the z direction using the piezo stage; the maximum average power of the system is 20 mW at 100%. The laser power is defined as percentage in Photonic Professional GT+ and this same convention will be followed through the rest of this chapter. After completion of the 3D printing, the sample can be developed into poly(glycidyl methacrylate (PGMEA) and isopropanol for about 17 and 5 minutes, respectively.

6.3 Calibration procedure

6.3.1 Voxels calibration

In multi-photon polymerization, the polymerized portion of material at the focal spot of the laser is called *voxel*. Its shape and dimension are determined by the asymmetric point spread function (PSF) of the objective lens, and they constitute the fundamental building block of the final 3D printed objects. Since a waveguide (a line) can be considered as a continuum of voxels, knowing the voxel scaling law as well as their dimensions and shape is a very important information to estimate how many of them are required in order to code in the DeScribe environment and, therefore, to build the final object; moreover it helps to know how much time is required to finalize the print. Each 3D printing system is different and laser power as well as the environmental conditions play a role: for this reason and despite the dimensions of the voxels has been previously reported for other 3D printing Nanoscribe systems [162], we have calibrated our system by measuring the x-dimension of printed lines using the 63× magnification objective and the IP-dip resist in dill configuration. After a preliminary experiment which made us exclude laser power levels below 35% and above 75% of the maximum power because of insufficient degree of polymerization and the formation of microexplosions, we have printed arrays of line sets consisting of 5x5, 5x1 and 3x1 voxels, focusing the laser 0.6 µm into a regular glass substrate. The automatic interface-finder of the system detects the interface between the resist and glass substrate by sensing the refractive index difference between them, ensuring we don't overestimate the voxel dimension. We performed a power sweep of the pulsed laser from 35% to 75%, at the recommended scanning speed of 10000 µm/s and 0.2 µm hatching distance. The high aspect ratio resulting from the 5x1 voxels structure made the lines structurally unstable (yellow box in Figure 6.3 (a)), therefore, we only measured the width of the 5x5 and 3x1 voxels objects using a Zeiss LEO 1550 scanning electron microscope (SEM) and plotted it as a function of the power (Figure 6.3 (b)).

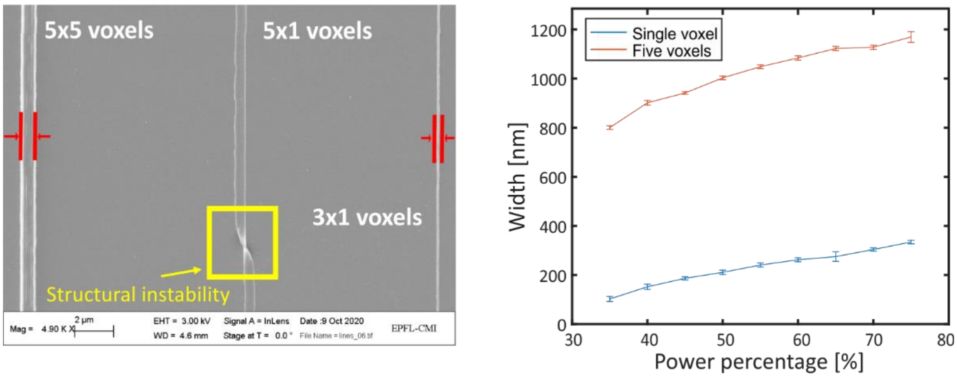

(a)

(b)

Figure 6.3 (a) Example of a SEM image showing the three printed lines composed of 5x5, 5x1 and 3x1 voxels at a power level of 35% and 10000 µm/s writing speed. The red arrows indicate the width dimension we have measured for the calibration of the printed 5 x 5 and 3 x 1 voxels line sets, while the yellow box shows the structural instability of a 5 x 1 voxels structure because of the high aspect ratio. (b) Voxel scaling law as a function of power percentage for 5 x 5 (red), and 3 x 1 (blue) voxels line sets.

As already demonstrated in the previous chapters, the line dimensions increase with increased laser power because of the higher energy which is delivered from the system. The data points in Figure 6.3 (b) were obtained by measuring the width (indicated in red in Figure 6.3 (a)) of three different printed structures as a result of 5x5 and 3x1 voxels line sets, respectively, showing a minimum and a maximum width of 102 and 334 nm for the 3x1 voxels structures, respectively. 5 x 5 voxels minimum and maximum line widths measure 800 and 1170 nm, respectively, as depicted in the plot in Figure 6.3 (b). The line dimensions have been measured using the embedded SEM software measuring tool; because the motion stages in a SEM system don't allow for a full 90° tip/tilt inclination, an uncertainty degree regarding the measurement of the height of the structures is introduced; therefore, we have estimated it considering the voxel height to width aspect ratio (2.5:1) reported by Nanoscribe GmbH.

In this work we propose a single-step additive manufacturing of step-index (STIN) refractive index photonic waveguides, where the high refractive index cores are surrounded by low refractive index cladding (Figure 6.4 (a)). The waveguides are the result of constant laser power irradiation and speed across their core, embedded horizontally (perpendicularly to the optical axis) inside the shared cladding. The difference between the refractive indices is achieved by fine tuning the printing parameters after a careful optimization which maximized this difference, taking into account their final optical and structural properties, such as uniformity and geometrical fidelity after sample development. We have implemented this calibration procedure both for the cladding and the cores.

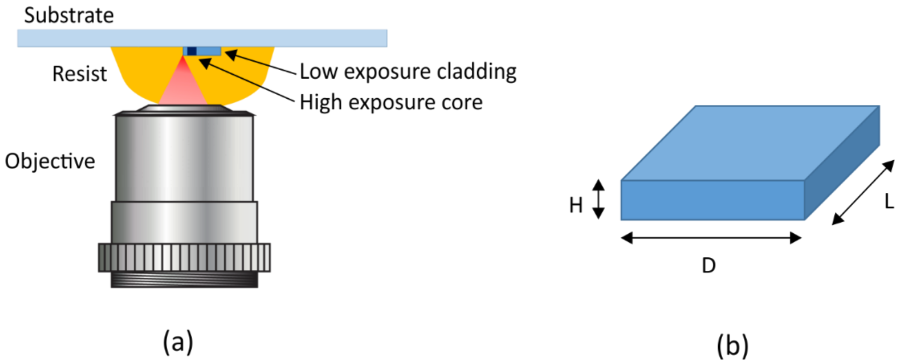

Figure 6.4 (a) 3D printing of photonic waveguides using Photonic Professional GT+ with a 63× magnification objective and the IP-dip resist in dill: high refractive index cores (high exposure) are embedded into lower refractive index cladding (low exposure). (b) Schematic of a 40 x 13 x2 00 µm (D x H x L) block for the calibration of the cladding. Power percentage was swept between 35% and 45%; scanning speed ranged between 6000 and 10000 µm/s.

6.3.2 Cladding calibration

The waveguide bundle cladding needs to have minimized refractive index and must show a uniform profile along the entire sample length. Besides low refractive index, laser power and scanning speed need to be in the right combination to guarantee structural integrity and geometrical fidelity with the desired structure. To this end, we have printed 40 x 13 x 200 µm objects (D x H x L in Figure 6.4 (b)), sweeping the laser power from 35% to 45% (with a step ΔP=1%), and increasing speed from 6000 to 10000 µm/s (Δv=1000 µm/s). The printing was executed layer by layer, at 0.1 and 0.3 hatching and slicing distance, respectively. Following the completion of the 3D printing, we developed the sample in PGMEA and in isopropanol for about twelve and five minutes, respectively. We used digital holography to retrieve the phase accumulation throughout all the structures, fully immersed into a refractive index matching Silicon oil. The hologram and the wrapped phase extraction from a printed object using 40% of the power and 7000 µm/s is shown in Figure 6.5 (a) and Figure 6.5 (b), respectively. Because of the periodicity of the cosine function describing the interference term in the superposition of the object and reference fields during the hologram recording, phase wrapping often takes place in phase reconstruction procedures. Therefore, phase jumps of 2π can appear between two adjacent camera pixels, while one would need to generate continuously phase distributions in order to correctly reconstruct the refractive index distribution of the object. For this purpose we have implemented the PUMA phase unwrapping algorithm into the digital holographic reconstruction Matlab code, for the generation of a smooth, unwrapped phase 2D distribution of the object [163]. The unwrapped phase reconstruction of the 3D printed object is shown in Figure 6.5 (c), where the 2π jumps of the phase between two adjacent pixels are no longer present, ensuring a correct refractive index difference evaluation.

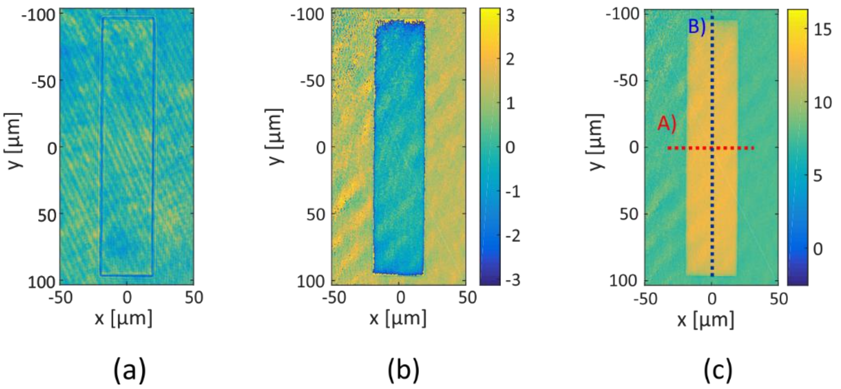

Figure 6.5 Hologram (a), wrapped (b) and PUMA unwrapped 2D phase map (c) of a 3D printed block at 40% laser power and 7000 µm/s scanning speed. A) and B) represent the transversal and longitudinal averaged cross cut profiles as a function of laser power percentage (and constant speed v=7000 µm/s).

The 2D map of the extracted phase not only gives a quantitative measurement of the refractive index, but it also provides important information about the geometrical resemblance with the desired model. The transversal (A in Figure 6.5 (c)) and longitudinal (B in Figure 6.5 (c)) phase profiles are reported in Figure 6.6 (a) and (b) and they result from the profiles averaging over the entire length and width of the object. As it can be easily seen in both cross cuts, the effect of the power increase (and constant speed) is reflected in a higher phase accumulation across the printed volume. Moreover, the effects of the aberrations from the printing lens are more evident at lower laser power percentages, yielding less polymerization because of the intensity decrease which takes place at the edges of the field of view. This can limit their applicability to narrower physical dimensions, in the face of the lowest refractive index. In order to guarantee both low refractive index, and good geometrical fidelity at reasonable sample length and fabrication time, we have set the calibration power to be 40% and the scanning speed at 7000 µm/s; Appendix 5 reports the full calibration of the cladding for all the scanning speeds and power percentages we have tested.

For a better understanding of the optical behaviour of the material, and to facilitate the choice of the right parameters to use, we have mapped the refractive index difference between the polymerized objects and the background, as a function of power percentage and speed (Figure 6.6 (c)). We have measured a minimum and a maximum Δn of 0.02 and 0.045 between the 3D-printed structures and the background, respectively.

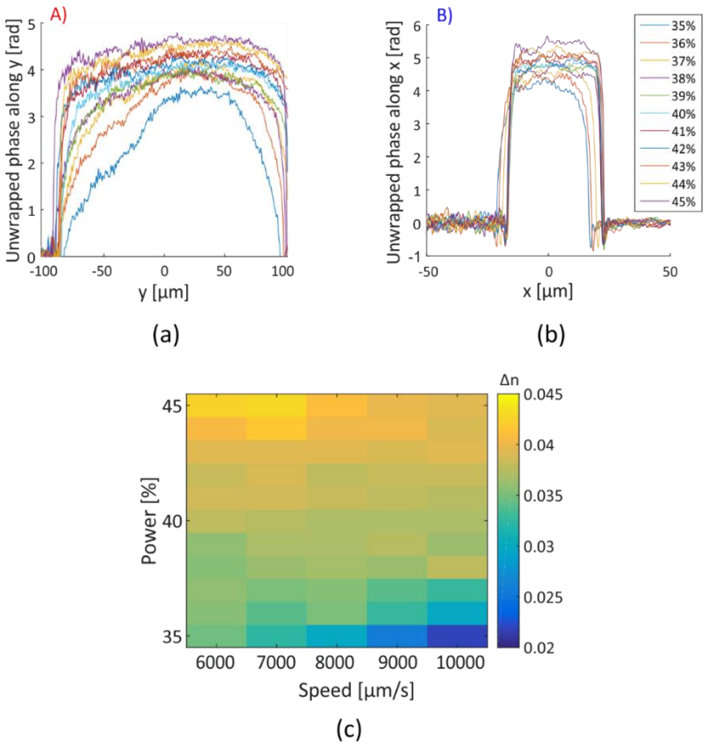

(a) (b)

(c)

Figure 6.6 Longitudinal (a) and transversal (b) averaged cross cut profiles as a function of laser power percentage (and constant speed v=7000 µm/s).The effect of the lens aberrations results in a lower polymerization efficiency at the edges of the field of view, limiting the printable length dimension when lower laser power percentages are used; this effect is more evident across the longitudinal dimension compared to the transversal dimension which measures only 40 µm. (c) 2D mapping of the refractive index difference between the printed objects and the index matching oil as a function of the laser power percentage and the scanning speed, extrapolated from the cladding calibration; we have measured a minimum and a maximum Δn of 0.02 and 0.04, respectively.

6.4 Step-index (STIN) multi-core waveguide bundle 3D printing

6.4.1 Vertical vs horizontal waveguides 3D printing approach

After we have carefully optimized the printing parameters for the cladding, we have implemented two possible configurations for the 3D structuring of STIN optical waveguides to identify the suitable parameters range for the printing of the cores, and to further explore the printing potentials of the Nanoscribe Photonic Professional GT+ system: one vertical (Figure 6.7 (a)) and one horizontal (Figure 6.7 (b)) bottom-up printing approach. In both cases, the cores are surrounded by the same cladding material, using 40% of the laser power (8 mW) and 7000 µm/s writing speed. The print proceeds in horizontal lines which are printed consecutively to form individual layers. Once the total structure base dimension is reached, the piezo stage moves downwards, allowing for the consecutive layer to be printed. The hatching and stitching of the lines are 0.1 and 0.3 µm respectively.

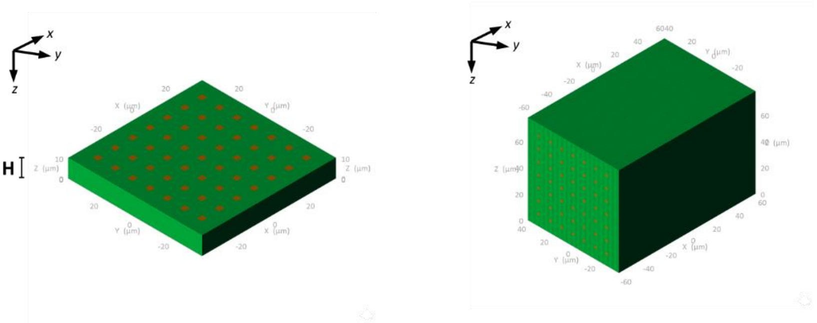

(a) (b)

Figure 6.7 Vertical (a) and horizontal (b) bottom-up printing approach of STIN multicore fiber bundles using Nanoscribe GmbH Photonic Professional GT+. In (a) the waveguide cores lay perpendicularly to the x-y plane, while in (b) they are printed in a parallel fashion, perpendicularly to the optical axis.

Firstly, we have 3D printed cylindrical waveguides with a diameter D=3 μm and height H=20 μm, in a vertical, bottom-up printing configuration. After a quick calibration, we have identified 55%-65% as the correct power percentage range for the cores print, above which we would damage the structures. In order to extrapolate the refractive index difference scaling law as a function of the parameters, we have printed waveguides at 58% (11.6 mW), 61% (12.2 mW), and 64% (12.8 mW), and varying speed from 6000 to 10000 μm/s. Digital holography revealed the difference in the accumulated phase through the 20 μm high cores and the shared cladding; the refractive index difference can be retrieved from the profile cross-cuts traced along the sample base dimension, as depicted in red in Figure 6.8 (a). The 2D phase PUMA reconstructed map for a 20 μm high waveguide bundle, with $v_{core}= v_{cladding}$=7000 μm/s and P_{core}=64% and $P_{cladding}$=40% is shown in Figure 6.8 (a), and the profile cross-cuts traced along the sample base dimension in Figure 6.8 (b).

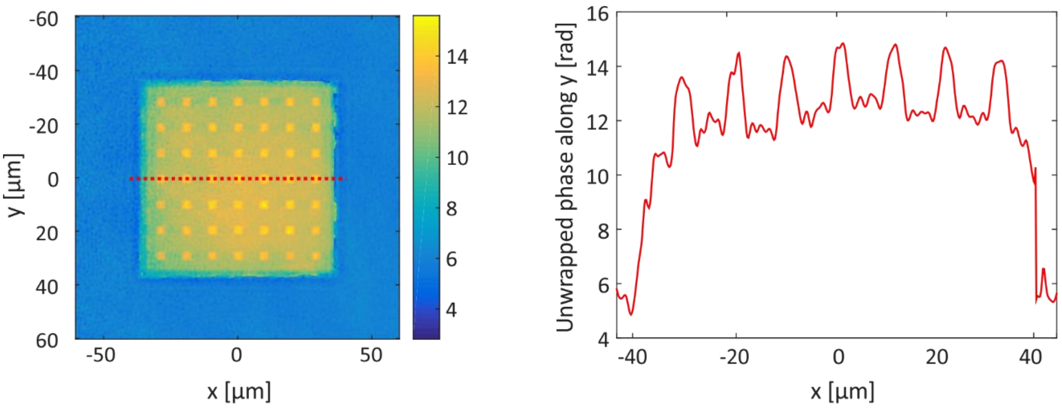

(a) (b)

Figure 6.8 (a) Unwrapped 2D phase map PUMA reconstruction of a 20 μm high STIN multicore fiber bundle printed using a Photonic Professional GT+ system. The cladding and core power percentage are set at 40% and 64%, respectively; the speed is 7000 μm/s for both cores and cladding. (b) Phase profile along the cross-cut (highlighted in red in (a)); the phase difference between cores and cladding measures 3 rad on average.

Knowing the real physical dimension of the object is extremely important to retrieve the correct refractive index. For this purpose we have coated the 3D printed structures with 10 nm thin layer of gold using a single chamber sputterer (Alliance Concept DP-650) and observed them into a scanning electron microscope (SEM Zeiss LEO 1550). As one can observe in Figure 6.9 (a), different exposure zones experience a different shrinkage, resulting in an additional protrusion in correspondence of the cores (inset in Figure 6.9 (a)). This ledge measures 300 nm circa, which leads to additional 1.5774 rad in the phase accumulation measured by the interferogram. Taking this into consideration, the refractive index difference scaling law at the experimental parameters we have tested is depicted in Figure 6.9 (b), ranging from a minimum of ~0.002 to a maximum of ~0.008; the mean and standard deviation values have been measured over five waveguides.

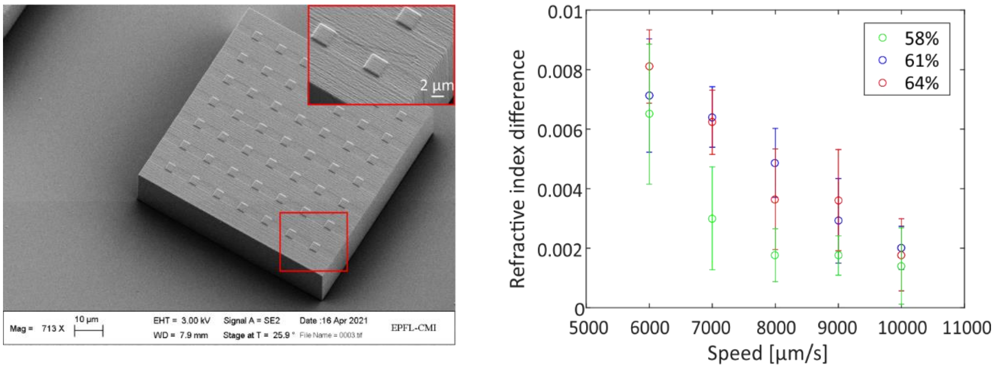

(a) (b)

Figure 6.9 (a) SEM image of a 7 x 7, 20 µm high waveguide bundle fabricated at $P_{cladding}$=40%, P_{core}=64%, and v=7000 µm/s; as it can be seen in the red framed inset, different exposure zones experience a different shrinkage, resulting in an additional protrusion in correspondence of the cores. The waveguides measure ~3 µm in size. (b) Refractive index difference scaling law of waveguides fabricated at 58% (11.6 mW), 61% (12.2 mW), 64% (12.8 mW), and varying speed from 6000 to 10000 µm/s; the experimental fabrication parameters for the cladding are constant ($P_{cladding}$=40%, v=7000 µm/s). The mean and standard deviation values have been measured over five waveguides.

Finally, we have established the printing power and speed for both cladding ($P_{cladding}$=40%, v=7000 µm/s) and cores (P_{core}=64%, v=7000 µm/s), and we have printed cylindrical waveguides with a diameter D=3 µm at variable heights, in order to explore the system potentials for the printing of high structures (Figure 6.10 (a)). The maximum height reachable from the piezo stage in dill configuration using the 63× magnification objective is 300 µm; we have printed STIN multicore fiber bundles at heights H=150, 100, 50 and 20 µm. As one can see from the phase contrast top view images reported in Figure 6.10 (b) to (e), the parameters we have found to be optimal for the refractive index difference maximization no longer work for more than a couple of tens µm-high objects. This is possibly due to cumulative exposure effects, resulting in microexplosions and material damages, as they are visible on the sample surface. For this reason, we have implemented a second printing approach, according to which the waveguides are printed perpendicularly to the optical axis. Because of the limited travel range of the piezo stages in the x-y directions, which is 300 µm, the stitching of blocks is required, representing an additional parameter to be explored during the 3D printing.

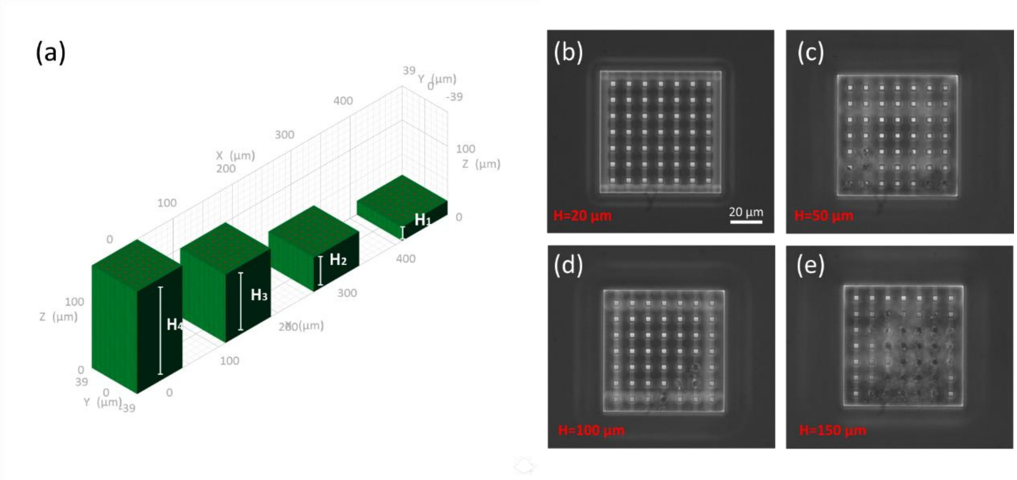

Figure 6.10 (a) DeScribe 3D rendering of vertical multicore fiber bundles designed at variable heights H=150, 100, 50 and 20 µm. Phase contrast microscopy images of waveguide bundles with H_1= 20 µm (b), H_2= 50 µm (c), H_3= 100 µm (d) and H_4= 150 µm (e). At $P_{cladding}$=40%, v=7000 µm/s and P_{core}=64%, v=7000 µm/s, microexplosions irreversibly damage the waveguide bundles higher than 20 µm.

6.4.2 Horizontal waveguides 3D printing approach

The 3D printing of mm-long, highly resolved polymer structures using the dill configuration and the 63× magnification objective requires blocks stitching. Once the object exceeds the field of view of the printing optics, the stage needs to move sequentially in x-y, in order to allow for the following block to be printed. The waveguide cores need to be continuous and homogeneous at the block-block interface, and therefore the stitching should guarantee adhesion and structural integrity from one printed block to the other. To this end, we have explored two possible printing configurations for the fabrication of horizontal STIN multicore fiber bundles using Nanoscribe GmbH, which are exemplified in Figure 6.11 (a) and (b); the first one proceeds as one block is fully printed, while the second prints subunits of blocks organized in layers, as it proceeds parallel to the working plane. The first approach (Figure 6.11 (c)-(d)) results in damaged optical interfaces between the different stitching blocks if compared to the second one (Figure 6.11 (e)-(f)). This is possibly due to an overexposure which takes place because of constructive interference as a result of laser beam reflections from the close by printed block as the print proceeds from left to right. As it is visible from the phase contrast microscopy images in Figure 6.11 (c) and (e), and more clearly from the bright field microscopy images in Figure 6.11 (d) and (f), the block junctions of 3D printed fiber bundles following the first approach are damaged and appear black under bright field illumination, while the second ones appear undamaged and look transparent (Figure 6.11 (f)). An optimal stitching distance between the blocks has been found to be 0.15 µm.

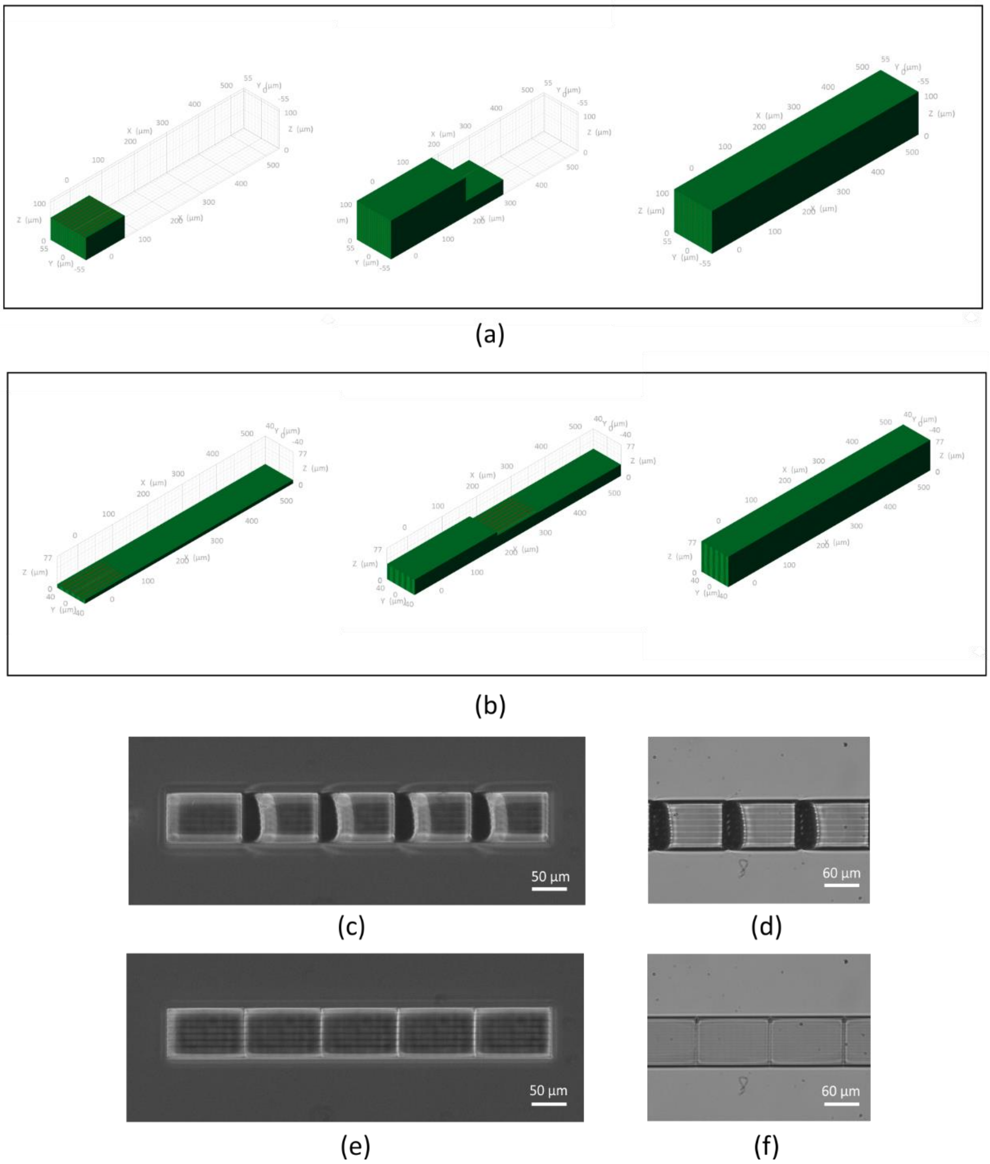
(a)

(b)

(c) (d)

(e) (f)

Figure 6.11 (a) Block-by-block and (b) layer-by-layer 3D printing approaches for the printing of horizontal STIN rectangular optical waveguides using Nanoscribe GmbH Photonic Professional GT+. Phase contrast (c) and bright field (d) microscopy of a waveguide bundle composed of 5 blocks following the block-by-block approach; phase contrast (e) and bright field (f) microscopy of a waveguide bundle composed of 5 blocks and 5 layers following the layer-by-layer approach. In both cases the printing parameters are the same ($P_{cladding}$=40%, v=7000 µm/s and P_{core}=64%, v=7000 µm/s), the waveguide pitch is 10 µm and one single block measures 120 µm. Hatching, slicing and stitching measure 0.1, 0.3 and 0.15 µm, respectively.

However, besides the structural integrity and, most importantly the material refractive index, there are other important parameters and experimental settings to be considered for a successful 3D printing of waveguide bundles. Figure 6.12 (a) shows a 3 x 3 waveguide bundle with a hatching distance of 0.2 µm; in our experiments we have set it to 0.1 µm in order to ensure surface homogeneity and no air gaps between the printed lines. Moreover, short structures suffer of detachment from the glass substrate after development, as depicted in Figure 6.12 (b), compromising holographic and light coupling measurements. Another important step to be carefully undertaken is the development of the object using solvents after the print is concluded. The standard procedure suggested by Nanoscribe GmbH includes 17 minutes of developments in PGMEA and 5 minutes in isopropanol; to avoid aggressive chemical dissolution, we have reduced the development time inside PGMEA to 12 minutes, avoiding material etching at the junctions (Figure 6.12 (c)).

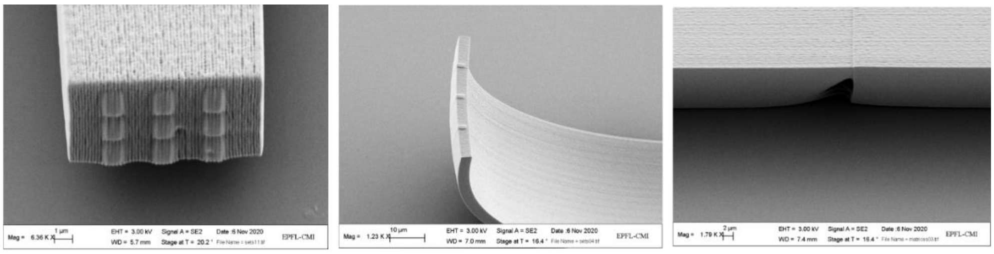
(a) (b) (c)

Figure 6.12 (a) SEM images of a 3 x 3 waveguide bundle with a hatching distance of 0.2 µm; (b) sample detachment from the glass substrate and (c) aggressive sample development in PGMEA causing material etching at the junctions.

6.5 Light coupling into 3D printed STIN multi-core waveguide bundles

In order to measure the transmission loss properties of STIN waveguides printed using IP-dip and the Nanoscribe apparatus, we have printed two identical samples at two different lengths, 840 and 600 µm, respectively. We have used $P_{cladding}$=38%, P_{core}=61%, and v=7000 µm/s for both cores and cladding. We have coupled a 10 µm diameter incoherent white light beam into three different waveguides at each of the printed lengths, 30 µm distant from one another, and measured the output intensities at 535/43, 561/14, 592/43 nm, 609/50 nm, and 675/53 nm colored filters. Propagation losses primarily depend on strong scattering and material absorption [164]. Figure 6.13 shows the transmission loss we have measured as a result of the intensity power ratios between the outputs recorded at the major length and the ones measured at the shorter length, averaged over three waveguides; the inset in Figure 6.13 shows the waveguide output recorded at 609/50 nm. These waveguides exhibit losses of 8 dB/mm at shorter wavelengths, down to ~2.5 dB/mm above 600 nm wavelength. Despite material absorption, the high losses we have measured in the 500-600 nm wavelength region of the electromagnetic spectrum are mostly due to scattering caused by the rough polymerized surface, which proceeds voxel by voxel. This, together with the physical constraints imprinted by Nanoscribe GmbH limits the fabrication of STIN waveguide of this type only to mm-sized dimensions.

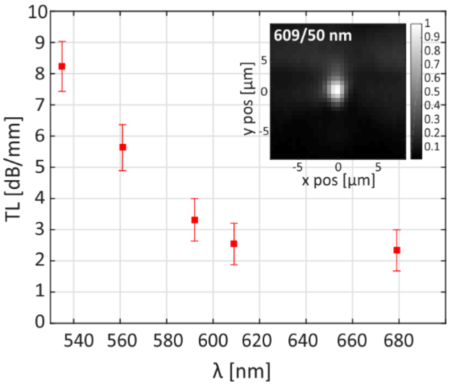

Figure 6.13 Transmission loss in dB/mm of the rectangular STIN optical waveguides fabricated Nanoscribe Photonic Professional GT+. Inset shows the output intensity profile of one waveguide recorded at 609/50 nm wavelength filter. The loss at short wavelengths is highly affected from scattering, most probably due to material roughness.

6.6 BPM Simulations

We simulated the light propagating in the STIN waveguides using BPM; we chose a computational grid of ~50 µm x 50 µm. Based on the geometry and the measurements we performed, we have considered STIN optical waveguides with lateral dimensions W=2 µm and H=2.5 µm, which determines the single mode condition at Δn=0.007 refractive index difference (Figure 6.14 (a)). We have simulated the propagation of a 1.4 µm FWHM Gaussian beam and retrieved the mode of the STIN waveguide after 10 mm of propagation; the resulting mode for λ=600 nm is shown in Figure 6.14 (b). The numerical aperture of the waveguides is calculated to be NA=0.2 at 600 nm wavelength.

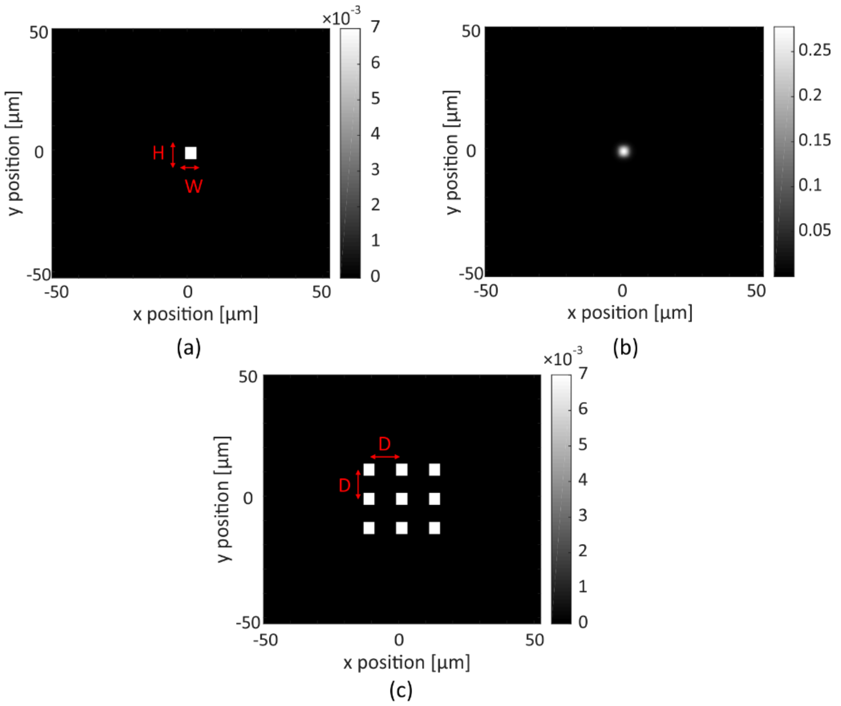

Figure 6.14 (a) Refractive index distribution of a 2 µm x 2.5 µm (W x H) STIN optical waveguide. (b) Mode intensity distribution of the waveguide at λ=600 nm. (c) Refractive index distribution of a 3 x 3 STIN waveguide grid for cross-talk simulations.

This has been done also for the boundary wavelengths emitted from our thermal light, namely 500 and 700 nm. We have simulated the cross-talk over a total length of 10 mm, by placing the waveguides at a separation D=6 µm in a 3 x 3 matrix arrangement (Figure 6.14 (c)). Each mode profile has been coupled in the central waveguide, and the xz-yz propagation profiles for λ=500 nm, λ=600 nm and λ=700 nm have been monitored over 10 mm propagation distance, as shown in Figure 6.15.

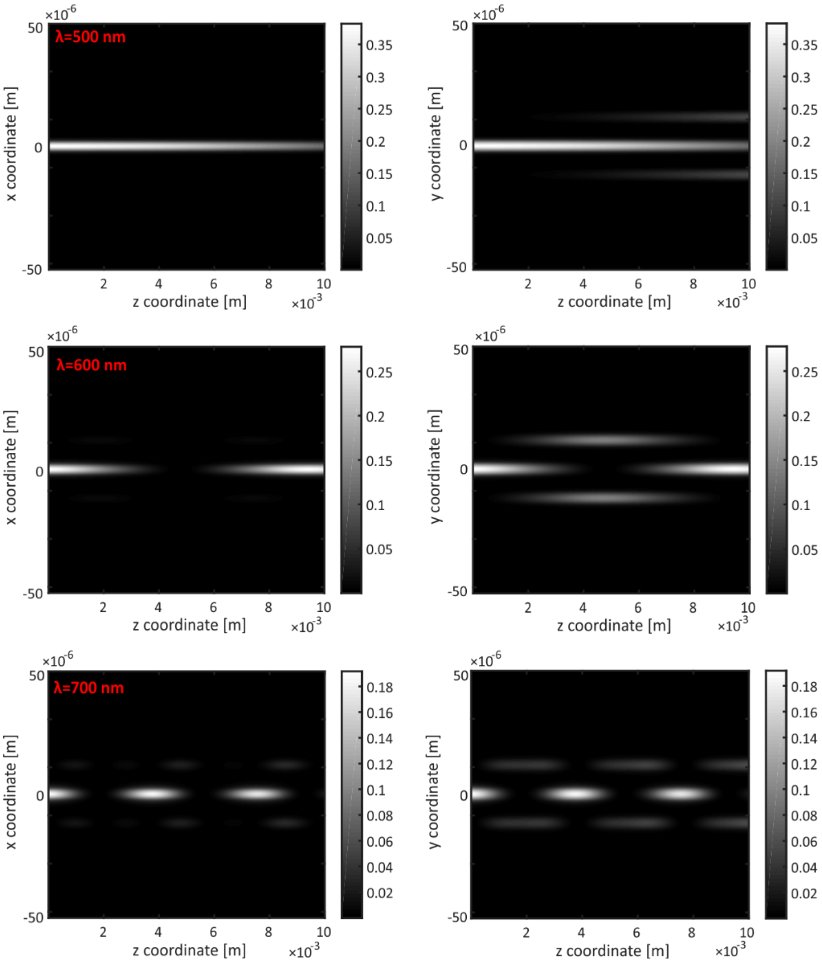

Figure 6.15 xz (first column) and yz (second column) propagation profiles at λ=500 nm, λ=600 nm and λ=700 nm and 10 mm propagation distance, considering the propagation of the mode at each simulated wavelength and the refractive index distribution shown in Figure 6.14 (c).

As expected, crosstalk is more severe at the higher wavelength, and this is visible already after 500 µm propagation distance. Moreover, the effect of the asymmetrical core dimension reflects on a different coupling length in the xz and zy propagation planes, because of higher proximity of the cores in the longitudinal direction.

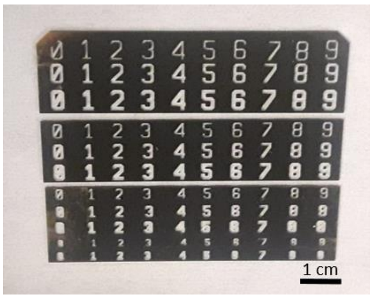

Figure 6.16 Custom made sample target, fabricated by means of standard sputtering and photolithographic techniques. This target contains digits from 0 to 9, with different sizes and feature thicknesses.

Based on the optimal printing parameters we have identified and the BPM simulations we have performed to predict the cross-talk behaviour, we fabricated a 720 µm long, 12 x 12 STIN waveguide bundle, with an interwaveguide distance

D= 10 µm. In order to explore its imaging capabilities, we have fabricated a custom made sample target containing digits from 0 to 9, with different sizes and feature thicknesses (Figure 6.16). The pattern has been realized on a glass wafer and fabricated by means of standard photolithographic techniques, after being sputtered with a 30 nm thin layer of titanium and 100 nm of gold.

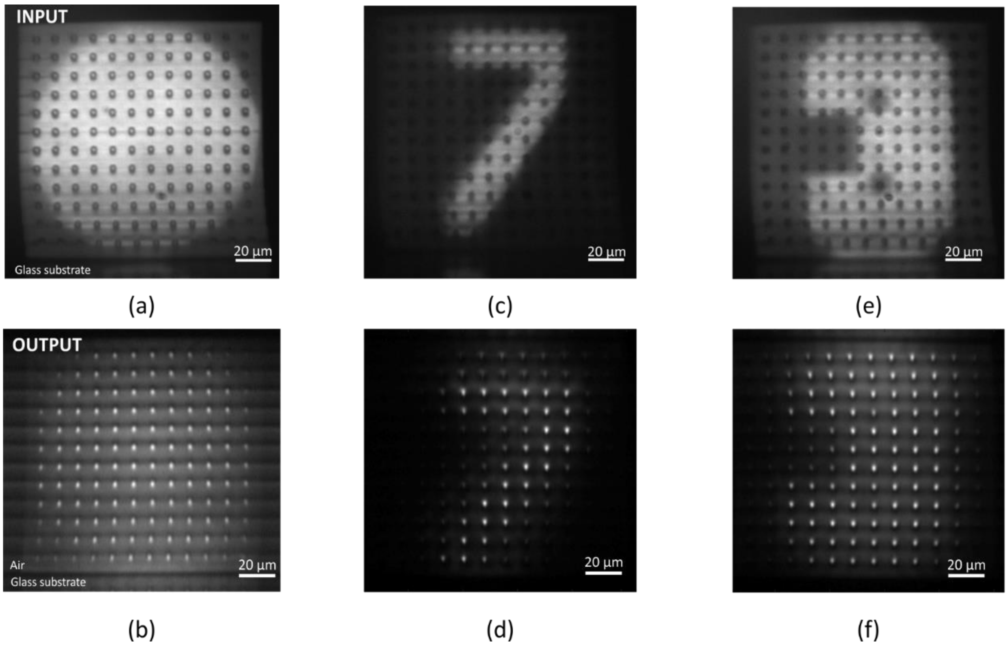

Figure 6.17 Input (a) and output (b) camera images of the 12 x 12 STIN waveguide bundle with incoherent light illumination and no image pattern projected. In (c) and (e) two different digits are projected from a custom made pattern, recorded in reflection on the input camera (CAM2 in Figure 5.8); (d) and (f) show the transmitted, pixelated version of the digits delivered from the waveguide bundle and recorded in transmission by means of the output camera (CAM1 in Figure 5.8).

Figure 6.17 (a) and (b) show the proximal and the distal end of the waveguide bundle in reflection and transmission respectively, when incoherent white light is coupled using the set up in Figure 5.8. Figure 6.17 (c) and (e) show two digits with different thicknesses from the gold target, and recorded in reflection, while (d) and (f) correspond to their transmitted and pixelated version at the distal side of the waveguide bundle. As we can see from Figure 6.17 (d) and (f), moderate light cross-talk is still present, making part of the light escaping the fiber cores. In the next subchapter I am going to investigate how DNN techniques can reconstruct scrambled images, when the recognition of the patterns becomes more challenging because of the cross-talk and the noise present in the experimental data.

6.7 Image reconstruction using deep neural networks (DNNs)

6.7.1 Convolutional U-net DNNs

Machine learning (ML) is a subunit of *artificial intelligence* systems (AI) and identifies the study of mathematical algorithms for the prediction and/or decision making of a system, when this is trained using the raw data. Contrary to AI systems, where a fully mathematical description is required in order to solve a problem by means of a computer, ML algorithms are capable of optimizing it in a dynamic way, thanks to their capability of extracting important features from the data, after being exposed to them [165]. *Deep learning* is again part of machine learning algorithms, where the term "deep" refers to the total number of the computational layers implemented for feature extraction and recognition in the algorithm. Deep neural networks (DNNs) consist in algorithms which are organized into nested layers, governed by mathematical operations and connected with each other in a nonlinear way [165, 166]. The principle of DNNs is founded on how the human brain works: when a certain input reaches a certain threshold, the neuron fires and transmit an output information. The artificial entity assigned to a neuron is called *perceptron* (or node); from each perceptron, the output can be mapped by means of specific weights and nonlinear functions. In DNN, generally, many perceptrons are needed to map a nonlinear problem, and perceptrons from one layer can be (or not) connected to all the perceptrons of the following layer. The functions which regulate the transition from one convolutional layer to the other are called *activation functions*, and they determine when a node will fire and its output value when it will reach the corresponding nodes in the following layer of the stack. The artificial neural networks (ANN) which are made by connecting each perceptron in one layer to all the perceptrons of the following one throughout the whole network, are called *fully connected networks* (FCNs), while *convolutional neural networks* (CNNs) are built with perceptrons being connected to a smaller area of nodes in the previous layer. As implied by the name, CNNs rely on a convolution operation to map an input to an output; therefore, they use 2D-weights matrices instead of single perceptrons to extract the information from one input and map it into an output, often referred as convolutional kernels. This operation simplifies the problem leading to a more computationally efficient algorithm if compared to FCNs.

A DNN needs to be trained in order to produce targeted outputs; this step consists of the optimization of the weights during the layer-to-layer convolution, during which the weights are updated to minimize the *error function*. In addition, the type of error function can be selected according to what the DNN needs to perform; intuitively, it gives the difference between the ground truth and the network prediction. DNN in the presence of a ground truth are denominated *supervised networks*. The minimization of the error function is achieved using gradient-descent based error backpropagation, which calculates the partial derivatives of the error function for all the weights of the specific node (or layer of nodes), so that it identifies the weights which affect the most the output predicted value. Each iteration for updating the weights in a learning unit is called a *batch*. The training cycle where the network ‘sees’ all the training data is called an *epoch*. Hence, the number of epochs determines how many times the network sees the all training dataset.

As we already discussed in this thesis, the resolution of the bundle depends on the core-to-core spacing, which is limited by the light cross-talk among the cores. Intensive research has focused on methodologies about how to increase the resolution in MCF bundles, such as by inducing small changes in the periodicity of the cores, and/or by slightly modifying the core size within the same fiber bundle [103, 104]. Also the addition of distal lenses [86], as well as wavefront shaping techniques have shown remarkable resolution improvements by exploiting the NA of the fiber for point scanning imaging [92, 167, 168]. Deep learning has shown pixelation-free imaging through fiber bundles [169, 170]; in this work we investigated how a ‘U-net‘-type CNN reconstructs the output images from the waveguide bundle we have fabricated.

The U-net structure we used is depicted in Figure 6.18; as one can see from the two examples in Figure 6.17 (c) and (e), we projected a series of digits with different sizes and thicknesses for testing the trained network with experimental data, using a custom made sample target. A U-net CNN architecture generally comprises a convolutional encoding front-end for downsampling, and a deconvolutional decoding back-end for upsampling. Apart from the convolution and activation operations, our convolutional layer of the U-net comprises, in turn, a maxpooling layer which downsamples the resulting portion of the image which has been convolved with the kernel, considering the maximum value of each local patch of elements.

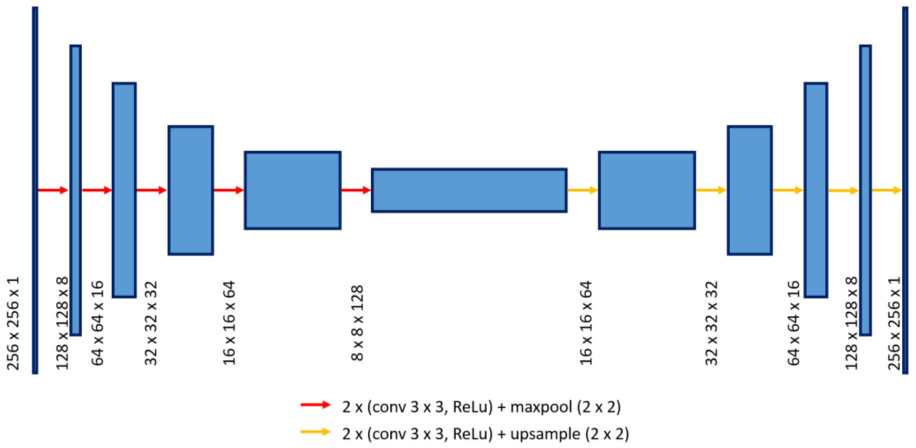
256 x 256 x 1
128 x 128 x 8
64 x 64 x 16
32 x 32 x 32
16 x 16 x 64
8 x 8 x 128
16 x 16 x 64
32 x 32 x 32
64 x 64 x 16
128 x 128 x 8
256 x 256 x 1
2 x (conv 3 x 3, ReLu) + maxpool (2 x 2)
2 x (conv 3 x 3, ReLu) + upsample (2 x 2)

Figure 6.18 U-net type DNN architecture used to reconstruct the output images from the fiber bundle.

The choice of each DNN parameter, such as the activation function, the size of the kernel, the duration of the epoch and the size of data batches is not trivial and in general needs to be optimized based on the task that the DNN needs to perform. In this work, we implemented our DNN algorithm in Keras, a high-level application programming interface (API) that works on top of Tensorflow, allowing the interfacing with the coding in a user-friendly way.

Both for the training of the network and the reconstruction of the images from the waveguide bundle, we have used a rectified linear (*ReLu*) activation function (Equation 46); $f(x)$ in Equation 46 denotes the nonlinear function within each node belonging to the convolved layers. The optimizer we used to minimize the mean squared error loss function (Equation 47) is an Adam optimizer; N, y_{pred} and y_{true} in Equation 47 are the number of examples in a single batch, the output predicted by the network and the ground truth, respectively.

$$f(x) = \begin{cases} x, & if\ x \geq 0 \\ 0, & if\ x < 0 \end{cases}$$

Equation 46 Rectified linear activation function.

$$MSE = \frac{1}{N}\sum_{i}^{N}(y_{pred} - y_{true})^2$$

Equation 47 Mean squared error loss function.

6.7.2 Training and testing with synthetic data

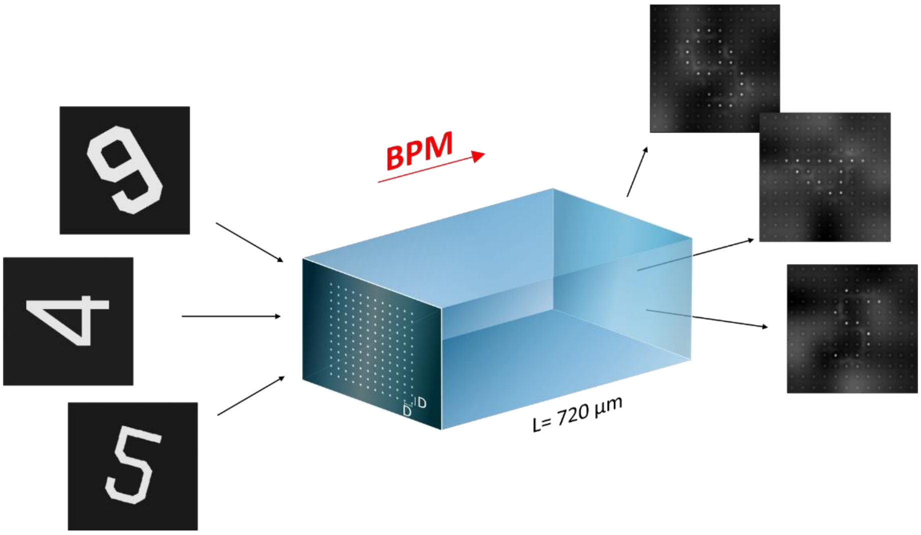

Figure 6.19 Schematic of synthetic dataset creation for the training of the network. 1170 digits have been propagated through a 12 x 12 STIN waveguide bundle with core dimensions W=2 µm, H=2.5 µm and refractive index difference Δn=0.007. We set the illumination wavelength λ=600 nm, the sample length to be L=720 µm and the waveguide pitch D=10 µm.

In order to efficiently reconstruct the images using the DNN schematically drawn in Figure 6.18, we synthetically enlarged the dataset by propagating 1170 different replicas of digits through the waveguide bundle using BPM (Figure 6.19). We have created a synthetic dataset by rotating and scaling the layout of the patterned digits (reported in Figure 6.16) and recorded every output intensity by simulating a 12 x 12 STIN waveguide bundle with Δn=0.007 and core dimensions W=2 µm and H=2.5 µm. The bundle length coincides with the physical length of the sample which is L=720 µm, as well as the waveguide pitch (D=10 µm); the source wavelength is λ=600 nm.

Experimental data exhibited moderate to low contrast, as well as additional background noise, most likely due to stray light. For this reason, after we have recorded the output intensity for each of the propagated digits (one example is reported in Figure 6.20 (a)), we additionally simulated the propagation of a plane wave through the bundle and added the result to each of the digit output intensities (Figure 6.20 (b)), so that the ratio between the intensities of the cores illuminated by the input pattern and the others is on average 20%. Subsequently, we added a background noise with Gaussian distribution to mimic the noise in the experimental data (Figure 6.20 (c)).

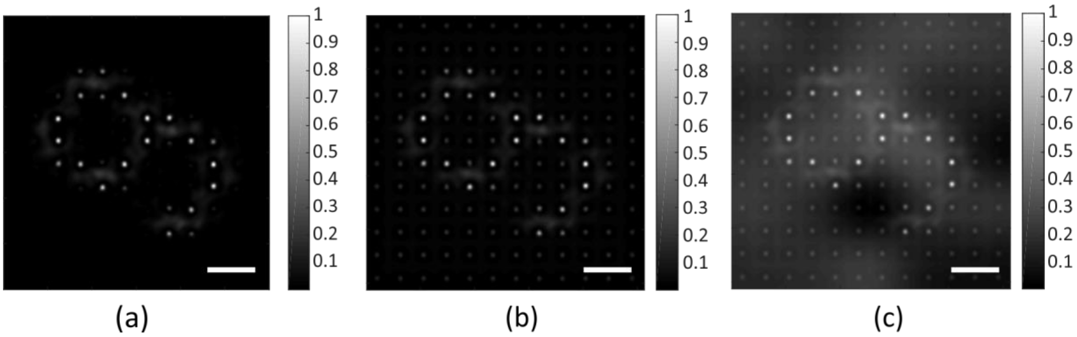

Figure 6.20 (a) BPM output intensity of a digit, propagated in the bundle for 720 µm propagation distance; digit output intensity with a superimposed propagated plane wave (b) and a Gaussian-like noise distribution (c); scale bar measures 20 µm.

The resulting 1170 distal pattern images were randomly split into 1053 for training and 117 for testing (10%). The training set has been split, in turn, into 210 examples for validation (20%) and 843 examples for training (80%), and processed in batches of 20, shuffling them at every epoch to minimize over fitting; the training proceeded for a maximum of 30 epochs. The Adam optimizer we used had a learning rate of 1x10^{-4}. In order to evaluate the quality of the reconstruction of the network, we monitored the learning curves of the training and the validation datasets, displaying the MSE (mean square error) and MAE (mean absolute error), both reported in Figure 6.21.

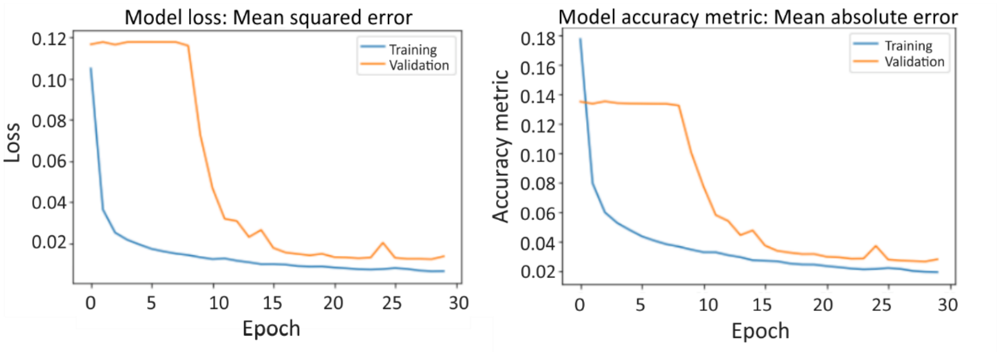

(a) (b)

Figure 6.21 Mean squared error (a) and mean absolute error (b) of the training and validation datasets as a function of the epoch number.

As one can see from Figure 6.21 (a) and (b), the problem is not generalized until epoch number 8 or 9, after which the validation curve decreases, almost converging with the training curve; this means the network has been successfully trained. Figure 6.22 shows some examples of the DNN image reconstruction using the synthetic testing data: the first row shows five pixelated digits obtained from the BPM simulations, which now serve as inputs to the DNN, while the second and the third rows report the reconstructed digits and the ground truths, respectively. The size of the original images is 256 x 256 pixels both before downsampling (DNN input) and after upsampling (DNN reconstruction); we registered a MSE=0.015 and a MAE=0.03 over 117 test examples. In general, we can see that the DNN can successfully reconstruct the images with good quality; the U-net model can reconstruct quality enhanced images from the fiber bundle, removing the pixelation effect due to the fiber cores and bypassing the blurring effect due to core-to-core coupling.

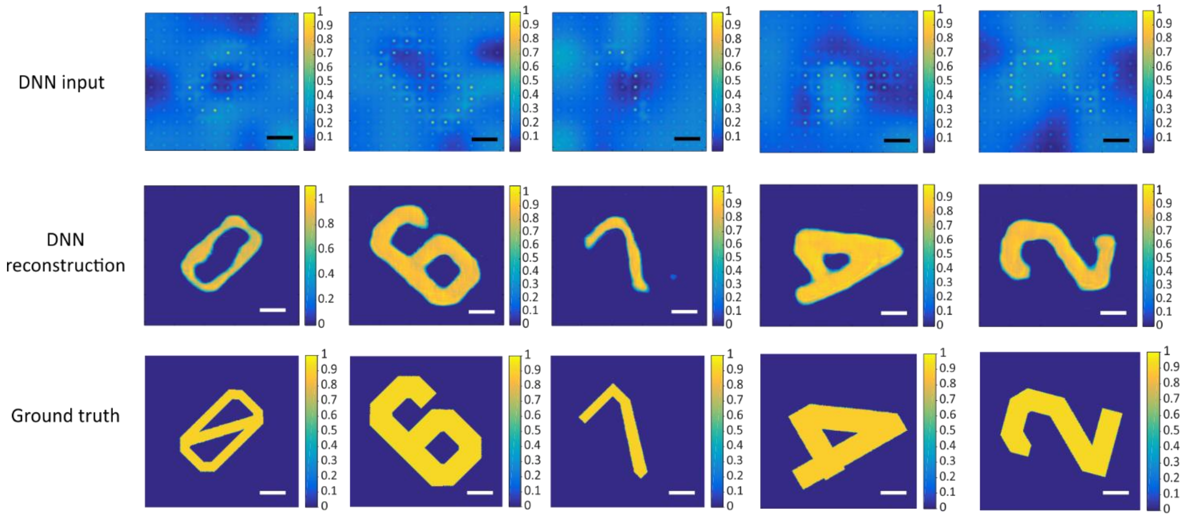

Figure 6.22 Five examples of synthetic inputs we used to test the DNN (first row), their corresponding reconstruction (second row) and the ground truths used for the training (third row); scale bars measure 20 µm.

6.7.3 Test results with experimental data

Custom made target of digits, whose layout is used to generate an augmented synthetic dataset, has been used to evaluate the U-net reconstruction performance in the case of experimental data. We have measured the output intensity from the 720 µm long waveguide bundle we fabricated using Nanoscribe (Figure 6.17), when the digits from the custom made sample target are projected to the proximal bundle facet. Also in this case the U-net shows good reconstruction performances, despite the light cross-talk and the pixelated nature of the images. The first row in Figure 6.23 shows some of the waveguide bundle output intensities recorded by means of CAM1, which now correspond to the DNN input, while the second and the third rows show the reconstructed digit from the DNN and the corresponding ground truth, respectively. MSE and MAE are also reported in Figure 6.23 for each reconstructed digit, where scale bars measure 20 µm. Depending on the thickness, size and complexity of the patterned digit, the delivering and recognition of the image at the fiber end can be challenging, as one can notice by observing the images in the first row of Figure 6.23. The use of DNN for image reconstruction provides an efficient platform for improved and accurate rendering of fiber bundle images and turns to be a valuable tool to extract the desired information from the raw images captured on our camera, as exemplified in the DNN reconstructed images in the second row of Figure 6.23.

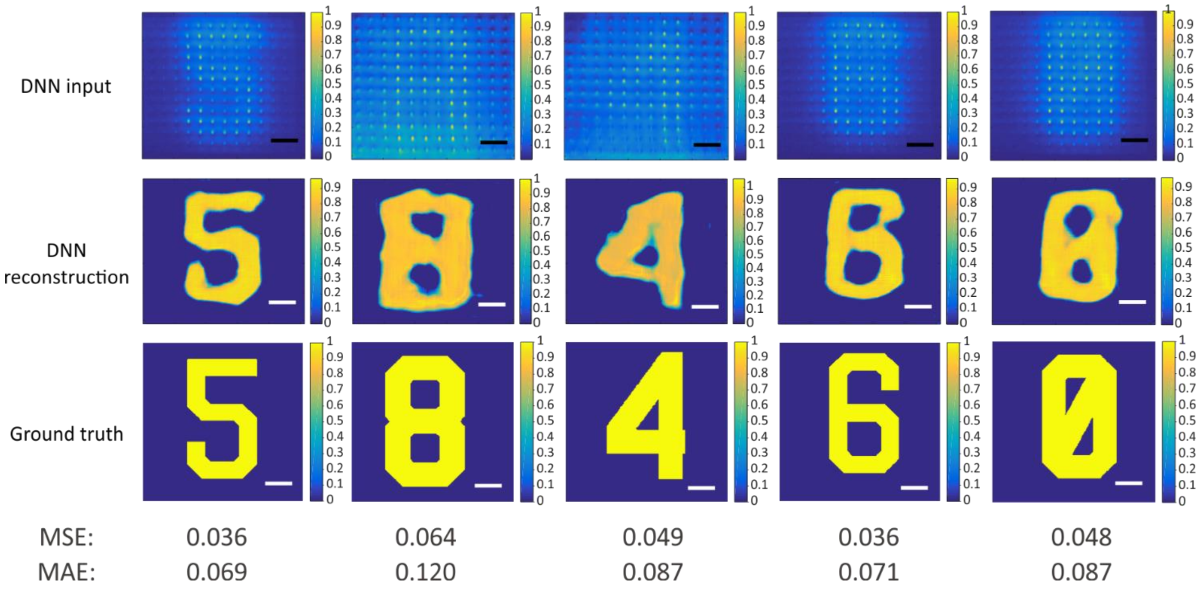

Figure 6.23 Output intensity from the fiber bundle, fabricated using Nanoscribe Photonic Professional GT+, recorded by means of CAM1 (first row) and DNN reconstructed images and corresponding ground truths (second and third rows); scale bars measure 20 µm.

6.8 Summary

In this chapter, I reported the fabrication of STIN rectangular optical waveguides in a horizontal, bottom-up printing approach, using Nanoscribe GmbH Photonic Professional GT+. I show a full calibration of the printing parameters, such as laser power and motion speed for the realization of undamaged structures with maximized refractive index difference between cores and cladding. We identified $P_{cladding}$=38% (7.6 mW), P_{core}=61% (12.2 mW), and v=7000 µm/s for both cores and cladding as the optimal parameter combination for the fabrication of 720 µm long STIN waveguide bundles using this technique. We characterized the waveguides in terms of refractive index difference and transmission loss, reporting a maximum Δn=0.007 and a minimum transmission loss of ~2.5 dB/mm above 600 nm wavelength.

Moreover, we built a CNN of the U-net type to reconstruct the images from a custom made sample target, after they have been delivered to the fiber bundle end. After we have trained the network with an enlarged synthetic dataset using BPM, the DNN technique showed improved resolution images both from simulation and experimental datasets, turning out to be an efficient platform for improved and accurate rendering of fiber bundle images.

Chapter 7 Summary and outlook

In this thesis, I have investigated novel materials for the fabrication of polymer waveguides in PDMS and other innovative materials using the LDW technique. The aim of this work was, in particular, a polymer optical waveguide bundle for imaging applications. Multiphoton LDW was the technique of choice in this work owing to its capability of fabricating high precision 3D microstructures. The core of this work consists of the investigation of monomers and photoinitiators suitable for host-guest fabrication through photopolymerization in a cured PDMS substrate. We extensively searched and tested a number of small, nonpolar polymerizable monomers that could penetrate the PDMS matrix efficiently and polymerizes under the irradiation of a femtosecond-pulsed laser. Our materials of choice converged to two systems: phenylacetylene monomer without photoinitiator and divinylbenzene monomer with commercial Irgacure OXE02 as a photoinitiator.

In the course of this research, we have established a complete platform for the fabrication and characterization of optical waveguides in PDMS. We have built a LDW fabrication system integrating a femtosecond Ti:Sapphire tunable laser and mechanical and precision piezo stages for nm-resolution positioning. An interferometric imaging system was used to measure the refractive index difference between core and cladding. We also constructed a light coupling and microscopic imaging system to quantify the transmission loss in the fabricated waveguides.

We have achieved, for the first time, photoinitiator-free multiphoton-induced polymerization in phenylacetylene, which was employed in the fabrication of optical waveguides in PDMS. For this purpose, we have tuned the laser wavelength to 680 nm, such that the absorption band of the phenylacetylene monomer is reached via multi-photon absorption. To optimize the fabrication parameters, we wrote and characterized the waveguides at writing speeds ranging between 0.5 and 1.5 mm/s, at a laser peak intensity between 1.6×10^{12} and 2.4×10^{12} W/cm^2, and at a focusing depth between 800 µm and 1.3 mm below the sample top surface. Because of the dense π-electrons in phenylacetylene, we achieved a small (1.3 µm) waveguide width and a high refractive index contrast ($\Delta n \geq 0.06$) between the waveguide core and the PDMS cladding. This allowed for efficient waveguiding with a core size of 1.3 µm with a measured loss of 0.03 dB/cm in the spectral band of 650-700 nm. However, our study also reveal that the waveguides fabricated using phenylacetylene monomer are subject to excessive defects due to irreversible material damage as a result of self-focusing and beam collapse inherent in the polymerization process during fabrication.

To tackle the self-focusing problem and minimize the fabrication defects, we investigated a different chemistry involving divinylbenzene monomer and the commercial PI Irgacure OXE02. Using this process, we have demonstrate the fabrication of long, submicron-sized, largely defect-free optical waveguides in PDMS. The new chemical scheme allowed for lower writing intensities and higher writing speeds compared with the phenylacetylene process. This results in a lower refractive index contrast (Δn below the measurable level of the characterization system) and an increased, but nearly flat, transmission loss (13 dB/cm) over the spectral range of 535–679 nm in the 0.5 µm wide waveguide. In order to improve the light confinement and reduce the transmission loss, we investigated a multi-track fabrication strategy to increase the waveguide width from ∼0.5 to ∼3.5 µm. The compound waveguides were fabricated with a nominal focal intensity of 1.78×10^{12} W/cm^2 and a writing velocity of 3.2 mm/s, resulting in a Δn of 0.005. Among the compound waveguides, the double-tracks exhibit a transmission loss ranging from 6.5 dB/cm at 535 nm to 2.2 dB/cm at 710 nm, where the loss scales with power -4 of the wavelength, indicating that the loss is originated form Rayleigh-scattering. The transmission loss in the triple-tracks deviates from a Rayleigh-scattering regime on the longer wavelength side, ranging from 12.4 dB/cm at 535 nm to 0.1 dB/cm at 710 nm, possibly because of constructive interference due to the larger and more complex refractive index structures in the triple-track waveguides.

Together with our project partner Sonova, we have implemented a PDMS optical waveguide bundle for cochlear micro-endoscopy to be embedded in a cochlear implant. The main idea is to fabricate a 4-cm long polymer-based optical waveguides bundle in PDMS using MP-LDW, which acts as a multicore fiber endoscope to give visual feedback to the surgeon while inserting the cochlear implant. The process of choice is the divinylbenzene/Irgacure OXE02 scheme owing to its defect-free results. However, due to the small waveguide size, the low refractive index contrast, and the long distance that the waveguides stretch in parallel, crosstalk between the waveguide channels has been found to be significant. In order to acquire the theoretical impulse response and gain deeper insights into the process of inter-waveguide coupling, we performed simulations of light propagation inside the waveguide structures using the BPM with empirically relevant parameters. At Δn of 0.005, the BPM simulations suggested an optimal inter-waveguide distance of 20 µm. Triple-track waveguides showed better light confinement and less crosstalk compared with double-track waveguides at any sample length. Using the triple-track structure, we fabricated a pilot structure of 6×6 matrices of triple-track waveguides and characterized their performance in incoherent imaging. Furthermore, we have achieved the fabrication of full 4-cm long, 12 x 12 waveguide bundles. The image transmission through these type of waveguides could be further improved by optimizing the imaging conditions and the pattern projection at the bundle proximal facet.

In addition to the fabrication of polymer optical waveguides in PDMS, we also investigated the fabrication of µm–sized STIN optical waveguides using a commercial 3D printer. We combined low and high exposure regions to form cladding and cores of the waveguides, respectively, and performed a thorough calibration to identify the correct parameters range to avoid material damage, guaranteeing geometrical resemblance with the desired design. We have scanned the power percentage of the laser between 35% and 45% and the writing speed between 6000 and 10000 µm/s for the cladding. Finally, the optimal range fell within 38% and 40% for the cladding and 58%-63% for the cores; the fabrication speed was set at the optimal value of 7000 µm/s both for cladding and cores. The maximum achievable refractive index difference using this technique was measured to be $\Delta n_{core-cladding} \sim 0.008$. STIN waveguides have been fabricated following two different approaches, a vertical fabrication approach which resulted in overexposed material, and a more efficient horizontal fabrication approach which preserves material integrity. Transmission loss was found to be highly dominated by scattering, most probably due to structural inhomogeneity of the waveguide voxels. We have measured a high transmission loss of 5.5-8 dB/mm in 515-568 nm wavelength range, and a lower transmission loss of 2-3 dB/mm in 572-700 nm band. Moreover, we demonstrated significant improvements in the resolution of the image delivered by the waveguide bundle using a convolutional neural network, which was trained using an enlarged synthetic dataset obtained with BPM. The DNN reconstruction removes the discretization artefacts due to the waveguide sampling, and the background noise due to crosstalk, showing improved resolution both in simulated and experimental datasets.

As I described in this thesis, the fabrication of polymer waveguides in PDMS was performed in the open air with oxygen present in the system. Oxygen is well-known to be a polymerization retarder in these types of systems, thus we do believe that significant improvements could arise from a nitrogen-purged DVB, and partially phenylacetylene. The self-focusing problem can be addressed by implementing a feedback closed-loop, capable of monitoring and controlling the laser intensity at the focus from fluorescence live-measurements, using an electro-optic modulator inserted in the laser path. This would allow also for the achievement of a higher refractive index difference between the polymer cores and the PDMS cladding. Moreover, we think that the loading feature of PMDS could turn to be very interesting by using more established polymerizing resins, such as IP-dip, as it has been already demonstrated for other bulk materials [171]. IP-dip is much more viscous than DVB or phenylacetylene, it would indeed require chemical manipulation in order to penetrate the PDMS framework in an efficient way. This could be verified by using a surfactant in order to enlarge the nm-sized pores of cured PDMS to 100-200 nm-sized air voids, still ensuring optical clarity. Bending, as well as mechanical tests also constitute an important milestone to be reached for the completeness of this work, together with a full imaging bundle prototype fabrication.

Overall, we believe that DNNs reconstruction techniques could greatly improve the imaging capabilities of such bundles, improving optical resolution and removing noise artefacts due excessive to core-to-core coupling. We expect that such waveguides will receive a wide range of applications in biosensors, microfluidic flow cytometry, wearable and implanted photonic devices, electro-elastic optical modulators, flexible optical circuit boards, and optical neural networks.

Appendix

Appendix 1

In Chapter 1 I discussed the working principle of optical fibers in the wealky guiding approximation ($\frac{n_1}{n_2} \cong 1$). Knowing the propagation constants and predicting how many fiber modes and what the light distribution inside the core would be is very important to understand and simulate the optical properties of an optical waveguide. In order to do so, an electromagnetic analysis is required: we need to find solutions for the electromagnetic field by solving the Maxwell's equations.

The general form of Maxwell's equations is:

$$\nabla \times \mathbf{E} = -\frac{\partial \mathbf{B}}{\partial \mathrm{t}}$$

E. 1

$$\nabla \times \mathbf{H} = \frac{\partial \mathbf{D}}{\partial \mathrm{t}} + \mathbf{J}_{\mathrm{free}}$$

E. 2

with:

$$\nabla \cdot \mathbf{D} = \boldsymbol{\rho}_{\mathrm{free}}$$

E. 3

$$\nabla \cdot \mathbf{B} = 0$$

E. 4

where $\mathbf{E}$ is the electric field ($\left[\frac{\mathrm{V}}{\mathrm{m}}\right]$), $\mathbf{B}$ is the magnetic flux density ($\left[\frac{\mathrm{Vs}}{\mathrm{m}^2}\right]$), $\mathbf{H}$ is magnetic field ($\left[\frac{\mathrm{A}}{\mathrm{m}}\right]$) and $\mathbf{D}$ is the electric flux density ($\left[\frac{\mathrm{As}}{\mathrm{m}^2}\right]$); ρ_{free} is the density of free charges ($\left[\frac{\mathrm{As}}{\mathrm{m}^3}\right]$) and $\mathbf{J}_{\mathrm{free}}$ is the current density ($\left[\frac{\mathrm{A}}{\mathrm{m}^2}\right]$). Bold style indicates vector entities and ∇ is the Nabla operator.

The constitutive relations of the medium are:

$$\mathbf{D} = \varepsilon_0\mathbf{E} + \mathbf{P} = \varepsilon_0\mathbf{E} + \varepsilon_0\chi\mathbf{E} = \varepsilon_0(1+\chi)\mathbf{E}=\varepsilon_0\varepsilon_r\mathbf{E}=\varepsilon\mathbf{E}$$

E. 5

$$\mathbf{B} = \mu_0\mathbf{H} + \mathbf{M}$$

E. 6

$$\mathbf{J}_{\mathrm{free}} = \sigma\mathbf{E} + \mathbf{J}_{\mathrm{e}}$$

E. 7

$\mathbf{P}$ is the electric polarization vector and is linearly related to the elctric field $\mathbf{E}$; ε_0 and χ are the free space electrical permittivity and susceptibility. μ_0 is the free space permeability and $\mathbf{M}$ is the magnetic polarization ($\left[\frac{\mathrm{Vs}}{\mathrm{m}^2}\right]$), and for a not ferromagnetic material:

$$\mathbf{M} = 0$$

E. 8

If we consider a nondispersive, and dielectric material (that is homogeneous and isotropic), then:

$$\rho_{\mathrm{free}} = 0$$

E. 9

$$\mathbf{J}_{\mathbf{free}} = 0$$

E. 10

where the electrical condutctiviy σ and the external currents $\mathbf{J_e}$ are zero. Therefore, we come to a more simple form of the Maxwell's equations:

$$\nabla \times \mathbf{E} = -\mu_0 \frac{\partial \mathbf{H}}{\partial \mathrm{t}}$$

E. 11

$$\nabla \times \mathbf{H} = \varepsilon \frac{\partial \mathbf{E}}{\partial \mathrm{t}}$$

E. 12

and:

$$\nabla \cdot \mathbf{D} = 0$$

E. 13

$$\nabla \cdot \mathbf{B} = 0$$

E. 14

If we apply the curl operator on both sides of E. 11, an by knowing that:

$$\nabla \times \nabla \times \mathbf{E} = \nabla\nabla \cdot \mathbf{E} - \nabla^2\mathbf{E} = -\nabla^2\mathbf{E}$$

E. 15

we obtain the wave equation, both for the electric and magnetic field:

$$-\nabla^2\mathbf{E} = -\frac{1}{\mathrm{c}^2}\frac{\partial^2\mathbf{E}}{\partial \mathrm{t}^2}(1+\chi) \Rightarrow \nabla^2\mathbf{E} - \frac{\mathrm{n}^2}{\mathrm{c}^2}\frac{\partial^2\mathbf{E}}{\partial \mathrm{t}^2} = 0$$

E. 16

$$\nabla^2\mathbf{H} - \frac{\mathrm{n}^2}{\mathrm{c}^2}\frac{\partial^2\mathbf{H}}{\partial \mathrm{t}^2} = 0$$

E. 17

These are the Helmoltz equation for the electric and magnetic field and it is satisfied for all their components.

For the sake of simplicity we solve the equations for the electric field only, by considering the step-index optical fiber structure shown in Figure 1.2, with core refractive index n_1 and refractive index n_2 for the cladding; because of the simmetry of the system, it is more convenient to write the electric field and the equations in cylindrical coordinates.

We can write the electric field in cylindrical coordinates as:

$$\mathbf{E}(\rho,\theta,z,t) = \mathbf{E}(\rho,\theta,z)e^{j\omega t} = (E_\rho\hat{r} + E_\theta\hat{\theta} + E_z\hat{z})e^{j\omega t}$$

E. 18

where: $E_{\rho,\theta,z} = \left|E_{\rho,\theta,z}\right|e^{-j\beta z}$

so:

$$\mathbf{E}(\rho,\theta,z,t) = (\left|E_\rho\right|\hat{\mathbf{r}} + |E_\theta|\widehat{\boldsymbol{\theta}} + |+E_z|\hat{z})\ e^{j(\omega t-\beta z)}$$

E. 19

For each component $E_{\rho,\theta,z}$ of the electric (and magnetic) field we can rewrite the Helmoltz equation in cylindrical coordinates:

$$\frac{\partial^2 E_{\rho,\theta,z}}{\partial\rho^2} + \frac{1}{\rho}\frac{\partial E_{\rho,\theta,z}}{\partial\rho} + \frac{1}{\rho^2}\frac{\partial^2 E_{\rho,\theta,z}}{\partial\theta^2} + \frac{\partial^2 E_{\rho,\theta,z}}{\partial z^2} - \frac{n^2}{c^2}\frac{\partial^2}{\partial t^2}E_{\rho,\theta,z} = 0$$

E. 20

and in the frequency Fourier domain:

$$\frac{\partial^2 \widetilde{E}_{\rho,\theta,z}}{\partial\rho^2} + \frac{1}{\rho}\frac{\partial \widetilde{E}_{\rho,\theta,z}}{\partial\rho} + \frac{1}{\rho^2}\frac{\partial^2 \widetilde{E}_{\rho,\theta,z}}{\partial\theta^2} + \frac{\partial^2 \widetilde{E}_{\rho,\theta,z}}{\partial z^2} + n^2k_0^2\widetilde{E}_{\rho,\theta,z} = 0$$

E. 21

being $\widetilde{E}(\rho,\theta,z,\omega)$ the expression of the field in the frequency domain.

In order to solve the Helmoltz equation for all the electric field components, we use the method of separation of variables, according to which we define:

$$\widetilde{E}_{\rho,\theta,z,\omega} = \widetilde{R}(\rho)\widetilde{\Theta}(\theta)\tilde{Z}(z)\widetilde{\Omega}(\omega)$$

E. 22

By plugging E. 22 into E. 21, and by considering only one of the electric field components, we obtain:

$$\widetilde{\Theta}(\theta)\tilde{Z}(z)\widetilde{\Omega}(\omega)\frac{\partial^2\widetilde{R}(\rho)}{\partial\rho^2} + \widetilde{\Theta}(\theta)\tilde{Z}(z)\widetilde{\Omega}(\omega)\frac{1}{\rho}\frac{\partial\widetilde{R}(\rho)}{\partial\rho} + \widetilde{R}(\rho)\tilde{Z}(z)\widetilde{\Omega}(\omega)\frac{1}{\rho^2}\frac{\partial^2\widetilde{\Theta}(\theta)}{\partial\theta^2} + \widetilde{R}(\rho)\widetilde{\Theta}(\theta)\widetilde{\Omega}(\omega)\frac{\partial^2\tilde{Z}(z)}{\partial z^2}$$
$$+ n^2k_0^2(\rho)\widetilde{\Theta}(\theta)\tilde{Z}(z)\widetilde{\Omega}(\omega) = 0$$

E. 23

In order to satisfy this equation, we can set each of the term equal to zero; moreover, if we add and substract the same quantity on left side of this equation ($\pm\left(\frac{l^2}{\rho^2}\widetilde{R}(\rho)\widetilde{\Theta}(\theta)\tilde{Z}(z) + \beta^2\widetilde{R}(\rho)\widetilde{\Theta}(\theta)\tilde{Z}(z)\right)$), the result will not change, and by assuming all the variables being independent from each other, we obtain three differential equations:

$$\frac{\partial^2\tilde{Z}(z)}{\partial z^2}+\beta^2\tilde{Z}(z)=0$$

E. 24

$$\frac{\partial^2\tilde{\Theta}(\theta)}{\partial\theta^2}+l^2\tilde{\Theta}(\theta)=0$$

E. 25

$$\tilde{\Theta}(\theta)\tilde{Z}(z)\frac{\partial^2\tilde{R}(\rho)}{\partial\rho^2}+\tilde{\Theta}(\theta)\tilde{Z}(z)\frac{1}{\rho}\frac{\partial\tilde{R}(\rho)}{\partial\rho}+\tilde{R}(\rho)\tilde{\Theta}(\theta)\tilde{Z}(z)(n^2k_0^2-\frac{l^2}{\rho^2}-\beta^2)=0$$

E. 26

Solution for E. 24 and E. 25 can be written in the form:

$$\tilde{Z}(z)=e^{-j\beta z}$$

E. 27

$$\tilde{\Theta}(\theta)=e^{jl\theta}$$

E. 28

E. 26 is the Bessel equation and its solutions are the Bessel and the modified Bessel functions of first kind and second kind. In order to select proper solutions, we need to consider that for $r \longrightarrow \infty$ the radial distribution of the fiel should decay to zero, while for $r \longrightarrow 0$ it should not tend to infinity. Based on these considerations, and splitting the analysis in the two different regions of the optical fiber (core and cladding) we consider proper solutions for the E. 28:

$$\tilde{R}(\rho)=\begin{cases}AJ_l(k_T\rho), & \rho\leq a\\ BK_l(\gamma\rho), & \rho>a\end{cases}$$

E. 29

where A and B are two constants, l is the order of the Bessel function and:

$$k_T=\sqrt{k^2n_1^2-\beta^2}$$

$$\gamma=\sqrt{\beta^2-k^2n_0^2}$$

E. 30

k_T and γ are the transverse parameters related to the propagation constant and they describe how the field decays in the core and in the cladding region, respectively. The electric field and its derivative needs to be continuous at the boundary $\rho = a$; by applying this boundary condition we obtain the characteristic equation for an optical fiber:

$$k_Ta\frac{J_{l\pm1}(k_Ta)}{J_l(k_Ta)}=\pm\gamma a\frac{K_{l\pm1}(\gamma a)}{K_l(\gamma a)}$$

E. 31

If we consider that:

$$u=k_Ta=a\sqrt{k^2n_1^2-\beta^2}$$

$$\mathrm{w} = \gamma \mathrm{a} = \mathrm{a}\sqrt{\beta^2 - \mathrm{k}^2 \mathrm{n}_0^2}$$

E. 32

and:

$$\mathrm{u}^2 + \mathrm{w}^2 = \mathrm{k}^2(\mathrm{n}_1^2 - \mathrm{n}_0^2)\mathrm{a}^2 = \mathrm{v}^2$$

E. 33

being v is the *fiber parameter* related to the waveguide properties, such as numerical aperture and radius, and to the light wavelength, it appears immediately clear that E. 31 can be solved graphically. For each value l=0,±1,±2,… , there exist multiple solutions (m) for u and w, thus there are multiple intersections between E. 31 and E. 33 by considering that that $\mathrm{u} > 0$ and $\mathrm{w} < \mathrm{v}$. Knowing u and w allows for the calculation of the transverse parameters and for a full computation of the modes propagating inside the optical fiber.

Appendix 2

In Chapter 1 I described the free-radical chain polymerization mechanism and focused on the importance of the two-photon absorption cross-section $\delta_{2\mathrm{A}}$. The light absorption mechanism is the key aspect for understanding the intrinsic physical differences between one and two-photon polymerization mechanisms. To model the kinetics of both, we first have to describe how a focused light beam propagates within a photopolymer and how it is absorbed. This can be done by simulating how a certain initial monomer concentration $[\mathrm{M}_0]$ is converted into a polymer, and for this purpose I used the software *Matlab*. In this derivation we don't consider the influence of scavengers and nonlocal effects, such as diffusion.

Appendix 2.1

Initiating Gaussian beam

Because of the symmetry of the problem, we consider a 2D model in the *xy* space; *z* is the optical beam propagation direction and is considered to be the axis from the focusing optics (e.g. microscope objective). Assuming linearly polarized light, the x-propagating component of the electric field of a initiating Gaussian beam focused in a photopolymer can be written as [66]:

$$\mathrm{E}_\mathrm{x}(\mathrm{y},\mathrm{z}) = \mathrm{E}_0 \frac{\omega_0}{\omega(\mathrm{z})} \mathrm{e}^{\frac{\mathrm{y}^2}{\omega(\mathrm{z})^2}} \mathrm{e}^{-\mathrm{i}(\frac{\mathrm{ky}^2}{2\mathrm{R}(\mathrm{z})}+\mathrm{kz}-\eta(\mathrm{z}))}$$

E. 34

with:

- E_0 nominal electric field in $\left[\frac{\mathrm{V}}{\mathrm{m}}\right]$:

$$\mathrm{E}_0 = \sqrt{\frac{2\phi_0}{\mathrm{cn}_0\varepsilon_0}}$$

E. 35

- ω_0 beam waist at the focus in $[\mathrm{m}]$

$$\omega_0 = \frac{\lambda}{\pi n_0 NA}$$

E. 36

- $\omega(z)$ beam waist at depth z in the photopolymer, in $[m]$:

$$\omega(z) = \omega_0 \sqrt{\left(\frac{z}{z_R}\right)^2 + 1}$$

E. 37

- $R(z)$ the wavefront radius of curvature at a distance z from the optics, in $[m]$:

$$R(z) = z\left(\left(\frac{z}{z_R}\right)^2 + 1\right)$$

E. 38

- $\eta(z)$ Gouy phase:

$$\eta(z) = \tan^{-1}\left(\frac{z}{z_R}\right)$$

E. 39

- k wavenumber in $[m^{-1}]$

In E. 35 we can find:

- ϕ_0 the nominal beam intensity in $\left[\frac{W}{m^2}\right]$:

$$\phi_0 = \frac{2P_{av}}{\pi\omega_0^2}$$

E. 40

- the speed of light c=2.99792458 $\left[\frac{m}{s}\right]$
- n_0 refractive index of the photopolymer
- ε_0=8.854187818 $[\frac{F}{m}]$ the vacuum permittivity

where: P_{av} is the average optical power, measured after the focusing optics in $[W]$.

Moreover:

- λ is the illumination wavelength in $[m]$
- NA is the numerical aperture of the focusing optics
- z_R is the Rayleigh range in $[m]$:

$$z_R = \frac{\pi n_0 \omega_0^2}{\lambda}$$

E. 41

Finally, the intensity propagation profile can be expressed as:

$$\phi(y,z) = \frac{1}{2} c n_0 \varepsilon_0 |E_x(y,z)|^2$$

E. 42

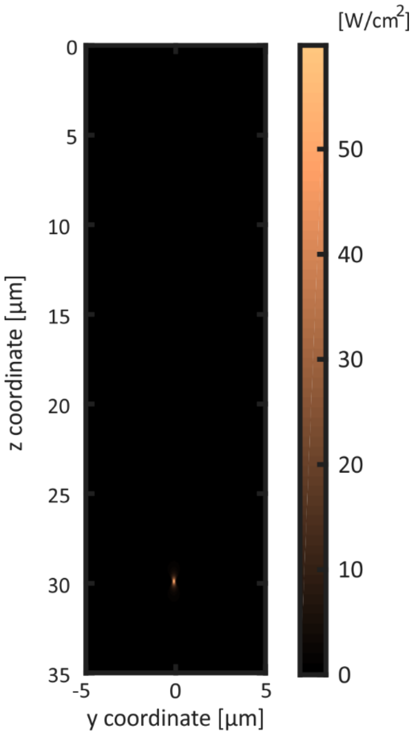

Figure A2.1 Initiating beam intensity spatial distribution and simulation orientation. The beam is focused in z= 30 µm into the photo-polymer; the refractive index of the material is considered to be n_0=1.5 at 340 nmwavelength and NA= 0.7. The average optical power is P_{av}=10 nW.

Appendix 2.2

One-photon polymerization

The *rate of polymerization* R_p can be defined as the rate at which the monomers disappear during the polymerization reaction [108]. Under the *steady-state approximation*, according to which the concentration of radicals instantaneously increases and then reaches a saturation level, it can be expressed as follows:

$$R_p = -\frac{d[M(t)]}{dt} = k_p[M(t)]\sqrt{\frac{R_i}{2k_t}}$$

E. 43

being $[M(t)]$ the monomer concentration, R_i the initiation rate, and k_p and k_t the propagation and termination constants, respectively. The rate of initiation R_i is the fundamental parameter which regulates the amount of photoactive molecules which are created at a certain moment of the process, and at any point (y,z) into the material:

$$\mathrm{R}_{\mathrm{i}_{1\mathrm{PP}}} = 2\mathrm{fI}_{\mathrm{a}}$$

E. 44

The initiation rate R_{i} (E. 44) depends on the photoinitiator efficiency f and the volumetric absorbed light I_{a}; this expression follows the convention according to which one photoinitiator yields two radicals, and this motivates the presence of the factor 2. f is in general a factor ≤ 1 and represents the percentage probability of the photoinitiator of yielding two radicals.

In linear processes and assuming a Gaussian beam illumination profile (Figure A2.1), the volumetric absorbed light I_{a} corresponds to the z-derivative of the absorbed light intensity between two different planes along the optical propagation [108], and therefore it can be expressed as:

$$\mathrm{I}_{\mathrm{a}} = \varepsilon[\mathrm{I}_0]\phi(\mathrm{y},\mathrm{z})\mathrm{e}^{-\varepsilon[\mathrm{I}_0]\Delta\mathrm{z}}$$

E. 45

where $\Delta\mathrm{z}$ corresponds to the travelling distance of light into the material, and $[\mathrm{I}_0]$ is the initial photoinitiator concentration. By plugging E. 42 into E. 45, one can find the spatial distribution of the initiated molecules, and therefore the one-photon polymerization profile (Figure 1.14 (a)). Figure A2.1 shows the computed intensity distribution for a Gaussian beam focused in z=30 µm into a photopolymer having refractive index n=1.5 at λ=340 nm wavelength. The NA of the focusing objective is considered to be 0.7, the average power is P_{av}=10 nW and the exposure time is set to be t_{exp}=0.05 s.

Table 3 summarizes the physical parameters used in the one-photon polymerization profile distribution simulation exemplified in Figure 1.14 (a).

Parameter	Value	Unit
$\boldsymbol{\lambda}$	340	nm
NA	0.7	-
$\boldsymbol{n_0}$	1.5	-
$\boldsymbol{P_{av}}$	10	nW
$\boldsymbol{[PI_0]}$	0.01	mol/L
$\boldsymbol{[M_0]}$	3.1	mol/L
$\boldsymbol{f}$	0.8	-
$\boldsymbol{\varepsilon}$	1.75 10^4 [172]	L/mol/cm
$\boldsymbol{k_p}$	10^3 [108]	L/mol/s
$\boldsymbol{k_t}$	10^7 [108]	L/mol/s
$\boldsymbol{t_{exp}}$	0.05	s

Table 3 Physical parameters for the computation of the one-photon polymerization profile.

Appendix 2.3

Two-photon polymerization

The main difference between one-photon and two-photon polymerization mechanisms is that, while in 1PP the initiation rate R_{i} is linearly proportional to the photoinitating beam intensity, in two-photon polymerization R_{i} depends on the square of the flux of the initiating beam (Figure A2.2) [36]:

$$\mathrm{R}_{\mathrm{i}_{2\mathrm{PP}}} = -\frac{\mathrm{d}\,[\mathrm{I(t)}]}{\mathrm{dt}} = \frac{1}{2}\delta_{2\mathrm{A}}[\mathrm{I(t)}]\mathrm{F}^2$$

E. 46

With δ_{2A} being the two-photon absorption cross-section and F the photon flux of the photoinitiating beam ($\left[\frac{\text{photons}}{\text{s cm}^2}\right]$); the factor $\frac{1}{2}$ indicates that two photons are generally required to create one excited state.

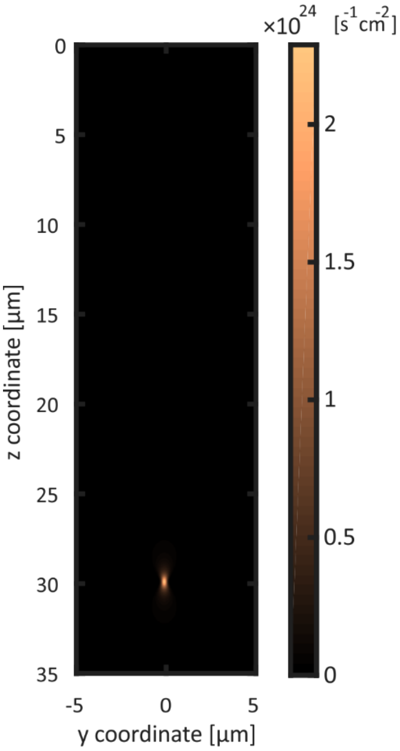

Figure A2.2 Photon flux square spatial profile.

E. 46 is solved for:

$$[\mathrm{I(t)}] = [I_0]e^{-\frac{1}{2}\delta_{2A}F^2t}$$

E. 47

In two-photon polymerization, femtosecond pulsed lasers are focused in order to trigger the photopolymerization reaction; considering the physical parameters listed in Table 4, and τ being the time interval in which the laser is on during the reaction, the amount of polymer molecules created in $t = \tau$, is showed in Figure 1.14 (b).

Parameter	Value	Unit
$\boldsymbol{\lambda}$	680	nm
NA	0.7	-
$\boldsymbol{n_0}$	1.5	-
$\boldsymbol{P_{av}}$	10	nW
RR	80	MHz
Δt	140	fs
$\boldsymbol{[PI_0]}$	0.01	mol/L
$\boldsymbol{[M_0]}$	3.1	mol/L
$\boldsymbol{f}$	0.9	-
$\boldsymbol{\delta_{2A}}$	35 [124]	GM
$\boldsymbol{k_p}$	10^3 [108]	L/mol/s
$\boldsymbol{k_t}$	10^7 [108]	L/mol/s
$\boldsymbol{v}$	5	µm/s

Table 4 Physical parameters for the computation of the two-photon polymerization profile.

Appendix 3

As I presented in Chapter 3 and Chapter 4, phenylacetylene and divinylbenzene (DVB) were found to be working candidates for the fabrication of optical waveguides inside PDMS through multiphoton polymerization. Their molecular structure is reported in Figure A3.1.

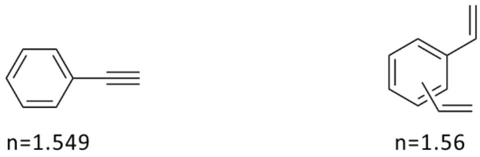

(a) (b)

Figure A3.1 Molecular structure of phenylacetylene (a) and divinylbenzene (b).

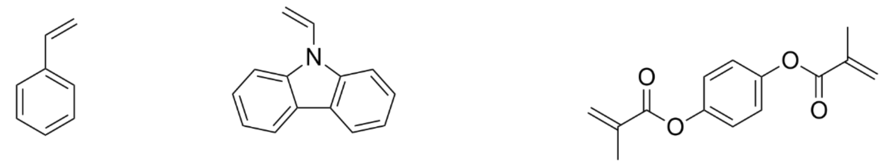

Styrene
n=1.55

9-Vinylcarbazole (solid)
n=1.68

1,4-Phenylene dimethacrylate (solid)
n=1.515

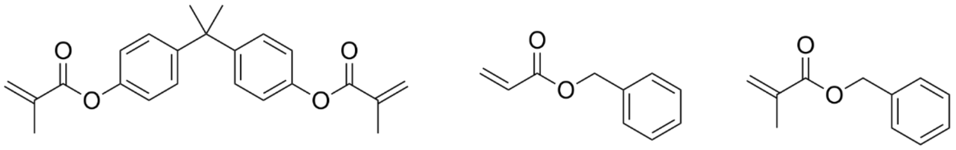

Bisphenol A dimethacrylate (solid)
n=1.54

Benzyl acrylate
n=1.52

Benzyl methacrylate
n=1.51

Figure A3.2 Monomers with high refractive indices.

Many monomer-photoinitiator combinations were tested in the early stage of the project.

Figure A3.2 shows all the monomers with high refractive indices (n > 1.5) we have tested throughout this research. The photoinitiators we have selected for testing are reported in Figure A3.3.

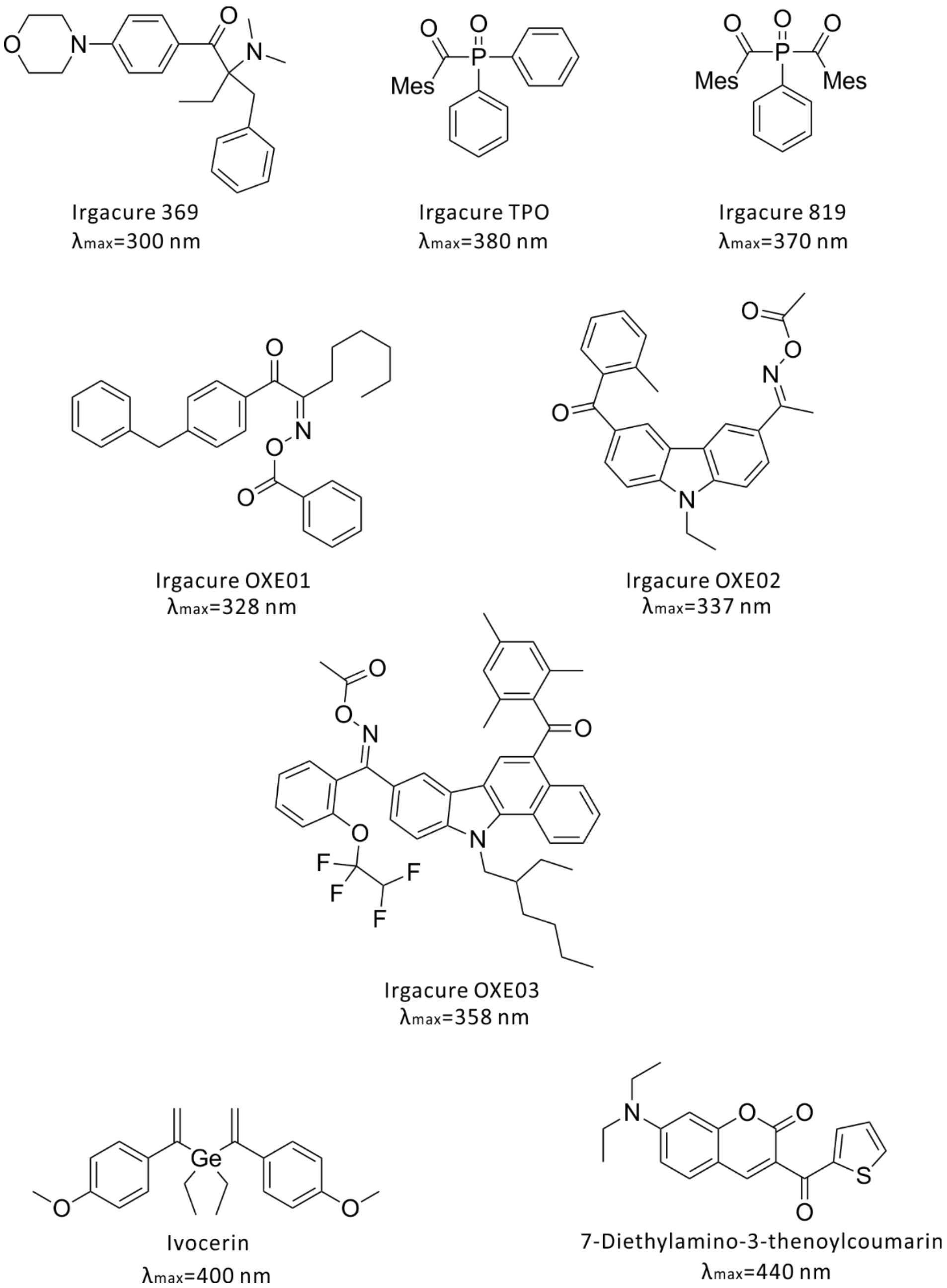

Irgacure 369
λmax=300 nm

Irgacure TPO
λmax=380 nm

Irgacure 819
λmax=370 nm

Irgacure OXE01
λmax=328 nm

Irgacure OXE02
λmax=337 nm

Irgacure OXE03
λmax=358 nm

Ivocerin
λmax=400 nm

7-Diethylamino-3-thenoylcoumarin
λmax=440 nm

Figure A3.3 Commercially available photoinitiators.

Different combinations of monomers, crosslinkers and commercially available photoinitiators were tested by one-photon polymerization (UV irradiation) first. The promising formulations were then tested by two-photon polymerization and they are summarized in Table 5.

Monomer	Crosslinker	Crosslinker [wt%]	PI	PI [wt%]	λ_{2PP}[nm]	Polymerization	Waveguiding
Phenylacetylene	-	-	-	-	680	yes	yes
Phenylacetylene	-	-	DETC	1		yes	no
Phenylacetylene	-	-	Irgacure 819	2	740	no	-
Phenylacetylene	-	-	Irgacure OXE01	2	680	yes	no

Divinylbenzene	-	-	-	-	680	no	-
Divinylbenzene	-	-	Irgacure OXE02	1	680	yes	yes
Divinylbenzene	-	-	Irgacure OXE02	2.5	680	yes	yes
Divinylbenzene	-	-	Irgacure OXE02	5	680	yes	yes
Divinylbenzene	-	-	Irgacure OXE01	1	680	yes	no
Divinylbenzene	-	-	Irgacure OXE01	2	680	yes	no
Divinylbenzene	-	-	Irgacure OXE01	5	680	yes	no
Divinylbenzene	-	-	Irgacure OXE01	10	680	yes	no
Divinylbenzene	-	-	Irgacure OXE03	1	720	yes	no
Divinylbenzene	-	-	Irgacure OXE03	1	720	yes	no
Divinylbenzene	-	-	Irgacure OXE03	5	720	yes	no
Divinylbenzene	-	-	Irgacure OXE03	10	720	yes	no
Styrene	-	-	-	-	680	no	-
Styrene	-	-	DETC	0.25	780	yes	no
Styrene	-	-	DETC	0.5	780	yes	no
Styrene	-	-	DETC	0.75	780	yes	no
Styrene	-	-	DETC	1	780	yes	no
Styrene	-	-	DETC	1.5	780	yes	no
Styrene	-	-	DETC	2	780	yes	no
Styrene	-	-	Ivocerin	1	800	yes	no
Styrene	-	-	Irgacure OXE01	0.75	680	yes	no
Styrene	-	-	Irgacure OXE01	1	680	yes	no
Styrene	-	-	Irgacure OXE01	2.5	680	yes	no
Styrene	DVB	20	Irgacure OXE01	1	680	yes	no
Styrene	DVB	20	Irgacure OXE01	2.5	680	yes	no
Styrene	DVB	20	Irgacure OXE01	5	680	no	-
Styrene	DVB	20	Irgacure OXE02	2.5	680	no	-
Styrene	DVB	20	Irgacure OXE03	2.5	720	no	-
Styrene	DVB	20	Irgacure TPO	2.5	760	no	-
Styrene	DVB	20	Irgacure 819	2.5	740	no	-
Styrene	-	-	Irgacure 369	0.5	680	yes	no
Styrene	-	-	Irgacure 369	0.75	680	yes	no
Styrene	DVB	20	Irgacure 369	2.5	680	yes	no

Table 5 Monomer/PI combinations we have tested throughout the project.

The main results can be summarized as follows:

- Phenylacetylene doesn’t polymerize in the presence of 7-diethylamino-3-thenoylcoumarin (DETC) and Irgacure 819;
- Phenylacetylene polymerizes in the presence of Irgacure OXE01 but there is no waveguiding;
- Phenylacetylene can polymerize thanks to self-initiation without a photoinitiator; the resulting waveguides can guide light;
- DVB doesn’t polymerize without a photoinitiator; DVB polymerizes in the presence of Irgacure OXE01 and Irgacure OXE03 but there is no waveguiding;
- DVB polymerizes in the presence of Irgacure OXE02 and the resulting waveguides can guide light;
- Styrene doesn’t polymerize without a PI;
- Styrene doesn’t polymerize in the presence of Irgacure OXE02, Irgacure OXE03, Irgacure TPO and Irgacure 819;
- Ivocerin, Irgacure OXE01 and Irgacure 369 can trigger the styrene polymerization reaction but waveguides don’t guide light;
- Irgacure 819 did not yield the photopolymerization of any of the monomers we have tested;

- Acrylate-based monomers always failed in our experiments, most likely due to their slight polar nature and poor solubility in PDMS.

Although DETC and Irgacure OXE01 successfully triggered the photopolymerization reaction of the monomers we have selected, no waveguiding effects were observed; this is possibly due to absorption caused by the presence of the PI molecules in the waveguide structure. Moreover, waveguides fabricated based on styrene were frail and did not sustain the solvent process to remove unreacted monomer and PI, possibly due to a small molecular weight in the polymer product and the lack of crosslinking.

Appendix 4

Silicon wafers have been manufactured at the Center of Micro and Nano-Technology of EPFL (CMi) and sent to Sonova. The process flow for the realization of the wafers (Figure A4.1) consists of a standard photolithography fabrication method; here I report the photolithographic procedure for the fabrication of Wafer 4. A thin layer of suitable photoresist (2 µm) has been spin coated and exposed to laser light of appropriate wavelength for removal in a mask-less direct laser writing tool (Heidelberg MLA 150). After developing of the photoresist, the molding grooves have been etched into silica by means of a HF chemistry etcher (SPTS uEtch). The remaining photoresist has been stripped and a second pattern has been created onto silicon by means of a fluorine chemistry etcher (AMS 200 Alcatel SE) for the realization of the grooved structures. The desired dimensions of the structures were achieved with high accuracy.

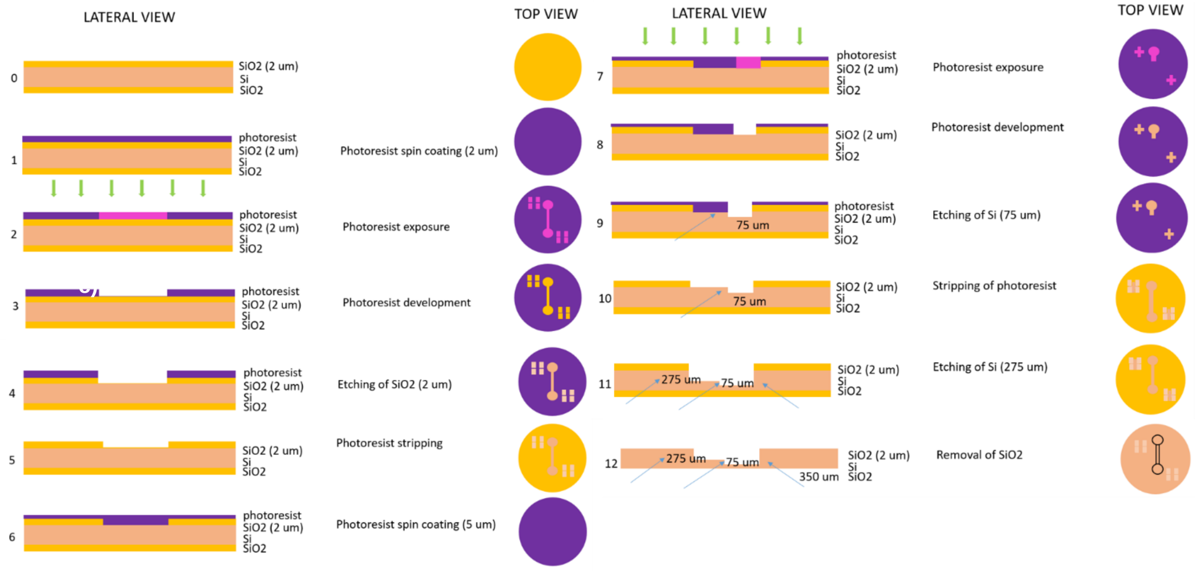
LATERAL VIEW
TOP VIEW
0
SiO2 (2 um)
Si
SiO2
1
photoresist
SiO2 (2 um)
Si
SiO2
Photoresist spin coating (2 um)
2
photoresist
SiO2 (2 um)
Si
SiO2
Photoresist exposure
3
photoresist
SiO2 (2 um)
Si
SiO2
Photoresist development
4
photoresist
SiO2 (2 um)
Si
SiO2
Etching of SiO2 (2 um)
5
SiO2 (2 um)
Si
SiO2
Photoresist stripping
6
photoresist
SiO2 (2 um)
Si
SiO2
Photoresist spin coating (5 um)
LATERAL VIEW
TOP VIEW
7
photoresist
SiO2 (2 um)
Si
SiO2
Photoresist exposure
8
SiO2 (2 um)
Si
SiO2
Photoresist development
9
75 um
photoresist
SiO2 (2 um)
Si
SiO2
Etching of Si (75 um)
10
75 um
SiO2 (2 um)
Si
SiO2
Stripping of photoresist
11
275 um
75 um
SiO2 (2 um)
Si
SiO2
Etching of Si (275 um)
12
275 um
75 um
350 um
SiO2 (2 um)
Si
SiO2
Removal of SiO2

Figure A4.1 Photolithographic process flow for the fabrication of Silicon dioxide grooved wafers for the PDMS microendoscope prototype realization.

Appendix 5

In Paragraph 6.3.2 of Chapter 6 I have described the procedure for the calibration of the cladding. We have printed structures like the one depicted in Figure 6.4 (b), at varying laser power percentage (from 35% to 45 %) and writing speed (from 6000 to 10000 µm/s). The goal of this calibration was to identify the experimental parameters for the 3D printing of undamaged, uniform, and homogeneous objects where higher refractive index cores have to be embedded.

The geometries need to resemble the designed model and show uniform phase accumulation from holographic measurements. Here, I report the full calibration data we have extrapolated from the recorded holograms. Figure A5.1 and Figure A5.2 show the longitudinal and transversal cross-sectional profiles averaged along the whole sample dimensions, respectively. As the writing speed is increased, the printed object shows deteriorated phase profiles in terms of homogeneity, and the average value decreases. In other words, at reduced speed it takes higher power percentages to have resembling samples and homogeneous refractive index value along their length.

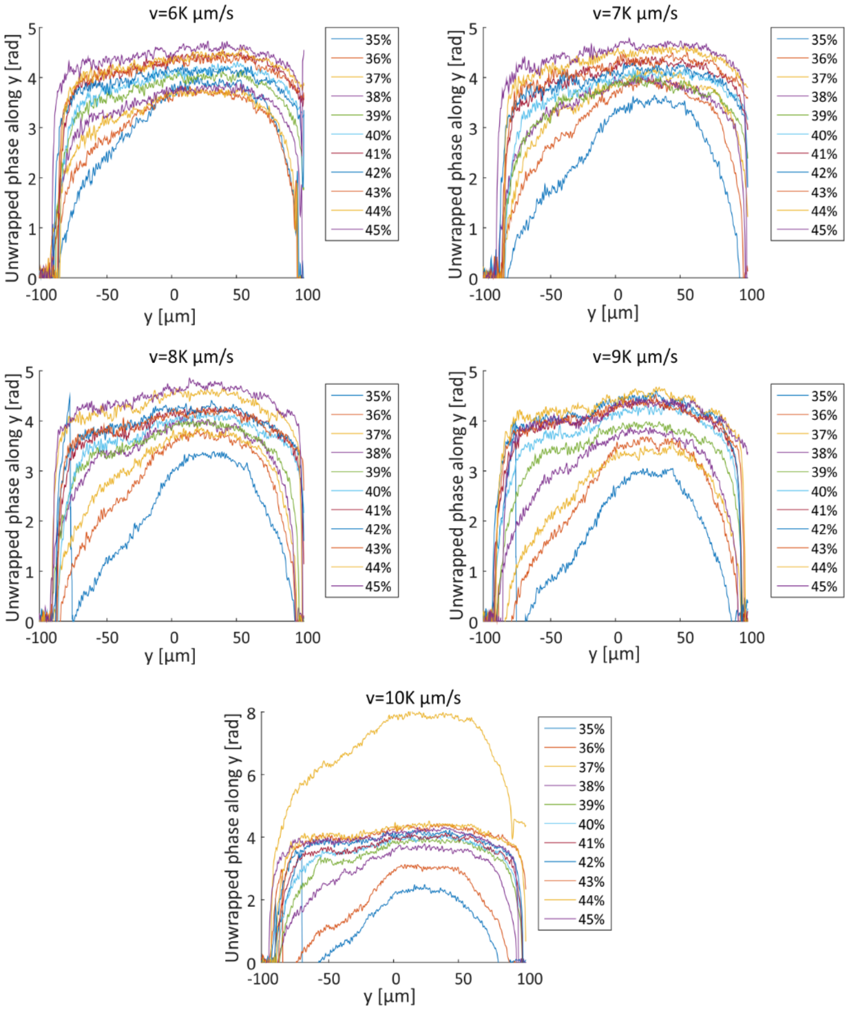

Figure A5.1 Longitudinal phase accumulations of 40 x 13 x 200 µm objects (D x H x L in Figure 6.4 (b)) for the cladding calibration.

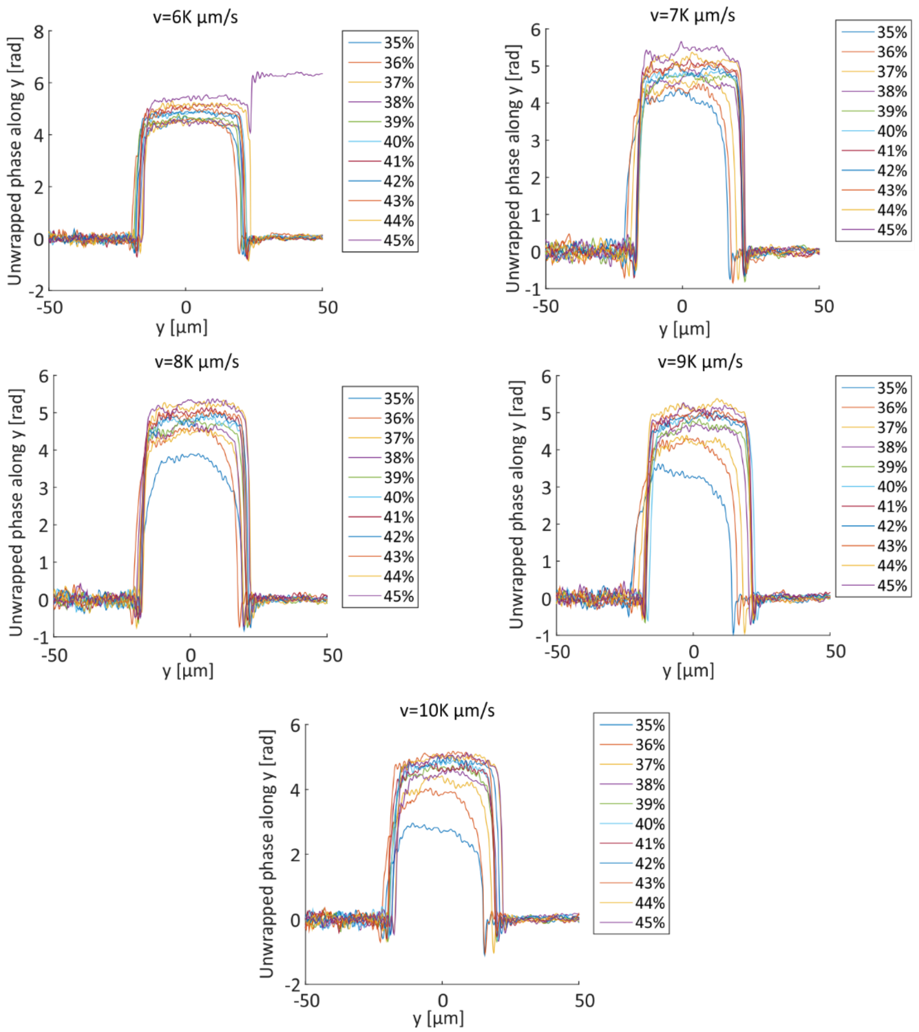

Figure A5.2 Longitudinal phase accumulations of 40 x 13 x 200 µm objects (D x H x L in Figure 6.4 (b)) for the cladding calibration.

References

1. Amiri, I.S., et al., *Introduction to Photonics: Principles and the Most Recent Applications of Microstructures.* Micromachines, 2018. **9**(9): p. 452.
2. Selvaraja, S.K. and P. Sethi, *Review on Optical Waveguides*. 2018.
3. Azadeh, M., *Fiber optics engineering*. 2009: Springer.
4. Richardson, D.J., J.M. Fini, and L.E. Nelson, *Space-division multiplexing in optical fibres.* Nature photonics, 2013. **7**(5): p. 354-362.
5. Zervas, M.N. and C.A. Codemard, *High power fiber lasers: a review.* IEEE Journal of selected topics in Quantum Electronics, 2014. **20**(5): p. 219-241.
6. Fermann, M.E. and I. Hartl, *Ultrafast fiber laser technology.* IEEE Journal of Selected Topics in Quantum Electronics, 2009. **15**(1): p. 191-206.
7. Udd, E. and W.B. Spillman Jr, *Fiber optic sensors: an introduction for engineers and scientists*. 2011: John Wiley & Sons.
8. Katzir, A., *Lasers and optical fibers in medicine*. 2012: Elsevier.
9. Ma, H., A.K.-Y. Jen, and L.R. Dalton, *Polymer-Based Optical Waveguides: Materials, Processing, and Devices.* Advanced Materials, 2002. **14**(19): p. 1339-1365.
10. Tong, X.C., *Polymer-Based Optical Waveguides*, in *Advanced Materials for Integrated Optical Waveguides*. 2014, Springer International Publishing: Cham. p. 377-418.
11. Han, X.-Y., et al., *Recent progress of imprinted polymer photonic waveguide devices and applications.* Polymers, 2018. **10**(6): p. 603.
12. Nieweglowski, K., et al., *Optical coupling with flexible polymer waveguides for chip-to-chip interconnects in electronic systems.* Microelectronics Reliability, 2018. **84**: p. 121-126.
13. Dangel, R., et al., *Polymer waveguides for electro-optical integration in data centers and high-performance computers.* Optics Express, 2015. **23**(4): p. 4736-4750.
14. Soma, K. and T. Ishigure, *Fabrication of a Graded-Index Circular-Core Polymer Parallel Optical Waveguide Using a Microdispenser for a High-Density Optical Printed Circuit Board.* IEEE Journal of Selected Topics in Quantum Electronics, 2013. **19**(2): p. 3600310-3600310.
15. Dangel, R., et al., *Polymer-Waveguide-Based Board-Level Optical Interconnect Technology for Datacom Applications.* IEEE Transactions on Advanced Packaging, 2008. **31**(4): p. 759-767.
16. Choi, C., et al., *Flexible Optical Waveguide Film Fabrications and Optoelectronic Devices Integration for Fully Embedded Board-Level Optical Interconnects.* Journal of Lightwave Technology, 2004. **22**(9): p. 2168.
17. Parks, J.W. and H. Schmidt, *Flexible optofluidic waveguide platform with multi-dimensional reconfigurability.* Scientific Reports, 2016. **6**: p. 33008.
18. Asghari, F., et al., *Biodegradable and biocompatible polymers for tissue engineering application: a review.* Artificial Cells, Nanomedicine, and Biotechnology, 2017. **45**(2): p. 185-192.
19. Choi, M., et al., *Step-Index Optical Fiber Made of Biocompatible Hydrogels.* Advanced Materials, 2015. **27**(27): p. 4081-4086.
20. Yetisen, A.K., et al., *Glucose-Sensitive Hydrogel Optical Fibers Functionalized with Phenylboronic Acid.* Advanced Materials, 2017. **29**: p. 1606380.
21. Zeng, W., et al., *Fiber-Based Wearable Electronics: A Review of Materials, Fabrication, Devices, and Applications.* Advanced Materials, 2014. **26**(31): p. 5310-5336.
22. Guo, J., et al., *Stretchable and Temperature-Sensitive Polymer Optical Fibers for Wearable Health Monitoring.* Advanced Functional Materials, 2019. **29**(33): p. 1902898.
23. Jorfi, M., et al., *Physiologically responsive, mechanically adaptive polymer optical fibers for optogenetics.* Optics Letters, 2014. **39**(10): p. 2872-2875.

24. Park, S., et al., *One-step optogenetics with multifunctional flexible polymer fibers.* Nature Neuroscience, 2017. **20**(4): p. 612-619.
25. Rubehn, B., et al. *Polymer-based shaft microelectrodes with optical and fluidic capabilities as a tool for optogenetics*. in *2011 Annual International Conference of the IEEE Engineering in Medicine and Biology Society*. 2011.
26. Wang, Z., et al., *Measurements of scattered light on a microchip flow cytometer with integrated polymer based optical elements.* Lab on a Chip, 2004. **4**(4): p. 372-377.
27. Baum, A., et al., *Mechanisms of femtosecond laser-induced refractive index modification of poly(methyl methacrylate).* Journal of the Optical Society of America B, 2010. **27**(1): p. 107-111.
28. Pätzold, W.M., A. Demircan, and U. Morgner, *Low-loss curved waveguides in polymers written with a femtosecond laser.* Optics Express, 2017. **25**(1): p. 263-270.
29. Pätzold, W.M., et al., *Cascaded-focus laser writing of low-loss waveguides in polymers.* Optics Letters, 2016. **41**(6): p. 1269-1272.
30. Amirsolaimani, B., et al. *Electro-optic polymer channel waveguide fabrication using multiphoton direct laser writing*. in *2015 IEEE Optical Interconnects Conference (OI)*. 2015.
31. Lindenmann, N., et al., *Photonic wire bonding: a novel concept for chip-scale interconnects.* Optics Express, 2012. **20**(16): p. 17667-17677.
32. Zgraggen, E., et al., *Laser Direct Writing of Single-Mode Polysiloxane Optical Waveguides and Devices.* Journal of Lightwave Technology, 2014. **32**(17): p. 3036-3042.
33. Wang, S., V. Vaidyanathan, and B. Borden, *Polymer optical channel waveguide components fabricated by using a laser direct writing system.* Journal of Applied Science & Engineering Technology, 2009. **3**.
34. Elmogi, A., et al., *Comparison of epoxy-and siloxane-based single-mode optical waveguides defined by direct-write lithography.* Optical Materials, 2016. **52**: p. 26-31.
35. Prajzler, V., et al., *Flexible polymer planar optical waveguides.* Radioengineering, 2014. **23**(3): p. 776-782.
36. Baldacchini, T., *Three-dimensional microfabrication using two-photon polymerization: fundamentals, technology, and applications*. 2015: William Andrew.
37. Gattass, R.R. and E. Mazur, *Femtosecond laser micromachining in transparent materials.* Nature Photonics, 2008. **2**: p. 219.
38. Maruo, S., O. Nakamura, and S. Kawata, *Three-dimensional microfabrication with two-photon-absorbed photopolymerization.* Optics letters, 1997. **22**(2): p. 132-134.
39. Pao, Y.H. and P. Rentzepis, *Laser-induced production of free radicals in organic compounds.* Applied Physics Letters, 1965. **6**(5): p. 93-95.
40. Cabrera, M., J. Jezequel, and J. Andre, *Three-dimensional machining by laser photopolymerization.* Lasers in Polymer Science Technology, 1989: p. 73-95.
41. Wu, E.-S., et al., *Two-photon lithography for microelectronic application*. Microlithography '92. Vol. 1674. 1992: SPIE.
42. Cumpston, B.H., et al., *Two-photon polymerization initiators for three-dimensional optical data storage and microfabrication.* Nature, 1999. **398**(6722): p. 51-54.
43. Farsari, M. and B.N. Chichkov, *Two-photon fabrication.* Nature Photonics, 2009. **3**(8): p. 450-452.
44. Maruo, S., K. Ikuta, and K. Hayato. *Light-driven MEMS made by high-speed two-photon microstereolithography*. in *Technical Digest. MEMS 2001. 14th IEEE International Conference on Micro Electro Mechanical Systems (Cat. No. 01CH37090)*. 2001. IEEE.
45. Schizas, C., et al., *On the design and fabrication by two-photon polymerization of a readily assembled micro-valve.* The International Journal of Advanced Manufacturing Technology, 2010. **48**(5-8): p. 435-441.
46. Ovsianikov, A., A. Ostendorf, and B.N. Chichkov, *Three-dimensional photofabrication with femtosecond lasers for applications in photonics and biomedicine.* Applied Surface Science, 2007. **253**(15): p. 6599-6602.
47. Xing, J.-F., M.-L. Zheng, and X.-M. Duan, *Two-photon polymerization microfabrication of hydrogels: an advanced 3D printing technology for tissue engineering and drug delivery.* Chemical Society Reviews, 2015. **44**(15): p. 5031-5039.
48. Sakellari, I., et al., *Two-photon polymerization of titanium-containing sol–gel composites for three-dimensional structure fabrication.* Applied Physics A, 2010. **100**(2): p. 359-364.
49. Amato, L., et al., *Integrated three-dimensional filter separates nanoscale from microscale elements in a microfluidic chip.* Lab on a Chip, 2012. **12**(6): p. 1135-1142.
50. Serbin, J., et al., *Femtosecond laser-induced two-photon polymerization of inorganic–organic hybrid materials for applications in photonics.* Optics letters, 2003. **28**(5): p. 301-303.

51. Vázquez, R.M., et al., *Fabrication of binary Fresnel lenses in PMMA by femtosecond laser surface ablation.* Optics Express, 2011. **19**(12): p. 11597-11604.
52. Cojoc, G., et al., *Optical micro-structures fabricated on top of optical fibers by means of two-photon photopolymerization.* Microelectronic Engineering, 2010. **87**(5-8): p. 876-879.
53. Malinauskas, M., et al., *Femtosecond laser polymerization of hybrid/integrated micro-optical elements and their characterization.* Journal of Optics, 2010. **12**(12): p. 124010.
54. Gissibl, T., et al., *Two-photon direct laser writing of ultracompact multi-lens objectives.* Nature Photonics, 2016. **10**(8): p. 554-560.
55. Bichler, S., et al. *Two-photon patterning of optical waveguides in flexible polymers*. in *Linear and Nonlinear Optics of Organic Materials IX*. 2009. International Society for Optics and Photonics.
56. Nguyen, D.H., et al. *Three-dimensional buried polymer waveguides via femtosecond direct laser writing with two-photon absorption*. in *Micro-Optics 2014*. 2014. International Society for Optics and Photonics.
57. Nguyen, H.H.D., et al., *Photo-structurable polymer for interlayer single-mode waveguide fabrication by femtosecond laser writing.* Optical Materials, 2017. **66**: p. 110-116.
58. Infuehr, R., et al., *Functional polymers by two-photon 3D lithography*. Vol. 254. 2007. 836-840.
59. Woods, R., et al., *3D optical waveguides produced by two photon photopolymerisation of a flexible silanol terminated polysiloxane containing acrylate functional groups.* Optical Materials Express, 2014. **4**(3): p. 486-498.
60. Schneider, F., et al., *Process and material properties of polydimethylsiloxane (PDMS) for Optical MEMS.* Sensors and Actuators A: Physical, 2009. **151**(2): p. 95-99.
61. Schneider, F., et al., *Mechanical properties of silicones for MEMS.* Journal of Micromechanics and Microengineering, 2008. **18**(6): p. 065008.
62. Mata, A., A.J. Fleischman, and S. Roy, *Characterization of Polydimethylsiloxane (PDMS) Properties for Biomedical Micro/Nanosystems.* Biomedical Microdevices, 2005. **7**(4): p. 281-293.
63. Mogensen, K.B., et al., *Integration of polymer waveguides for optical detection in microfabricated chemical analysis systems.* Applied Optics, 2003. **42**(19): p. 4072-4079.
64. Song, W., A.E. Vasdekis, and D. Psaltis, *Elastomer based tunable optofluidic devices.* Lab on a Chip, 2012. **12**(19): p. 3590-3597.
65. Okamoto, K., *Fundamentals of optical waveguides*. 2006: Academic press.
66. Saleh, B.E. and M.C. Teich, *Fundamentals of photonics*. 2019: john Wiley & sons.
67. Bianchi, S. and R. Di Leonardo, *A multi-mode fiber probe for holographic micromanipulation and microscopy.* Lab on a Chip, 2012. **12**(3): p. 635-639.
68. Caravaca-Aguirre, A.M., et al., *Real-time resilient focusing through a bending multimode fiber.* Optics express, 2013. **21**(10): p. 12881-12887.
69. Papadopoulos, I.N., et al., *Focusing and scanning light through a multimode optical fiber using digital phase conjugation.* Optics express, 2012. **20**(10): p. 10583-10590.
70. Papadopoulos, I.N., et al., *High-resolution, lensless endoscope based on digital scanning through a multimode optical fiber.* Biomedical optics express, 2013. **4**(2): p. 260-270.
71. Čižmár, T. and K. Dholakia, *Exploiting multimode waveguides for pure fibre-based imaging.* Nature communications, 2012. **3**(1): p. 1-9.
72. Choi, Y., et al., *Scanner-free and wide-field endoscopic imaging by using a single multimode optical fiber.* Physical review letters, 2012. **109**(20): p. 203901.
73. Kakkava, E., et al., *Deep learning-based image classification through a multimode fiber in the presence of wavelength drift.* Applied Sciences, 2020. **10**(11): p. 3816.
74. Kakkava, E., et al., *Imaging through multimode fibers using deep learning: The effects of intensity versus holographic recording of the speckle pattern.* Optical Fiber Technology, 2019. **52**: p. 101985.
75. Borhani, N., et al., *Learning to see through multimode fibers.* Optica, 2018. **5**(8): p. 960-966.
76. Rahmani, B., et al., *Multimode optical fiber transmission with a deep learning network.* Light: Science & Applications, 2018. **7**(1): p. 1-11.
77. Reed, W.A., M.F. Yan, and M.J. Schnitzer, *Gradient-index fiber-optic microprobes for minimally invasive in vivo low-coherence interferometry.* Optics Letters, 2002. **27**(20): p. 1794-1796.
78. Mao, Y., et al., *Graded-index fiber lens proposed for ultrasmall probes used in biomedical imaging.* Applied Optics, 2007. **46**(23): p. 5887-5894.
79. Pochechuev, M., I. Fedotov, and A. Zheltikov, *An ultraslim all-fiber microendoscope for depth-resolved imaging.* Applied Physics Letters, 2018. **113**(19): p. 191102.
80. Scolaro, L., et al., *High-sensitivity anastigmatic imaging needle for optical coherence tomography.* Optics Letters, 2012. **37**(24): p. 5247-5249.

81. Subramanian, K., et al., *Kagome fiber based ultrafast laser microsurgery probe delivering micro-Joule pulse energies.* Biomedical Optics Express, 2016. **7**(11): p. 4639-4653.
82. Conkey, D.B., et al., *High power, ultrashort pulse control through a multi-core fiber for ablation.* Optics express, 2017. **25**(10): p. 11491-11502.
83. Beaudou, B., et al., *Millijoule laser pulse delivery for spark ignition through kagome hollow-core fiber.* Optics letters, 2012. **37**(9): p. 1430-1432.
84. Choi, H.Y., et al., *Single-body lensed photonic crystal fibers as side-viewing probes for optical imaging systems.* Optics Letters, 2008. **33**(1): p. 34-36.
85. Choi, H.Y., et al. *Side-imaging lensed photonic crystal fiber probe*. in *Coherence Domain Optical Methods and Optical Coherence Tomography in Biomedicine XII*. 2008. International Society for Optics and Photonics.
86. Gmitro, A.F. and D. Aziz, *Confocal microscopy through a fiber-optic imaging bundle.* Optics Letters, 1993. **18**(8): p. 565-567.
87. Gmitro, A.F., A.R. Rouse, and A. Kano. *In vivo fluorescence confocal microendoscopy*. in *Proceedings IEEE International Symposium on Biomedical Imaging*. 2002.
88. Dubaj, V., et al., *Optic fibre bundle contact imaging probe employing a laser scanning confocal microscope.* Journal of Microscopy, 2002. **207**(2): p. 108-117.
89. Göbel, W., et al., *Miniaturized two-photon microscope based on a flexible coherent fiber bundle and a gradient-index lens objective.* Optics letters, 2004. **29**(21): p. 2521-2523.
90. Garofalakis, A., et al., *Characterization of a multicore fiber image guide for nonlinear endoscopic imaging using two-photon fluorescence and second-harmonic generation.* Journal of Biomedical Optics, 2019. **24**(10): p. 106004.
91. Warren, S.C., et al., *Adaptive multiphoton endomicroscopy through a dynamically deformed multicore optical fiber using proximal detection.* Optics Express, 2016. **24**(19): p. 21474-21484.
92. Conkey, D., et al., *Lensless two-photon imaging through a multicore fiber with coherence-gated digital phase conjugation.* Journal of Biomedical Optics, 2016. **21**(4): p. 045002.
93. Kostuk, R.K. and J. Carriere, *Interconnect characteristics of fiber image guides.* Applied Optics, 2001. **40**(15): p. 2428-2434.
94. Kosaka, H., et al., *A two-dimensional optical parallel transmission using a vertical-cavity surface-emitting laser array module and an image fiber.* IEEE Photonics Technology Letters, 1997. **9**(2): p. 253-255.
95. Li, Y., et al., *Fiber-image-guide-based bit-parallel optical interconnects.* Applied Optics, 1996. **35**(35): p. 6920-6933.
96. Wurster, L.M., et al., *Endoscopic optical coherence tomography with a flexible fiber bundle.* Journal of biomedical optics, 2018. **23**(6): p. 066001.
97. Xie, T., et al., *Fiber-optic-bundle-based optical coherence tomography.* Optics letters, 2005. **30**(14): p. 1803-1805.
98. Amatore, C., et al., *Remote fluorescence imaging of dynamic concentration profiles with micrometer resolution using a coherent optical fiber bundle.* Analytical chemistry, 2004. **76**(24): p. 7202-7210.
99. Shahmoon, A., et al., *In vivo minimally invasive interstitial multi-functional microendoscopy.* Scientific reports, 2013. **3**(1): p. 1-7.
100. Orth, A., et al., *Optical fiber bundles: Ultra-slim light field imaging probes.* Science advances, 2019. **5**(4): p. eaav1555.
101. Andresen, E.R., et al., *Ultrathin endoscopes based on multicore fibers and adaptive optics: a status review and perspectives.* Journal of biomedical optics, 2016. **21**(12): p. 121506.
102. Steelman, Z.A., et al., *Comparison of imaging fiber bundles for coherence-domain imaging.* Applied optics, 2018. **57**(6): p. 1455-1462.
103. Reichenbach, K.L. and C. Xu, *Numerical analysis of light propagation in image fibers or coherent fiber bundles.* Optics express, 2007. **15**(5): p. 2151-2165.
104. Chen, X., K.L. Reichenbach, and C. Xu, *Experimental and theoretical analysis of core-to-core coupling on fiber bundle imaging.* Optics express, 2008. **16**(26): p. 21598-21607.
105. Ortega-Quijano, N., F. Fanjul-Vélez, and J.L. Arce-Diego, *Optical crosstalk influence in fiber imaging endoscopes design.* Optics Communications, 2010. **283**(4): p. 633-638.
106. Kim, D., et al., *Toward a miniature endomicroscope: pixelation-free and diffraction-limited imaging through a fiber bundle.* Optics letters, 2014. **39**(7): p. 1921-1924.
107. Boyd, R.W., *Nonlinear optics*. 2020: Academic press.
108. Odian, G., *Principles of polymerization*. 2004: John Wiley & Sons.
109. Sun, H.-B., S. Matsuo, and H. Misawa, *Three-dimensional photonic crystal structures achieved with two-photon-absorption photopolymerization of resin.* Applied physics letters, 1999. **74**(6): p. 786-788.
110. Nguyen, L.H., M. Straub, and M. Gu, *Acrylate-based photopolymer for two-photon microfabrication and photonic applications.* Advanced Functional Materials, 2005. **15**(2): p. 209-216.

111. Göppert-Mayer, M., *Über Elementarakte mit zwei Quantensprüngen.* Annalen der Physik, 1931. **401**(3): p. 273-294.
112. Reinhardt, B.A., et al., *Highly active two-photon dyes: design, synthesis, and characterization toward application.* Chemistry of Materials, 1998. **10**(7): p. 1863-1874.
113. Morales, A.R., et al., *Design, synthesis, and structural and spectroscopic studies of push–pull two-photon absorbing chromophores with acceptor groups of varying strength.* The Journal of organic chemistry, 2013. **78**(3): p. 1014-1025.
114. Kannan, R., et al., *Diphenylaminofluorene-based two-photon-absorbing chromophores with various π-electron acceptors.* Chemistry of Materials, 2001. **13**(5): p. 1896-1904.
115. Lee, S., et al., *Dependence of the Two-Photon Absorption Cross Section on the Conjugation of the Phenylacetylene Linker in Dipolar Donor− Bridge− Acceptor Chromophores.* The Journal of Physical Chemistry A, 2005. **109**(43): p. 9767-9774.
116. Barzoukas, M. and M. Blanchard-Desce, *Molecular engineering of push–pull dipolar and quadrupolar molecules for two-photon absorption: A multivalence-bond states approach.* The Journal of Chemical Physics, 2000. **113**(10): p. 3951-3959.
117. Norman, P., Y. Luo, and H. Ågren, *Large two-photon absorption cross sections in two-dimensional, charge-transfer, cumulene-containing aromatic molecules.* The Journal of chemical physics, 1999. **111**(17): p. 7758-7765.
118. Pond, S.J., et al., *One-and two-photon spectroscopy of donor− acceptor− donor distyrylbenzene derivatives: effect of cyano substitution and distortion from planarity.* The Journal of Physical Chemistry A, 2002. **106**(47): p. 11470-11480.
119. Fang, Z., et al., *Bridged triphenylamine-based dendrimers: tuning enhanced two-photon absorption performance with locked molecular planarity.* Organic letters, 2009. **11**(1): p. 1-4.
120. Xu, C. and W.W. Webb, *Measurement of two-photon excitation cross sections of molecular fluorophores with data from 690 to 1050 nm.* JOSA B, 1996. **13**(3): p. 481-491.
121. Panusa, G., et al., *Photoinitiator-free multi-photon fabrication of compact optical waveguides in polydimethylsiloxane.* Optical Materials Express, 2019. **9**(1): p. 128-138.
122. Panusa, G., et al., *Fabrication of Sub-Micron Polymer Waveguides through Two-Photon Polymerization in Polydimethylsiloxane.* Polymers, 2020. **12**(11): p. 2485.
123. Goodman, J.W., *Introduction to Fourier optics*. 2005: Roberts and Company Publishers.
124. Schafer, K.J., et al., *Two-photon absorption cross-sections of common photoinitiators.* Journal of Photochemistry and Photobiology A: Chemistry, 2004. **162**(2): p. 497-502.
125. Pucher, N., et al., *Structure–Activity Relationship in D-π-A-π-D-Based Photoinitiators for the Two-Photon-Induced Photopolymerization Process*. Vol. 42. 2009. 6519-6528.
126. Liska, R. and B. Seidl, *1,5-Diphenyl-1,4-diyn-3-one: A highly efficient photoinitiator.* Journal of Polymer Science Part A: Polymer Chemistry, 2005. **43**(1): p. 101-111.
127. Lee, J.N., C. Park, and G.M. Whitesides, *Solvent Compatibility of Poly(dimethylsiloxane)-Based Microfluidic Devices.* Analytical Chemistry, 2003. **75**(23): p. 6544-6554.
128. Silva Soares, L.E., A.A. Martin, and A.L. Barbosa Pinheiro, *Degree of conversion of composite resin: a Raman study.* Journal of clinical laser medicine & surgery, 2003. **21**(6): p. 357-362.
129. Decker, C. and K. Moussa, *A new method for monitoring ultra-fast photopolymerizations by real-time infra-red (RTIR) spectroscopy.* Die Makromolekulare Chemie: Macromolecular Chemistry and Physics, 1988. **189**(10): p. 2381-2394.
130. Jiang, L.J., et al., *Two-photon polymerization: investigation of chemical and mechanical properties of resins using Raman microspectroscopy.* Optics letters, 2014. **39**(10): p. 3034-3037.
131. Lee, T.W., K. Kim, and M.S. Kim, *Raman spectroscopy of phenylacetylene adsorbed on silver surfaces.* Journal of molecular structure, 1992. **274**: p. 59-73.
132. Abramczyk, H. and G. Waliszewska, *Raman Spectra of Phenylacetylene in Acetonitrile and Methylcyclohexane at Low Temperatures. 2. Structural Order and Vibrational Relaxation in Frozen Matrices at 77 K.* The Journal of Physical Chemistry A, 1998. **102**(40): p. 7765-7771.
133. Cai, D., et al., *Raman, mid-infrared, near-infrared and ultraviolet–visible spectroscopy of PDMS silicone rubber for characterization of polymer optical waveguide materials.* Journal of Molecular Structure, 2010. **976**(1): p. 274-281.
134. Boyd, R.W., *Nonlinear Optics, Third Edition*. 2008: Academic Press, Inc.
135. Kewitsch, A.S. and A. Yariv, *Self-focusing and self-trapping of optical beams upon photopolymerization.* Optics Letters, 1996. **21**(1): p. 24-26.
136. Neher, D., et al., *Third-harmonic generation in polyphenylacetylene: Exact determination of nonlinear optical susceptibilities in ultrathin films.* Chemical Physics Letters, 1989. **163**(2): p. 116-122.

137. Cumpston, B.H., et al., *Two-photon polymerization initiators for three-dimensional optical data storage and microfabrication.* Nature, 1999. **398**(6722): p. 51-54.
138. Li, Z., et al., *A Straightforward Synthesis and Structure–Activity Relationship of Highly Efficient Initiators for Two-Photon Polymerization.* Macromolecules, 2013. **46**(2): p. 352-361.
139. Stankova, N.E., et al., *Optical properties of polydimethylsiloxane (PDMS) during nanosecond laser processing.* Applied Surface Science, 2016. **374**: p. 96-103.
140. Barr, S., E. Hill, and A. Bayat, *Patterning of novel breast implant surfaces by enhancing silicone biocompatibility, using biomimetic topographies.* Eplasty, 2010. **10**: p. e31-e31.
141. Antikainen, A., R.-J. Essiambre, and G.P. Agrawal, *Determination of modes of elliptical waveguides with ellipse transformation perturbation theory.* Optica, 2017. **4**(12): p. 1510-1513.
142. Feng, T., et al., *Pulse-propagation modeling and experiment for femtosecond-laser writing of waveguide in Nd: YAG.* Crystals, 2019. **9**(8): p. 434.
143. Sumetsky, M., *How thin can a microfiber be and still guide light?* Optics letters, 2006. **31**(7): p. 870-872.
144. Bhanu, V.A. and K. Kishore, *Role of oxygen in polymerization reactions.* Chemical Reviews, 1991. **91**(2): p. 99-117.
145. Home, H., B.H. Consumer, and D. Depot, *The Incidence of Hearing Loss Around the World.*
146. Ristok, S., et al., *Stitching-free 3D printing of millimeter-sized highly transparent spherical and aspherical optical components.* Optical Materials Express, 2020. **10**(10): p. 2370-2378.
147. Bogucki, A., et al., *Ultra-long-working-distance spectroscopy of single nanostructures with aspherical solid immersion microlenses.* Light: Science & Applications, 2020. **9**(1): p. 48.
148. Ocier, C.R., et al., *Direct laser writing of volumetric gradient index lenses and waveguides.* Light: Science & Applications, 2020. **9**(1): p. 1-14.
149. Balli, F., et al., *An ultrabroadband 3D achromatic metalens.* Nanophotonics, 2021. **10**(4): p. 1259-1264.
150. Gehring, H., et al., *Low-loss fiber-to-chip couplers with ultrawide optical bandwidth.* APL Photonics, 2019. **4**(1): p. 010801.
151. Dietrich, P.-I., et al., *In situ 3D nanoprinting of free-form coupling elements for hybrid photonic integration.* Nature Photonics, 2018. **12**(4): p. 241-247.
152. Bogucki, A., et al., *Optical fiber micro-connector with nanometer positioning precision for rapid prototyping of photonic devices.* Optics express, 2018. **26**(9): p. 11513-11518.
153. Gissibl, T., et al., *Sub-micrometre accurate free-form optics by three-dimensional printing on single-mode fibres.* Nature Communications, 2016. **7**(1): p. 1-9.
154. Gissibl, T., M. Schmid, and H. Giessen, *Spatial beam intensity shaping using phase masks on single-mode optical fibers fabricated by femtosecond direct laser writing.* Optica, 2016. **3**(4): p. 448-451.
155. Bertoncini, A. and C. Liberale, *3D printed waveguides based on photonic crystal fiber designs for complex fiber-end photonic devices.* Optica, 2020. **7**(11): p. 1487-1494.
156. Yu, J., et al., *3D nanoprinted kinoform spiral zone plates on fiber facets for high-efficiency focused vortex beam generation.* Optics Express, 2020. **28**(25): p. 38127-38139.
157. Li, J., et al., *Ultrathin monolithic 3D printed optical coherence tomography endoscopy for preclinical and clinical use.* Light: Science & Applications, 2020. **9**(1): p. 1-10.
158. Blaicher, M., et al., *Hybrid multi-chip assembly of optical communication engines by in situ 3D nano-lithography.* Light: Science & Applications, 2020. **9**(1): p. 1-11.
159. Moughames, J., et al., *Three-dimensional waveguide interconnects for scalable integration of photonic neural networks.* Optica, 2020. **7**(6): p. 640-646.
160. Jain, C., et al., *Hollow core light cage: trapping light behind bars.* ACS Photonics, 2018. **6**(3): p. 649-658.
161. Kim, J., et al., *The Optofluidic Light Cage – On-Chip Integrated Spectroscopy Using an Antiresonance Hollow Core Waveguide.* Analytical Chemistry, 2021. **93**(2): p. 752-760.
162. Guney, M. and G. Fedder, *Estimation of line dimensions in 3D direct laser writing lithography.* Journal of Micromechanics and Microengineering, 2016. **26**(10): p. 105011.
163. Bioucas-Dias, J.M. and G. Valadao, *Phase unwrapping via graph cuts.* IEEE Transactions on Image processing, 2007. **16**(3): p. 698-709.
164. Schmid, M., D. Ludescher, and H. Giessen, *Optical properties of photoresists for femtosecond 3D printing: refractive index, extinction, luminescence-dose dependence, aging, heat treatment and comparison between 1-photon and 2-photon exposure.* Optical Materials Express, 2019. **9**(12): p. 4564-4577.
165. Goodfellow, I., et al., *Deep learning*. Vol. 1. 2016: MIT press Cambridge.
166. LeCun, Y., Y. Bengio, and G. Hinton, *Deep learning.* Nature, 2015. **521**(7553): p. 436-444.
167. Stasio, N., et al., *Light control in a multicore fiber using the memory effect.* Optics express, 2015. **23**(23): p. 30532-30544.

168. Sun, J., N. Koukourakis, and J.W. Czarske, *Complex Wavefront Shaping through a Multi-Core Fiber.* Applied Sciences, 2021. **11**(9): p. 3949.

169. Shao, J., et al., *Fiber bundle imaging resolution enhancement using deep learning.* Optics express, 2019. **27**(11): p. 15880-15890.

170. Shao, J., et al., *Fiber bundle image restoration using deep learning.* Optics letters, 2019. **44**(5): p. 1080-1083.

171. Ocier, C.R., et al., *Direct laser writing of volumetric gradient index lenses and waveguides.* Light: Science & Applications, 2020. **9**(1): p. 196.

172. Fast, D.E., et al., *Wavelength-dependent photochemistry of oxime ester photoinitiators.* Macromolecules, 2017. **50**(5): p. 1815-1823.

Giulia Panusa

PERSONAL INFORMATION

- Born in Rome, Italy, 07.12.1989
- Email : giulia.panusa@epfl.ch - giulia.panusa@gmail.com
- Phone : +41 078 9576959
- Address : EPFL STI IMT LO
  BM 4106 (Bâtiment BM)
  Station 17, CH-1015, Lausanne

STRENGHTS

- PhD in Photonics at EPFL + Nanotechnology Engineering *cum laude*
- 4 years of hands-on experience in optical set ups design, soft matter handling, two-photon polymerization, 3D-printing, microfabrication techniques
- Digital holography, interferometry
- Optical microscopy, optical fibers, simulations of optical waveguides using beam propagation method (BPM)

RESEARCH EXPERIENCE

Nov. 2016-Present

PhD candidate – Optical scientist

Optics Laboratory, Swiss Federal Institute of Technology Lausanne, EPFL

Advisor: Prof. Demetri Psaltis

- Implementation of a process for the fabrication and characterization of polymer optical waveguides in polydimethylsilossane (PDMS) using multiphoton polymerization techniques for the realization of an imaging biomedical device
- Expertise in optical design, digital holography, optical fibers, soft matter handling (PDMS), microscopy techniques, automation using Matlab
- Optical microscopy, spectroscopy
- Expertise in clean room facilities (PDMS line, Nanoscribe GmbH Photonic Professional GT, etc)

- Data analysis, simulations using the beam propagation method (BPM), image processing (Image J, Matlab), image reconstruction by means of deep neural networks (DNNs) techniques

EDUCATION

PhD in Photonics *Nov. 2016-Present*

Optics Laboratory, Swiss Federal Institute of Technology Lausanne, EPFL

Advisor: Prof. Demetri Psaltis

Thesis: *'3D fabrication of sub-micron optical waveguides in PDMS and other polymer materials'*

MCs in Nanotechnology Engineering *Oct. 2012-July 2016*

Università La Sapienza di Roma

Advisor: Prof. Antonio d'Alessandro

Thesis: '*Fabrication of PDMS Optical Waveguides through Two-Photon Polymerization for Cochlear Microendoscopy'*

BCs in Electronic and Telecommunication Engineering *Sep. 2008-Sep 2012*

Università La Sapienza di Roma

Advisor: Prof. Emanuele Piuzzi

Thesis: '*DAQ based Virtual Instrument LabView for Transthoracic Impedance Acquirement and Analysis'*

High School *Sep. 2003-Jul 2008*

Liceo Classico G. Carducci, Merano, BZ, Italy

TECHNICAL SKILLS

- **Optical systems design:** two-photon polymerization 3D printing, interferometry, digital holography, optical waveguides light transmission platforms;
- **Optics:** optical microscopy (confocal, phase, SEM), spectroscopy (Raman), optical fibers, metrology;
- **Cleanroom facilities:** PDMS line, Nanoscribe GmbH Photonic Professional GT+, Bruker Dektak XT Mechanical Profilometer, ACS200 coater and developer, Heidelberg maskless aligner MLA 150, Alcatel AMS200 DSE Plasma etcher, SPTS APS Dielectric plasma etcher, single chamber sputterer Alliance Concept DP650 and wet bench desiccators;
- **Sample preparation:** PDMS and soft material handling.

TEACHING EXPERIENCE

- Teaching assistant for "Mise à Niveau (MAN)", supervising and grading the exams during the spring semester 2017 at EPFL;
- Supervision of a master student for a semester project during fall semester 2017 at EPFL;
- Teaching assistant and exam supervision of the course "Optical engineering II" at EPFL (spring semesters 2017, 2018, 2019);

LANGUAGE AND IT SKILLS

- **Italian** (native), **English** (C1), **German** (C1), **French** (B1/A2)
- **Programming** Matlab, DeScribe; **Data analysis** Origin Pro, Microsoft Excel; **Others** Coreldraw, Image J, Zemax.

AWARDS

- Best Poster award in NAMIS International Summer school Seattle (2018);
- Best Poster award in 'Photonics Integration: advanced materials, new technologies and applications' International Summer school Erice (2016);
- Admission to the Doctoral Program 'Information and Communication Technology', XXXII Cycle, Università La Sapienza di Roma.

LIST OF PUBLICATIONS

Peer-reviewed articles

- ❖ Panusa, G., Pu, Y., Wang, J., Moser, C., & Psaltis, D. (2020). Fabrication of Sub-Micron Polymer Waveguides through Two-Photon Polymerization in Polydimethylsiloxane. Polymers 2020, 12(11), 2485; https://doi.org/10.3390/polym12112485.
- ❖ Pradeep Vallachira Warriam Sasikumar; Eike Müller; Pierrick Clement; Jongmoon Jang; Eirini Kakkava; Giulia Panusa; Demetri Psaltis; Katharina Maniura-Weber; Markus Rottmar; Juergen Brugger; Gurdial Blugan (2020) In Vitro Cytocompatibility Assessment of Ti-Modified, Silicon-oxycarbide-Based, Polymer-Derived, Ceramic-Implantable Electrodes under Pacing Conditions. ACS Applied Materials & Interfaces (IF 8.758) Pub Date : 2020-04-03, doi: 10.1021/acsami.0c01465.
- ❖ Panusa, G., Pu, Y., Wang, J., Moser, C., & Psaltis, D. (2019). Photoinitiator-free multi-photon fabrication of compact optical waveguides in polydimethylsiloxane. Optical Materials Express, 9(1), 128-138. doi: 10.1364/OME.9.000128.

- ❖ P. Vallachira Warriam, G. Blugan, N. Casati, E. Kakkava, G. Panusa, D. Psaltis, J. Kuebler, " Polymer derived silicon oxycarbide ceramic monoliths: Microstructure development and associated materials properties ", Ceramics International 44 (17), 20961-20967 (2018).

Conference papers and presentations

- ❖ International Conference on Solid-State Sensors, Actuators and Microsystems, 20 - 25 June 2021, 'A glass-like carbon MEMS strain sensor', Transducers 2021 Virtual Conference, J. Jang, G. Panusa, G. Boero, J. Brugger (poster).

- Conference on Photonics & Electromagnetics research Symposium 2019 (PIERS 2019), Rome, Italy, Europe, 17-20 June 2019 , “Multi-Photon Fabrication of Ultra-compact Optical Waveguides in Polydimethylsiloxane'', G. Panusa, Y. Pu, J. Wang, C. Moser, D. Psaltis (Oral presentation).
- Fio + LS 2018, Washington DC, 16 – 20 September 2018, “Multi-Photon Fabrication of Ultra-compact Optical Waveguides in Polydimethylsiloxane'', G. Panusa, Y. Pu, J. Wang, C. Moser, D. Psaltis (Oral presentation).
- SPIE Optics + Photonics, San Diego, California, US, 11-15 August 2018, Photoinitiator-free Laser Fabrication of Ultra-compact, Low-loss Waveguides in Polydimethylsiloxane '' G. Panusa, Y. Pu, J. Wang, C. Moser, D. Psaltis (Invited talk).
- CLEO Pacific Rim 2018, Conference on Laser and Electro- Optics, 29 July - 3 August 2018, Hong Kong, “Multi-Photon Fabrication of Ultra-compact Optical Waveguides in Polydimethylsiloxane'', Y. Pu, G. Panusa, J. Wang, C. Moser, D. Psaltis (Oral presentation).
- Conference on Optical MEMS and Nanophotonics 2018 (OMN2018), Lausanne, Switzerland, Europe, 29 July - 2 August 2018, “Multi-Photon Fabrication of Ultra-compact Optical Waveguides in Polydimethylsiloxane'', G. Panusa, Y. Pu, J. Wang, C. Moser, D. Psaltis (Oral presentation).
- CTI Project #19279.2 PFNM-NM; Final report
- CTI Project #19279.2 PFNM-NM; Interim Reports 2 and 3.
- Biweekly update meetings CTI Endoscope meeting with Sonova AG partner.

Lausanne, May 2021

Ce document a été imprimé au Centre d’impression EPFL,
imprimerie climatiquement neutre, certifiée myClimate.